

**HETEROGENEOUS HYDROLYSIS WITH ZINC VAPOR UNDER A
TEMPERATURE GRADIENT FOR EFFICIENT SOLAR HYDROGEN
PRODUCTION**

by

Matthew D. Lindemer

A dissertation submitted to the Faculty of the University of Delaware in partial fulfillment of the requirements for the degree of Doctor of Philosophy in Mechanical Engineering

2017

© 2017 Matthew D. Lindemer
All Rights Reserved

**HETEROGENEOUS HYDROLYSIS WITH ZINC VAPOR UNDER A
TEMPERATURE GRADIENT FOR EFFICIENT SOLAR HYDROGEN
PRODUCTION**

by

Matthew D. Lindemer

Approved: _____
Suresh G. Advani, Ph.D.
Chair of the Department of Mechanical Engineering

Approved: _____
Babatunde A. Ogunnaike, Ph.D.
Dean of the College of Engineering

Approved: _____
Ann L. Ardis, Ph.D.
Senior Vice Provost for Graduate and Professional Education

I certify that I have read this dissertation and that in my opinion it meets the academic and professional standard required by the University as a dissertation for the degree of Doctor of Philosophy.

Signed: _____
Suresh G. Advani, Ph.D.
Professor in charge of dissertation

I certify that I have read this dissertation and that in my opinion it meets the academic and professional standard required by the University as a dissertation for the degree of Doctor of Philosophy.

Signed: _____
Ajay K. Prasad, Ph.D.
Professor in charge of dissertation

I certify that I have read this dissertation and that in my opinion it meets the academic and professional standard required by the University as a dissertation for the degree of Doctor of Philosophy.

Signed: _____
Joseph P. Feser, Ph.D.
Member of dissertation committee

I certify that I have read this dissertation and that in my opinion it meets the academic and professional standard required by the University as a dissertation for the degree of Doctor of Philosophy.

Signed: _____
Bingjun Xu, Ph.D.
Member of dissertation committee

ACKNOWLEDGEMENTS

Funding for this work was provided by the Federal Transit Administration, the Air Products and Chemicals, Inc. Ph.D. Fellowship, and the University of Delaware's NSF-IGERT "Sustainable Energy from Solar Hydrogen" program. Acknowledgment is also due to Mr. Adam Kinzey for help with the reactor fabrication, and Dr. Erik Koepf for help with the reactor design and recommendations on the method of chemical analysis. Special thanks are due to my advisors Dr. Suresh Advani and Dr. Ajay Prasad for their continued support and guidance. Finally, I would like to thank my family and friends for their ongoing encouragement and support during my time in graduate school.

TABLE OF CONTENTS

LIST OF TABLES	ix
LIST OF FIGURES	x
NOMENCLATURE	xviii
ABSTRACT	xxiii
PREFACE	xxv
 Chapter	
1 INTRODUCTION	1
1.1 Motivation	1
1.2 Solar Energy Technologies	3
1.3 Renewable Fuels	4
1.4 Solar Thermochemical Cycles	6
1.5 The Zn/ZnO Thermochemical Cycle	8
1.5.1 Reduction Step	11
1.5.2 Quench Step and Recombination Reaction	12
1.5.3 Hydrolysis Step	16
1.6 Considerations for Hydrolysis Reactor Design	18
1.7 Organization of Thesis	20
2 HETEROGENEOUS HYDROLYSIS WITH ZN VAPOR UNDER A TEMPERATURE GRADIENT: MODELING AND EFFICIENCY ANALYSIS	22
2.1 Heterogeneous Hydrolysis with Zn _(g)	22
2.2 Reactor Model	27
2.3 Model Validation	30
2.4 Thermodynamic Analysis	31
2.5 Results	35
2.5.1 Effect of Temperature Gradient	35

2.5.2	Effect of Equilibrium Assumption	39
2.5.3	Conditions for Zn Condensation	39
2.5.4	Effect of Incomplete Quench Conversion	41
2.6	Conclusions	43
3	EXPERIMENTAL INVESTIGATION OF HETEROGENEOUS HYDROLYSIS WITH ZN VAPOR UNDER A TEMPERATURE GRADIENT	46
3.1	Introduction	46
3.2	Experimental Method	47
3.2.1	Apparatus	47
3.2.2	Experimental Procedure	49
3.2.3	Product Analysis	50
3.3	Results and Discussion	52
3.4	Conclusions	58
4	BACKGROUND ON LATTICE BOLTZMANN METHODS	65
4.1	Background on the Boltzmann Equation	65
4.2	Lattice Boltzmann Model for Incompressible Fluid Flow	68
4.2.1	Multiple-Relaxation-Time Schemes	72
4.2.2	No-Slip Boundary Condition Implementation	74
4.2.3	Advantages of LBM	77
4.3	Lattice Boltzmann Models for Heat/Mass Transport	78
4.3.1	D2Q5 model	80
4.4	Extension to Axisymmetric Coordinates	81
5	LATTICE BOLTZMANN SIMULATION OF A REACTIVE GAS/SOLID PRECIPITATION PROCESS IN A CIRCULAR TUBE	84
5.1	Introduction	84

5.2	LB Models for Flow and Mass Transport	87
5.2.1	Multiple-Relaxation-Time (MRT) Model for Axisymmetric Incompressible Fluid Flow	87
5.2.2	Multiple-Relaxation-Time (MRT) Model for Mass Transport	90
5.3	Model Description	91
5.3.1	Flow Boundary Conditions	91
5.3.2	Mass Transfer Boundary Conditions	94
5.3.3	Non-Dimensional Parameters	96
5.4	Model Validations	97
5.5	Results and Discussion	99
5.5.1	Effect of Re	101
5.5.2	Effect of Da	102
5.5.3	Effect of Sc	104
5.5.4	Effect of Q_A/Q_C	105
5.5.5	Effect of $\phi_{(s)}$	106
5.5.6	Effect of Da_2 with Variable Kinetics	108
5.5.7	Comparison to Experiments	111
5.6	Conclusions	115
6	CONCLUSIONS AND FUTURE WORK	117
6.1	Conclusions	117
6.1.1	Original Contributions	119
6.2	Recommendations for Future Work	119
6.2.1	Improvement of Current Reactor Design	119
6.2.2	Further Confirmation of Equilibrium Shift	120
6.2.3	Removal of ZnO Deposits	120
6.2.4	Two-Step Heterogeneous Hydrolysis of Solar Zn	121
6.2.5	Improvements to LB Model	125
6.2.6	Investigation of Heat Recovery	127
6.3	Future of Solar Thermochemical Cycles	129
6.3.1	Materials	129

6.3.2	Reactor Design	131
6.3.3	Future of the Zn/ZnO Cycle	132
BIBLIOGRAPHY		133
Appendix		
A ADDITIONAL DESIGN DETAILS FOR LABORATORY-SCALE HYDROLYSIS REACTOR		145
B LATTICE BOLTZMANN PROGRAMMING GUIDE		163
B.1	General Programming Approach	163
B.2	Programming for Gas/solid Reactive Precipitation Model	164
C VALIDATION OF LATTICE BOLTZMANN CODES		166
C.1	Cartesian D2Q9 Flow and Mass Transfer Model	166
C.1.1	Couette Flow with Wall Injection and Asymmetric Wall Concentrations	167
C.1.2	Plane Poiseuille Flow with Asymmetric Wall Concentrations	173
C.1.3	Squeezing Flow between Parallel Plates	178
C.2	Axisymmetric D2Q9 MRT Flow Model	181
C.2.1	Squeezing Flow in an Annular Region	181
C.2.2	Squeezing Flow in a Contracting Tube	184
C.2.3	Starting Transient Poiseuille Flow	187
C.3	Axisymmetric D2Q5 MRT Model for Mass Transfer	190
C.3.1	Steady Convective-Diffusion in an Annular Region with Wall Injection	190
C.3.2	Periodic Convective-Diffusion in Slug Flow	192
C.4	Third-Kind Mass Transfer Boundary Condition and Interface Tracking	195
D PERMISSION FROM ELSEVIER		197
E PUBLICATIONS		198

LIST OF TABLES

2.1	Variation of the reaction rate constant k with temperature as determined in Ref. [22]. The averages of the two values at both 900K and 1100K are used in the current model.	25
3.1	Operating conditions and Zn to ZnO conversions for different experiments	54
3.2	Comparison of current results to previous work	58

LIST OF FIGURES

1.1	Schematic of the different steps and material flows in the Zn/ZnO thermochemical cycle for hydrogen production	8
2.1	Equilibrium constant for heterogeneous hydrolysis with Zn vapor and Zn saturation pressure vs. temperature.	23
2.2	Schematic of the plug flow reactor model. The molar flow rate of each species j is updated for each volume 1, 2, 3, . . . based on the reaction on the tube wall.	27
2.3	Validation of numerical model: Numerical results (symbols) compare well with analytical results (lines) for the evolution of molar flux of species A for various temperatures	31
2.4	Schematic of hydrogen production via the Zn/ZnO thermochemical cycle. Material flows are shown in blue, heat flows in orange, and work in green.	33
2.5	Thermodynamic calculations for instantaneous temperature drop from T_i to $800K$ (limiting case for temperature gradient operation)	36
2.6	Thermodynamic calculations for constant temperature operation; $S = 1.0, 2.0$	37
2.7	Thermodynamic calculations for $\frac{dT^*}{dz^*} = 0.5$	38
2.8	Degree of saturation predicted by the model under kinetics-limited conditions. In each case, P_{Zn} drops from 0.5 to below 0.1 in the first 1% of the reactor length due to the mixture being initially very far from equilibrium. The partial pressure of Zn remains well below the saturation pressure, so Zn vapor condensation is not expected.	40
2.9	Evolution of Zn partial pressure with temperature for mass transfer-limited conditions for different reactor radii and temperature gradients for a constant inlet velocity.	42

2.10	Effect of quench conversion on cycle efficiency and heat recovery from hydrolysis with $S = 1.0$, $T_i = 1180$, and an instantaneous temperature drop.	43
3.1	Schematic of experimental setup.	48
3.2	Two-chamber pressure measurement setup used for determining Zn mass in reaction tube samples.	51
3.3	Calibration curve used for determining Zn mass in reaction tube samples.	51
3.4	Reaction tube after an experiment.	52
3.5	ZnO deposits in the entrance region of a reaction tube.	53
3.6	A reaction tube with significant ZnO deposition near the tube entrance.	53
3.7	A reaction tube that is nearly clogged in the entrance region.	60
3.8	Profiles of Zn/ZnO deposits and temperature for Experiment 1, with $T_{max} = 1123$, $T_{min} = 693$, $\dot{n}_{H_2O}/\dot{n}_{Zn} = 16.1$, $\dot{n}_{N_2}/\dot{n}_{Zn} = 0.25$, and $\dot{n}_{tot} = 0.014$ (mol/min).	60
3.9	Profiles of Zn/ZnO deposits and temperature for Experiment 2, with $T_{max} = 1143$, $T_{min} = 747$, $\dot{n}_{H_2O}/\dot{n}_{Zn} = 5.2$, $\dot{n}_{N_2}/\dot{n}_{Zn} = 1.17$, and $\dot{n}_{tot} = 0.016$ (mol/min).	61
3.10	Profiles of Zn/ZnO deposits and temperature for Experiment 4, with $T_{max} = 1133$, $T_{min} = 776$, $\dot{n}_{H_2O}/\dot{n}_{Zn} = 5.14$, $\dot{n}_{N_2}/\dot{n}_{Zn} = 3.62$, and $\dot{n}_{tot} = 0.013$ (mol/min).	61
3.11	Profiles of Zn/ZnO deposits and temperature for Experiment 7, with $T_{max} = 1163$, $T_{min} = 732$, $\dot{n}_{H_2O}/\dot{n}_{Zn} = 2.9$, $\dot{n}_{N_2}/\dot{n}_{Zn} = 0.95$, and $\dot{n}_{tot} = 0.0058$ (mol/min).	62
3.12	Profiles of Zn/ZnO deposits and temperature for Experiment 9, with $T_{max} = 1158$, $T_{min} = 766$, $\dot{n}_{H_2O}/\dot{n}_{Zn} = 1.13$, $\dot{n}_{N_2}/\dot{n}_{Zn} = 0.49$, and $\dot{n}_{tot} = 0.0059$ (mol/min).	62

3.13	Profiles of Zn/ZnO deposits and temperature for Experiment 10, with $T_{max} = 1153$, $T_{min} = 781$, $\dot{n}_{H_2O}/\dot{n}_{Zn} = 0.87$, $\dot{n}_{N_2}/\dot{n}_{Zn} = 0.76$, and $\dot{n}_{tot} = 0.0085$ (mol/min).	63
3.14	SEM image of particulate matter found at exit of reactor in Experiment 7. The arrows indicate ZnO nanowires that grew on homogeneously condensed Zn particles.	63
3.15	SEM image of Zn/ZnO deposits on the inner surface of a reactor tube for Experiment 7. The larger particles are partially oxidized Zn particles. The surface they sit on is a layer of ZnO deposited heterogeneously.	64
3.16	Zn to ZnO conversions vs. $N_2 : Zn$ and $H_2O : Zn$ ratios for various experiments. When a large excess of steam is available, complete conversion is possible. Conversions are generally smaller when lower amounts of steam and inert gas are used due to increased Zn condensation.	64
4.1	Schematic of discrete velocities in the D2Q9 LB model	71
4.2	Schematic of bounce-back with discrete velocity \vec{e}_a intersecting the solid boundary, as well as the incoming population $\vec{e}_{\bar{a}}$	75
4.3	Example of perfect bounce back to point x_{-1} when the $\Delta = 0.5$, i.e., the wall is halfway between the boundary node and the nearest fluid node.	75
4.4	When $\Delta < 0.5$, the approach is to solve at time t , for a fictitious population (in red) that will bounce back exactly to x_{-1} from the wall at $t + 1$	76
4.5	When $\Delta > 0.5$, the approach is to solve the value of $f_a(x_{-1})$ at $t + 1$, knowing that the value of $f_a(x_{-1})$ at t will nearly bounce back (in red), and can thus be used as an interpolation point.	77
4.6	D2Q5 lattice Boltzmann model	80
5.1	Schematic of tube reactor. The wall of the Zn-vapor supply tube shown in grey separates the core and annular flow regions, and the modeled region is enclosed by the blue rectangle.	92
5.2	Schematic of boundary treatment at solid-fluid interface.	95

5.3	Schematics of validation problems I-IV.	98
5.4	Contours of u_z (lattice units) for $Sc = 0.7$, $Da = 1.0$, and $Re = 1.0$, at $t^* = 612.5, 6862.5, 9362.5$. The dashed white line indicates the deposition profile at each time step.	99
5.5	Contours of ϕ for $Sc = 0.7$, $Da = 1.0$, and $Re = 1.0$, at $t^* = 612.5, 6862.5, 9362.5$. The dashed white line indicates the deposition profile at each time step.	100
5.6	Deposition profiles for different values of Re , with $Da = 20.0$, $Sc = 0.7$, $Q_A/Q_C = 1.0$. Results for $t^* = 456.2$ are shown in blue, $t^* = 925.0$ in green, and $t^* = 1393.8$ in red.	102
5.7	Deposition profiles for different values of Re , with $Da = 20.0$, $Sc = 0.7$, $Q_A/Q_C = 1.0$. Results for $t^* = 167.0$ are shown in blue, $t^* = 508.0$ in green, and $t^* = 848.9$ in red.	103
5.8	Deposition profiles for different values of Da , $Re = 10.0$, $Sc = 0.7$, $Q_A/Q_C = 5.0$	104
5.9	Deposition profiles for different values of Da , $Re = 10.0$, $Sc = 0.7$, $Q_A/Q_C = 5.0$. Results for $t^* = 249.5$ are shown in blue, $t^* = 758.8$ in green, and $t^* = 1268.1$ in red.	105
5.10	Deposition profiles for different values of Sc , $Pe = 10.0$, $Da = 20.0$, $Q_A/Q_C = 5.0$ at $t^* = 102.1$ (blue) $t^* = 311.1$ (green) and $t^* = 519.4$ (red).	106
5.11	Deposition profiles for different values of Q_A/Q_C , $Re = 1.0$, $Sc = 0.7$, $Da = 10.0$. Results for $t^* = 1237.5$ are shown in blue, $t^* = 1862.5$ in green, and $t^* = 2487.5$ in red.	107
5.12	Deposition profiles for different values of $\phi_{(s)}$, $Re = 10.0$, $Sc = 0.7$, $Da = 10.0$, and $Q_A/Q_C = 5.0$	108
5.13	Deposition profiles for the varying kinetics case with $Sc = 1.0$, $Da = 0.1$, $Q_A/Q_C = 5.0$, and various values of Re . Results for $t^* = 1516.6$ are shown in blue, $t^* = 7707.1$ in green, and $t^* = 13897.6$ in red	109

5.14	Deposition profiles for the varying kinetics case with $Re = 1.0$, $Sc = 1.0$, $Da = 0.1$, $Q_A/Q_C = 5.0$, and various values of z_0 . Results for $t^* = 1516.6$ are shown in blue, $t^* = 7707.1$ in green, and $t^* = 13897.6$ in red	111
5.15	Deposition profiles for the varying kinetics case with $Re = 1.0$, $Sc = 1.0$, $Da = 0.1$, $Q_A/Q_C = 5.0$, and various values of k_2/k_1 . Results for $t^* = 1516.6$ are shown in blue, $t^* = 7707.1$ in green, and $t^* = 13897.6$ in red	112
5.16	Comparison of constant temperature experimental data from Experiment 4 (top) with simulation for similar values of non-dimensional parameters (bottom).	113
5.17	Comparison of non-isothermal experimental data from Experiment 4 (top) with simulation for similar values of non-dimensional parameters (bottom).	114
6.1	Passivated and exposed Zn after the quench step	123
6.2	Schematic of two-step hydrolysis of solar Zn. Evaporation and oxidation are conducted in separate steps, preventing passivation of Zn particles	124
A.1	Technical drawing of flange support.	146
A.2	Technical drawing of plate 1 (outlet).	147
A.3	Technical drawing of plate 1 (inlet).	148
A.4	Technical drawing of plate 2 (outlet).	149
A.5	Technical drawing of plate 2 (inlet).	150
A.6	Technical drawing of plate 3 (outlet).	151
A.7	Technical drawing of plate 3 (inlet).	152
A.8	Technical drawing of pressing ring.	153
A.9	Technical drawing of flange.	154
A.10	Technical drawing of outlet plate.	155

A.11	Technical drawing of inlet plate.	156
A.12	Technical drawing of heater base.	157
A.13	Technical drawing of thermocouple insert.	158
A.14	Cross-section of entrance sealing assembly.	159
A.15	Assembled reactor with heater made transparent.	160
A.16	View of assembled laboratory-scale hydrolysis reactor. Insulation has been removed from sealing assemblies at inlet and outlet.	161
A.17	Inlet sealing assembly. Steam enters from boiler, on bottom left, with inert gas flows enter just above. Heating tape has been wrapped around these components, as well as the entrance sealing assembly.	161
A.18	Rendering of mating of Zn tube (left) and reaction tube (right), with TC insert surrounding both. Steam flows in the narrow annular region between the tapered end of the Zn tube and the reaction tube.	162
B.1	Flowchart of lattice Boltzmann simulation subroutines.	165
C.1	Solution for horizontal velocity in Couette flow with wall injection.	169
C.2	Solution for horizontal mass flux in Couette flow with wall injection.	170
C.3	Solution for vertical mass flux in Couette flow with wall injection.	171
C.4	Solution for concentration in Couette flow with wall injection	172
C.5	Velocity solution for plane Poiseuille flow with asymmetric wall concentrations	174
C.6	Solution for horizontal mass flux in plane Poiseuille flow with asymmetric wall concentrations.	175
C.7	Solution for vertical mass flux in plane Poiseuille flow with asymmetric wall concentrations.	176
C.8	Solution for concentration in plane Poiseuille flow with asymmetric wall concentrations.	177

C.9	Contours of axial velocity for squeezing flow between parallel plates at $h = 0.5H$ (lattice units).	179
C.10	Profiles of x-velocity relative error at $x = 0$ for squeezing flow between parallel plates.	180
C.11	Profiles of y-velocity relative error at $x = 0$ for squeezing flow between parallel plates.	180
C.12	Contours of z-velocity for squeezing flow in an annular region (lattice units).	182
C.13	Contours of r-velocity for squeezing flow in an annular region (lattice units).	182
C.14	Profiles of r-velocity relative error for BGK case, squeezing flow in an annular region.	183
C.15	Profiles of r-velocity relative error for MRT case, squeezing flow in an annular region.	183
C.16	Relative error profiles for u_r at $z = L/2$ and $Re = 0.001$ for flow in a contracting tube of initial radius R_0 and half-length L at different values of R/R_0	185
C.17	Relative error profiles for u_z at $z = L/2$ and $Re = 0.001$ for flow in a contracting tube of initial radius R_0 and half-length L at different values of R/R_0	186
C.18	Relative error profiles for u_z for $Re = 10$ for starting Poiseuille flow at different values of non-dimensional time $t\nu/R^2$	188
C.19	Evolution of velocity profile for starting transient Poiseuille flow . . .	189
C.20	Profile of relative error for species concentration ϕ for convective-diffusion in an annular region with wall injection for various values of Pe	191
C.21	Contours of concentration for periodic convective-diffusion in slug flow	193
C.22	Normalized cumulative global error \mathbf{E}_2 after one period Γ for $St = 20$, $Pe = 20$ for periodic diffusion in slug flow.	194

C.23	Validation of third-kind boundary mass transfer boundary treatment and interface tracking scheme for slow growth with kinetics-limited reaction. Here, the time is scaled as $t^* = tD/L^2$	196
D.1	Elsevier Table of Author Rights [151]	197

NOMENCLATURE

<i>a</i>	body acceleration [$\frac{m}{s^2}$]
<i>A</i>	molar flow rate of ZnO into dissociation reactor [$\frac{mol}{s}$]
<i>c</i>	sound speed ($=\frac{\delta x}{\delta t}$) [$\frac{m}{s}$ or lattice units]
<i>C</i>	solar concentration ratio (=10,000)
<i>c_p</i>	molar constant pressure specific heat [$\frac{J}{molK}$]
<i>D</i>	mass diffusivity [$\frac{m^2}{s}$]
<i>Da</i>	Damköhler number
\vec{e}	discrete velocity vector (lattice units)
<i>E</i>	internal energy [$\frac{kJ}{kg}$]
<i>E</i>	error
<i>f</i>	fluid velocity distribution function
<i>g</i>	concentration distribution function
<i>G</i>	Gibbs free energy [$\frac{kJ}{mol}$]
<i>G</i>	flow source term
<i>h</i>	mass or heat transfer coefficient [$\frac{m}{s}$ or $\frac{W}{mK}$]
<i>H</i>	enthalpy [$\frac{kJ}{mol}$]
<i>HR</i>	heat recovery factor
<i>i</i>	imaginary unit
<i>I</i>	terrestrial solar irradiance ($1000\frac{W}{m^2}$)
<i>I</i>	modified Bessel function
<i>J</i>	molar flux [$\frac{mol}{m^2s}$]
<i>J</i>	Bessel function
<i>K</i>	equilibrium constant [<i>atm</i> or <i>atm</i> ⁻¹]
<i>k</i>	reaction rate constant [$\frac{mol}{atm^2m^2s}$]

\mathbf{k}	spatial frequency [m^{-1}]
L	reactor length [m]
m	mass [g]
M	molar mass [$\frac{g}{mol}$]
\mathbf{M}	collision matrix
Ma	Mach number
n	number of moles [mol]
\dot{n}	molar flow rate [$\frac{mol}{s}$]
N	number of lattice units
P	pressure or partial pressure [atm]
Pe	Peclet number ($= \frac{u_{av}R}{D}$)
q	heat transfer rate [W]
Q	volumetric flow rate [$\frac{m^3}{s}$]
r	radial coordinate
R	radius [m]
\mathbf{R}	mass transfer source term
Re	Reynolds number ($= \frac{u_{av}N_r}{\nu}$)
R_u	universal gas constant ($8.314 \frac{J}{molK}$)
r''	reaction rate [$\frac{mol}{m^2s}$]
S	water to Zn stoichiometry
\mathcal{S}	source term
Sc	Schmidt number ($= \frac{\nu}{D}$)
St	Strouhal number ($= \sqrt{\frac{R^2}{\Gamma D}}$)
T	temperature [K]
t	time [s]
\vec{u}	hydrodynamic fluid velocity [$\frac{m}{s}$]
v	microscopic fluid velocity [$\frac{mol}{s}$]
w	weight function
\mathcal{W}	wall location function

W	power [kW]
x	molar fraction
\vec{x}	position vector
t	time [s]
z	axial coordinate [m]

Greek symbols:

α	fractional yield of hydrolysis reactor
β	fractional yield of quench process
γ	specific heat ratio
Γ	time period
Δ	change in quantity
ϵ	asymptotic expansion parameter
η	efficiency
θ	local angle of curved solid boundary [rad]
κ	dimensional relaxation time
λ	Bessel function roots
Λ	source term weight function
ν	kinematic viscosity [$\frac{m^2}{s}$]
ρ	fluid density [$\frac{kg}{m^3}$]
σ	Stefan-Boltzmann constant ($= 5.67 \times 10^{-8} [\frac{W}{m^2K^4}]$)
σ	Bessel function parameter
τ	dimensionless relaxation time
ϕ	molar concentration [$\frac{mol}{m^3}$]
Φ	molar flux [$\frac{mol}{m^2s}$]
χ	ratio of total Zn vapor to inert gas
ω	collision operator
ω	time frequency [s^{-1}]
Ω	relaxation time vector

Subscripts:

-3	third-nearest fluid node to boundary
-2	second-nearest fluid node to boundary
-1	nearest fluid node to boundary
0	reference value
1	referring to core region radius
2	referring to annular region inner radius
a	discrete velocity index
\bar{a}	opposite direction to a
A	referring to annular region
amb	ambient temperature (298 K)
(aq)	aqueous solution
atm	atmospheric pressure (1 atm)
av	average quantity
b	direction normal to a
\bar{b}	opposite direction to b
B	nearest solid node to boundary
C	referring to core region
dep	deposited mass
eq	equilibrium condition
exp	referring to duration of experiment
f	final value
F	referring to flow model
(g)	gas state
H_2	H_2 product
H_2O	H_2O reactant
i	inlet value or inner radius
$init$	initial
j	index

<i>(l)</i>	liquid state
<i>LBM</i>	lattice Boltzmann results
<i>max</i>	maximum
<i>n</i>	inward normal to solid boundary
<i>N₂</i>	<i>N₂</i> carrier gas
<i>o</i>	outlet value or outer radius
<i>r</i>	in radial direction
<i>(s)</i>	solid state
<i>sat</i>	at saturation point
<i>tot</i>	total
<i>tube</i>	referring to reaction tube mass
<i>w</i>	referring to value on solid boundary (wall)
<i>x</i>	horizontal direction in Cartesian coordinates
<i>y</i>	vertical direction in Cartesian coordinates
<i>z</i>	in axial direction
<i>Zn</i>	<i>Zn</i> reactant
<i>ZnO</i>	<i>ZnO</i> product

Superscripts:

<i>eq</i>	equilibrium condition
<i>f</i>	forward reaction
<i>r</i>	reverse reaction

ABSTRACT

Thermochemical cycles driven by concentrated sunlight are a promising method of producing hydrogen in a renewable manner. One such cycle that has received considerable attention is the two-step Zn/ZnO thermochemical cycle. The current work focuses on the hydrolysis step of the cycle wherein water vapor is reduced by Zn to produce hydrogen. A novel approach in which the oxidation reaction is conducted heterogeneously under an axial temperature gradient has been suggested as a promising method for quickly and reliably splitting water using a relatively low percentage of inert carrier gas in the mixture. Simulations and experiments were conducted in order to gain insight into the oxidation of Zn with water vapor, to help identify optimal reactor design and operating parameters, and to demonstrate proof-of-concept for this approach.

A thermodynamic model of the complete Zn/ZnO thermochemical cycle was used along with a simplified model of a non-isothermal heterogeneous hydrolysis reactor in order to highlight the effect of different hydrolysis conditions on the overall solar-to-chemical exergy efficiency, as well as the potential for heat recovery during hydrolysis. The effects of the reactor's temperature profile and mass transfer were also investigated using the model to highlight the potential for Zn condensation during the reaction.

A laboratory-scale reactor was also developed in order to demonstrate the heterogeneous hydrolysis under cooling conditions, and to quantify the Zn to ZnO conversion under different temperature ranges, and combinations of inert gas, steam, and Zn flow rates. The reactor is a tube furnace with a series of interior quartz tubes that form separate Zn evaporation and heterogeneous reaction zones. A wet chemical method was used to determine the respective amounts of ZnO that was deposited by the reaction as well as any Zn that condensed in the reaction tube.

A numerical model was also developed which accounts for the effects of incompressible fluid flow, mass transfer, reaction kinetics, as well as the accumulation of solid ZnO deposits in order to form a basis for predicting the transient behavior of a single reaction channel in heterogeneous hydrolysis reactor utilizing Zn vapor. The lattice Boltzmann method was used for this model because of its simplicity in handling of moving boundaries with complex shapes as well as the ease and efficiency of implementing the algorithm in a parallel computing environment. A parametric study was conducted in order to characterize the performance of the reactor channel for different non-dimensional parameters.

PREFACE

This work began as part of the National Science Foundation’s Integrative Graduate Education and Research Traineeship (IGERT) program “Sustainable Energy from Solar Hydrogen” at the University of Delaware. The goal of the IGERT program is to train the next generation of scientists to have the interdisciplinary knowledge and training to solve complex problems with societal and scientific importance at the national and international level. As one of several chemical, mechanical, electrical, and materials engineers at the University of Delaware to begin their graduate research in solar hydrogen production as IGERT fellows, my education has benefited greatly from participation in the program. The interdisciplinary nature of both the program and the field of solar fuels production are reflected in this work, which contains elements of both mechanical and chemical engineering.

Chapter 1

INTRODUCTION

1.1 Motivation

The Intergovernmental Panel on Climate Change has established with a high degree of confidence that anthropogenic activities, especially those related to energy conversion, are influencing the chemical, physical, and biological processes that govern Earth's climate. These effects can potentially lead to destructive and costly changes worldwide [1]. It has also long been theorized that eventually fossil fuels may become increasingly difficult to extract from the earth and less profitable over time [2]. Thus, the world's future power and fuel infrastructure should utilize renewable sources of energy that do not contribute to climate change.

While the use of renewable energy is on the rise in the US, the use of natural gas (NG) and natural gas liquids (NGLs) has risen even more quickly in recent years, a trend which is expected to continue [3]. The widespread use of hydraulic fracturing, also known as "fracking" has led to a large increase in the supply of easily recoverable natural gas and liquids in the US. Thus, natural gas has become a relatively inexpensive source of fuel for heating applications, electricity generation, and as a feedstock to produce numerous chemicals and plastics. Many industries are projected to exploit the current low prices of NG and demand increasing amounts of electricity through 2040 [3]. Since all forms of natural gas utilization involve combustion, it is a fuel that releases CO₂ and thus contributes to climate change.

For all countries, reliance on imported oil and natural gas can also be a source of geopolitical conflict and economic distress [4]. Countries that rely on neighboring countries for pipelined oil and gas, for instance, are to an extent at the behest of their

neighbors when making policy decisions regarding their own economy and environment. Strategic relationships between countries based on energy security may also be strained due to ideological conflicts, which can decrease the stability of energy supply and prices worldwide. Thus, the ability for all countries to control their own sources of power and fuel is an important step toward global security, sustainability, and economic progress. The US still operates at a net trade deficit in energy in terms of dollar value [5].

For all of these reasons, there has been growing interest in the development of renewable energy technologies in recent decades. The word “renewable” in this context implies that the energy is derived from a source that can replenish itself on a human timescale, rather than on a geological timescale. Energy sources such as coal and oil technically do replenish themselves over time, however they are being converted for human use at a much faster rate.

Two forms of renewable energy that have been utilized for thousands of years are hydro and wind power, dating back to the ancient Greece and ancient China, respectively [6, 7]. Hydropower represents the majority of worldwide renewable electricity generation. Both of these technologies require a match between the geographic locations that can reliably convert wind and hydro energy to electricity and the local demand for electricity. Although the US has historically devoted significant attention to the development of hydropower technology, there are still opportunities for new projects and improvements in current systems [8]. However, interest in installing new wind and hydropower has been somewhat undermined by speculation about the potential effects of climate change on wind and runoff patterns, as well as the potential for drought in areas that currently have adequate rainfall for hydropower [9, 10].

Apart from radioactive materials, the sun is the ultimate source of energy on Earth and can be utilized in many ways for both power and fuel production applications. The power delivered to the Earth’s surface by the sun at any time is $1.05 \times 10^5 \text{ TW}$ at an average normal incidence of $1 \frac{\text{kW}}{\text{m}^2}$. The global power needs for the year 2050 are projected to be around 25-30 TW, thus if the sunlight from 1% of the Earth’s surface is converted with 10% efficiency, the sun is capable of providing enough energy to

satisfy future demands for energy several times over [11]. Solar energy is not evenly distributed across the world, but has the potential to be implemented in many of the world's major population centers.

1.2 Solar Energy Technologies

Solar energy can be collected and utilized in several different ways. The most widely-known method is photovoltaic (PV) modules, in which the incoming stream of photons from the sun induces a direct electrical current using a semi-conducting material [12]. PV systems are highly modular and therefore do not require central generation nor any kind of distribution network for the electricity produced, however they can also feed electricity into the existing electrical grid.

The second category of solar energy collection is solar thermal energy. Here, the solar radiation is used to heat and/or vaporize a working fluid, from which mechanical power can be extracted through traditional heat engines such as the Rankine engine or Stirling engine. This mechanical power can then be converted to electrical power using an electrical generator. The solar radiation can be concentrated to a focal point atop a receiver tower using automated sun-tracking mirrors known as heliostats. It is also possible to collect solar radiation using a single parabolic dish focusing into a receiver, or by using a series of parabolic trough reflectors with vacuum absorber tubes. These approaches are commonly known as concentrated solar power (CSP) [11]. Using the solar tower approach, solar radiation can be concentrated to thousands of times the average incident radiation on Earth if enough heliostats are used.

Finally, there are also hybrid electrical/thermal methods of solar heat and power generation. This approach involves using a combined PV module/thermal collector which is essentially an actively-cooled PV module. The working fluid simultaneously cools the PV panel, thereby increasing the efficiency of solar electricity generation at lower temperatures, and also absorbs thermal energy which is then used to power a heat engine for additional electricity generation, or to power a heating/refrigeration

cycle for heating and cooling needs. These units are typically optimized to supply the needs of a single building or residence [13].

An important issue inherent in all forms of solar energy collection, as well as wind power, is the intermittent availability of the energy resource. The sun has both daily and seasonal cycles of availability and hence a storage mechanism is needed for optimal utilization. One simple method of storing solar or wind energy is pumped water storage, in which water is pumped uphill using electricity, and then run through a hydro turbine to produce electricity at a later time. Another simple method of storing electricity from these sources is using batteries and capacitors. In CSP systems, where it is desirable to be able to store thermal energy at very high temperatures in order to maximize the efficiency of conversion via heat engines, a method that has received considerable attention for energy storage is molten salt storage [14]. In this storage mechanism, a salt mixture with a low melting point can be pumped through the solar receiver to be heated, and then run through a heat exchanger to produce steam in order to drive a turbine.

Rather than storing renewable energy as potential energy or sensible heat, it is also possible to store previously collected solar energy in the form of chemical fuels. The fuels can be either stored and converted in a central location, locally at point sources such as residences, piped to other locations, or used in transportation applications such as cars, buses, and airplanes.

1.3 Renewable Fuels

The transportation sector represents a huge potential for reducing fossil fuel usage and avoiding greenhouse gas emissions. Roughly one-third of all greenhouse gas emissions in the US are associated with the transportation sector [15]. These can be eliminated via several pathways. The first is the adoption of electric vehicles using either wind energy or solar power (or any combination of non-fossil fuel sources) as a source of electrical charge. The other is the adoption of fuel cell cars using carbon-neutral fuels such as hydrogen. Polymer electrolyte membrane (PEM) fuels,

for instance, convert hydrogen and oxygen into water, along with electricity which can power a vehicle's electric motor. Hence, if the hydrogen is originally derived from water, the material cycle is completely sustainable, carbon-neutral, and also avoids many of the air quality issues associated with combustion of fossil fuels. For these reasons, both fuel cell electric vehicles and to a lesser extent hydrogen internal combustion engine vehicles have received increased attention in recent decades [16].

It is likely that the greenhouse gas reductions in the transportation section will be accomplished through a combination of the aforementioned approaches and technology, along with continued improvements in the efficiency of current technologies. Well-designed policies can help encourage the adoption of new technologies and the necessary infrastructure. Some of these policies have already been adopted. For example, the California Environmental Protection Agency's Zero Emission Vehicle program, which has been adopted by nine states, represents 33% of the total U.S. market for new light-duty vehicles in 2015 [17].

Two renewable fuels that have received considerable attention are carbon monoxide (CO) and hydrogen (H₂). A mixture of the two (synthesis gas, or syngas) can be used as a feedstock to the Fischer-Tropsch process in order to produce synthetic combustible liquid fuels, which are readily utilized by the current liquid fuel infrastructure and vehicle technology [18]. Alternatively, they both can be combusted to supply heat energy. Deriving the carbon in synthetic fuels from atmospheric CO₂ represents a carbon-neutral fuel, as the CO₂ product from combustion returns to the atmosphere [19].

In addition, H₂ can be utilized in fuel cells to produce electricity, and because the product of this reaction is water, H₂ is likewise a carbon-neutral fuel. The dual role of hydrogen both as a fuel and as a temporary storage medium for solar energy (or other intermittent sources) is a fundamental component of the hydrogen economy [20]. Thus, the development of more efficient devices for hydrogen conversion also has a synergistic role with the utilization of solar energy.

There are numerous approaches to creating fuels using solar energy. The first

is the photoelectrochemical approach, in which photo-sensitive materials are used as an anode and cathode in an electrochemical cell that splits water. Similarly, there are photo-electrical methods. A common example of this would be using electrical energy from a PV panel to drive electrolysis. Next, there is the photobiological approach, in which microorganisms such as algae are used to generate hydrogen via biological processes. Finally, there is the solar thermochemical approach, in which heat in the form of solar radiation is used to drive chemical reactions to produce fuels [21].

1.4 Solar Thermochemical Cycles

The decomposition of water into hydrogen and oxygen at high temperature, also known as thermolysis, was first considered as a route to the large-scale water-splitting using concentrated sunlight in the 1970s [22]. The high theoretical exergy efficiency is due to the very high temperatures (i.e., over 3000°C) that are required to achieve an appreciable amount of hydrogen in the gas mixture, and which also increases the Carnot efficiency of the process [22]. However, there are practical limits to such an approach, namely finding reactor materials that can withstand the extremely high temperatures, and finding a method of separating hydrogen and oxygen at high temperature. Numerous chemical pathways involving intermediary chemical reactions have been proposed in order to split water thermochemically at lower temperatures, several of which are based on metal oxides [23]. These reaction pathways are referred to as thermochemical cycles.

Thermochemical cycles such as the sulfur-iodine cycle originally gained attention decades ago as a way of producing hydrogen using the waste heat from nuclear power plants [24]. There has been renewed interest in similar methods in the past two decades as thermochemical cycles also lend themselves to implementation using solar energy as a source of heat.

In a metal oxide-based thermochemical cycle, a metal oxide is first reduced, i.e., loses oxygen atoms, under heat and low oxygen partial pressure. The reduced metal

oxide is then reacted with an oxidant, such as water or CO_2 , in order to produce the desired fuel (H_2 or CO).

Metal oxides that have received interest for use in solar thermochemical cycles include Fe_2O_3 , MgO , and Al_2O_3 , and ZnO [25]. There are many factors to consider when choosing a metal oxide cycle for solar thermochemical water-splitting, such as the maximum required temperature of the cycle being compatible with CSP systems, the number and complexity of reactions, cost and abundance of the metal oxide, the theoretical exergy efficiency, and the oxygen looping capacity of the metal [26]. ZnO has long been a popular candidate as it naturally satisfies all of these requirements rather well.

1.5 The Zn/ZnO Thermochemical Cycle

A schematic of the Zn/ZnO cycle is shown in Fig. 1.1.

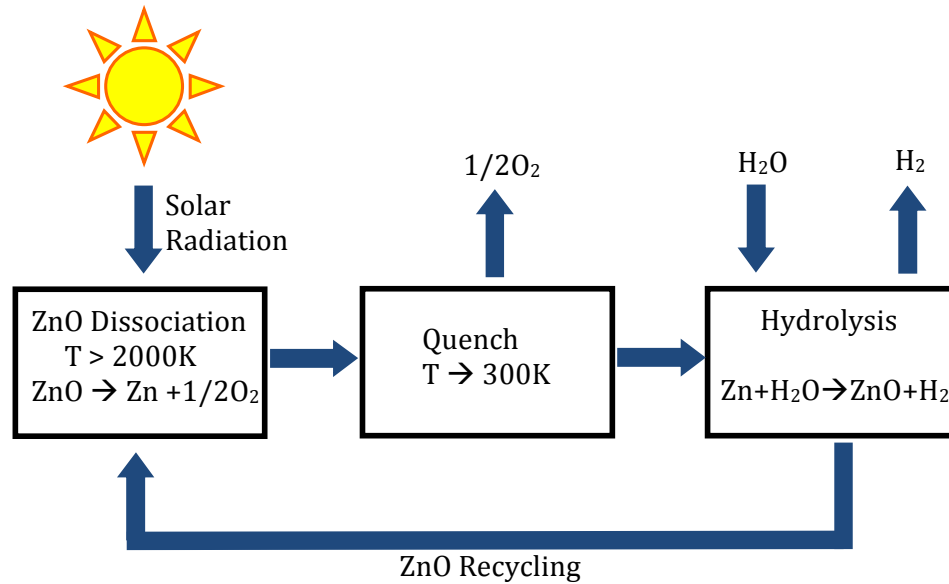


Figure 1.1: Schematic of the different steps and material flows in the Zn/ZnO thermochemical cycle for hydrogen production

In the first step, ZnO is dissociated endothermically under concentrated solar energy at around 2300K to form Zn vapor and oxygen. After this dissociation, the Zn vapor must be condensed into solid Zn through cold inert gas injection, also called quenching [27]. This is done in order to prevent recombination of Zn and O₂, which is thermodynamically favored at lower temperatures [25]. The solid Zn can then be separated from the oxygen gas easily at room temperature. In the second step, the Zn is reacted with steam to form H₂ and ZnO. This water-splitting step is also known as the hydrolysis step. The ZnO is then recycled back to the first step, completing the material cycle. Thus, the net inputs to the process are water and solar energy, and the net outputs are hydrogen and oxygen.

A well-to-wheel efficiency and life cycle impact analysis (LCI) showed that the

Zn/ZnO cycle with on-site hydrolysis and hydrogen pipelining out-competes solar thermal electricity generation followed by electrolysis with regard to greenhouse gas emissions and electricity generation, and scored similarly on LCI metrics [28]. The greenhouse gas emissions per passenger kilometer for fuel cell cars using pipelined hydrogen from the Zn/ZnO cycle were found to be reduced by 70% of the value for advanced oil-based fuels/powertrains. Most environmental impacts of CSP systems are due to the manufacturing processes of the plant itself. Thus, the Zn/ZnO cycle is a promising option for supplying fuel for next-generation vehicles compared to other methods of solar water-splitting.

In the Zn/ZnO cycle, the Zn metal is essentially acting as an oxygen carrier that removes oxygen from water, and then releases the oxygen in a separate step. The reduction of ZnO is represented below:



For ZnO reduction, at 2340K and atmospheric pressure, $\Delta G = 0 \frac{\text{kJ}}{\text{mol}}$ and $\Delta H = 395 \frac{\text{kJ}}{\text{mol}}$ [29]. Compared to many other metal oxides, the temperature for which $\Delta G = 0$ for the reduction step is significantly lower for ZnO. In fact, the reduction temperature for ZnO is lower than that for any other two-step water-splitting thermochemical cycle in which complete metal oxide reduction is possible [30].

Another advantage of the ZnO cycle is that there is a good match between the reduction temperature, i.e., where $\Delta G = 0$, and the temperature where radiation absorption efficiency is highest. The absorption efficiency of a perfectly insulated blackbody receiver is given by :

$$\eta_{\text{absorption}} = 1 - \frac{\sigma T_{\text{receiver}}^4}{IC} \quad (1.2)$$

and the Carnot efficiency by:

$$\eta_{\text{Carnot}} = 1 - \frac{T_{\text{amb}}}{T_{\text{receiver}}} \quad (1.3)$$

where σ is the Stefan-Boltzmann constant, I is the incident solar radiation, C is the concentration factor, $T_{receiver}$ is the temperature of the receiver, and $T_{amb} = 298K$. The product of these two efficiencies can be considered the upper limit efficiency for a process utilizing concentrated solar radiation as a heat input [31]. As $T_{receiver}$ increases, the Carnot efficiency increases, meaning that any heat harnessed at $T_{receiver}$ can be used more efficiently, however the radiation losses from the receiver to the ambient also increase. This implies that there is an optimal value of $T_{receiver}$ for any combination of the other variables. For the global average incident solar radiation of $1000W/m^2$ and $C = 20,000$, the optimum value of $T_{receiver} \approx 2000K$. For lower levels of concentration, the optimum temperatures are lower, down to $T_{receiver} \approx 1250K$ for $C = 2,000$ [25]. Thus, as the level of solar concentration increases, consistent with a large-scale solar thermochemical plant, the the ideal efficiency of the process is maximized near the temperature where $\Delta G = 0$ for ZnO reduction.

Another important consideration that sets ZnO apart from other metal oxide candidates is that it has a high change in oxygen content during reduction. If the reduction of a general metal oxide is expressed as:



then for ZnO, $x = y = 1$ and $\delta = y$. The case of $\delta = y$ is very desirable for looping the most oxygen through the system per unit of solid mass. There are some materials that do not satisfy this requirement. For example, cerium dioxide, while having a lower range of reduction temperatures, has $\delta < y$, meaning that it is only partially reducible. This implies that more solid mass must be moved through the system per unit of fuel produced. For ZnO, the fuel yield per unit mass has a maximum of $12.3 \frac{mmol}{g}$, but for cerium dioxide (for partial reduction at $T_{red} = 1800K$, $P_{O_2,red} = 10^{-2}$) the fuel yield is only $0.12 \frac{mmol}{g}$ [86].

Moreover, the Zn/ZnO cycle has a relatively high theoretical exergy efficiency.

Considering the net solar heat input to the process as:

$$q_{solar} = \left(1 - \frac{\sigma T_{red}^4}{IC}\right) \dot{n} \Delta H_{ZnO \rightarrow Zn+1/2O_2} \quad (1.5)$$

where \dot{n} is the molar flow rate of ZnO into the receiver, and the exergy efficiency as:

$$\eta_{exergy} = \frac{W_{FC}}{q_{solar}} \quad (1.6)$$

with $W_{FC} = -\dot{n} \Delta G_{H_2+1/2O_2 \rightarrow H_2O}$ (the work produced by an ideal fuel cell), the theoretical exergy efficiency of the process was found to be 29 % when the level of solar concentration C is 5,000 suns, and 36% at a solar concentration of 10,000 suns [31]. This analysis included the assumptions that all of the other sub-processes (quench, hydrolysis) are completed with 100% conversion, and that there is no energy lost in separating the inert gas used in quenching.

1.5.1 Reduction Step

There have been numerous demonstrations of reactor designs for ZnO reduction, both at the laboratory scale, and at the pilot plant scale. One early laboratory-scale design used a rotating cavity to maintain contact between small ZnO particles and directly irradiated alumina tiles using centrifugal force [32]. In this design, the axis of rotation is horizontal, as is the incoming beam of radiation. A more recent laboratory-scale design used a downward beam configuration as well as a gravity feeding system in order to flow ZnO powder down alumina tiles from metered-gear feeders [33, 34]. This design also uses a vortex flow of inert gas injected under the inlet window in order to prevent Zn and ZnO from depositing on the window, which can cause uneven heating and cracking of the window [35]. This design successfully demonstrated the carbothermic reduction of ZnO under high solid reactant feed rates, as well as successful performance of the reactant feeding and vortex flow sub-systems [36]. Additional details on the design considerations in solar reactor/receiver design can be found in [34].

The solar thermal reduction of ZnO has recently been demonstrated at the pilot plant scale at the National Center for Scientific Research in Odeillo, France [37, 38].

The MWSF (Mega-Watt Solar Furnace) in Odeillo consists of a field of 63 heliostats which focus sunlight into a parabolic concentrator, which then focuses in the aperture of a solar receiver, and can deliver solar radiation at a mean concentration of 3500 suns. A 100kW receiver/reactor design by ETH Zurich was tested at radiative fluxes of up to 4477 suns, and achieved solid product Zn contents of 12-49% for one experimental campaign, and 5-44% for the other.

The yield of Zn that did not recombine during the quench step was found to be largely dependent on the quenching flow rate of inert gas, with higher flow rates giving higher Zn yields. The amount of inert gas being used was also rather large, with the molar fraction of Zn vapor being $< 0.1\%$ in the quench gas mixture [37]. This study demonstrated successful scale-up of the rotating cavity solar receiver/reactor for ZnO reduction discussed in [39] from the laboratory-scale solar simulator to a full-sized heliostat field research facility, which was discussed in [40]. This work also successfully applied the vortex flow visualization and optimization approach presented in [35] to a large-scale reactor [41]. Although the purpose of this experimental study was mostly to test the thermal and optical performance of the receiver/reactor under real conditions, these results show that the current state of quenching technology has much room for improvement. The quench step may not be economically feasible with the current technology due to the large amount of inert gas required for high Zn yields, and due to the energy and capital cost of separating the inert/O₂ mixture for re-use.

1.5.2 Quench Step and Recombination Reaction

Quenching the gaseous effluents of the dissociation of ZnO has been cited as a major challenge associated with the Zn/ZnO cycle, mainly due to the loss of recuperable heat and need for separating inert gas [42]. Rapid gas injection is required to dilute and cool the mixture of Zn vapor and oxygen to the point that the kinetics of the recombination reaction, given by:



are suppressed, increasing the Zn yield from the reduction step. A study of the gas phase equilibrium of the dissociation of ZnO found that $\text{ZnO}_{(g)}$ does not exist in any appreciable amount [43]. Thus, the reaction of $\text{Zn}_{(g)}$ and oxygen is heterogeneous, and the two vapors can coexist in the absence of a solid reaction site.

The recombination reaction was studied in the context of the Zn/ZnO cycle by allowing a mixture of Zn vapor and oxygen to condense and react on the surface of a temperature-gradient quartz tube, and then studying the deposits by transmission electron microscopy. It was found that at close to 1000K, the predominant form of deposits were ZnO due to the recombination reaction, with increasing amounts of Zn being deposited through condensation as the temperature decreased [44]. By examining the morphologies of the deposited Zn/ZnO, it was determined that Zn particles that were deposited could later undergo oxidation on the tube surface, but this effect was diminished for larger droplets, due to a lower specific surface area. It was also observed that Zn deposited in the liquid state underwent more subsequent reoxidation than did solid particles [44]. This experimental setup was later used in order to analyze the kinetics and mass transfer of the recombination reaction [45]. It was found in this study that the reaction rate being observed was actually the rate of mass transfer, and the inherent kinetics of the surface reaction are very high and difficult to measure [45].

A numerical kinetic aerosol model of the quench step was later developed, which captured the effects of Zn droplet nucleation as well as oxidation on the droplet/particle surface, and additional condensation of Zn on the partially oxidized surface over time [46]. The cooling rate was varied from 5,000-500,000 K/s, and only stoichiometric mixtures of Zn vapor and oxygen were simulated. It was found that the resulting degree of oxidation was relatively insensitive to the cooling rate, with the product being 85-87% ZnO in all cases. The complex behavior of the system was elucidated by superimposing the change of P_{Zn} from the simulation results with the phase diagram of Zn. As cooling progresses, the Zn becomes over-saturated. Once a Zn droplet is present as a reaction surface, oxidation begins, as well as continued condensation of Zn on the resulting Zn/ZnO particle surface. Any initially condensed Zn is somewhat

“preserved” by the formation of a ZnO layer on the particle surface, which tends to prevent further oxidation. Both Zn condensation and oxidation decrease P_{Zn} quickly relative to the cooling rate, eventually moving the system away from saturation conditions, thus allowing continued oxidation on the existing Zn/ZnO particle, but not continued condensation. This causes the system to tend toward ZnO formation rather than Zn condensation, as any Zn left in the vapor state can no longer condense (and thus be partially preserved under ZnO), but rather can only react with oxygen at this point [46].

The strategy proposed to prevent the system from re-crossing the saturation curve too quickly is to begin with a high degree of dilution, i.e., a lower P_{Zn} . With a lower initial P_{Zn} , as the temperature drops, the system can stay in Zn saturation conditions for longer, as the slope of the saturation curve is lower at low P_{Zn} [46]. This effect has been confirmed experimentally; a specially designed quench device which allows for initial dilution and rapid cooling in separate steps, was tested with a solar thermogravimetric reactor. It was found that using inert gas flow rates of 170-1500 times the reactant feeding rate, it was possible to achieve Zn yields of 40-94%, at quench rates of 20,000-120,000 K/s [47]. These two studies illustrate the need for high degrees of Zn dilution to achieve an effective quench step, which combined with the practical limit to the amount of inert gas that can be feasibly used in the process suggests that the quench step may only be realized by using air as the quench gas, rather than a purified inert gas. Using air, the rate of oxidation would presumably be faster due to the presence of additional oxygen, but is possible that the additional condensation and cooling achievable by injecting larger amounts of air may cancel the faster rate of oxidation that this approach would cause, while still avoiding the need for inert gas recycling. However, there is no data available on this approach.

The separation of Ar and N₂ from O₂ is energetically expensive, as it is typically done by cryogenic distillation, as discussed in [48]. This study provided a value of 20kJ/mol of the gas mixture as the energetic cost of gas separation, which is mostly due to the compression of the gases required to liquify them. This value can be computed

by considering the isothermal compression of an ideal gas to 100 bar and the efficiency range of commercial turbo compressors [49]. Comparing this value to the upper limit to the work output of a fuel cell using hydrogen fuel, i.e., the heat of water formation (237kJ/mol), it is apparent that the molar ratio of inert gas used to hydrogen produced must be limited to about 12 or less for a net work output from the process. Considering that this ratio is often greater than 100 in practice [47], much improvement is needed in the reduction and quench steps to lower the amount of inert gas usage if a practical process is to be pursued.

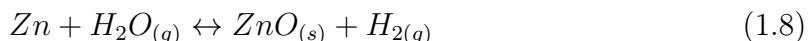
Argon has typically been used as the inert gas in the Zn/ZnO cycle rather than N₂, in order to avoid complications from NO_x formation, which can occur at temperatures above 1,300C [50]. In addition, the heat capacity of Ar is significantly lower than that of N₂, which has proved advantageous in high temperature experimental reactors using significant amounts of inert gas. Ar is much less abundant than N₂ in air, thus if all Ar supplied to the process is from distilling air, the energetic cost will be very high compared to N₂. However, if the thermochemical plant includes a dedicated gas separation unit for separating Ar and O₂, the cost is greatly reduced in comparison, as the work input for compression depends on the total mass flow of gas, and much more Ar would be purified per unit of total gas input.

Rather than using cryogenic distillation, it has also been proposed to use a secondary solar thermochemical cycle for the sole purpose of separating oxygen and inert gas in a fuel producing thermochemical cycle [51]. The approach would be to use as much quenching gas as is necessary after ZnO reduction, and then use the oxygen/inert gas mixture to oxidize Cu₂O to 2CuO, thereby removing the oxygen from the inert gas. It is then possible to reduce CuO in an air atmosphere (thereby avoiding the use of additional inert gas) near 1350K using an additional solar receiver reactor, although the equilibrium does not favor complete reduction of CuO under these conditions [52]. This approach is found to be feasible in principle, however additional complexity and expenditure is still being introduced, and a fair comparison to the cost of conventional inert gas separation has not yet been made [51].

1.5.3 Hydrolysis Step

Although inert gas usage in the quench step is often cited as the key drawback to the Zn/ZnO cycle, many issues also remain in the hydrolysis (water-splitting) step of the cycle, including inert gas usage. For an efficient cycle, the reduction step, quench step, and hydrolysis step all need to be performed efficiently. However, until recently, very little progress had been made in efficiently splitting water using Zn, and the amount of inert gas used in many approaches is unacceptably high, as in the quench step.

The hydrolysis reaction is exothermic, and is represented below:



In Eq. 1.8, the phase of Zn is not specified as it can be reacted as a solid, liquid, or gas. The oxidation of solid Zn has been observed to occur at an average rate of $2 \times 10^{-8} \frac{\text{mol}}{\text{cm}^2\text{s}}$ at 323K in a 94% relative humidity nitrogen atmosphere [53]. The oxidation of liquid Zn was studied by bubbling steam through liquid Zn [54], and the maximum reaction rate was reported to be on the order of $1 \times 10^{-7} \frac{\text{mol}}{\text{cm}^2\text{s}}$. It was found that the oxidation of solid and liquid Zn is limited by the passivation of the Zn surface by formation of a solid ZnO layer [55]. The passivation of Zn surfaces by oxidants is a well-known phenomenon, which has been studied in other contexts [56, 57].

A two-regime kinetic model was proposed for the oxidation of Zn particles. The first stage is a fast surface reaction of steam with solid or liquid Zn. The second stage is described by a diffusion-limited shrinking-core model in which the rate-limiting mechanism is the solid-state diffusion of Zn through the passivating ZnO layer formed on the surface [55]. Thus, the formation of a ZnO layer on Zn particle surfaces is found to help the process efficiency in the quench step by preventing further recombination, but it detracts from efficiency in the hydrolysis step by limiting the conversion.

In order to achieve fast, complete oxidation of Zn by steam for hydrogen production, it was proposed to rapidly cool Zn vapor into nanoparticles and nanodroplets

in a steam atmosphere, thus enhancing the active surface area and decreasing the limit to conversion from the passivating layer. This aerosolized reaction also allows for continuous recovery of high ZnO-content particles. However, as discussed in [58], the passivation effect was found to be significant, even when the Zn particles are very small [53, 54, 56, 57, 59–62]. Hydrolysis of Zn particles has been investigated both by thermogravimetric analysis (TGA) [53, 56, 57, 59–62] and in aerosol reactors that form Zn nanoparticles in-situ via the quenching of Zn vapor [55, 63–71]. In the latter case, although the maximum recorded ZnO content of nanoparticles that were recoverable at the reactor outlet is 80% [64], most studies report ZnO contents under 40% [63, 65–67, 71]. The low ZnO content of recovered particles is attributable to the passivation of the Zn particle surface. Moreover, significant amounts of inert gas were used to rapidly condense Zn vapor into small particles.

Several authors found that in addition to hydrolysis by Zn nanoparticles, the heterogeneous reaction of Zn vapor with steam also occurred on the reactor’s inner surfaces [55, 60, 70]. Essentially, when attempting to form Zn nanoparticles and droplets by quenching of Zn vapor, some Zn vapor does not condense, or evaporates from previously formed particles. This Zn vapor is then available to react heterogeneously with steam on exposed surfaces, including Zn/ZnO particles. In such an aerosol-based approach, the heterogeneous hydrolysis with Zn contributes to the adhesion of Zn/ZnO particles to the reactor’s inner surfaces, as the deposited ZnO acts as a bonding medium [67]. This decreases the product particle yield (ideally pure ZnO) at the reactor outlet. Thus, although the heterogeneous reaction represents a second pathway for hydrolysis, it may actually reduce the effectiveness of a high-throughput aerosol-based approach, unless special design considerations are made [72]. Moreover, it has been suggested in [71] that the heterogeneous reaction is in fact the dominant mode of hydrolysis in nanoparticle-based approaches.

The work in [73–75] investigated the effect of solid ZnO and Al₂O₃ diluents on the reaction of solid Zn with steam and CO₂ in the 623 – 673K range. It was concluded that the sublimation and subsequent heterogeneous reaction of Zn vapor with steam

on neighboring ZnO particles can lead to high degrees of conversion. However, the proposed reaction mechanism suggests that complete conversion may only be possible with a relatively high proportion of ZnO diluents, and a high proportion of inert gas, which is not favorable from a thermodynamic efficiency point of view. As discussed in [76] in the context of the ceria cycle, if the desired fuel stock (H_2 or CO) is only a small proportion of the product gas, then there is a significant energetic cost in its purification before it can be utilized.

In this work, it is suggested that the fast heterogeneous oxidation of Zn vapor with steam can be utilized and optimized under a *negative axial temperature gradient* in order to achieve very high conversions quickly, as well as reduce the need for inert carrier gas in the process.

1.6 Considerations for Hydrolysis Reactor Design

There are many important considerations for designing a reactor utilizing heterogeneous hydrolysis with Zn vapor. First, the temperature conditions that result in the highest Zn conversion, heat recovery from hydrolysis, and total cycle efficiency should be identified, considering the effects of reaction equilibrium, inert gas usage, and the required pre-heating of reactants and inert gas. Isothermal and non-isothermal operation should both be explored to determine which is more favorable in theory. Identifying conditions where the condensation of Zn vapor, which leads to incomplete reaction, should also be a priority.

Preliminary experimental investigations under the expected operating conditions are important in the development of a real reactor. Experimental work can often identify issues that theoretical analysis cannot, and can also serve as proof-of-concept before pursuing additional research. Thus, the development and experimentation with a laboratory-scale reactor is an important step in exploring the feasibility of a new reactor concept.

Since the hydrolysis reactor is exothermic, it is desirable to recover the heat of this reaction to use for pre-heating of hydrolysis reactants, or preheating of ZnO

before reduction. Thus, it is important to investigate the heat transfer that is required both to maintain the optimal temperature conditions, effectively recover the heat of the hydrolysis reaction, and to prevent condensation of Zn.

The deposition of solid ZnO from the gas phase reaction is a unique feature of heterogeneous hydrolysis with Zn vapor. Thus, it is important to have a basis of predicting the deposition of ZnO in the reactor, and how these deposits change over time. This is of particular importance because significant deposition of ZnO concentrated at one axial location could eventually interfere with the flow of gases, and it is better to find conditions that evenly distribute the deposits and allow for longer operation before shutdown is necessary. The deposits would also have an effect on the heat transfer out of the reactor, which would be important to account for in investigating the recovery of the heat of reaction.

These effects would be of particular importance if a “monolith” reactor is pursued. In this approach, the reactor would essentially be a series of small channels in which the reaction proceeds. These channels could be part of a larger metal or ceramic structure, or could possibly even be built out of molded ZnO. If the reaction proceeds on a ZnO substrate, this makes recovery of the deposits and recycling to the reduction step more simple. This type of reactor would lend itself to batch operation, i.e., the reactor would have to be periodically shut down to remove the ZnO deposits, or to replace the channels.

Although a monolith reactor is the simplest possible design, a process that operates without shutdown, and which continuously yields ZnO as a product is more ideal. It is also possible to perform the reaction in an aerosol reactor, in which aerosolized ZnO particles are used as the reaction substrate, and then recovered at the reactor outlet. However, in this approach, some amount of uncontrolled reaction would still occur on reactor walls, and these would become significant over time. Therefore, in either case it is important to understand the transient accumulation of ZnO deposits. Such simulations involving coupled fluid flow, mass transport, and irregularly shaped moving boundaries are easily handled using lattice Boltzmann methods.

Finally, it is desirable that the reactor be compatible with the upstream and downstream sub-processes of the Zn/ZnO cycle. Namely, the reactor should be able to utilize the direct product of the quench step, which is usually a powder mixture of Zn and ZnO, and the hydrolysis product should ideally be a pure ZnO powder that can be readily recycled to the reduction step of the process.

All of these considerations will be addressed to varying extents, either in the body of the thesis, or in the conclusions (Chapter 5.6) as recommendations for future work.

1.7 Organization of Thesis

The remainder of the thesis is organized as follows. In Chapter 2, a model and thermodynamic analysis of the heterogeneous hydrolysis with Zn vapor under a temperature gradient are presented to investigate the effects of different temperature conditions on the heterogeneous hydrolysis reaction and its effects on the total efficiency of the Zn/ZnO cycle. In Chapter 3, an experimental investigation of the reaction is performed using a laboratory-scale non-isothermal reactor, as proof-of-concept for the theoretical predictions made in Chapter 2. In Chapter 4, background material on lattice Boltzmann methods is presented, as a short introduction to the methods used in Chapter 5. In Chapter 5, lattice Boltzmann simulations of the reactive precipitation of ZnO are presented in order to understand the effects of flow, mass transfer, and kinetics on the transient accumulation of ZnO deposits in a circular tube due to heterogeneous hydrolysis with Zn vapor. In Chapter 6, overall conclusions as well as recommendations for future work, as well as a short statement on the future direction of the field of solar thermochemical hydrogen production are presented.

The appendices to the thesis are as follows: Appendix A contains additional design details on the laboratory-scale reactor described in Chapter 3. Appendix B contains a short guide on programming for the lattice Boltzmann method. Appendix C contains results from flow and mass transfer problems that were used to validate the lattice Boltzmann code used in Chapter 5, as well as similar precursors to this

code. Appendix [D](#) contains a statement on the reproduction of work contained in published Elsevier journal articles, and a list of the journal articles containing the material presented in this thesis are included in Appendix [E](#).

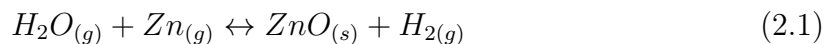
Chapter 2

HETEROGENEOUS HYDROLYSIS WITH ZN VAPOR UNDER A TEMPERATURE GRADIENT: MODELING AND EFFICIENCY ANALYSIS

In this chapter, we investigate the two-step Zn/ZnO thermochemical cycle for the production of solar hydrogen. We focus on the hydrolysis step of the cycle wherein Zn is oxidized with water vapor to produce hydrogen. A novel approach wherein the oxidation reaction of Zn vapor is conducted under an axial temperature gradient in a tubular reactor is suggested as a promising method for efficiently splitting water using a low percentage of inert carrier gas in the mixture. We report numerical results from a reactor model to gain insight into the heterogeneous oxidation of Zn with water vapor under an axial temperature gradient, and to highlight the effect of the reactor's performance on the total cycle efficiency. The results show that using an optimal temperature difference, the maximum cycle efficiency for the temperature gradient case is up to 38% higher than that for isothermal conditions. The equilibrium Zn conversion and inert gas usage in the hydrolysis step have the largest effects on cycle efficiency, while the exact cooling rate has a much smaller effect on cycle efficiency. The mass transfer conditions and temperature gradient determine whether the gas mixture will reach saturation conditions, which should be avoided in order to achieve complete conversion.

2.1 Heterogeneous Hydrolysis with $Zn_{(g)}$

The heterogeneous oxidation of Zn vapor with steam on a solid surface is represented below:



The reaction is heterogeneous in the sense that the two vapors are reacting only on a solid reaction site. The gas-phase equilibrium of this reaction was investigated by Reisman et al. [77], who found the equilibrium constant for the reverse reaction, K_{eq}^r (i.e., the reduction of solid ZnO by H_2). The reverse reaction equilibrium constant is defined in terms of the equilibrium constant for the forward reaction K_{eq}^f as:

$$K_{eq}^f = \frac{P_{H_2}}{P_{H_2O}P_{Zn}} = (K_{eq}^r)^{-1} \quad (2.2)$$

where P denotes the partial pressures of the various gas-phase species. Reisman et al. [77] found that the following relation fit their data:

$$\log_{10} K_{eq}^r = \frac{-11794}{T} + 8.040 \quad (2.3)$$

The variation of K_{eq}^f with temperature is shown in Fig. 2.1, along with the variation of the saturation pressure of Zn and temperature.

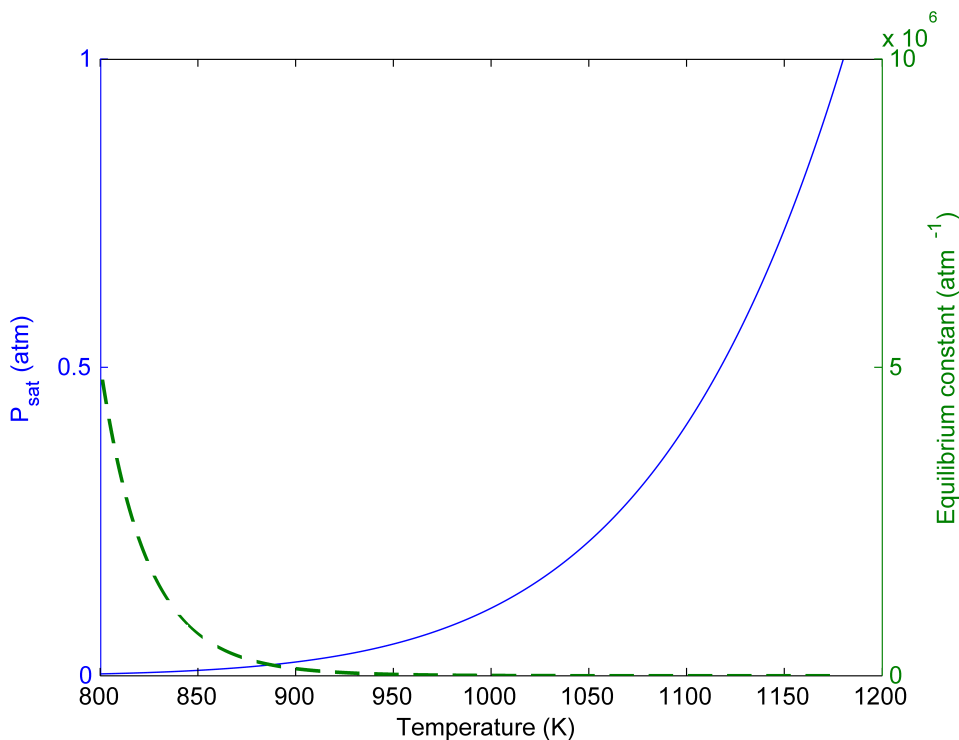


Figure 2.1: Equilibrium constant for heterogeneous hydrolysis with Zn vapor and Zn saturation pressure vs. temperature.

As temperature increases, the equilibrium constant decreases, and the reverse (endothermic) reaction is favored, forming less H_2 and ZnO . The equilibrium conversion can be improved at any temperature by beginning the reaction with a higher molar ratio of steam to Zn, however this approach may compromise efficiency and heat recovery because of the heat input required to generate additional steam. At atmospheric pressure and 800K, the conversion of Zn to ZnO is thermodynamically favored, however the saturation pressure of Zn (as predicted by [78]) is very low, as shown in Fig. 2.1. The heterogeneous reaction of $\text{Zn}_{(g)}$ with CO , $\text{CO}_{2(g)}$, and $\text{H}_2\text{O}_{(g)}$ was first investigated in the context of Zn smelting [79–85]. Clarke and Fray [79] flowed a Zn/steam/ N_2 gas mixture through 5-10 mm diameter silica reaction tubes and then weighed the deposits section by section to obtain a kinetic expression for the forward reaction. Venstrom and Davidson [86] later determined that the silica tube diameter used in [79] was too large to accurately determine the inherent reaction kinetics as the experiments had been actually conducted in a mass transfer-limited regime, leading instead to the measurement of the Zn mass transfer rate. A similar experiment to Clarke and Fray’s was repeated using a smaller bore (4 mm diameter) quartz tube [86]. However, the reaction rate proved to be still faster than the mass transfer rate even with the smaller bore tube. Their results were thus interpreted using a numerical mass transfer model, so that the reaction rate could be obtained in terms of the predicted partial pressure of each reactant immediately adjacent to the tube wall. The kinetic expression reported by [86] is given as:

$$r'' = k(T) \left(P_{\text{Zn}} P_{\text{H}_2\text{O}} - \frac{P_{\text{H}_2}}{K_{eq}^f} \right) \quad (2.4)$$

The reaction is second order globally and reversible, and is first order with respect to both Zn and H_2O .

The variation of the calculated rate constant k is given in Table 1. The rate constant k has a minimum near 1050K, which is thought to be due to a change in the reaction mechanism with temperature [86]. In many homogeneous reactions, the kinetic constant will only increase with temperature, as in the common Arrhenius rate law [87]. For the heterogeneous hydrolysis of Zn, there could be a temperature-sensitive

precursor step in the surface reaction, such as the adsorption of one of the species onto the reaction site before reaction, which is acting as the rate-limiting step for some temperatures [86].

Table 2.1: Variation of the reaction rate constant k with temperature as determined in Ref. [22]. The averages of the two values at both 900K and 1100K are used in the current model.

Temperature (K)	k ($\frac{mol}{atm^2 m^2 s}$)
800	199
900	59
900	60
1000	6.8
1050	3.4
1100	14.5
1100	17.5

In all cases, the reaction was found to be much faster than the alternative mode of hydrolysis using Zn nanoparticles and nanodroplets. The reaction rates were found to be on the order of $1 \times 10^{-7} \frac{mol}{cm^2 s}$ at 800K and $1 \times 10^{-5} \frac{mol}{cm^2 s}$ at 1100K. Hence, this mode of hydrolysis offers substantial improvements in achievable reaction rates compared to the hydrolysis of solid or liquid Zn. More importantly, for the heterogeneous hydrolysis of Zn, the kinetic limit imposed by the formation of the passivating ZnO layer is eliminated, as the reaction proceeds on previously deposited layers of ZnO product.

The equilibrium conditions for the forward reaction were also investigated via Gibbs free energy minimization using a thermodynamic database [86]. It was predicted that a stoichiometric mixture of Zn vapor and steam would achieve around 99% conversion at 800K to about 93% conversion at 1100K. The Gibbs free energy is most negative at 800K which is close to the melting point of Zn, hence the formation of ZnO is favored at the melting point of Zn rather than its boiling point [86].

In order to quantify the effect of these improvements in conversion on cycle efficiency, Venstrom and Davidson [88] re-derived the theoretical exergy efficiency, similar to [31], but in a way that allowed for incomplete conversion during both the quench and hydrolysis steps. An average Zn recovery of 61% was assumed during quenching,

followed by an assumed conversion of 20% for the nanoparticle hydrolysis approach, and 100% conversion for the heterogeneous hydrolysis of Zn vapor. It was found that the cycle efficiency increased from about 4% in the former case to 16% in the latter case [88]. However, this analysis does not account for conversion limits due to gas phase equilibria, and the assumption of 100% conversion during heterogeneous hydrolysis at constant temperature would not hold true in practice.

The gas-phase heterogeneous hydrolysis approach presents a trade-off that is of great practical importance. Since the Zn cannot be evaporated directly into the steam due to the passivating layer of ZnO that was found to form on liquid Zn [54], the Zn vapor must be introduced into the reactor via a carrier stream of inert gas. At 800K and atmospheric pressure, where complete oxidation of Zn is possible, the saturation pressure of Zn in the gas mixture (as predicted by the Antoine equation [78]) is very low, and a higher proportion of carrier gas must be used to transport the Zn vapor. Hence, there would be a large energy and capital cost associated with inert gas separation and recycling. At temperatures approaching the boiling point of Zn, inert gas requirements are much lower, but the gas-phase equilibrium does not favor complete conversion of Zn to ZnO.

In light of the effects of temperature on the reaction equilibrium, it has been proposed to operate the heterogeneous hydrolysis reaction under a temperature gradient [86]. The approach is to begin the reaction at close to the boiling point of Zn (1180K), where the saturation pressure of Zn is high enough to allow a stoichiometric mixture of Zn vapor and steam without over-saturating the mixture, and minimizing inert gas requirements. It is then desirable to decrease the temperature as the reaction proceeds, approaching around 800K, where the equilibrium conditions favor complete conversion of Zn [86]. However, it is also desirable to avoid over-saturating the mixture with Zn by cooling too rapidly as this would form Zn droplets and particles. As discussed previously, complete oxidation of solid and liquid Zn is limited by the formation of a passivating ZnO layer, and thus over-saturation can be considered a loss mechanism. As long as the system temperature is decreased slowly relative to the decrease in P_{Zn} from the consumption of Zn by the reaction such that $P_{Zn} \leq P_{sat}$ for the

entire temperature path, it should be possible to drive the reaction toward complete conversion without over-saturating the mixture with Zn. Thus, it should be possible to achieve complete conversion of Zn with a minimal expenditure of inert gas, while also forming a high-purity ZnO product that can be recycled back into the dissociation step of the thermochemical cycle.

2.2 Reactor Model

In order to couple the experimental data on kinetics and equilibrium to different temperature conditions, a plug-flow, kinetics-limited model of a single small tube reactor is considered [89]. The purpose of this reactor model is ultimately to quantify the effects of an externally-imposed temperature gradient, as well as the inlet hydrolysis temperature, on Zn conversion, heat recuperation, and total cycle efficiency. Hence, we are more interested in determining upper limits of theoretical efficiency than modeling in detail a particular reactor design. The optimal inlet temperature is of particular interest because there is a trade-off between the smaller amount of inert gas needed to convey Zn vapor at a high temperature and the additional sensible heat that must be supplied to the reactants.

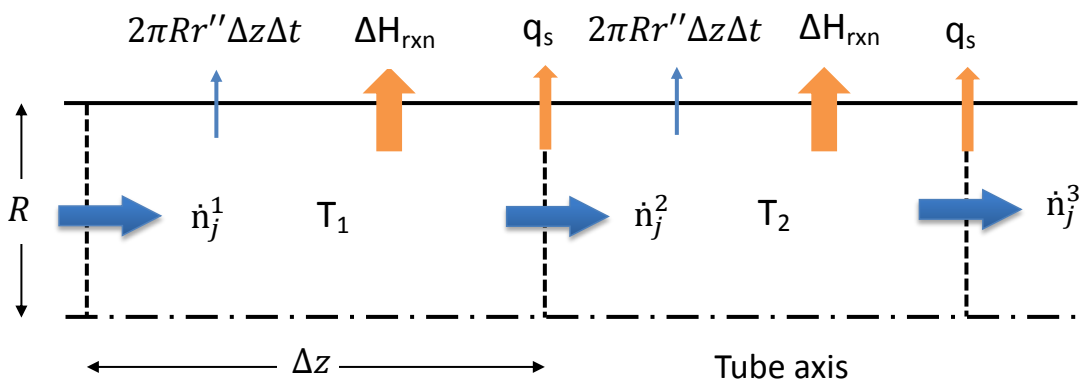


Figure 2.2: Schematic of the plug flow reactor model. The molar flow rate of each species j is updated for each volume 1, 2, 3, ... based on the reaction on the tube wall.

The reaction rate r'' is a function of temperature and the local composition of the gas, and is defined by the kinetic expression derived in [86], shown in Eq. 2.4.

The forward reaction equilibrium constant at the local temperature is found using the expression derived in [77] and shown in Eq. 2.3. It is assumed that the tube temperature is a known function $T(z)$, which is uniform over the tube cross-section. Although for a real reactor, the temperature would be coupled to both the flow and the external thermal conditions, here we use $T(z)$ as a forcing parameter, and assume for each case that the fluid flow and heat transfer out of the tube are such that this temperature profile is maintained. The reactor is modeled as a series of reactions at constant pressure and temperature, followed by a constant pressure sensible heat loss, q_s , as shown in Fig. 2.2. It is assumed that the tube diameter is small enough that the reaction is not mass transfer-limited. This assumption is generally justifiable for low values of Damköhler number, which is defined as the ratio of the reaction rate to the mass transfer rate. For our application, we define the Damköhler number as:

$$Da = \frac{kP_{Zn}RR_uT_i}{D_{Zn}} \quad (2.5)$$

where R is the tube radius and D_{Zn} is the mass diffusion coefficient of Zn in Ar given in [45]. This implies that for a real reactor with typical values of relevant variables, one would require $R < 0.1\text{mm}$ to ensure $Da < 0.1$, and thus ensure that the reaction is not mass-transfer limited. Although this case may be impractical, we examine it as a limiting case, and other limiting cases will be discussed in Section 2.5.

All gases are assumed to be ideal. We assume that Zn initially evaporates into an inert gas at atmospheric pressure and initial temperature T_i and forms a saturated mixture, so that the partial pressures of the two gases are related by:

$$\frac{P_{Zn,i}}{P_{inert}} = \chi = \frac{P_{sat}(T_i)}{P_{atm} - P_{sat}(T_i)} \quad (2.6)$$

where $P_{sat}(T_i)$ is the saturation pressure of Zn at T_i . This mixture then mixes instantaneously with steam at the channel entrance. The initial stoichiometry of steam to Zn, S , is defined according to the ideal gas assumption as:

$$\frac{P_{H_2O,i}}{P_{Zn,i}} = S \quad (2.7)$$

Assuming the total pressure after mixing is P_{atm} , the initial partial pressure of Zn is then given by

$$P_{Zn,i} = \frac{P_{atm}}{1 + S + \frac{1}{x}} \quad (2.8)$$

As shown in Fig. 2.2, the molar consumption of Zn (and H₂O) is equal to the product of the reaction rate and the surface area of the channel wall over an axial increment Δz as:

$$\frac{dn_{Zn}}{dt} = r''(2\pi R\Delta z) \quad (2.9)$$

The time step Δt thus approximates the time that the volume of gas in a given incremental tube section of length Δz can react on the tube surface before moving into the next incremental section of the tube. The rate of Zn consumption in Eq. 2.9 is discretized in time according to a first-order finite difference approximation [90], so that over a single time step, the mole fraction, x , of Zn (as well as the other species) can be updated according to the local rate of consumption (for Zn and H₂O) or production (for H₂):

$$x_{Zn,z+\Delta z} = \frac{n_{Zn} - 2\pi R\Delta z\Delta tr''}{n_{Zn} + n_{H_2O} + n_{inert} + n_{H_2} - 2\pi R\Delta z\Delta tr''} \quad (2.10)$$

The partial pressures of each species can be calculated from the molar fractions according to:

$$P_j = P_{tot}x_j \quad (2.11)$$

The plug-flow velocity is updated according to the change in the molar flux, J , again using the ideal gas law.

$$J_{j,z+\Delta z} = J_j - \frac{2r''\Delta z}{R} \quad (2.12)$$

$$u_{z+\Delta z} = \frac{\sum_j J_{j,z+\Delta z} R_u T_{z+\Delta z}}{P_{tot,z+\Delta z}} \quad (2.13)$$

where the axial increment Δz is defined as the product of the velocity u of the gas mixture moving through the channel and the time increment:

$$\Delta z = u\Delta t \quad (2.14)$$

where Δt is fixed.

The axial increment Δz is then updated according to the new flow velocity using Eq. 2.14. Using the initial partial pressures of each reactant, the assumed temperature profile $T(z)$, and the initial flow velocity, the solution is marched from $z = 0$ to $z = L$, updating each quantity as defined above. The reactor length L is chosen to be long enough to allow all simulations to reach equilibrium. Additional details about this method can be found in [89].

2.3 Model Validation

To validate the model, we assume a simple reaction $A \rightarrow B$, with second-order kinetics on the tube wall defined by:

$$r'' = k(T)P_A^2 \quad (2.15)$$

The values of $k(T)$ are chosen to be in the same range as those used in the model, shown in Table 2.1. By balancing moles of A in and out of a small section of the channel with length dz , one obtains:

$$\pi R^2 \frac{dJ_A}{dz} = 2\pi R r'' \quad (2.16)$$

Equation 2.16 can also be derived from Eqs. 2.9 and 2.14; here we express the reaction rate in terms of the molar flux to solve for the molar flux variation analytically. At $z = 0$, we assume $P_{A,i} = 1.0$ atm, $J_A = J_{A,i}$, and molar concentration $C_A = C_{A,i}$. The temperature is held constant for the length of the reaction channel. The analytical solution for the molar flux of A is then given by:

$$J_A(z) = \frac{1}{\frac{1}{J_{A,i}} + \frac{2k(T)z}{R} \left(\frac{C_{A,i} R_u T}{J_{A,i}} \right)^2} \quad (2.17)$$

The numerical model developed here is validated against this solution for the entire range of temperatures of interest, with all other values in the model (flow velocity, tube radius, etc.) held equal to those used in the hydrolysis reaction simulation. The results are shown in Fig. 2.3. The values of $k(T)$ used for different temperatures are shown in Table 2.1. The agreement is very good for all cases, with negligible error even in the first 0.1% of the reaction channel. The discretization for the reactor model is chosen based on the accuracy of these results.

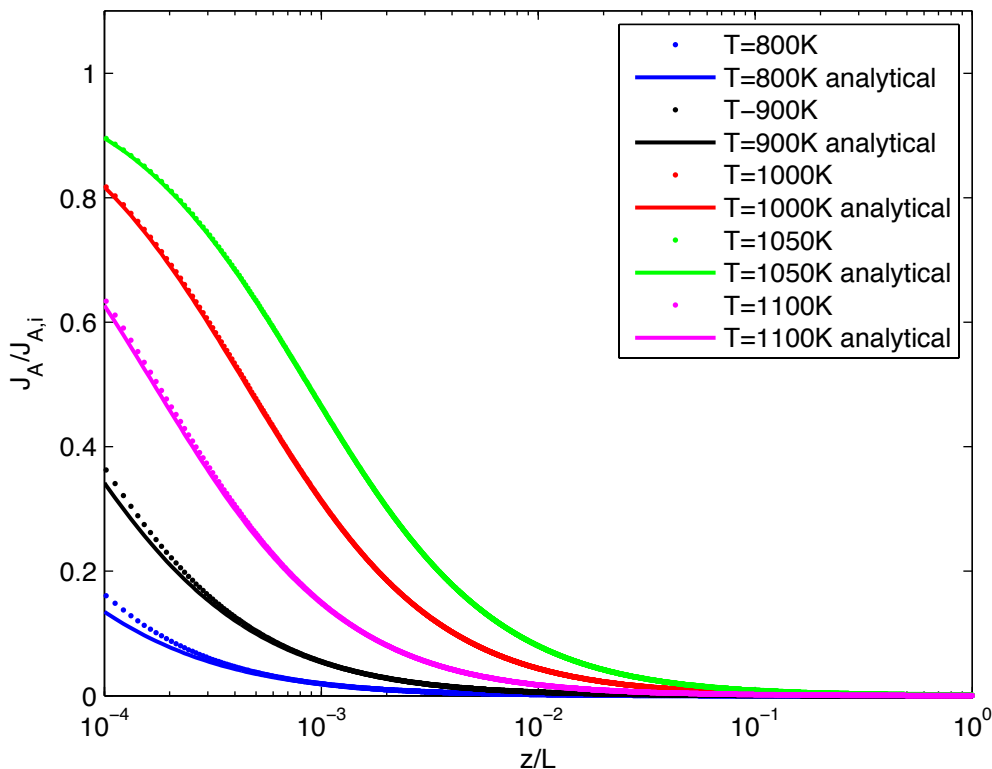


Figure 2.3: Validation of numerical model: Numerical results (symbols) compare well with analytical results (lines) for the evolution of molar flux of species A for various temperatures

2.4 Thermodynamic Analysis

The cycle efficiency is analyzed using a similar approach to the one in [88]. A schematic of the total process with the relevant mass and energy flows is shown in Fig. 2.4. The goal of this analysis is to highlight the effect of the hydrolysis reactor on

the total cycle efficiency for different conditions, hence the important heat inputs to the process are considered to be the solar energy input to the endothermic dissociation reactor and the net heat input to the exothermic hydrolysis reactor. As seen in Fig. 2.4, no material moves in or out of the control volume, only heat and work flows. Thus, the cycle is analogous to a heat engine. It is assumed that the output of the hydrolysis reactor is 1 mol/s of H₂ and ZnO for all cases considered, as shown in Fig. 2.4. The necessary molar flow rate of ZnO into the solar dissociation reactor is then calculated as:

$$A = \frac{1}{\alpha\beta} \quad (2.18)$$

where α and β are the fractional yields of hydrolysis and quench processes, respectively. α is calculated as:

$$\alpha = 1 - \frac{\dot{n}_{Zn,o}}{\dot{n}_{Zn,i}} \quad (2.19)$$

where $N_{Zn,i}$ and $N_{Zn,o}$ are the inlet and outlet molar flow rates of Zn to and from the hydrolysis reactor, respectively.

The solar dissociation reactor is assumed to operate at full conversion; i.e., every mole of ZnO supplied to the reactor is assumed to dissociate completely to Zn and O₂. The dissociated Zn and O₂ then go to the quencher, where the two are separated without any work or heat recovery, as shown in Fig. 2.4. This assumption is used to decouple these effects from the analysis. The 0.5 mol/s of O₂ necessary to react with 1 mol/s of H₂ is sent from the quencher to an ideal fuel cell, while the rest of the yielded O₂ reacts with unreacted Zn from the hydrolysis reactor's exit stream. This product ZnO is recycled to the dissociation reactor. The heat of this Zn oxidation is also not recovered. Any recombined ZnO from the quencher is also recycled to the dissociation reactor. The 1 mol/s of product H₂O from the fuel cell is sent to the hydrolysis reactor. The Zn that is successfully recovered by the quencher is also sent to the hydrolysis reactor. The H₂/inert (assumed to be Ar) product gas from the hydrolysis reactor is sent to the gas separator, and the 1 mol/s of product H₂ is sent

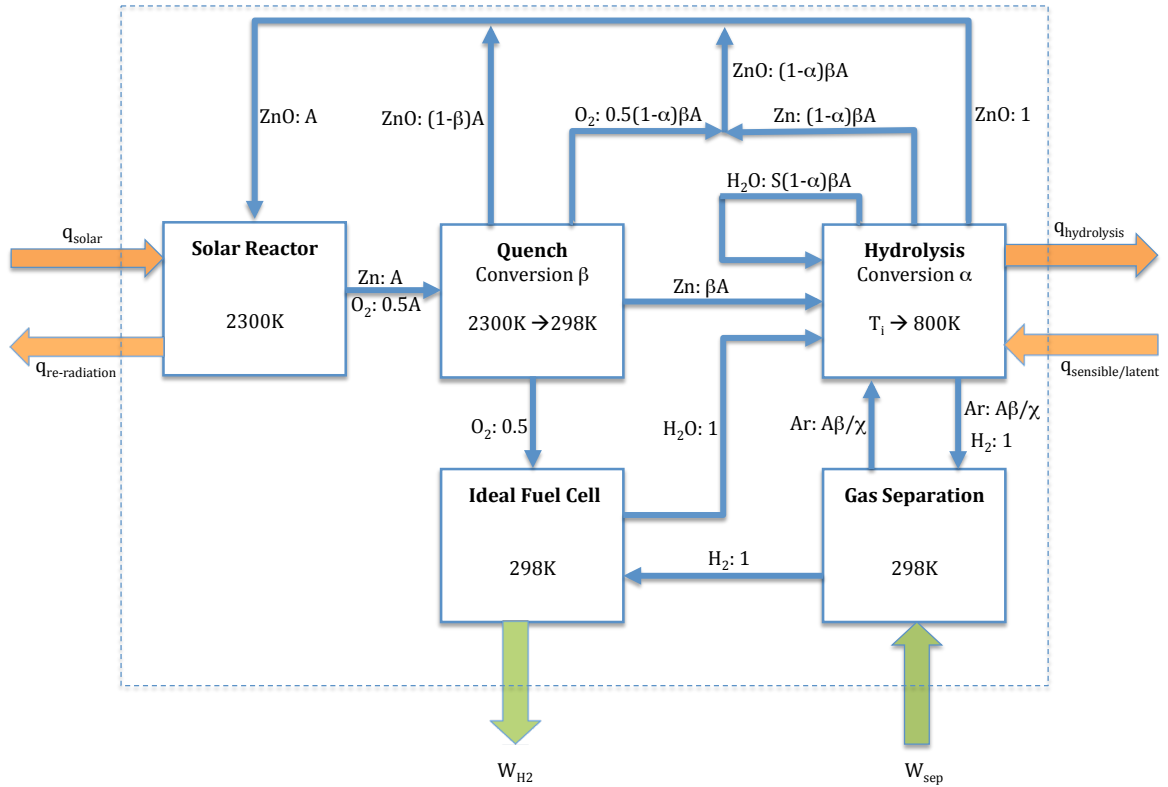


Figure 2.4: Schematic of hydrogen production via the Zn/ZnO thermochemical cycle. Material flows are shown in blue, heat flows in orange, and work in green.

to the fuel cell. The 1 mol/s ZnO product of the hydrolysis reactor is recycled to the dissociation reactor.

Based on the assumed temperature conditions for hydrolysis and dissociation, the required heat inputs to the process can be calculated. Data for specific heat and enthalpy were taken from [91] for ZnO and from [92] for all other species. The total heat rejected by hydrolysis is obtained from the numerical model in Section 2.2. The total heat of reaction is integrated numerically from the reaction rate profile predicted

from the reactor model and the assumed channel temperature profile.

$$q_{hydrolysis} = \int_0^L (2\pi R \Delta H_{rxn}(T(z)) r''(z) + q_s(T(z))) dz \quad (2.20)$$

where ΔH_{rxn} and q_s are the heat rejected from hydrolysis and the sensible heat change of the gas mixture, respectively, across each control volume in the reactor model as shown in Fig. 2.2.

Assuming a perfectly insulated blackbody cavity/receiver with no convective or conductive losses to the ambient, the gross power input to the dissociation reactor, including re-radiated heat, is given by [25]:

$$q_{solar} = \frac{A(\int_{T_{amb}}^{T_{solar}} c_{P,ZnO} dT + \Delta H_{diss})}{1 - \frac{\sigma T_{solar}^4}{IC}} \quad (2.21)$$

where $T_{amb} = 293\text{K}$, $T_{solar} = 2300\text{K}$, I is the average solar terrestrial irradiance (1000 W/m^2), and $C = 10,000$ is the solar concentration factor, for all cases. The work output from the fuel cell is assumed to be the Gibbs free energy of water formation from hydrogen and oxygen at the ambient temperature, and is given by:

$$W_{H_2} = \dot{n}_{H_2} \Delta G_{H_2+O_2 \rightarrow H_2O, T_{amb}} \quad (2.22)$$

It is assumed that the hydrogen yielded in each model calculation is separated from the inert gas using a membrane-based separation system operating at 50 bar (P_2). The work required to separate the two gases is assumed to be the work associated with the ideal adiabatic compression of the gas mixture to 50 bar at ambient temperature:

$$W_{sep} = \frac{(\dot{n}_{Ar} + \dot{n}_{H_2}) R_u T_{amb}}{\gamma - 1} \left(\left(\frac{P_2}{P_{atm}} \right)^{\frac{\gamma-1}{\gamma}} - 1 \right) \quad (2.23)$$

where γ is the average specific heat ratio of the mixture H_2/Ar mixture. The cycle efficiency is then defined as the net work output divided by the net heat input:

$$\eta_{cycle} = \frac{W_{H_2} - W_{sep}}{q_{hydrolysis} + q_{sensible+latent} + q_{solar}} \quad (2.24)$$

We also define a heat recovery factor:

$$HR = -\frac{Q_{hydrolysis}}{Q_{sensible+latent}} \quad (2.25)$$

where $q_{sensible+latent}$ is the heat required to bring the Zn, H₂O, and inert gas from T_{amb} to T_i , as well as to vaporize Zn and H₂O. The heat recovery factor is thus a measure of potential autothermicity of the hydrolysis process for different conditions.

For the temperature-gradient cases, we define the non-dimensional temperature gradient as:

$$\frac{dT^*}{dz^*} = -\frac{dT}{dz} \frac{L}{T_o} \quad (2.26)$$

where L is assumed to be $500R$ and $T_o = 800\text{K}$ for all cases. Thus, a positive $\frac{dT^*}{dz^*}$ corresponds to a negative temperature gradient. To put this metric into physical terms, for a reaction channel radius of 1mm, a non-dimensional temperature gradient of 0.475 would correspond to a temperature decrease from 1180K to 800K over a length of 50cm. For an initial molar flow rate of 1×10^{-6} mol/s of Zn, this temperature drop can be achieved by driving 1×10^{-5} mol/s of H₂O initially at 400K in counter flow through an annular gap around the reaction tube. This flow of steam would be sufficient to absorb the heat of the hydrolysis reaction and sensible heat change of the various species in the reactor tube (about 2.3×10^{-4} kW), while undergoing a temperature rise from 400K to nearly 1180K. A portion of this steam could then be used as a reactant during hydrolysis, and the remainder for pre-heating Zn, for example. Increasing the assumed length of the reactor causes no appreciable changes in the model results.

2.5 Results

2.5.1 Effect of Temperature Gradient

Figures 2.5 and 2.6 show reactor model results for the two limiting cases of temperature gradient conditions. Figure 2.5 shows the cycle efficiency and extent of Zn conversion for an instantaneous drop in temperature from T_i to T_o , which is equivalent to an infinite temperature gradient, and Figure 2.6 shows the corresponding results for the case where the temperature is held constant at T_i , which is equivalent to a zero

temperature gradient. β is assumed to be 1.0 for both cases. With $S = 1.0$, the maximum cycle efficiency for the infinite temperature gradient case is 33.81%, while that for the constant temperature case is 24.5%. Without recovery of the heat of hydrolysis, the maximum efficiencies for the two cases are 24.61% and 19.5%, respectively. In both cases, as the initial temperature (or constant temperature, for the latter case) decreases, the cycle efficiency drops to 0 due to the increasing cost of inert gas separation and heating the inert gas to T_i , as the proportion of inert gas in the mixture increases exponentially.

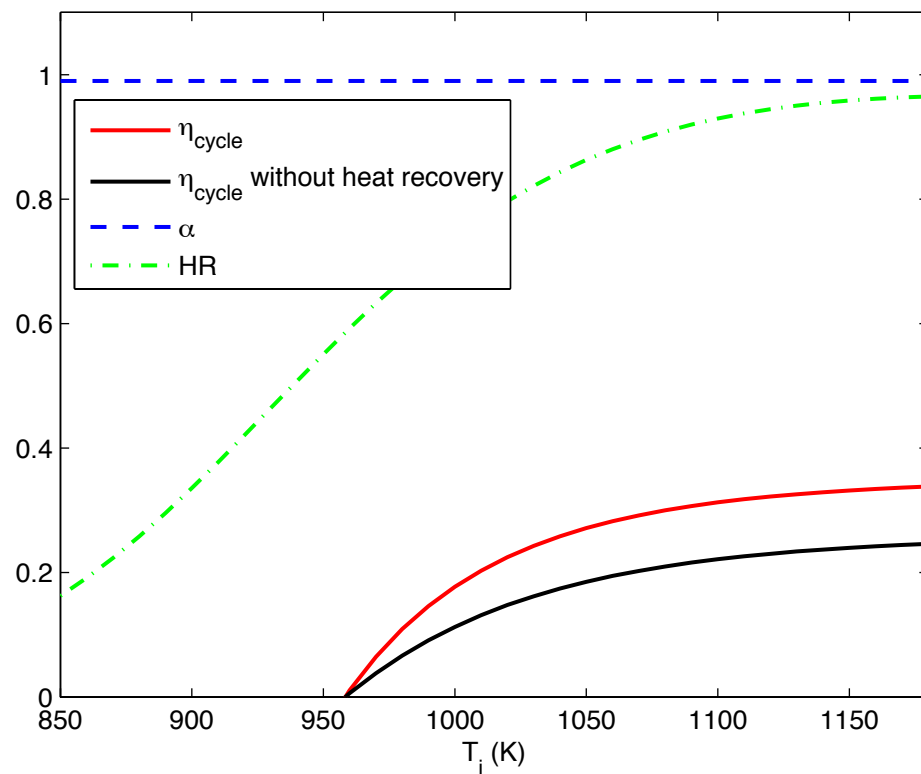


Figure 2.5: Thermodynamic calculations for instantaneous temperature drop from T_i to 800K (limiting case for temperature gradient operation)

With $S = 1.0$, the conversion at 1180K for the constant temperature case is only around 86%, while it is over 99% for the instantaneous temperature drop from 1180K to 800K. This is due to the shifting of equilibrium toward complete conversion of Zn as temperature decreases. A similar trend was found using Gibbs energy minimization

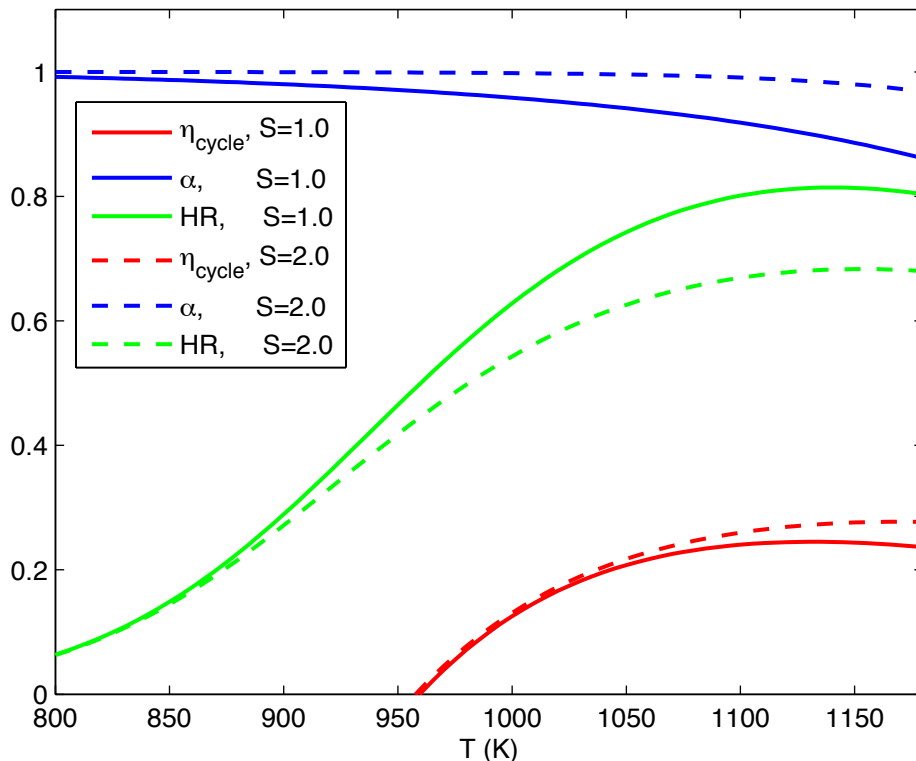


Figure 2.6: Thermodynamic calculations for constant temperature operation; $S = 1.0, 2.0$.

in [88]. For the constant temperature case, the heat of hydrolysis can supply up to 81.5% of the heat required to bring the reactants up to the initial temperature. For an instantaneous temperature drop, the maximum heat recovery factor is 96%. It was found in [88] that at 1185K, 95% of the sensible and latent heats of the reactants could be supplied by the hydrolysis reaction, assuming complete conversion at this temperature, which agrees well with the current results.

Figure 2.6 also shows that doubling the initial proportion of H_2O to $S = 2.0$ increases the maximum Zn conversion to 97% for the constant temperature case. With these assumptions, the maximum efficiency with heat recovery is still limited to 27.7% due to the additional sensible and latent heat required to generate high temperature steam. Without heat recovery, the maximum efficiency is 21.8% for this case, and the heat of hydrolysis is at most 68% of the total sensible and latent heat of the reactants.

Figure 2.7 shows the results for a temperature gradient of $\frac{dT^*}{dz^*} = 0.5$. The results are very close to those for the instantaneous temperature drop case, with over 99% conversion and 32.68% cycle efficiency with $T_i = 1180\text{K}$. The heat recovery is also just above 93% at maximum efficiency. Changing $\frac{dT^*}{dz^*}$ has very little effect on efficiency, heat recovery and conversion (less than 1%), as long as $\frac{dT^*}{dz^*} > 0.475$. For $\frac{dT^*}{dz^*} = 0.475$, which implies that the final temperature of 800K is reached exactly at the exit for an initial temperature of 1180K, the maximum efficiency is 32.68%. However, $\frac{dT^*}{dz^*} \rightarrow 0.0$ results in an outlet temperature $T_o > 800\text{K}$ for all T_i , and the efficiency begins to drop off quickly due to incomplete conversion of Zn.

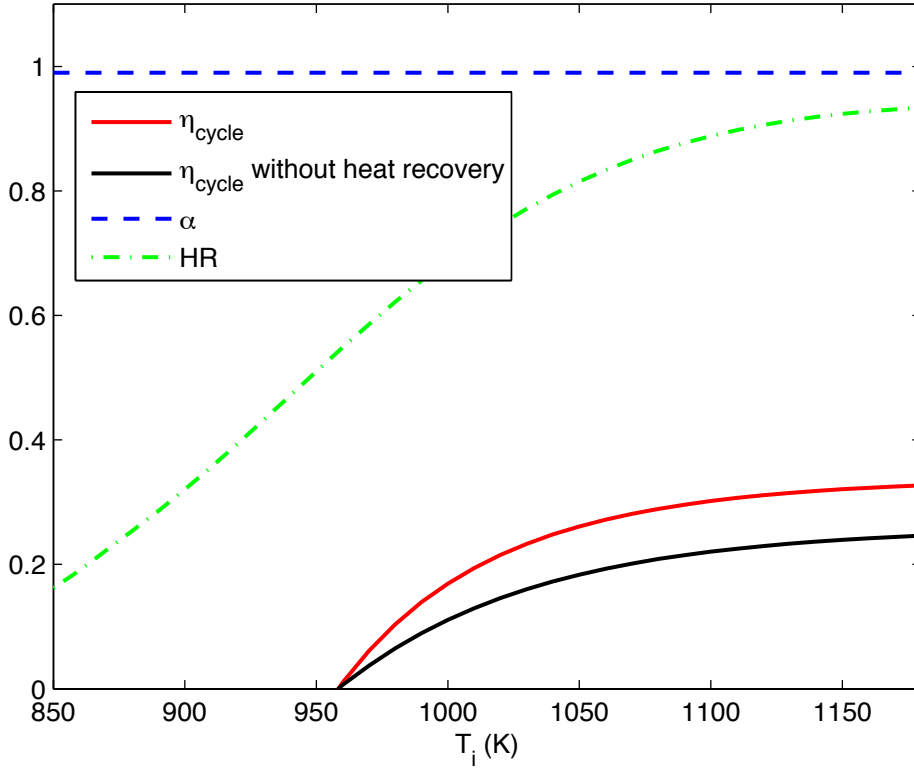


Figure 2.7: Thermodynamic calculations for $\frac{dT^*}{dz^*} = 0.5$.

2.5.2 Effect of Equilibrium Assumption

Regarding the reaction rate, an additional assumption that can be made is that the specific surface area available for the heterogeneous reaction is high enough that the reaction is in equilibrium everywhere in the reactor. Then, for any temperature, the equilibrium constant and initial gas composition will uniquely determine the composition of the gas mixture, as well as the reaction rate for any temperature. The local reaction rate and composition can simply be updated by solution of ΔP in:

$$K_{eq,(T-\Delta T)} = \frac{P_{H_2} + \Delta P}{(P_{Zn} - \Delta P)(P_{H_2O} - \Delta P)} \quad (2.27)$$

When implemented in the numerical solution, the results are virtually indistinguishable from the results assuming reaction-limited conditions. The equilibrium assumption is only accurate when the diffusion length scale is very small, and thus essentially represents the same physical case as the kinetic-limited model.

2.5.3 Conditions for Zn Condensation

In order to verify that condensation of Zn vapor would not occur under a linearly decreasing wall temperature condition, it is interesting to examine the evolution of the Zn partial pressure over the range of temperatures encountered by the reactive flow. These curves are shown for $\frac{dT^*}{dz^*}$ of 0.5 and 5.8 in Fig. 2.8 along with the saturation curve of Zn as predicted by the Antoine equation [78]. It is apparent that when the reaction rate is not limited by mass transfer, the axial temperature drop will not cause over-saturation of the gas mixture with Zn. However, this case is not necessarily practical due to the very fast kinetics of the reaction, and the very small diffusion length scale necessary to achieve kinetics-limited conditions. As the temperature gradient increases, the path of P_{Zn} vs. T gets closer to P_{sat} , because the reactive flow is cooled faster compared to the progress of the reaction.

The effect of mass transfer was examined in order to illustrate that, in a real reactor, over-saturation of the mixture is possible if the diffusion length scale is too large. As a conservative "worst-case" scenario, we consider a constant pressure reactor model with infinite kinetics, and reaction assumed to be limited by the diffusion of Zn

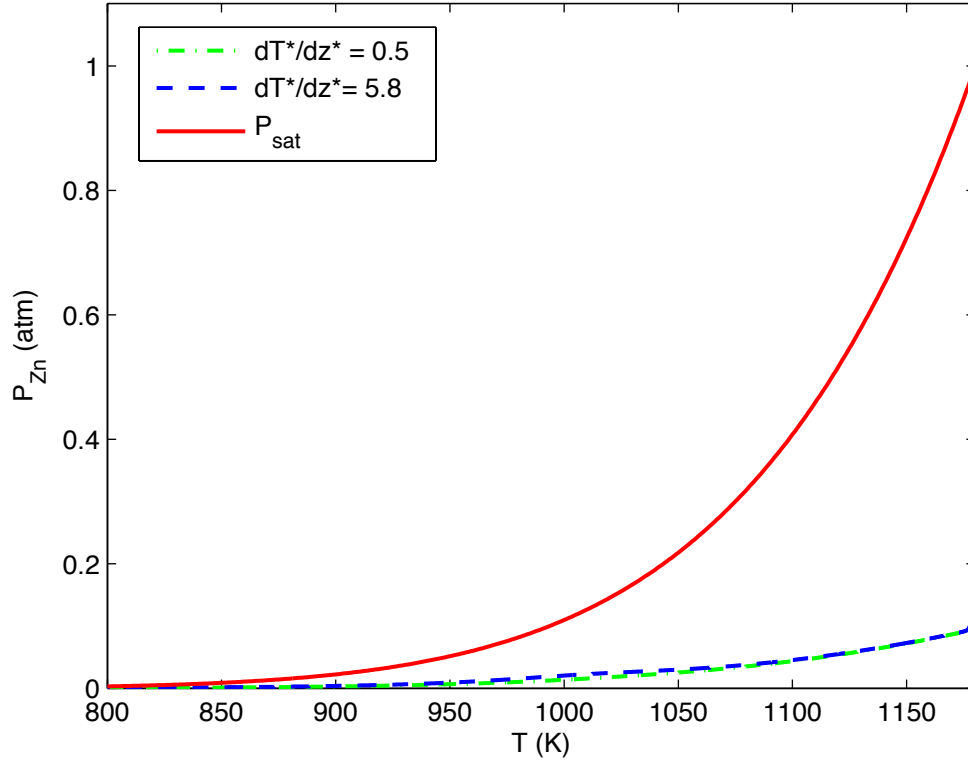


Figure 2.8: Degree of saturation predicted by the model under kinetics-limited conditions. In each case, P_{Zn} drops from 0.5 to below 0.1 in the first 1% of the reactor length due to the mixture being initially very far from equilibrium. The partial pressure of Zn remains well below the saturation pressure, so Zn vapor condensation is not expected.

to the tube wall. Then, the partial pressure of Zn at the wall is zero everywhere, and the mass transfer coefficient is given by [93]:

$$Sh = 3.66 = \frac{2Rh}{D_{Zn}} \quad (2.28)$$

and the reaction rate is given by:

$$r'' = h \frac{P_{Zn}}{R_u T} \quad (2.29)$$

The diffusion coefficient of Zn in Ar at 1 atm and 1250K is taken from [45] and adjusted to the theoretical value at 800K according to kinetic theory [93]. This is done to simulate the slowest rate of diffusion that would be encountered in this temperature

range. The model was run for various tube radii and temperature gradients. Figure 2.9 shows the predicted evolution of Zn partial pressure with temperature, along with the saturation pressure curve for Zn. It is seen that when the tube radius is 20mm and with a temperature gradient of $\frac{dT^*}{dz^*} = 5.8$, the slow diffusion of Zn to the wall retards the reaction to such an extent that the imposed temperature gradient causes P_{Zn} to exceed P_{sat} near 1100K, which leads to the condensation of Zn. When the tube radius is reduced to 5mm, $P_{Zn} < P_{sat}$ for all temperatures and Zn condensation is avoided. Thus, for a practical reactor that does not operate under purely kinetics-limited conditions, care must be taken when applying the negative temperature gradient so as not to cool the mixture too rapidly relative to the possible rate of mass transfer and reaction. The predicted cycle efficiency, heat recovery factor, and Zn conversion α do not differ substantially from the results with kinetics-limited reaction or the equilibrium assumption.

2.5.4 Effect of Incomplete Quench Conversion

Finally, to obtain a more realistic picture of the efficiency of the process, the effect of incomplete quench conversion can be studied by varying β . An imperfect quench process increases the total amount of ZnO that must be dissociated per unit of hydrogen produced. Secondly, if one assumes that the product of the quench process is a powder mixture of Zn and ZnO that cannot be easily separated, then there is an additional parasitic heat loss that must be incurred while heating the mixture to vaporize Zn in the hydrolysis step, as the ZnO must be heated along with Zn. Figure 2.10 shows results for various values of β using $T_i = 1180\text{K}$ and $S = 1.0$, with an instantaneous temperature drop from 1180K to 800K. As β approaches 0, the efficiency likewise approaches zero primarily due to the rapidly increasing solar energy requirements per unit of hydrogen produced. The heat recovery factor likewise decreases, however to a lesser degree, due to the fact that the energy required to heat and vaporize Zn is an order of magnitude higher than that required to bring solid ZnO up to T_i . Thus the parasitic heating effect has a smaller impact on the autothermicity of the hydrolysis reactor. Assuming a value of $\beta = 0.61$ (which was found to be the

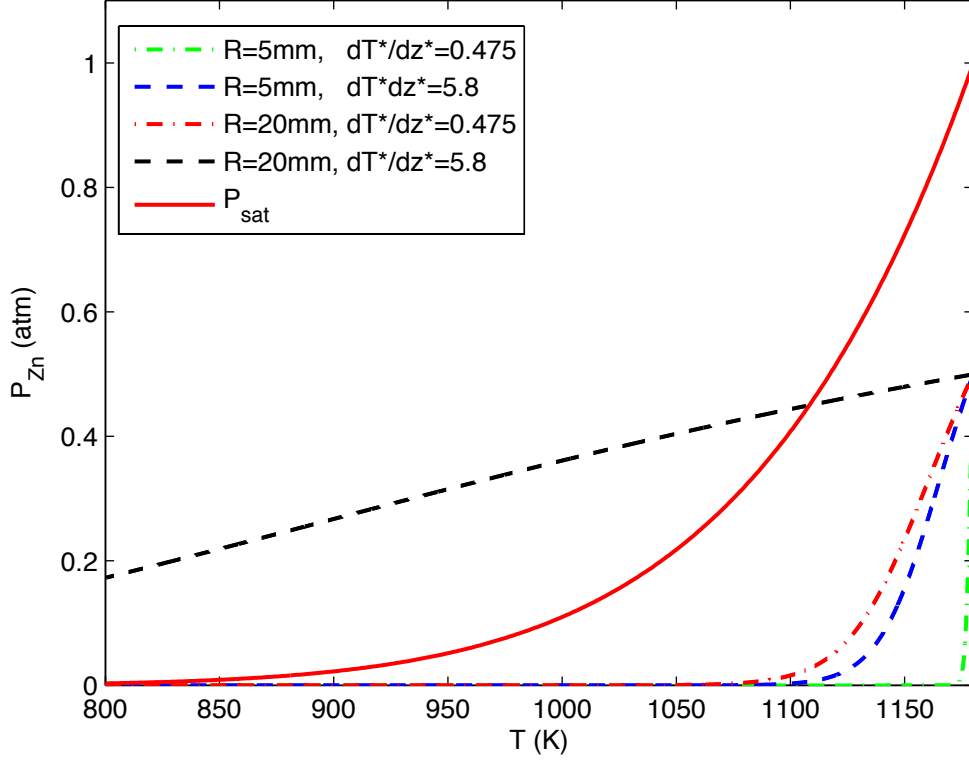


Figure 2.9: Evolution of Zn partial pressure with temperature for mass transfer-limited conditions for different reactor radii and temperature gradients for a constant inlet velocity.

average value for the quench device tested in [32]), for the instantaneous temperature drop case with other parameters as shown in Fig. 2.10, the predicted cycle efficiency is 20.2% assuming full heat recovery. In contrast, for the constant temperature case, the maximum efficiency is 15% with $S = 1.0$ and 17.5% with $S = 2.0$. Here, the efficiency increases with S because the increase in equilibrium conversion in the hydrolysis step more than compensates for the energy required to bring the additional steam up to the inlet temperature. Thus, for both the instantaneous temperature drop case and the constant temperature case, quench inefficiency leads to higher energy input to the solar reactor and increased parasitic heating of ZnO. As a result, the effect of incomplete hydrolysis conversion on efficiency becomes less significant, and the benefit of the temperature gradient approach is decreased.

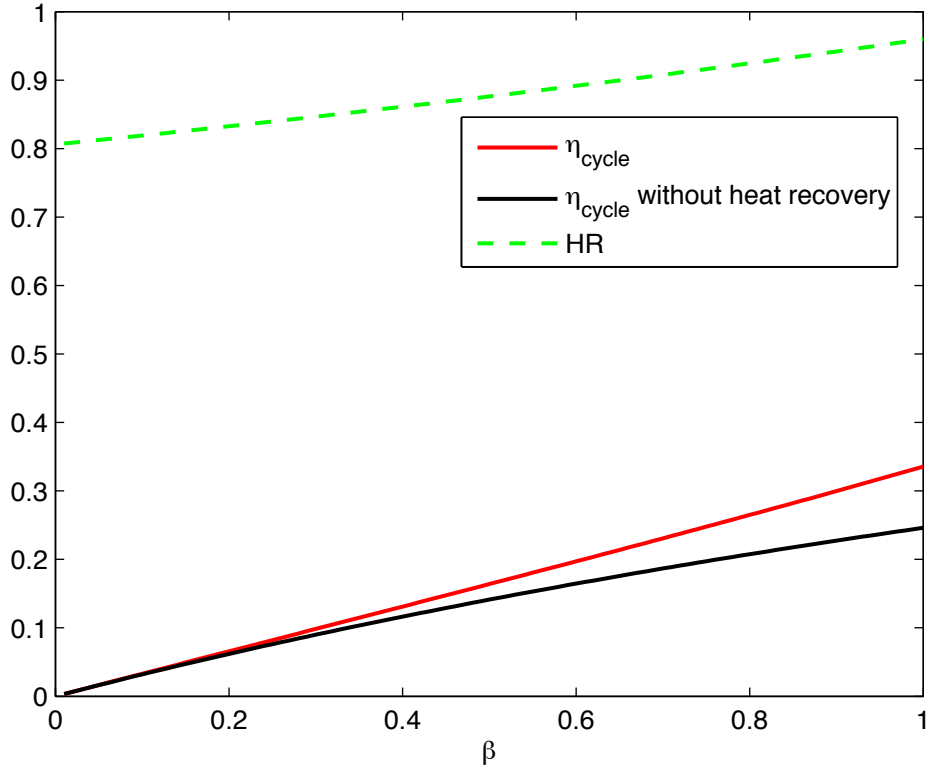


Figure 2.10: Effect of quench conversion on cycle efficiency and heat recovery from hydrolysis with $S = 1.0$, $T_i = 1180$, and an instantaneous temperature drop.

2.6 Conclusions

The results from this analysis show that using a negative axial temperature gradient during hydrolysis with Zn vapor may offer a substantial improvement in maximum cycle efficiency over simply reacting the Zn/H₂O mixture at constant temperature. The benefit to equilibrium conversion at reduced temperatures is mostly responsible for this increase in efficiency. The data also show that operating with an initial temperature close to the normal boiling point of Zn offers the maximum efficiency due to decreased inert gas requirements. With a 1 : 1 stoichiometry, the maximum efficiency for the temperature gradient case is around 38% higher than that of the constant temperature case. Even when the constant temperature case is optimized using a higher stoichiometry of H₂O:Zn, the efficiency for the temperature gradient case is 22% higher. However,

as conditions deviate from the ideal case, i.e., as the quench and/or solar reactor efficiencies decrease, this benefit becomes less significant owing to the large increase in solar energy required per unit of hydrogen produced. Further work is required to clarify the effects of different heat recovery capabilities on the maximum efficiencies expected from constant temperature operation vs. temperature gradient cases.

A practical reactor with a temperature gradient must be designed such that the drop in axial temperature is sufficiently slow relative to the mass transfer-limited reaction so as to avoid condensation of Zn vapor. Such condensation can lead to the formation of Zn particles and droplets which can undergo ZnO passivation leading to a severe curtailment of the hydrolysis reaction, which is precisely the rationale for the current heterogeneous reaction approach.

The maximum calculated efficiency and heat recuperation were found to be relatively insensitive to the assumption of a kinetics-limited reaction, a mass transfer-limited reaction, or the assumption of global gas phase equilibrium. Thus, the cycle efficiency depends more strongly on the initial temperature of the reactor (which determines inert gas requirements) and the final temperature of the reactor (which determines equilibrium conversions) than the temperature gradient, assuming that the gradient is such that Zn condensation does not occur. This implies that in addition to avoiding over-saturation of the mixture, the temperature gradient should be chosen to optimize heat recovery from the hydrolysis reaction. For example, much of the required heat input to the heterogeneous hydrolysis reaction is the latent heat of melting and vaporizing Zn. Thus, the reactor's temperature profile should be chosen so that the reaction rejects enough heat at or above the temperature of Zn evaporation T_i and the melting point of Zn, in order to supply this heat for these phase changes.

From an efficiency viewpoint the temperature gradient option is better than the constant temperature reactor. A temperature gradient also would lend itself more readily to the design of a combined reactor/heat exchanger, where the heat of the reaction is recovered by a fluid in counter-flow to the reactive flow, which would then naturally provide the desired negative temperature gradient. Note that some of the values presented in this Chapter are different than those that were published in [58], as

a minor correction has been made to the calculations. These changes will be reflected in a corrigendum to follow.

Chapter 3

EXPERIMENTAL INVESTIGATION OF HETEROGENEOUS HYDROLYSIS WITH ZN VAPOR UNDER A TEMPERATURE GRADIENT

In this chapter, the hydrolysis step of the Zn/ZnO thermochemical cycle for hydrogen production is experimentally investigated in a laboratory-scale tube-reactor. It is shown that complete conversion of Zn to ZnO is possible at steam-to-Zn stoichiometries greater than 5.0. As the steam-to-Zn stoichiometry approaches unity at reduced inert gas fractions, condensation of Zn on the reactor walls becomes more likely. In addition, the observed gas-phase equilibrium shift toward increased production of ZnO at temperatures under 800K is consistent with earlier theoretical predictions. While complete conversion with low inert gas and steam usage was not achieved, our approach shows great improvement over previous aerosol-based approaches when considering the total amounts of steam and inert gas used per unit of hydrogen produced. Therefore, the current temperature gradient approach is promising for the design of an efficient reactor for water splitting via Zn vapor.

3.1 Introduction

In the present work, we seek to experimentally demonstrate the theoretically predicted improvements in inert gas/steam usage and conversion described above. A non-isothermal reactor was constructed for this purpose and provides a falling temperature profile from nearly the boiling point of Zn to approximately the melting point of Zn. Varying amounts of steam and inert gas were injected in order to study the performance of the reactor, and to assess the feasibility of reliably splitting water using relatively small amounts of steam and inert gas for heterogeneous hydrolysis with Zn vapor. The design and operation of the reactor are described in Section 3.2.1, followed by the experimental procedure in Section 3.2.2 and the method of product analysis

in Section 3.2.3. In Section 5.5, several sets of experiments are described in detail in order to illustrate the major trends and features of the reactor’s performance. Finally, we present our conclusions in Section 5.6.

3.2 Experimental Method

3.2.1 Apparatus

The heterogeneous hydrolysis reactor used in this work is similar in design to those used in previous work on the heterogeneous oxidation of Zn by O₂ [44,45] as well as steam and CO₂ [86]. A series of concentric quartz tubes form the inner geometry of the reactor, all within an electric tube furnace (500W, Fibercraft). Similar to the design presented in [45], the reactor creates a negative axial temperature gradient, in order to study the heterogeneous reaction on the surface of a quartz tube under non-isothermal conditions. The key difference between this design and those used in the nanoparticle approach is that the steam flow is not intended to cool and condense the Zn vapor prior to the reaction. Instead, the reaction begins as soon as the Zn vapor is introduced into the steam co-flow.

As shown in Fig. 3.1, the total heated length of the reactor is 300mm. A 25mm OD quartz tube that forms the outermost wall of the reactor is housed within the tube furnace. Concentrically within this outer tube sits an 8mm OD Zn vapor supply tube, which contains an initially solid sample of Zn. During operation, the Zn melts and begins to vaporize; N₂ carrier gas is pumped into this tube in order to drive Zn vapor out of the tube tip. Steam is also fed to the reactor from a boiler that is supplied with water at a precise rate with a syringe pump as shown in Fig. 3.1. The Zn vapor tube tip is positioned centrally at the mouth of a 4 mm ID reaction tube with a small annular gap around it to allow the introduction of steam co-flow into the reaction tube. The junction of the Zn supply tube tip with the reaction tube is located at the center of the heated length, which is typically the hottest point in the reactor.

Between the outer quartz tube and the reaction tube sits an alumina insert, which has four type-K thermocouples (Omega TJ-CAXL-11-6G-18) embedded at 3cm intervals, beginning at the reaction tube entrance. These thermocouples allow for the

the temperature of the outer tube at the axial location where the reaction typically ends. The difference between the reaction tube temperature and the outer quartz tube temperature was estimated by simultaneously measuring the two temperatures under operational conditions with a purging nitrogen flow and no reactant flows.

3.2.2 Experimental Procedure

Prior to each experiment, Zn ingots (Fisher Scientific Z12-500) are cut into small sections ($\approx 250\text{mg}$) and placed inside of the Zn vapor supply tube. The Zn supply tube and reaction tube are then weighed and their initial masses are recorded. The reactor is then assembled, heated to a set point temperature of 670K, and purged with N_2 for 20 minutes in order to remove any water that may have condensed after previous experiments, as well as to desorb any O_2 and CO_2 that would be available to oxidize Zn. During this time, the boiler and steam line are allowed to heat to approximately 450K. The purging flow of N_2 to the Zn supply tube is then decreased to 3cc/min, and the auxiliary N_2 flow is set to the desired value. This small purging flow into the Zn supply tube is necessary to prevent back-diffusion and reaction of $\text{Zn}_{(\text{g})}$ and steam on the narrow tip of the Zn supply tube before the start of the experiment, which can cause clogging. The flow of steam is then activated and the desired maximum temperature T_{max} is then set with the temperature controller. A small amount of Zn evaporates and oxidizes during the ramping of the reactor temperature; separate measurements indicated that this amount of Zn is less than 5% of the typical Zn mass evaporated during an actual experiment. Once the reactor has reached a steady temperature profile, the carrier flow of N_2 is then introduced to the Zn supply tube, which marks the beginning of the experiment.

After each trial, the steam flow and the carrier N_2 flow to the Zn supply tube are stopped, while the auxiliary N_2 flow is increased for cooling purposes. The temperature controller is then turned off and the reactor is allowed to cool to room temperature. The evaporation tube and reaction tube are both removed and weighed. The reaction tube is then cut into small sections (1-1.5cm in length). The sections are weighed individually and their masses are recorded.

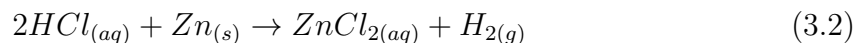
3.2.3 Product Analysis

The Zn/ZnO deposits were very difficult to remove from the reaction tube by mechanical means, so a chemical method was employed to measure the respective amounts of the two species within each section of the reaction tube. The mass of ZnO in a given tube section was calculated by:

$$m_{ZnO} = m_{tube,f} - m_{tube,init} - m_{Zn} \quad (3.1)$$

where $m_{tube,i}$ is the initial mass of the tube section with the Zn/ZnO deposit, $m_{tube,f}$ is the mass of the tube section with all deposits chemically removed, and m_{Zn} is the mass of deposited Zn determined from the volume of $H_{2(g)}$ produced upon reaction with an HCl solution.

The evolved $H_{2(g)}$ is measured by an addition funnel (Chemglass CG-1708-04) with an embedded pressure transducer (Honeywell 26PCCFB2G) which produces a voltage, as shown in Fig. 3.2. The addition funnel fits into a standard Erlenmeyer flask (500mL, 24/40 taper) with two PTFE O-rings (Kontes 676005-2440) to create a good seal. The unreacted reaction tube section initially sits in the flask, along with a magnetic stirrer. The initial voltage is recorded, then the flask is flooded with the HCl (150mL, 5M) from the addition funnel. Upon exposure to the HCl solution, the ZnO dissolves and the Zn reacts according to:



The final voltage produced by the H_2 pressure is recorded, and the tube section is removed, dried, and weighed. This pressure measurement method makes it possible to process many tube sections reliably and quickly. As shown in Fig. 3.3, a series of experiments with known Zn masses was conducted to construct a calibration curve of measured voltage vs. Zn mass. The method is found to produce a strong voltage signal even when the available mass of Zn is ≈ 1 mg.

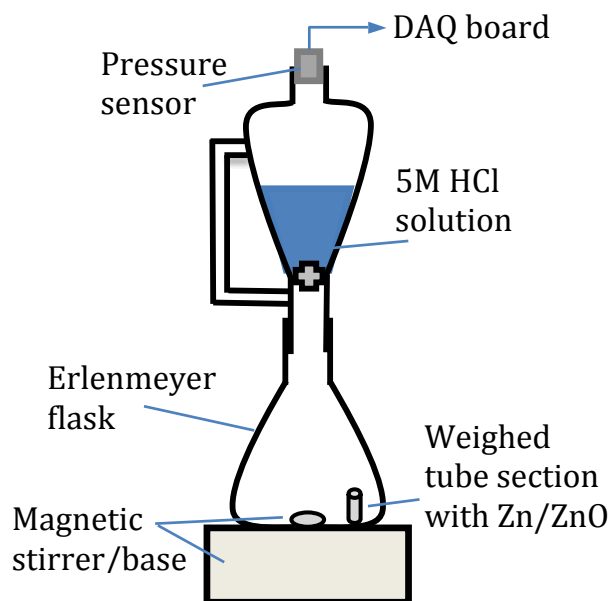


Figure 3.2: Two-chamber pressure measurement setup used for determining Zn mass in reaction tube samples.

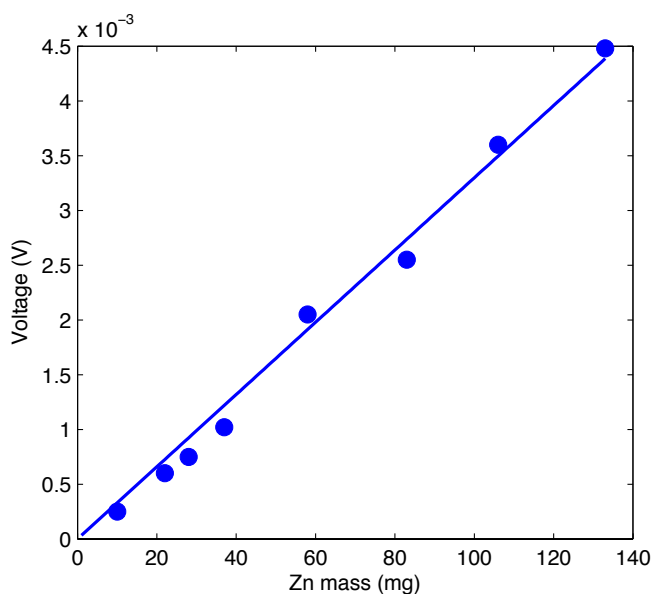


Figure 3.3: Calibration curve used for determining Zn mass in reaction tube samples.

Once the amounts of Zn and ZnO are determined for all tube sections from a

given experiment, the conversion of Zn to ZnO is calculated as:

$$Conversion = \frac{\sum_j m_{ZnO,j}/M_{ZnO}}{\sum_j m_{ZnO,j}/M_{ZnO} + \sum_j m_{Zn,j}/M_{Zn}} \quad (3.3)$$

where $m_{Zn,j}$ and $m_{ZnO,j}$ are the measured masses of Zn and ZnO, respectively, for the j th section of the given reaction tube, and M_{Zn} and M_{ZnO} are the molar masses of Zn and ZnO, respectively. The change in mass of the Zn tube during an experiment, Δm_{evap} , as well as the duration of the experiment are used to calculate the average Zn molar flow rate.

$$\dot{n}_{Zn} = \frac{\Delta m_{evap}}{M_{Zn} t_{exp}} \quad (3.4)$$

The experiment duration t_{exp} is taken to be the time that the N_2 carrier flow is active. The molar flow rate can also be calculated by the total moles of Zn and ZnO deposited in the reaction tube, which was found to agree well with the method shown above.

3.3 Results and Discussion

The appearance of a typical reaction tube after an experiment is shown in Fig. 3.4. The transition from primarily ZnO deposits on the left, which is the hottest section of the reactor, to a mixture of Zn/ZnO in the middle in light gray, with mostly Zn on the right. A band of ZnO deposits are also shown on the right, possibly due to the shifting of equilibrium in the cooler section of the tube.



Figure 3.4: Reaction tube after an experiment.

A cross section of the entrance region of the reaction tube is shown in Fig. 3.5. The deposits form a solid layer of ZnO which has been broken by cutting the tube open.



Figure 3.5: ZnO deposits in the entrance region of a reaction tube.



Figure 3.6: A reaction tube with significant ZnO deposition near the tube entrance.

A reaction tube with a significant amount of ZnO deposition at the tube entrance is shown in Fig. 3.6, and similarly in Fig. 3.7. Here, the deposits are seen to take an orange/yellow color. Deposits of Zn are seen in black further away from the entrance of the reaction tube in Fig. 3.6.

The operating conditions for different experiments are shown in Table 3.1. Experiment 1 has a large excess of steam and relatively little $N_{2(g)}$. It is apparent that

Table 3.1: Operating conditions and Zn to ZnO conversions for different experiments

	T_{max} (K)	T_{min} (K)	m_{dep} (g)	$\dot{n}_{H_2O}/\dot{n}_{Zn}$	$\dot{n}_{N_2}/\dot{n}_{Zn}$	\dot{n}_{tot} (mol/min)	Conversion (%)	Cycle efficiency (%)
1	1123	697	0.618	16.1	2.78	0.014	100	9.91
2	1143	747	1.151	5.2	1.17	0.016	88.3	17.4
3	1143	803	2.82	5.08	0.65	0.015	41.0	7.3
4	1133	776	0.485	5.14	3.62	0.013	58.3	7.2
5	1158	727	0.94	1.88	0.73	0.0056	36.1	7.9
6	1158	758	0.168	4.12	0.57	0.0049	98.8	22.9
7	1163	732	0.38	2.9	0.95	0.0058	80.5	18.9
8	1178	803	2.824	1.94	0.48	0.0054	33.5	7.6
9	1158	766	1.33	1.13	0.49	0.0066	41.9	10.6
10	1153	781	0.703	0.87	0.76	0.0085	46.7	11.8

there is no measurable amount of Zn deposited in the reactor, as shown by the flat line of Zn mass in Fig. 3.8, and thus the conversion is 100%. Near the 8cm axial position, there is a slight increase in the deposition of ZnO, which corresponds to decreasing temperature, as shown. This is likely evidence of the shift in gas-phase equilibrium toward formation of $H_{2(g)}$ and $ZnO_{(s)}$ with decreasing temperature. Experiment 2 has nominally the same total molar flow rate but slightly higher temperatures and a much lower stoichiometry of $H_{2O(g)}:Zn$ compared to Exp. 1. Here, due to the decreased amount of steam in the entrance region, a lower proportion of the Zn reacts near the entrance, and more ZnO forms downstream. In the cooler downstream region, the Zn partial pressure remains high enough that some Zn begins to condense and deposit around 5cm from the inlet, as shown in Fig. 3.9, and the overall conversion is 88.3%. Concurrent with this Zn deposition is a slight increase in ZnO deposition, similar to that in Exp. 1. Experiment 3 has very similar conditions to Exp. 2, but with a lower proportion of $N_{2(g)}$, leading to even higher Zn partial pressures, increased Zn deposition, and a much lower conversion of 41.0%. Experiment 4 has similar temperature and total molar flow conditions to Exps. 1-3, but a much higher proportion of $N_{2(g)}:Zn$. As shown in Fig. 3.10, the distribution of deposited mass is shifted even more toward the cooler region of the reactor compared to Figs. 3.8 and 3.9, likely due to the increased dilution by $N_{2(g)}$ and the resulting slower reaction kinetics at the entrance. Again,

the partial pressure of Zn remains high enough to lead to significant Zn deposition beginning near the 7cm position. A second peak of ZnO deposition is also apparent beginning near the 8cm position, due to lower temperatures favoring an increasing rate of ZnO formation.

As discussed in Section 3.1, the current method theoretically allows for complete Zn to ZnO conversion using very little inert gas and low $\text{H}_2\text{O}_{(g)}:\text{Zn}$ stoichiometries, so it was of particular interest to investigate these conditions. Experiments 5 and 6 have similar total molar flows, $\text{N}_{2(g)}:\text{Zn}$ ratios, and similar temperature ranges, however the $\text{H}_2\text{O}_{(g)}:\text{Zn}$ stoichiometry is more than twice as high for Exp. 6. There is a nearly complete conversion in Exp. 6, but a conversion of only 36.1% in Exp. 5. Experiment 7 has similar total molar flow and temperature to Exp. 5, however with slightly higher $\text{H}_2\text{O}_{(g)}:\text{Zn}$ and $\text{N}_{2(g)}:\text{Zn}$ ratios, yet the conversion is much higher, at 80.5%.

As shown in Fig. 3.11, the deposition profile for Exp. 8 is qualitatively very similar to Exp. 4, with the increase in ZnO deposition lagging slightly behind the onset of Zn condensation. Experiments 9 and 10, very nearly achieve the theoretical optimum operating conditions, with very little nitrogen and a $\text{H}_2\text{O}_{(g)}:\text{Zn}$ stoichiometry of 1, and achieve almost the same Zn to ZnO conversions of 42.0% and 46.7%, respectively. As shown in Figs. 3.12 and 3.13, the overall deposition profiles are also very similar, with very pronounced Zn condensation occurring beginning near the 7cm position, as well as a small degree of condensation occurring in the entrance region. Due to the very high initial partial pressures of Zn, it is likely that some degree of supersaturation occurred shortly after the gas entered the reaction tube for both experiments. Increases in ZnO deposition are again found in the cooler region of the reactor, although condensation of Zn is obviously the more dominant of the two processes under these conditions.

The current reactor design is unable to achieve complete conversion in most experiments for several reasons. First, the temperature profile created by the heater consistently experienced a sharp drop approaching the reactor outlet resulting in outlet temperatures that were slightly lower than that necessary for complete conversion. Second, the rate of reaction, which is largely diffusion-controlled for the given reactor tube radius, was too small in the hotter section of the reactor, which caused an elevated

Zn partial pressure as the flow entered the cooler section resulting in Zn condensation there. In order to remedy this, the reaction tube was packed with glass wool fibers in order to provide additional surface area for the reaction, however the pressure drop due to this packing interfered with the flow of steam from the boiler. Condensation in the cooler section of the reactor could also be prevented by reducing the overall flow rates of reactants, allowing for greater diffusion and reaction before cooling. However, our experimental setup did not permit us to reduce the flow rate of water below 0.05cc/min while still ensuring a steady flow of steam. For the chosen range of flow rates and reaction tube radius, the reactor could also be made longer to react more Zn before significant cooling of the reactants occurs.

In most experiments with incomplete conversion, a small amount of very fine grey powder was found at the outlet of the reactor, similar to that found in work on the Zn nanoparticle synthesis approach [63, 71]. As shown in Fig. 3.14, the dust collected in the outlet region consists of sub-micron-scale Zn particles with small wires of ZnO, similar to results found in [71]. This is indicative of homogeneous condensation of Zn followed by oxidation of the Zn surface as well as heterogeneous hydrolysis with still-available Zn vapor surrounding the particle, which deposit layer-by-layer to form the ZnO wires. The total mass of this powder is typically under 10mg, constituting a small percentage of the total Zn that is deposited in an experiment. Larger deposits of Zn were also found further upstream stuck to the reaction tube wall by a layer of solid ZnO that was deposited by the heterogeneous hydrolysis reaction, as shown in Fig. 3.15. These particles ranged from the micron scale to the millimeter scale further upstream. In hotter sections of the reactor, the deposited Zn was in the form of smooth droplets that had either formed from direct condensation onto the reaction tube walls, or from agglomeration of smaller, homogeneously-condensed droplets, or a combination of the two.

With the observation that Zn and ZnO are often co-deposited in the cooler section of the reaction tube, the question arises as to whether the measured ZnO was deposited due to the heterogeneous reaction or the oxidation of solid and liquid Zn that had condensed. As discussed in Section 3.1, Zn droplets and particles have been found

to follow a fast surface reaction followed by a much slower shrinking-core-model reaction that is limited by $\text{Zn}_{(s)}$ diffusion; this passivating effect is also stronger with increasing steam mole fraction [59]. However, in our case, there is also Zn vapor available that could react heterogeneously on deposited Zn, thereby further passivating it, as shown for the particles in Fig. 3.14. It was also found that the oxidation of liquid Zn by steam is not thermodynamically favored in this temperature range [54]. Moreover, the increases in ZnO and Zn deposition do not always coincide with one another, as shown in Figs. 3.10 and 3.11. Since the onset of increased ZnO deposition can occur before or after the onset of Zn condensation, it is more likely that the two are due to different phenomena, rather than both being the result of Zn deposition.

To summarize our findings, Fig. 3.16 demonstrates Zn to ZnO conversions approaching 100% using an excess of steam, and somewhat decreased conversions by using higher proportions of inert gas. When the proportions of both steam and inert gas are lowered, where it is energetically optimal to operate the reactor, the Zn to ZnO conversion is reduced. As shown in Table 3.2, the results of Exps. 9 and 10, while not achieving complete conversion, show great improvement over previous aerosol-based approaches to hydrolysis with Zn when considering the total amounts of steam and inert gas used per unit of hydrogen produced. The values from other authors are the minimum values that could be determined from the published data. Comparing Exps. 9 and 10 to the best case found in [55], which all have nearly the same conversion, the effect of excess steam and inert gas usage on cycle efficiency can be examined. Using the definition of overall thermal efficiency presented in [58] the cycle efficiencies for Exps. 9 and 10 would be 10.6% and 11.7%, respectively, whereas the case in [55] would not be a net producer of work due to the excessive cost of inert gas separation. Alternatively, if the efficiency were defined to include the work of inert gas separation in its denominator, Exps. 9 and 10 would have cycle efficiencies of 11.9% and 13.4%, respectively, and that of the case in [55] would be 3.3%. The highest efficiency that could be predicted from previous work would be from [65], which at 4.3% is approximately one-third of that demonstrated in Exps. 9 and 10. Although the previous authors do

not emphasize an attempt to minimize steam and inert gas usage, these calculated efficiency values highlight the benefits of the current hydrolysis reactor design. However, as shown in Table 1, the highest predicted efficiencies (using the definitions in [58]) correspond to Exps. 6 and 7, which have moderate amounts of inert gas and steam usage, but much higher conversions than Exps. 9 and 10. Thus, the degree of conversion during hydrolysis also has a significant effect on cycle efficiency, and optimal performance is obtained by maximizing conversion and minimizing both inert gas and steam usage.

Table 3.2: Comparison of current results to previous work

Author	Conversion (%)	H ₂ O:H ₂	inert:H ₂
Current (Exp. 9)	41.9	2.71	1.16
Current (Exp. 10)	46.7	1.851	1.62
[55]	41.0 (overall)	4.39	165.4
[67]	95.0 (overall) 19.0 (aerosol)	26.7	188.8
[64]	90.0 (overall) 80.0 (aerosol)	66.14	183.8
[65]	28.0 (overall) 11.0 (aerosol)	11.9	37.2
[70]	96.0 (overall)	51.02	348.33

3.4 Conclusions

A laboratory-scale reactor for studying the heterogeneous hydrolysis of steam by Zn vapor under a temperature gradient was developed and tested. The reactor features a quartz reaction tube housed within an electric tube furnace such that an axial temperature profile is imposed from nearly the boiling point of Zn at the inlet to approximately the melting point of Zn at the outlet. The reactor’s negative axial temperature gradient is aimed at minimizing carrier gas usage, and shifting the chemical equilibrium toward complete conversion of Zn to ZnO near the outlet. Following each experimental run, a wet chemical method is used to determine the Zn and ZnO deposition profiles along the length of the reaction tube. It is observed in several cases that the deposition of ZnO is markedly increased in the cooler section of

the reactor, despite the lower local partial pressure of $\text{Zn}_{(\text{g})}$. This observation provides evidence for the intended shift in chemical equilibrium that forms the basis for pursuing a temperature-gradient reactor. However, significant amounts of Zn condensation are also observed in the reactor, due to both homogeneous condensation of submicron Zn particles/droplets, as well as heterogeneous condensation of Zn on the reaction tube wall, with the latter being the dominant effect. Higher levels of condensation are observed with higher initial Zn concentrations.

The current design of the reactor does not allow straightforward recovery of the ZnO deposit from the reactor wall. The current work could be extended to achieve a continuous reactor design, for example, by using a sweep gas to evaporate the Zn out of the Zn/ZnO powder product of the quench step, which then reacts heterogeneously on the remaining ZnO particles downstream. This differs from the approach in [75], as evaporation and hydrolysis would occur in separate zones, thus preventing any passivation of the Zn particles. Here, the temperature gradient would enable the fast evaporation of Zn with minimal inert gas at high temperatures, followed by the equilibrium shift toward ZnO formation at lower temperatures.

The current work has demonstrated significant improvements over previous approaches in terms of minimizing steam and inert gas usage per unit of hydrogen produced. Thus, from an overall thermal efficiency standpoint, the current temperature-gradient approach represents a promising pathway for the hydrolysis step in the Zn/ZnO thermochemical cycle for renewable hydrogen production. It should be noted that material from this section was also published in [130].



Figure 3.7: A reaction tube that is nearly clogged in the entrance region.

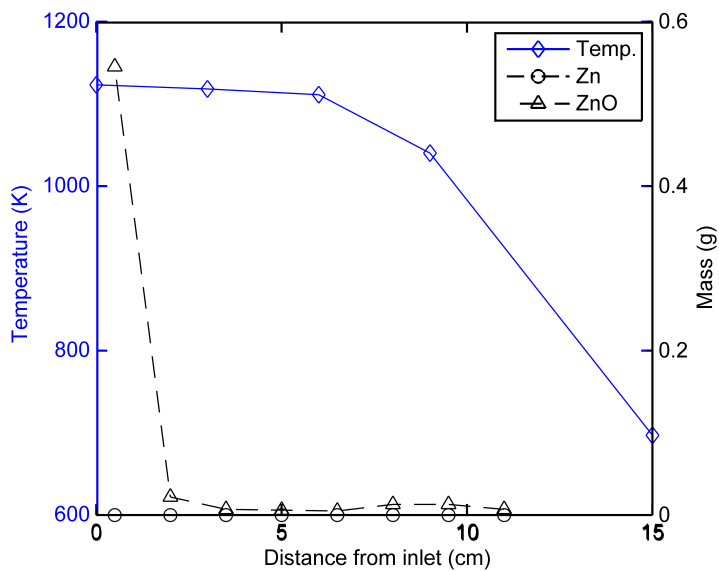


Figure 3.8: Profiles of Zn/ZnO deposits and temperature for Experiment 1, with $T_{max} = 1123$, $T_{min} = 693$, $\dot{n}_{H_2O}/\dot{n}_{Zn} = 16.1$, $\dot{n}_{N_2}/\dot{n}_{Zn} = 0.25$, and $\dot{n}_{tot} = 0.014$ (mol/min).

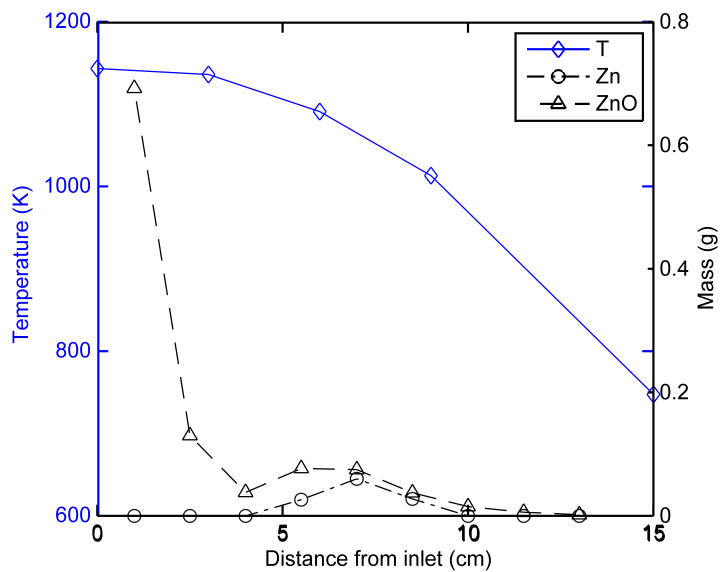


Figure 3.9: Profiles of Zn/ZnO deposits and temperature for Experiment 2, with $T_{max} = 1143$, $T_{min} = 747$, $\dot{n}_{H_2O}/\dot{n}_{Zn} = 5.2$, $\dot{n}_{N_2}/\dot{n}_{Zn} = 1.17$, and $\dot{n}_{tot} = 0.016$ (mol/min).

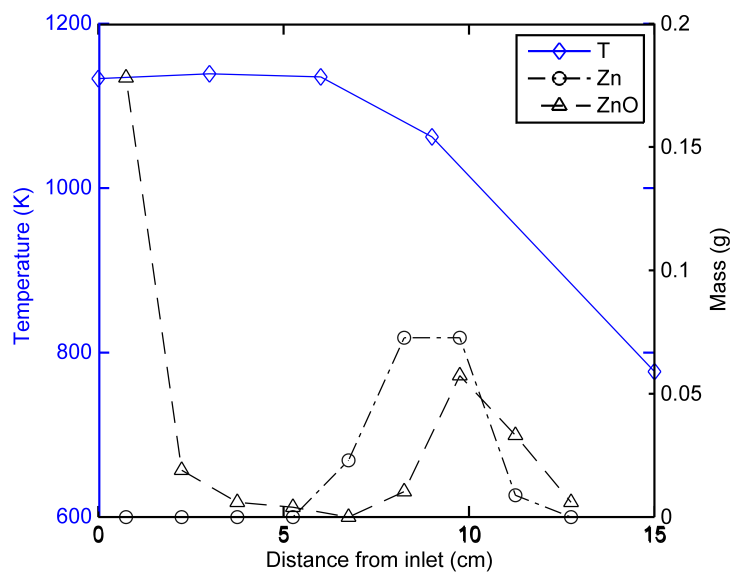


Figure 3.10: Profiles of Zn/ZnO deposits and temperature for Experiment 4, with $T_{max} = 1133$, $T_{min} = 776$, $\dot{n}_{H_2O}/\dot{n}_{Zn} = 5.14$, $\dot{n}_{N_2}/\dot{n}_{Zn} = 3.62$, and $\dot{n}_{tot} = 0.013$ (mol/min).

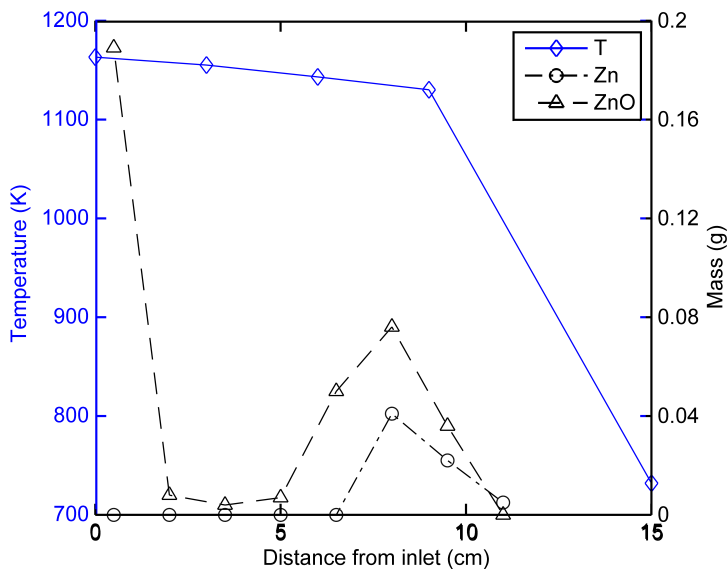


Figure 3.11: Profiles of Zn/ZnO deposits and temperature for Experiment 7, with $T_{max} = 1163$, $T_{min} = 732$, $\dot{n}_{H_2O}/\dot{n}_{Zn} = 2.9$, $\dot{n}_{N_2}/\dot{n}_{Zn} = 0.95$, and $\dot{n}_{tot} = 0.0058$ (mol/min).

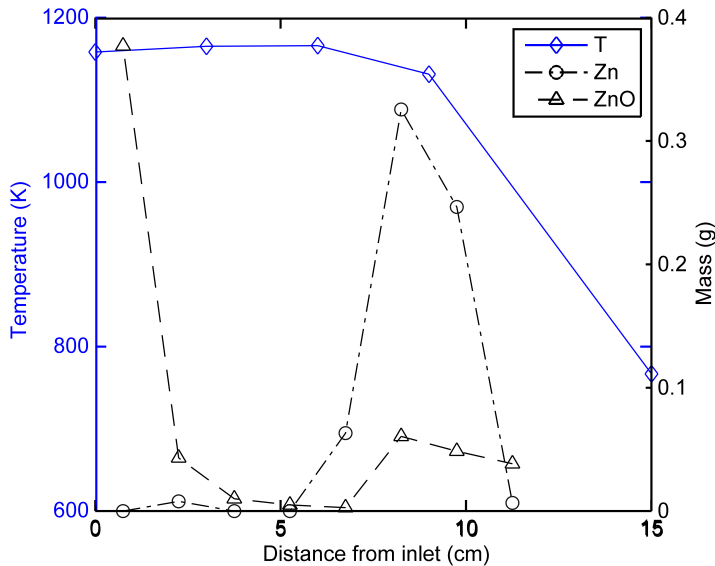


Figure 3.12: Profiles of Zn/ZnO deposits and temperature for Experiment 9, with $T_{max} = 1158$, $T_{min} = 766$, $\dot{n}_{H_2O}/\dot{n}_{Zn} = 1.13$, $\dot{n}_{N_2}/\dot{n}_{Zn} = 0.49$, and $\dot{n}_{tot} = 0.0059$ (mol/min).

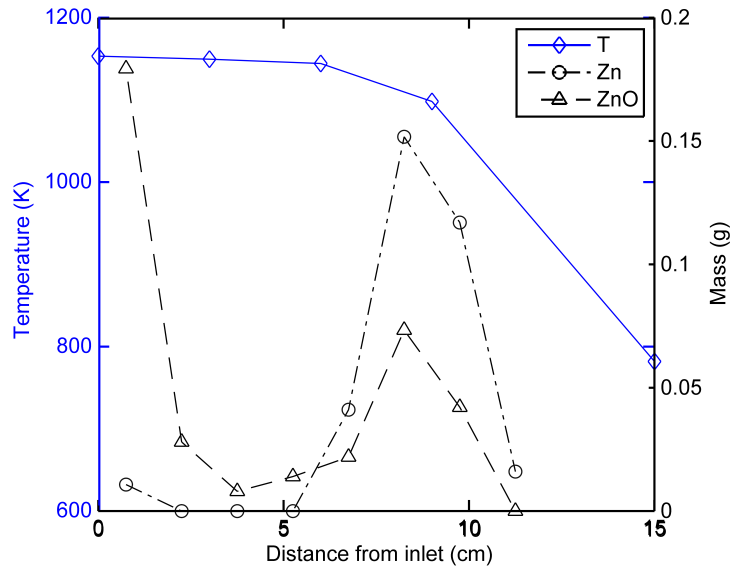


Figure 3.13: Profiles of Zn/ZnO deposits and temperature for Experiment 10, with $T_{max} = 1153$, $T_{min} = 781$, $\dot{n}_{H_2O}/\dot{n}_{Zn} = 0.87$, $\dot{n}_{N_2}/\dot{n}_{Zn} = 0.76$, and $\dot{n}_{tot} = 0.0085$ (mol/min).

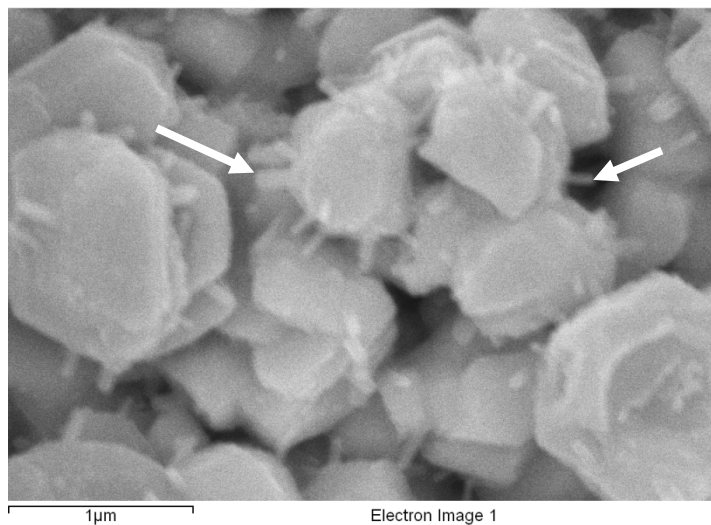


Figure 3.14: SEM image of particulate matter found at exit of reactor in Experiment 7. The arrows indicate ZnO nanowires that grew on homogeneously condensed Zn particles.

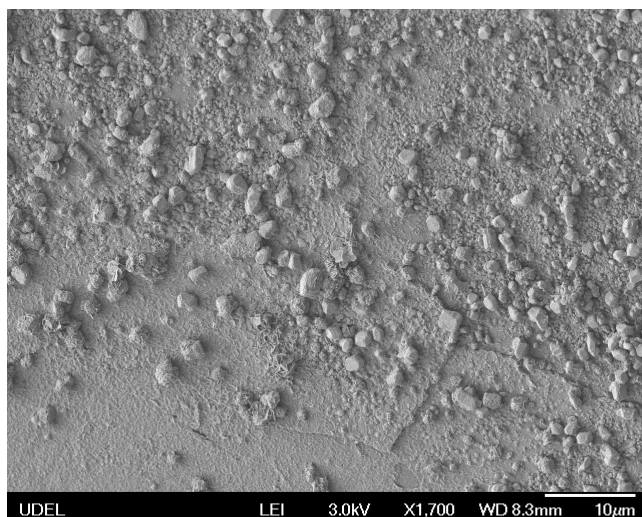


Figure 3.15: SEM image of Zn/ZnO deposits on the inner surface of a reactor tube for Experiment 7. The larger particles are partially oxidized Zn particles. The surface they sit on is a layer of ZnO deposited heterogeneously.

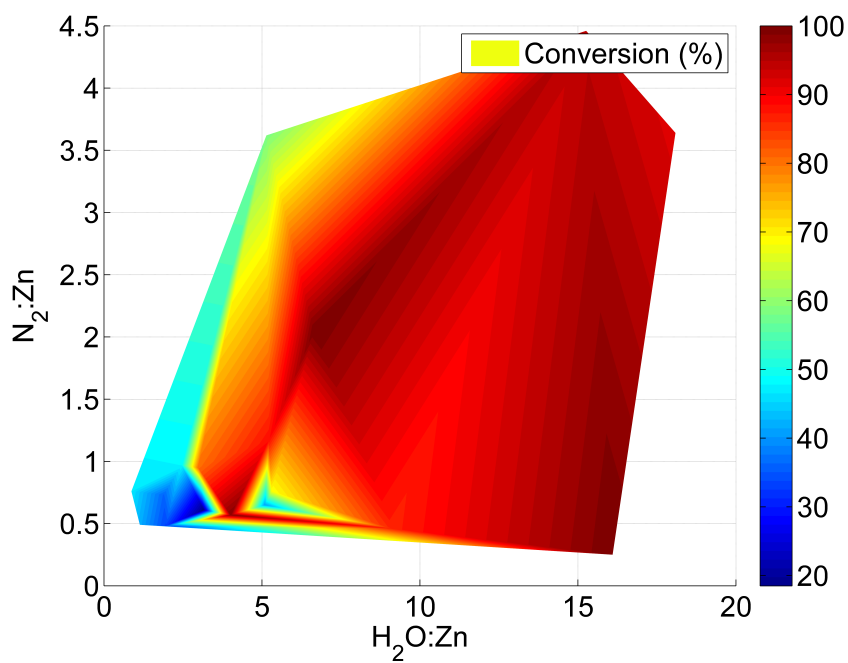


Figure 3.16: Zn to ZnO conversions vs. $N_2 : Zn$ and $H_2O : Zn$ ratios for various experiments. When a large excess of steam is available, complete conversion is possible. Conversions are generally smaller when lower amounts of steam and inert gas are used due to increased Zn condensation.

Chapter 4

BACKGROUND ON LATTICE BOLTZMANN METHODS

4.1 Background on the Boltzmann Equation

Lattice Boltzmann methods are a class of computational fluid dynamics methods based on the numerical solution of a discrete form of the Boltzmann equation. The Boltzmann equation is a well-known equation in statistical mechanics, and describes evolution of the velocity distribution function in a non-equilibrium thermodynamic system [95]. The velocity distribution function f describes the probability that a particle in a fluid will lie within a differential volume $d^3\vec{x}$ of position \vec{x} and with a velocity within a differential “volume” $d^3\vec{v}$ in the velocity space around velocity \vec{v} . The number density of particles in this spatial position and velocity “position” at time t can be written as $f(\vec{x}, \vec{v}, t)$, so that the overall number density of particles at this spatial position can be written by integrating the velocity distribution function over all possible velocities:

$$n(\vec{x}, t) = \int f(\vec{x}, \vec{v}, t) d^3\vec{v} \quad (4.1)$$

The typical macroscopic hydrodynamic variables of interest can be easily derived from the distribution function f . The fluid mass density can be found multiplying the number density by the individual particle mass m :

$$\rho(\vec{x}, t) = m \int f(\vec{x}, \vec{v}, t) d^3\vec{v} \quad (4.2)$$

The momentum in terms of hydrodynamic velocity $\vec{u}(\vec{x}, t)$ can similarly be found by integrating $f\vec{v}$ instead of f :

$$\rho(\vec{x}, t)\vec{u}(\vec{x}, t) = m \int f(\vec{x}, \vec{v}, t)\vec{v} d^3\vec{v} \quad (4.3)$$

Using the definition of the Boltzmann constant, the macroscopic internal energy of an ideal gas can also be found from taking the moment of f with $\frac{1}{2}|\vec{v} - \vec{u}|^2$, where $|\vec{v} - \vec{u}|$ is the “peculiar velocity”, which is related to the temperature [96].

$$\frac{3}{2}nk_B T = \rho E = m \int \frac{1}{2}|\vec{v} - \vec{u}|^2 f(\vec{x}, \vec{v}, t) d^3\vec{v} \quad (4.4)$$

Here, k_B is the Boltzmann constant, T is the temperature, and E is the internal energy per unit mass [97].

The value of f at thermodynamic equilibrium, $f^{eq}(\vec{v})$, is given by the Maxwell-Boltzmann distribution. This is a statistical distribution of microscopic velocities that depends on the hydrodynamic velocity, temperature, and the density of the fluid [95]. The distribution can be expressed as:

$$f^{eq}(\vec{v}) = \frac{\rho/m}{(2\pi R_u T)^{3/2}} \exp\left(\frac{-|\vec{v} - \vec{u}|^2}{2R_u T}\right) \quad (4.5)$$

It can be shown that the moments of $f^{eq}(\vec{v})$ satisfy the same relations as those of $f(\vec{x}, \vec{v}, t)$ [97], namely:

$$\rho = m \int f^{eq}(\vec{v}, t) d^3\vec{v} \quad (4.6)$$

$$\rho\vec{u} = m \int \vec{v} f^{eq}(\vec{v}, t) d^3\vec{v} \quad (4.7)$$

$$\rho E = m \int \frac{1}{2}|\vec{v} - \vec{u}|^2 f^{eq}(\vec{v}, t) d^3\vec{v} \quad (4.8)$$

The Boltzmann equation describes the evolution of the velocity distribution function f due to collisions between particles and external forces, and can be written as:

$$\left(\frac{\partial}{\partial t} + \vec{v} \cdot \nabla\right) f(\vec{v}, \vec{x}, t) = \omega(f) \quad (4.9)$$

where ω is a collision operator, which conserves mass, momentum, and energy. The collision operator can be formulated many different ways, depending on particular assumptions about the system. For the case of an ideal, dilute gas with perfect binary

collisions, and negligible intermolecular forces it can be shown that any integral moments of f with m , $m\vec{v}$, and $m|\vec{v} - \vec{u}|^2$ are zero [96]. Using this fact along with the moments derived above, and taking moments of Eq. 4.9, one can derive the continuity (mass conservation) equation [96]:

$$\frac{\partial}{\partial t}(\rho) + \nabla \cdot (\rho\vec{u}) = 0 \quad (4.10)$$

and the momentum equations [96]:

$$\frac{\partial}{\partial t}(\rho\vec{u}) + \nabla \cdot (\rho\vec{u}\vec{u}) = -\nabla P \quad (4.11)$$

where P is the symmetric pressure tensor, given in terms of f by [96]:

$$P = \frac{1}{3}m \int |\vec{v} - \vec{u}|^2 f(\vec{x}, \vec{v}, t) d^3\vec{v} \quad (4.12)$$

One can also derive the pressure heuristically from a kinetic theory analysis [98]. If one considers a particle with mass m moving in a volume of L^3 at speed v_x , then the change in momentum due to a collision with one of the “walls” of the container (perpendicular to its motion) is $mv_{in} - mv_{out} = mv_{in} - (-mv_{in}) = 2mv_x$, assuming a perfectly elastic collision. If this is averaged over N particles with average speed v_x , then the average force on the volume “wall” is $F = \frac{Nmv_x}{\Delta t}$. The “turnaround time” $\Delta t = L/v_x$ where L is the length scale of the volume element. Assuming spatial isotropy of the velocities, we can say that the total velocity of the particle $\bar{v}^2 = v_x^2 + v_y^2 + v_z^2 = 3v_x^2$, and so the pressure can be written as:

$$P = \frac{F}{L^2} = \frac{Nm\bar{v}^2}{3V} = \frac{nm\bar{v}^2}{3} \quad (4.13)$$

which is essentially the same as Eq. 4.12 with $\bar{v} = |\vec{v} - \vec{u}|$. Here, \bar{v} can be considered the “peculiar velocity” because the situation is the same if the entire system moves with hydrodynamic velocity \vec{u} . From Eq. 4.12, as well as the definition of the Boltzmann constant, we see that

$$\frac{3}{2}k_B T = \frac{1}{2}m\bar{v}^2 = \frac{3}{2n}P = \frac{m}{2n} \int |\vec{v} - \vec{u}|^2 f(\vec{x}, \vec{v}, t) d^3\vec{v} \quad (4.14)$$

which is consistent with Eq. 4.4.

Hence, under some simplifying assumptions, the Boltzmann equation is consistent with the ideal equation of state of a gas, as well as the conservation equations of mass and momentum which are typically of interest in engineering practice.

4.2 Lattice Boltzmann Model for Incompressible Fluid Flow

The goal of the lattice Boltzmann method is to find the hydrodynamic variables of interest by solving for the particle distribution functions f at a discrete set of uniformly-spaced node points (the lattice) and for a discrete set of particle velocities. In typical CFD schemes, the problem is only discretized in space and time, but for solution of the Boltzmann equation, the problem must also be discretized in the “velocity space”. The most common assumption in lattice Boltzmann schemes for incompressible fluid flow is that the collision operator $\omega(f)$ follows the so-called Bhatnagar-Gross-Krook (BGK) model [97], which states that

$$\omega = -\frac{1}{\kappa}(f(\vec{v}, \vec{x}, t) - f^{eq}(\vec{v}, t)) \quad (4.15)$$

where κ is a constant “relaxation time”. Thus, the collision is simply proportional to the non-equilibrium component of f . By integrating Eq. 4.9 over a time step δt , with the spatial and time steps linked by a discrete velocity \vec{e} so that $\delta\vec{x} = \vec{e}\delta t$, the discrete “lattice” form of the Boltzmann equation becomes [99]:

$$f(\vec{v}, \vec{x} + \vec{v}\delta t, t + \delta t) - f(\vec{v}, \vec{x}, t) = -\frac{1}{\tau}(f(\vec{v}, \vec{x}, t) - f^{eq}(\vec{v})) \quad (4.16)$$

where $\tau = \frac{\kappa}{\delta t}$ is the dimensionless relaxation time. The solution procedure for Eq. 4.16 can be separated into collision and streaming steps. During collision, the current values of $\rho(\vec{x}, t)$, $u(\vec{x}, t)$ are used to calculate the values of f_a^{eq} , where the subscript a is an index for the discrete velocities that are being tracked. The value of $f_a(\vec{x})$ is then updated as

$$\hat{f}_a(\vec{x}, t) = f_a(\vec{x}, t) - \frac{1}{\tau}(f_a(\vec{x}, t) - f_a^{eq}(t)) \quad (4.17)$$

where \hat{f} is the post-collision value of f . The post-collision value then streams to the neighboring lattice node at velocity \vec{e}_a over the next time step:

$$f_a(\vec{x} + \vec{e}_a \delta t, t + \delta t) = \hat{f}_a(\vec{x}, t) \quad (4.18)$$

The sum effect of these two steps is the same as what is prescribed in Eq. 4.16. The process is then repeated by finding the new values of $\rho(\vec{x}, t), u(\vec{x}, t)$, which are used to find f_a^{eq} .

The remaining problem is that the determination of ρ, u is done by continuous integration of the function f over a range of speeds v from $(0, \infty)$, as in Eqs. 4.2-4.3. In the LBM, it is only sought to track f_a for a discrete set of particle velocities with index a . Hence, the moments of f which determine the macroscopic variables must be found using quadrature rules. For consistency with the exact theory, it is required that:

$$\rho = \sum_a f_a = \sum_a f_a^{eq} \quad (4.19)$$

and

$$\rho \vec{u} = \sum_a \vec{e}_a f_a = \sum_a \vec{e}_a f_a^{eq} \quad (4.20)$$

where the summations can be considered akin to the integrations in Section 4.1. The exact form of f^{eq} according to the Maxwell-Boltzmann distribution poses a problem in satisfying Eqs. 4.19 and 4.20. For simplification, one can introduce the assumption of low Ma , or that $|u| \ll \sqrt{R_u T}$, and expand the equilibrium distribution using a Taylor series as:

$$f_a^{eq} = \frac{\rho/m}{(2\pi R_u T)^{3/2}} \exp\left(\frac{-v^2}{2R_u T}\right) \left(1 + \frac{\vec{u} \cdot \vec{v}}{R_u T} + \frac{(\vec{u} \cdot \vec{v})^2}{2(R_u T)^2} - \frac{\vec{u} \cdot \vec{u}}{2R_u T}\right) + O(Ma^3) \quad (4.21)$$

The moments can then be represented as having the form

$$I = \int g(\vec{s}) \exp(-|\vec{s}^2|) d^3 \vec{s} = \sum_i w_i G(\vec{s}_i) \quad (4.22)$$

with $\vec{s} = \sqrt{\frac{3}{2}} \frac{\vec{v}}{c}$, and $c = \sqrt{3RT}$, where the functions $g(\vec{s})$ are simply polynomials in \vec{v} . The values of \vec{s}_i and w_i can be found using Gauss-Hermite quadrature [97, 99]. For a two-dimensional model, this gives the discrete velocities as $e_x = 0, \pm c$ in the x-direction, and $e_y = 0, \pm c$ in the y-direction. The equilibrium distribution to $O(Ma^2)$ can then be written as:

$$f_a^{eq} = w_i \rho \left(1 + \frac{3\vec{e}_a \cdot \vec{u}}{c^2} + \frac{9(\vec{e}_a \cdot \vec{u})^2}{2c^4} - \frac{3\vec{u} \cdot \vec{u}}{2c^2} \right) \quad (4.23)$$

with

$$w_a = \begin{cases} \frac{4}{9} & : a = 0 \\ \frac{1}{9} & : a = 1, 2, 3, 4 \\ \frac{1}{36} & : a = 5, 6, 7, 8 \end{cases}$$

and, as shown in Fig. 4.1, the discrete velocities are:

$$\vec{e}_a = \begin{cases} (0, 0) & : a = 0 \\ (\cos[(a-1)\frac{\pi}{2}], \sin[(a-1)\frac{\pi}{2}])c & : a = 1, 2, 3, 4 \\ (\cos[(a-5)\frac{\pi}{2} + \frac{\pi}{4}], \sin[(a-5)\frac{\pi}{2} + \frac{\pi}{4}])\sqrt{2}c & : a = 5, 6, 7, 8 \end{cases}$$

One can easily show that this definition gives the correct density and momentum as in Eqs. 4.19 and 4.20.

This is called the D2Q9 (2 dimensions, 9 quantities) BGK scheme for incompressible fluid flow, and is presented in detail in [100]. This scheme replicates the incompressible Navier-Stokes equations:

$$\frac{\partial \vec{u}}{\partial t} + \vec{u} \cdot \nabla \vec{u} = -\frac{1}{\rho} \nabla P + \nu \nabla^2 \vec{u} \quad (4.24)$$

and

$$\nabla \cdot \vec{u} = 0 \quad (4.25)$$

with second-order accuracy.

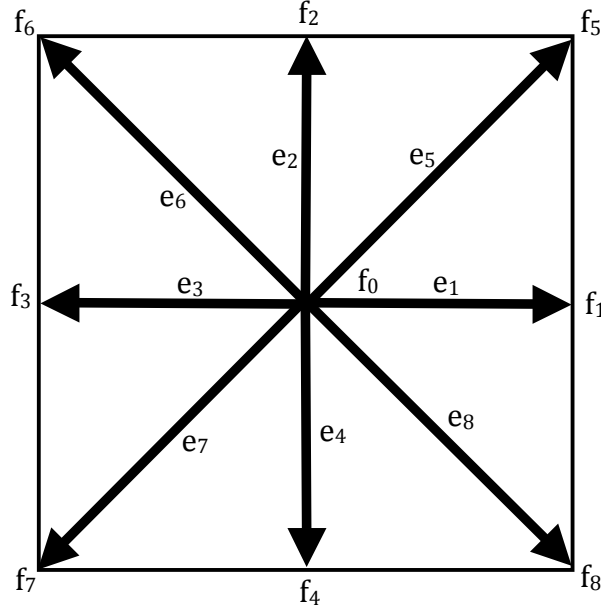


Figure 4.1: Schematic of discrete velocities in the D2Q9 LB model

This can be proven by a procedure called the Chapman-Enskog analysis [97]. This procedure is done by expanding the relevant variables in terms of a small parameter ϵ . Since it is already assumed that the value of Ma is low in order to expand the equilibrium distribution, one can assume $\epsilon \sim Ma$. Assuming that the deviation of f from f^{eq} remains small, f can be expanded near the thermodynamic equilibrium value as:

$$f_a = f_a^{eq} + \epsilon f_a^{(1)} + \epsilon^2 f_a^{(2)} + O(\epsilon^3) \quad (4.26)$$

and introduce the requirement

$$\sum_a f_a^{(n)} = \sum_a \vec{e}_a f_a^{(n)} = 0 \quad (4.27)$$

for $n > 1$. The time variable can be expanded as:

$$t = t^{(0)} + \epsilon t^{(1)} \quad (4.28)$$

Using a Taylor expansion, and using the fact that $\delta x = e_a \delta t$, one can write:

$$f_a(\vec{x} + \vec{e}_a \delta t, t + \delta t) - f_a(\vec{x}, t) = \epsilon \left(\frac{\partial}{\partial t} + \vec{e}_a \cdot \nabla \right) f_a(\vec{x}, t) + \frac{\epsilon^2}{2} \left(\frac{\partial}{\partial t} + \vec{e}_a \cdot \nabla \right)^2 f_a(\vec{x}, t) + O(\epsilon^3) \quad (4.29)$$

By expanding f_a in the discrete Boltzmann equation, forming new equations at each $O(\epsilon)$, and taking moments of these equations with e_a , one eventually obtains:

$$\frac{\partial}{\partial t}(\rho) + \frac{\partial(\rho u_j)}{\partial x_j} = 0 \quad (4.30)$$

from the first moment, and

$$\frac{\partial}{\partial t}(\rho u_k) + \frac{\partial}{\partial x_j} (P \delta_{kj} + \rho u_k u_j) = \frac{\partial}{\partial x_j} \left[\rho \frac{c^2}{3} \left(\tau - \frac{1}{2} \right) \delta t \left(\frac{\partial u_k}{\partial x_j} + \frac{\partial u_j}{\partial x_k} \right) + O(u^3) \right] \quad (4.31)$$

from the second. These are essentially the N-S equations where the kinematic viscosity ν is given in terms of the hydrodynamic relaxation time and the sound speed c as:

$$\nu = \left(\tau - \frac{1}{2} \right) \frac{c^2}{3} \delta t \quad (4.32)$$

Noting that in lattice units, $O(u) = O(Ma)$, so the extra term on the right hand side of the momentum equation 4.20 is a higher-order term, so that we can write the momentum equation as:

$$\frac{\partial \vec{u}}{\partial t} + \vec{u} \cdot \nabla \vec{u} = -\frac{1}{\rho} \nabla P + \nu \nabla^2 \vec{u} + O(Ma^3) \quad (4.33)$$

where the error term should be very small, consistent with the original assumption of low Ma . Additional details can be found in [100].

4.2.1 Multiple-Relaxation-Time Schemes

In the previous section, the collision operator was assumed to be the so-called BGK collision operator, in which all populations collide according to a single relaxation time τ defined by:

$$f(\vec{v}, \vec{x} + \vec{v} \delta t, t + \delta t) - f(\vec{v}, \vec{x}, t) = -\frac{1}{\tau} (f(\vec{v}, \vec{x}, t) - f^{eq}(\vec{v})) \quad (4.34)$$

It is also possible to construct schemes in which the moments of the populations f_a are relaxed at different rates, and then projected onto each population during collision. These are called multiple-relaxation-time schemes. These schemes are found to be generally more accurate and stable than the BGK model, and by choosing correctly the different relaxation times for each moment, the accuracy and stability characteristics of the scheme can be optimized for different applications.

For a multiple relaxation time scheme, the collision process can be written in vector form as:

$$|\hat{f} = \mathbf{M}^{-1}\mathbf{\Omega}\mathbf{M}|f \quad (4.35)$$

Here, $|f$ is the vector (f_0, f_1, \dots, f_8) , $|\hat{f}$ is similarly the post-collision vector, $\mathbf{\Omega} = \text{diag}(1/\tau_0, 1/\tau_1, \dots, 1/\tau_8)$, and \mathbf{M} is a matrix given by:

$$\mathbf{M} = \begin{pmatrix} 1 & 1 & 1 & 1 & 1 & 1 & 1 & 1 & 1 \\ -4 & -1 & -1 & -1 & -1 & 2 & 2 & 2 & 2 \\ 4 & -2 & -2 & -2 & -2 & 1 & 1 & 1 & 1 \\ 0 & 1 & 0 & -1 & 0 & 1 & -1 & -1 & 1 \\ 0 & -2 & 0 & 2 & 0 & 1 & -1 & -1 & 1 \\ 0 & 0 & 1 & 0 & -1 & 1 & 1 & -1 & -1 \\ 0 & 0 & -2 & 0 & 2 & 1 & 1 & -1 & -1 \\ 0 & 1 & -1 & 1 & -1 & 0 & 0 & 0 & 0 \\ 0 & 0 & 0 & 0 & 0 & 1 & -1 & 1 & -1 \end{pmatrix}.$$

Thus the vector $\mathbf{M}|f$ is a vector of moments of the populations f_i . The first moment is easily recognizable as the density, i.e., $\rho = \text{sum}(|f)$. The fourth and sixth moments are the x and y momentum, respectively. The other moments are non-conserved orthogonal moments which are constructed via the Gram-Schmidt orthogonalization process [101]. They include the kinetic energy, square of kinetic energy, x and y energy

fluxes, normal stress, and shear stress. The kinematic viscosity is recovered in terms of τ_8 , and is given similarly to the BGK model as:

$$\nu = \left(\tau_8 - \frac{1}{2} \right) \frac{c^2}{3} \delta t \quad (4.36)$$

It is necessary to take $\tau_7 = \tau_8$ to enforce isotropy [101]. The other values of τ can be adjusted as “tunable” parameters which will affect accuracy and stability differently for different problems.

4.2.2 No-Slip Boundary Condition Implementation

The most commonly used boundary condition used in fluid mechanics is the “no-slip condition”, in which there is no relative motion between a solid boundary and the fluid immediately adjacent to it, such that at the wall $\vec{u} = \vec{u}_w$ where \vec{u}_w is the velocity of the solid boundary. From the definition of the streaming/collision step described in Equation 4.16, we see that the populations f_a are determined by their values at neighboring fluid nodes at the previous time step. However, near a solid boundary, certain populations do not have a neighboring fluid node, and thus the post-collision values of populations pointing into the domain from the solid boundary must be determined using other known populations. One simple and popular method is the “bounce-back” method in which one sets

$$\hat{f}_{\bar{a}}(\vec{x}_b, t) = \hat{f}_a(\vec{x}_f, t) \quad (4.37)$$

where the a and \bar{a} directions are defined by:

$$\vec{e}_{\bar{a}} = -\vec{e}_a \quad (4.38)$$

as shown in Fig. 4.2.

This boundary condition implementation can be understood by realizing that there is no net momentum exchange between the fluid and the wall in the a direction at fluid node x_{-1} over each time step. It also conserves mass, because although one population is leaving the domain over each time step, it is essentially added back in the

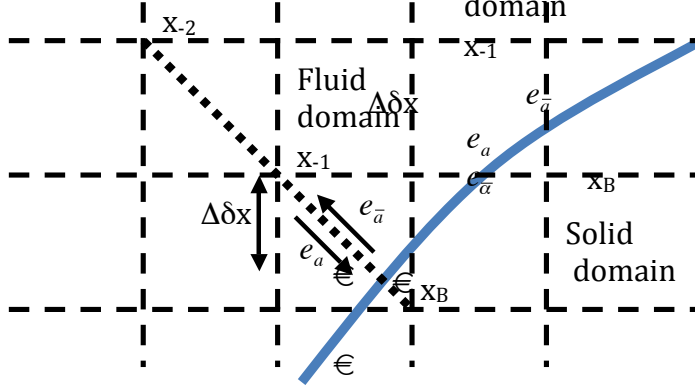


Figure 4.2: Schematic of bounce-back with discrete velocity \vec{e}_a intersecting the solid boundary, as well as the incoming population $\vec{e}_{\bar{a}}$

opposite direction, so that the sum of f_a is conserved at each boundary node. However, this method results in 2nd-order accuracy only for the case where $\Delta = 0.5$ [97], where $\Delta = |\mathbf{x}_{-1} - \mathbf{x}_w|/|\mathbf{x}_{-1} - \mathbf{x}_B|$. In other words, the location of the physical boundary needs to be considered to be one half lattice unit from the last fluid node.

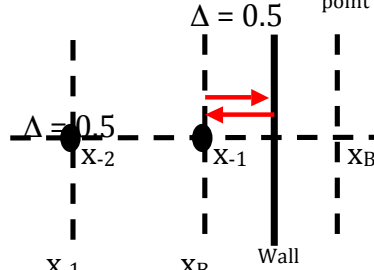


Figure 4.3: Example of perfect bounce back to point x_{-1} when the $\Delta = 0.5$, i.e., the wall is halfway between the boundary node and the nearest fluid node.

For moving boundaries, the situation is more complicated because $\Delta \neq 0.5$ in general. This can be understood by realizing that for $\Delta = 0.5$, the fictitious particle leaving x_{-1} takes exactly one time step to “bounce back” from the solid boundary, but if $\Delta > 0.5$, the particle does not quite reach x_{-1} , so that the boundary condition is effectively not being applied in the correct location, and this error propagates through the system.

For cases where $\Delta \neq 0.5$, accurate results can be achieved by determining the location of the “fictitious particle” that will bounce back exactly to x_{-1} , and determining the value of f_a based on interpolation between the known values at other fluid nodes [102]. This is called an interpolated bounce-back scheme. Using a three-point Lagrangian interpolation, this gives, for $\Delta < 0.5$:

$$\hat{f}_a(x_{-1}, t+1) = \Delta(2\Delta + 1)\hat{f}_a(x_{-1}, t) + (1 + 2\Delta)(1 - 2\Delta)\hat{f}_a(x_{-2}, t) - \Delta(1 - 2\Delta)\hat{f}_a(x_{-3}, t) \quad (4.39)$$

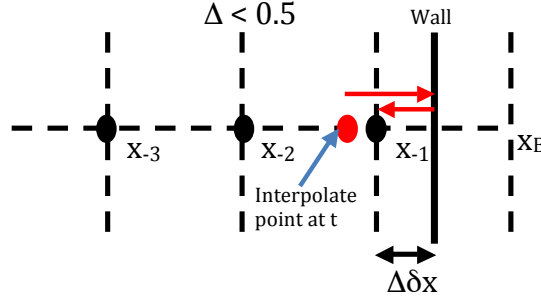


Figure 4.4: When $\Delta < 0.5$, the approach is to solve at time t , for a fictitious population (in red) that will bounce back exactly to x_{-1} from the wall at $t + 1$.

and for $\Delta > 0.5$

$$\hat{f}_a(x_{-1}, t+1) = \frac{1}{\Delta(2\Delta + 1)}\hat{f}_a(x_{-1}, t) + \frac{2\Delta - 1}{\Delta}\hat{f}_a(x_{-2}, t) - \frac{1 - 2\Delta}{1 + 2\Delta}\hat{f}_a(x_{-3}, t) \quad (4.40)$$

Note that for $\Delta = 0.5$, these two cases both reduce to the simple bounce-back case given by Eq. 4.37.

Finally, there is the case in which the boundary is in motion. This is dealt with by adding an appropriate acceleration term to the neighboring fluid. The velocity of the wall can be projected onto the directions of the discrete velocities that intersect with the solid boundaries. Thus, when the wall moves at velocity \vec{u}_w , the bounce back condition for $\Delta = 0.5$ can be written as:

$$\hat{f}_a(\vec{x}_{-1}, t) = \hat{f}_a(\vec{x}_{-1}, t) + 2w_a\rho\frac{3}{c^2}\vec{e}_a \cdot \vec{u}_w \quad (4.41)$$

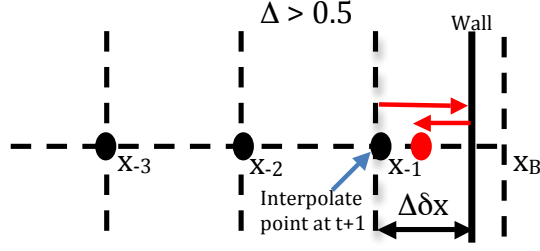


Figure 4.5: When $\Delta > 0.5$, the approach is to solve the value of $f_a(x_{-1})$ at $t + 1$, knowing that the value of $f_a(x_{-1})$ at t will nearly bounce back (in red), and can thus be used as an interpolation point.

This can be understood by realizing that

$$f_a^{eq} = w_a \rho \left(1 + \frac{3\vec{e}_a \cdot \vec{u}}{c^2} + \frac{9(\vec{e}_a \cdot \vec{u})^2}{2c^4} - \frac{3\vec{u} \cdot \vec{u}}{2c^2} \right) \quad (4.42)$$

so that by using $\vec{e}_{\bar{a}} = -\vec{e}_a$, one can show that

$$f_{\bar{a}}^{eq} = f_a^{eq} + 2w_a \rho \frac{3}{c^2} \vec{e}_{\bar{a}} \cdot \vec{u}_w \quad (4.43)$$

so that when the fluid velocity $\vec{u} = \vec{u}_w$, the nearest fluid node is defined as being in equilibrium with the wall. This term can simply be added to the interpolation scheme presented in [102] for the case with a moving boundary and $\Delta < 0.5$. For $\Delta > 0.5$, the force term should be multiplied by a correction of $1/\Delta(2\Delta + 1)$, which is found by considering the analytical solution for Couette flow [102], and gives second-order accurate results.

4.2.3 Advantages of LBM

It is apparent from the above sections that there are two unique features of the LBM when compared to other methods of CFD. The first feature is the locality of the algorithm. Aside from boundary conditions, the streaming step, i.e. Eq. 4.18, is the only step of the algorithm that requires communication between different node points, or in computational terms, different locations in memory. Thus, the majority of the algorithm can be performed by separate processors simultaneously, and the streaming step is the only step that will require communication between different processors [97].

In comparison, the finite-difference or finite-volume formulations of the Navier-Stokes equations require communication at many steps in the algorithm, as many spatial derivatives are discretized in the solution. Thus, the LBM can be run in parallel very efficiently, which gives significant advantages as the size of the problem grows.

The second advantage of the LBM is the implementation of the boundary conditions. As shown in Section 4.2.2, it is possible to maintain second-order accuracy without the boundary residing on regular lattice nodes. For moving/irregular boundaries, the situation is slightly more complicated, and involves populations at more than one point to enforce the boundary condition for each population. However, it is still relatively straightforward, and generally very few points adjacent the boundary are needed to implement the boundary conditions, which gives an advantage when the boundary geometry has a complex shape. The boundary can also be allowed to pass between lattice nodes, and the computational mesh does not need to be tailored to the physical geometry in any way. This saves considerable effort for the programmer, and also precludes “re-meshing” as the geometry of the fluid domain changes in time, which is a computationally expensive process in transient problems with moving boundaries, or suspended particles.

4.3 Lattice Boltzmann Models for Heat/Mass Transport

Section 4.2 outlines how a lattice Boltzmann model can simulate the continuity and momentum equations of fluid flow. The momentum equation, i.e., Eq. 4.24 can be described as a convective-diffusion equation for the fluid momentum. Hence, it seems reasonable that by changing the formulation of the lattice Boltzmann model slightly, it is possible to simulate the convective diffusion of other variables of interest, such as molar concentration, or internal energy.

Indeed, there are many lattice Boltzmann models for the convection-diffusion equation. The convective-diffusion equation can describe the one-way coupling of heat or mass transport to a fluid flow field. In modeling transport of chemical species, if the species is assumed to be dilute, then the assumption of a passive scalar (one-way

coupling) is accurate. The convective-diffusion equation with a general source term S is given below:

$$\frac{\partial \phi}{\partial t} + \nabla \cdot (\phi \vec{u}) = \nabla \cdot (D \nabla \phi) + \mathcal{S} \quad (4.44)$$

where ϕ is the scalar of interest, \vec{u} is the hydrodynamic velocity of the fluid, which is assumed to obey the Navier-Stokes equations and can be determined by the scheme given in Section 4.2, and D is the diffusion coefficient.

By defining a different type of velocity distribution function g , the convection-diffusion equation can be simulated numerically using a similar approach to the LBM for viscous fluids, as described in Section 4.2.

There are two unique features that make the problem of developing such a scheme unique from the LBM for fluid flow. First, in the convection-diffusion equation, there is only one variable of interest, ϕ . In the LBM scheme for fluid flow, both the density field ρ and the velocity field \vec{u} , which appear in equation 4.44 are uniquely determined by the populations f_i . Thus, consistent with one-way coupling, the moments of f_i will act as inputs to the LBM scheme for the CDE, but the CDE results do not affect the fluid flow in general. The second difference is that since the CDE is linear with respect to \vec{u} , it is possible to use lower-order (i.e., linear in \vec{u}) equilibrium distribution functions for the fictitious populations g_i . Thus, there are many D2Q4 and D2Q5 schemes, as well as D2Q9 schemes for the 2D CDE.

The post-collision distributions for mass transport can be given by:

$$\hat{g}_a(\vec{x}, t + \delta t) = g_a(\vec{x}, t) + \omega(g_a(\vec{x}, t)) + S_a(\vec{x}, t) \quad (4.45)$$

Where ω is a general collision operator, and S_i is a source term. For the BGK case, ω is defined by:

$$\omega = -\frac{1}{\tau}(g(\vec{v}, \vec{x}, t) - g^{eq}(\vec{v}, t)) \quad (4.46)$$

4.3.1 D2Q5 model

The D2Q5 model for the CDE is used in this work, as the literature is most extensively developed for this method, and it is considerably more computationally efficient than the D2Q9 model.

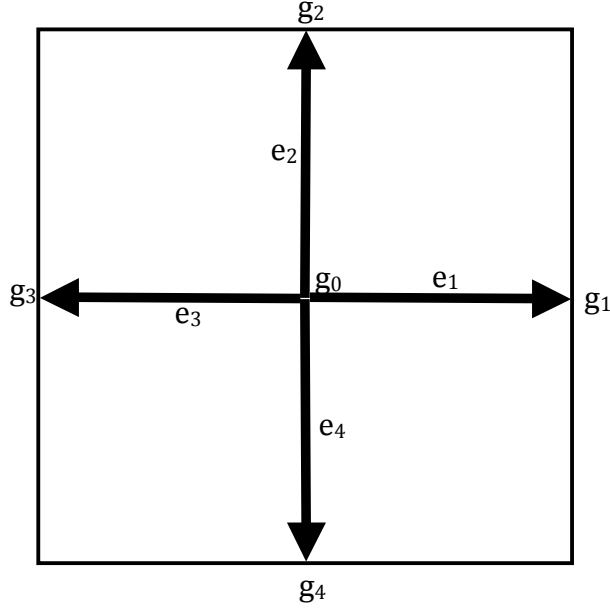


Figure 4.6: D2Q5 lattice Boltzmann model

As shown in Fig. 4.6, the five velocities used in the typical D2Q5 model, as described in [103], for example, are:

$$\vec{e}_a = \begin{cases} (0, 0) & : a = 0 \\ (\sin[(a-1)\frac{\pi}{2}], \cos[(a-1)\frac{\pi}{2}])c & : a = 1, 2, 3, 4 \end{cases}$$

The equilibrium distributions are given by:

$$g_a^{eq}(\vec{x}, t) = w_a \left(1 + 3 \frac{\delta t}{\delta x} (\vec{u} \cdot \vec{e}_a) \right) \quad (4.47)$$

which is essentially a linear expansion of the Maxwell-Boltzmann distribution.

The scalar variable ϕ , which could be internal energy, temperature, or molar concentration of a species, is calculated similarly to the density for the flow LBM:

$$\phi = \sum_{a=0}^4 g_a \quad (4.48)$$

By following a similar Chapman-Enskog procedure to the one described in Section 4.2, one can recover the CDE given in Eq. 4.44, plus a second-order error term, as in the flow model. The diffusivity (i.e., thermal diffusivity or mass diffusivity) is found in terms of the CDE relaxation time in a similar manner to the kinematic viscosity in the flow model, consistent with the analog between the fluid momentum equation and the CDE. The diffusivity is related to the species relaxation time τ_M , time step, and sound speed by:

$$D = \left(\tau_M - \frac{1}{2} \right) \frac{c^2}{3} \delta t \quad (4.49)$$

The boundary condition implementation for the CDE LBM is very similar to those for the flow model as well. There are numerous bounce-back methods that can be applied for both first and second-kind boundary conditions. In the former case, the incoming g_i populations are determined in terms of the outgoing populations with the requirement that the total change in solute mass (or internal energy) is constant over the time step for a Dirichlet boundary condition, or that the added mass is consistent with a known flux at the boundary integrated over the time step for a Neumann boundary condition. The method of assigning the incoming population is typically not unique, and there are several methods for each type of boundary condition [104, 105]

Similar to the LBM for fluid flow, multiple relaxation times are also available for the CDE LBM, for the D2Q4 model [106], the D2Q5 model [103] and D2Q9 method [107].

4.4 Extension to Axisymmetric Coordinates

The schemes presented in Sections 4.2 and 4.3.1 both assume a cartesian coordinate system, and the derivations of the scheme likewise assume the cartesian definition

of the gradient operator, divergence, etc. However, these schemes can be easily extended to axisymmetric cylindrical coordinates. The axisymmetric continuity equation can be written as:

$$\frac{\partial u_j}{\partial x_j} + \frac{u_r}{r} = 0 \quad (4.50)$$

where the repeated index j implies summation over the r, z coordinates. The momentum equation in direction k can be written as [108]:

$$\frac{\partial u_k}{\partial t} + u_j \frac{\partial (u_k)}{\partial x_j} = -\frac{1}{\rho} \frac{\partial P}{\partial x_k} + \nu \frac{\partial^2 u_k}{\partial x_j^2} + \frac{\nu}{r} \frac{\partial u_k}{\partial r} - \frac{2\nu u_k}{r^2} \delta_{ir} \quad (4.51)$$

where δ_{ij} is the Kronecker delta function. By substituting Eq. 4.50 into Eq. 4.51, one can write:

$$\frac{\partial u_k}{\partial t} + \frac{\partial (u_k u_j)}{\partial x_j} = -\frac{1}{\rho} \frac{\partial P}{\partial x_k} + \nu \frac{\partial}{\partial x_j} \left(\frac{\partial u_k}{\partial x_j} + \frac{\partial u_j}{\partial x_k} \right) + \mathcal{S}_F \quad (4.52)$$

with

$$\mathcal{S}_F = \frac{\nu}{r} \left(\frac{\partial u_i}{\partial r} + \frac{\partial u_r}{\partial x_k} \right) - \frac{u_k u_r}{r} - \frac{2\nu u_k}{r^2} \delta_{kr} \quad (4.53)$$

If one ignores the term \mathcal{S}_F , and considers the coordinates to be (x,y) rather than r, z , the momentum equation is identical to that for the cartesian coordinate system. Thus, the axisymmetric momentum equation is identical to the cartesian momentum equation with the addition of a particular momentum source term \mathcal{S}_F . Hence, using the typical BGK or MRT collision processes described in Eqs. 4.16 and 4.35 respectively, one recovers all terms in the axisymmetric momentum equation except for those in \mathcal{S}_F . The terms in \mathcal{S}_F can be recovered by adding an appropriate source term during the collision process [108].

Similarly, the CDE LBM can be extended to axisymmetric coordinates. The axisymmetric CDE is given by:

$$\frac{\partial \phi}{\partial t} + \frac{1}{r} \frac{\partial (r u_r \phi)}{\partial r} + \frac{\partial (u_z \phi)}{\partial z} = \frac{1}{r} \frac{\partial}{\partial r} \left(r D \frac{\partial \phi}{\partial r} \right) + \frac{\partial}{\partial z} \left(D \frac{\partial \phi}{\partial z} \right) \quad (4.54)$$

which, by expanding and re-grouping terms can be written in “psuedo-cartesian” form, as in Eq. 4.52:

$$\frac{\partial \phi}{\partial t} + \frac{\partial(u_r \phi)}{\partial r} + \frac{\partial(u_z \phi)}{\partial z} = \frac{\partial}{\partial r} \left(D \frac{\partial \phi}{\partial r} \right) + \frac{\partial}{\partial z} \left(D \frac{\partial \phi}{\partial z} \right) + \mathcal{S}_M \quad (4.55)$$

with

$$\mathcal{S}_M = -\frac{u_r \phi}{r} + \frac{D}{r} \frac{\partial \phi}{\partial r} \quad (4.56)$$

Thus, the D2Q5 method presented in Section 4.3.1 can be used with the source term \mathcal{S}_M added via a source term in the collision process [109]. The details for the addition of this source term will be presented in the following chapter.

The LBM is thus a highly local algorithm for simulating fluid flow and convective transport, compatible with both Cartesian and axisymmetric coordinates. The locality make is very well-suited for implementation with parallel processing. The boundary condition implementation is very simple even when the boundaries are complex, and second-order accuracy is retained even with a static, uniform grid. In Chapter 5, all of these features will be taken advantage of in order to simulate the transient deposition of ZnO in heterogeneous hydrolysis with Zn vapor, and to explain the development of the deposition profile under different flow, mass transfer, and kinetics conditions.

Chapter 5

LATTICE BOLTZMANN SIMULATION OF A REACTIVE GAS/SOLID PRECIPITATION PROCESS IN A CIRCULAR TUBE

In this chapter, the lattice Boltzmann method, as described in Chapter 4, is used to simulate the growth of a solid deposit on the walls of a circular tube due to a gas-to-solid reaction and precipitation process. This process is of particular interest for the design of reactors for the production of hydrogen by the heterogeneous hydrolysis of steam with Zn vapor in the Zn/ZnO thermochemical cycle. As experimentally observed in Chapter 3, the solid deposit of ZnO product on the tube wall evolves in time according to the time- and axially-varying convective-diffusive transport and reaction of Zn vapor with steam on the solid surface. A D2Q9 axisymmetric multiple-relaxation-time (MRT) lattice Boltzmann scheme is used to simulate incompressible fluid transport while a D2Q5 axisymmetric MRT lattice Boltzmann scheme is used to simulate the convective-diffusive transport of Zn vapor. The solid boundary is resolved at the sub-grid level using a piecewise-linear representation. A bounce-back method for the Zn concentration is used at the solid boundary to enforce a third-kind boundary condition with first-order kinetics, and an interpolated bounce-back method is used to enforce the no-slip condition for fluid flow at the solid boundary. The model is first validated against several analytical solutions, followed by a parametric study to understand the effect of Reynolds, Schmidt, and Damköhler numbers on the time evolution of the ZnO deposition profile along the tube axis.

5.1 Introduction

The simultaneous convective-diffusive transport of chemical species and their precipitation onto surfaces following reaction is relevant to many naturally-occurring and engineered systems. Significant amounts of precipitation can lead to complex

changes in the boundary geometry, which in turn affects the subsequent fluid flow and species transport. The development of accurate and computationally-efficient models for simulating flow and transport in reacting systems with complex and time-varying domain boundaries is therefore valuable in many applications.

Lattice Boltzmann methods (LBM) have been developed for fluid flow [100], heat and mass transport [110], as well as other physical phenomena such as acoustics and ion transport [111, 112]. Due to the local nature of the algorithm, lattice Boltzmann methods provide significant advantages in simulating systems with complex and changing geometries, when compared to the finite-difference solution of the Navier-Stokes (N-S) equations, which involves the discretization of numerous derivatives in space. Several LB models have been demonstrated which use one set of distribution functions to determine the velocity field, and an additional set to solve the convective-diffusion equation (CDE), which is coupled to the velocity field. These models can both be implemented with the single relaxation-time Bhatnagar-Gross-Krook (BGK) collision operator [110, 113, 114], as well as with multiple relaxation times [103].

The LBM for the CDE has been applied to many problems wherein it is desirable to exploit its benefits regarding irregular and/or moving boundaries. Kang et al. simulated the growth of crystals using the LBM to solve the N-S equations and the CDE with a first-order kinetic boundary condition [115]. The boundary condition was implemented using lattice-sized control volumes at the liquid/solid interface. Similar approaches were later used to model snow crystal growth in clouds [116] as well as the growth of hydrate crystals in geological CO₂ sequestration [117], and surface growth in reactive capillary-driven flow [118]. A similar approach was also used to model flow-related clotting in an investigation of blood clots [119], however, the passive scalar was treated with a first-order upwind scheme rather than the LBM. These studies used a “stair-case” approximation of the solid boundary, i.e. one in which the boundary does not cut through adjacent lattice boundaries, but rather is staggered between regular lattice nodes, resulting in a “pixelized” boundary. Some other studies have employed a sub-grid representation of the solid boundary, i.e. one not conforming to lattice boundaries. A lattice Boltzmann approach with an immersed sub-grid boundary was

recently used to simulate solid/liquid phase change [120]. Here, the curved boundary between the solid and liquid phases was approximated as piecewise linear between a set of Lagrangian points. In another investigation, the growth of dendrite formations in channel flow was simulated using a lattice Boltzmann model for the flow and a phase-field method for the combined mass transfer and solid boundary growth [121].

Although many applications of these methods occur in cylindrical geometries, i.e. flow in pipes and capillaries, much of the previous work on precipitation/dissolution models has assumed a Cartesian coordinate system. In the current work, we apply recently advanced multiple-relaxation-time lattice Boltzmann models for both incompressible fluid flow and mass transport in axisymmetric cylindrical coordinates. We also employ a new treatment for the third-kind boundary condition for mass transfer on curved boundaries.

The goal of our current work is to develop a basis for predicting the time- and axially-evolving profile of solid ZnO deposits in a non-isothermal tubular reactor designed for hydrogen production by the heterogeneous hydrolysis of steam with Zn vapor. Heterogeneous hydrolysis with Zn vapor offers a method of water-splitting with higher theoretical efficiency and reliability than previous aerosol-based reactors for hydrolysis with Zn in the Zn/ZnO solar thermochemical cycle [58,130]. The precipitation of solid ZnO during the hydrolysis reaction presents a unique consideration for the design and modeling of reactors for this process. Thus, characterizing the effect of flow, mass transfer, and reaction conditions on the transient accumulation of solid ZnO deposits are the primary reasons for developing the model. In addition, the numerical methods and results presented in this paper may also be useful in understanding reactive precipitation/dissolution processes in other industrial, environmental, and biological flows.

This chapter is organized as follows: In Section 5.2.1, we describe the mathematical models for flow and mass transport that are used in this work. Section 5.3 presents a detailed description of the assumptions and boundary conditions used for our simulations. Section 5.4 presents several validation studies that were used to verify

the accuracy of the current LB models. In Section 5.5, we present results and discussion from a parametric study to investigate the effects of the relevant non-dimensional parameters (Reynolds, Schmidt, and Damköhler numbers), other model-specific parameters, and axially-varying kinetics on the evolution of the ZnO precipitation profile. Finally, in Section 5.6, we present our conclusions.

5.2 LB Models for Flow and Mass Transport

5.2.1 Multiple-Relaxation-Time (MRT) Model for Axisymmetric Incompressible Fluid Flow

The D2Q9 scheme for axisymmetric incompressible fluid flow presented in [108] is used in the current work. This scheme replicates the incompressible Navier-Stokes equations in axisymmetric cylindrical coordinates, which can be written in indicial notation as:

$$\frac{\partial u_k}{\partial t} + \frac{\partial(u_k u_j)}{\partial x_j} = -\frac{1}{\rho} \frac{\partial P}{\partial x_k} + \nu \frac{\partial}{\partial x_j} \left(\frac{\partial u_k}{\partial x_j} + \frac{\partial u_j}{\partial x_k} \right) + \mathcal{S}_F \quad (5.1)$$

with

$$\mathcal{S}_F = \frac{\nu}{r} \left(\frac{\partial u_k}{\partial r} + \frac{\partial u_r}{\partial x_k} \right) - \frac{u_k u_r}{r} - \frac{2\nu u_k}{r^2} \delta_{kr} \quad (5.2)$$

by substituting the axisymmetric continuity equation:

$$\frac{\partial u_j}{\partial x_j} + \frac{u_r}{r} = 0 \quad (5.3)$$

into the momentum equation. Here, the momentum equation has been written in a “pseudo-Cartesian” form with the source term \mathcal{S}_F contributing the remaining terms in the axisymmetric momentum equation.

Here, the u_i represent the r (radial) and z (axial) components of the hydrodynamic velocity, ρ is the fluid density, P is the pressure, ν is the kinematic viscosity, and repeated indices imply summation over r, z . Reference [109] extended the BGK

scheme presented in [108] for implementation with the commonly used MRT collision operator presented in [101]. Using this approach, the collision process is described by:

$$|\hat{f} = |f - \mathbf{M}_F^{-1} \mathbf{\Omega}_F (\mathbf{M}_F |f - \mathbf{M}_F |f^{eq}) + \mathbf{G} \delta t \quad (5.4)$$

where $|f$ is the vector of pre-collision distribution functions (f_0, f_1, \dots, f_8) , $|\hat{f}$ is similarly the post-collision vector, $|f^{eq}$ is the equilibrium distribution vector, $\mathbf{\Omega}_F = \text{diag}(1/\tau_{F0}, 1/\tau_{F1}, \dots, 1/\tau_{F8})$ is a matrix of relaxation parameters, and \mathbf{M}_F is the collision matrix given by:

$$\mathbf{M}_F = \begin{pmatrix} 1 & 1 & 1 & 1 & 1 & 1 & 1 & 1 & 1 \\ -4 & -1 & -1 & -1 & -1 & 2 & 2 & 2 & 2 \\ 4 & -2 & -2 & -2 & -2 & 1 & 1 & 1 & 1 \\ 0 & 1 & 0 & -1 & 0 & 1 & -1 & -1 & 1 \\ 0 & -2 & 0 & 2 & 0 & 1 & -1 & -1 & 1 \\ 0 & 0 & 1 & 0 & -1 & 1 & 1 & -1 & -1 \\ 0 & 0 & -2 & 0 & 2 & 1 & 1 & -1 & -1 \\ 0 & 1 & -1 & 1 & -1 & 0 & 0 & 0 & 0 \\ 0 & 0 & 0 & 0 & 0 & 1 & -1 & 1 & -1 \end{pmatrix}.$$

The equilibrium distribution functions f_a^{eq} are defined by:

$$f_a^{eq} = w_a \left(\rho + \rho_0 \left[3 \frac{\vec{e}_a \cdot \vec{u}}{c^2} + \frac{9}{2} \frac{(\vec{e}_a \cdot \vec{u})^2}{2c^4} - \frac{3}{2} \frac{\vec{u} \cdot \vec{u}}{2c^2} \right] \right) \quad (5.5)$$

where ρ_0 is the average density, taken to be 1.0, and c is the sound speed, also taken to be 1.0. The components of the source term vector \mathbf{G} are given by:

$$G_a = -\frac{1}{r} \frac{2\tau_F - 1}{2\tau_F} e_{ar} (f_a - f_a^{eq}) - w_a \frac{\rho u_r}{r} - \frac{1}{6} e_{ak} \left(\frac{\rho u_k u_r}{r} + \frac{2\rho \nu u_j}{r^2} \delta_{kr} \right) \quad (5.6)$$

which correspond the source term S_F shown in Eq. 5.1, as shown by the Chapman-Enskog analysis in [108].

After the collision step, the post-collision distributions are then streamed to neighboring nodes according to:

$$f_a(\vec{x} + \vec{e}_a \delta t, t + \delta t) = \hat{f}_a(\vec{x}, t) \quad (5.7)$$

where the (r, z) -components of the discrete velocities \vec{e}_a are defined by:

$$\vec{e}_a = \begin{cases} (0, 0) & : a = 0 \\ (\sin[(a-1)\frac{\pi}{2}], \cos[(a-1)\frac{\pi}{2}])c & : a = 1, 2, 3, 4 \\ (\sin[(a-5)\frac{\pi}{2} + \frac{\pi}{4}], \cos[(a-5)\frac{\pi}{2} + \frac{\pi}{4}])\sqrt{2}c & : a = 5, 6, 7, 8 \end{cases}$$

The weight functions w_a are given by $w_0 = 4/9$, $w_a = 1/9$ for $a = 1 - 4$ and $w_a = 1/36$ for $a = 5 - 8$. Additional details, including the derivation of the scheme for the Cartesian BGK case, can be found in [100].

The kinematic viscosity ν is given in terms of the hydrodynamic relaxation time and the sound speed c as:

$$\nu = \left(\tau_F - \frac{1}{2} \right) \frac{c^2}{3} \delta t \quad (5.8)$$

where $\tau_F = \tau_{F7} = \tau_{F8}$.

After evolving the mesoscopic distribution functions throughout the domain, the local density is then given in terms of the distribution functions by:

$$\rho = \sum_{a=0}^8 f_a \quad (5.9)$$

the local pressure P is given by:

$$P = \rho \frac{c^2}{3} \quad (5.10)$$

and the velocities u_i are given as:

$$u_k = \frac{1}{\rho} \sum_{a=0}^8 \vec{e}_{ak} f_a \quad (5.11)$$

The hydrodynamic quantities are then used to find the equilibrium distributions f_a^{eq} at the next time step.

5.2.2 Multiple-Relaxation-Time (MRT) Model for Mass Transport

The D2Q5 model for the passive scalar presented in [109] is implemented in the current work. The passive scalar in this case is the molar concentration of the reactive species (Zn vapor). The concentration of Zn vapor is assumed to be sufficiently dilute such that the passive scalar approach is accurate.

This scheme replicates the axisymmetric CDE given by:

$$\frac{\partial \phi}{\partial t} + \frac{\partial(u_r \phi)}{\partial r} + \frac{\partial(u_z \phi)}{\partial z} = \frac{\partial}{\partial r} \left(D \frac{\partial \phi}{\partial r} \right) + \frac{\partial}{\partial z} \left(D \frac{\partial \phi}{\partial z} \right) + \mathcal{S}_M \quad (5.12)$$

with

$$\mathcal{S}_M = -\frac{u_r \phi}{r} + \frac{D}{r} \frac{\partial \phi}{\partial r} \quad (5.13)$$

where (u_r, u_z) are the hydrodynamic velocity components determined by the D2Q9 model presented in section 5.2.1, and D is the diffusion coefficient of the reactive species, assumed to be isotropic. Similar to the axisymmetric momentum equation, the CDE has been written in “pseudo-Cartesian” form with the source term \mathcal{S}_M contributing the axisymmetric terms.

The collision step for the mass transport model is described by:

$$|\hat{g} = |g - \mathbf{M}_M^{-1} \mathbf{\Omega}_M (\mathbf{M}_M |g - \mathbf{M}_M |g^{eq}) + \mathbf{R} \delta t \quad (5.14)$$

where $|g$ is the pre-collision vector (g_0, g_1, \dots, g_4) , $|\hat{g}$ is similarly the post-collision vector, $|g^{eq}$ is the equilibrium distribution vector, $\mathbf{\Omega}_M = \text{diag}(1/\tau_{M0}, 1/\tau_{M1}, \dots, 1/\tau_{M4})$, and \mathbf{M}_M is the collision matrix given by:

$$\mathbf{M}_M = \begin{vmatrix} 1 & 1 & 1 & 1 & 1 \\ 4 & -1 & -1 & -1 & -1 \\ 0 & 0 & 1 & 0 & -1 \\ 0 & -1 & 1 & -1 & 1 \\ 0 & 1 & 0 & -1 & 0 \end{vmatrix}.$$

and the (r, z) -components of the discrete velocities are given by:

$$\vec{e}_a = \begin{cases} (0, 0) & : a = 0 \\ (\sin[(a-1)\frac{\pi}{2}], \cos[(a-1)\frac{\pi}{2}])c & : a = 1, 2, 3, 4 \end{cases}$$

It should be noted that the collision matrix \mathbf{M}_M has been re-arranged from the definition given in [103] and [109] for consistency with the numbering of the discrete velocities \vec{e}_a used in the current work. The off-diagonal components of the relaxation matrix are assumed to be zero because diffusion is considered to be isotropic.

The components of the source term vector \mathbf{R} are given by:

$$R_a(\vec{x}, t) = -w_a \frac{u_r}{r} \sum_{a=0}^4 g_a^{eq} - w_a \frac{1}{r} \left(1 - \frac{1}{2\tau_M}\right) \frac{\delta x}{\delta t} \sum_{a=0}^4 e_{ar} (g_a - g_a^{eq}) \quad (5.15)$$

The equilibrium distributions are given by:

$$g_a^{eq}(\vec{x}, t) = w_a \left(1 + 3 \frac{\delta t}{\delta x} (\mathbf{u} \cdot \mathbf{e}_a)\right) \quad (5.16)$$

The post-collision distributions then stream to neighboring nodes at the next time step, as in the flow model, according to:

$$g_a(\vec{x} + \vec{e}_a \delta t, t + \delta t) = \hat{g}_a(\vec{x}, t) \quad (5.17)$$

The concentration is given by:

$$\phi = \sum_{a=0}^4 g_a \quad (5.18)$$

The diffusivity is related to the species relaxation time, time step, and sound speed by:

$$D = \left(\tau_M - \frac{1}{2}\right) \frac{c^2}{3} \delta t \quad (5.19)$$

where $\tau_M = \tau_{M2} = \tau_{M4}$.

5.3 Model Description

5.3.1 Flow Boundary Conditions

We consider a core-annular flow configuration as shown in Fig. 5.1 in which Zn vapor is fed to the central core and steam is fed to the annular region. At the inlet,

the velocity boundary condition (given in lattice units) in the core region ($0 < r < R_1$) is assumed to be fully-developed flow through a circular duct:

$$u_z(r, 0) = u_C \left(R_1^2 - r^2 \right) \quad (5.20)$$

Similarly we assume fully-developed flow through an annular duct as the inlet boundary condition for $R_2 < r < R$:

$$u_z(r, 0) = u_A \left((r^2 - R_1^2) - (R_2^2 - R_1^2) \ln \left(\frac{r}{R_1} \right) / \ln \left(\frac{R_2}{R_1} \right) \right) \quad (5.21)$$

where u_C and u_A are the characteristic velocities assigned in the core and annular regions, respectively. At the reactor inlet, the axial velocity u_z is assumed to be zero in the region $R_1 < r < R_2$ which corresponds to the wall thickness of the tube that introduces the core flow into the reactor. The radial velocity u_r is also assumed to be zero for all r at $z = 0$.

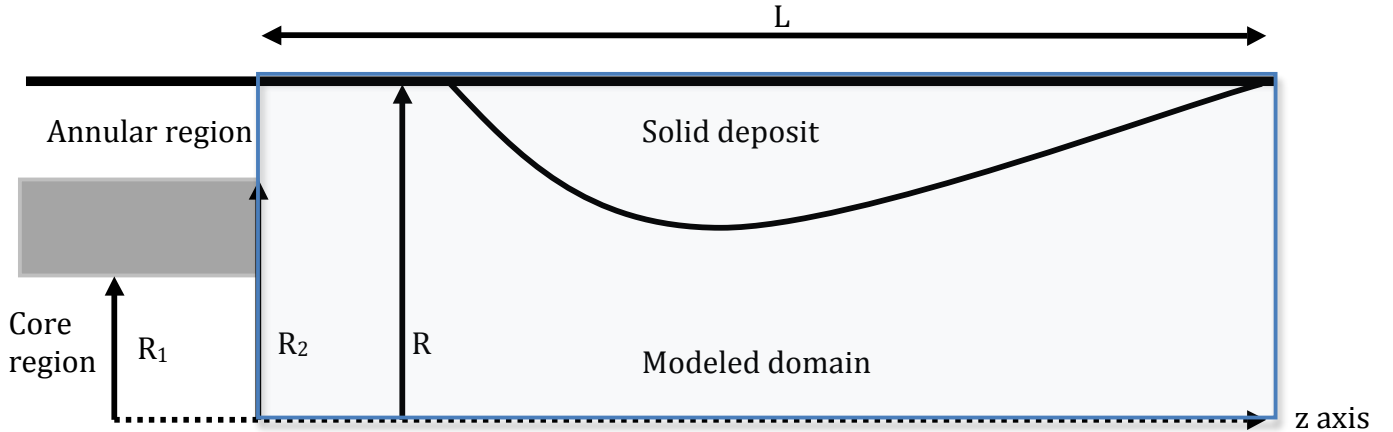


Figure 5.1: Schematic of tube reactor. The wall of the Zn-vapor supply tube shown in grey separates the core and annular flow regions, and the modeled region is enclosed by the blue rectangle.

At the outlet ($z = L$), a zero gradient outflow condition is assumed for both axial and radial velocity:

$$\frac{\partial u_z}{\partial z}(r, L) = \frac{\partial u_r}{\partial z}(r, L) = 0 \quad (5.22)$$

The velocities at both the inlet and outlet are specified using the method of Zou and He [122].

Along the z -axis ($r = 0$), a symmetry condition for the flow velocities is enforced by setting $f_2 = f_4$, $f_6 = f_7$, and $f_5 = f_8$, as discussed in [97]. Thus, the bottom row of lattice nodes resides on the line $r = 0$. All terms with a factor of $\frac{1}{r}$ in the collision step are neglected for these nodes, as they become zero when L'Hôpital's rule is applied at $r = 0$ [108, 123, 124].

The flow boundary condition on the solid boundary is implemented according to the interpolated bounce-back method for curved/moving boundaries presented in [102].

Along the tube wall, the growth of the solid precipitate is assumed to progress in the direction normal to the existing surface. The hydrodynamic velocity boundary condition for the solid boundary is determined by the growth rate of the solid layer projected onto each coordinate direction, similar to the condition in [125]:

$$u_{z,w}(z) = \frac{r'' \sin(\theta_w(z))}{\phi_{(s)}} \quad (5.23)$$

$$u_{r,w}(z) = \frac{r'' \cos(\theta_w(z))}{\phi_{(s)}} \quad (5.24)$$

where $\phi_{(s)}$ is the constant molar concentration of the bulk solid, which is taken to be 1000.0 unless otherwise stated, r'' is the local reaction rate, and $\theta_w(z)$ is the local angle of the curved solid boundary measured from the z -direction. The local angle of the wall is determined from the current shape of the solid deposit which is described by the curve $r = \mathcal{W}(z)$,

$$\theta_w(z) = \tan^{-1} \left(\frac{\mathcal{W}(z+1) - \mathcal{W}(z-1)}{2} \right) \quad (5.25)$$

When enforcing the bounce-back condition, the value of θ_w at the point of the outgoing population's intersection with the solid boundary is determined using quadratic Lagrangian interpolation at nearest-neighbor values of z , (i.e. at $z - 1$, z , $z + 1$), as the intersection point will not generally be on a node. The distance between a boundary node and the boundary (i.e. between x_f and x'_f in Fig. 5.2) is determined

by using a piecewise-linear representation of the boundary curve $r = \mathcal{W}(z)$, so that the computation is simple. This piecewise linear description is similar to that used in [126], however rather than using a dynamically-updated set of Lagrangian points to represent the interface, here, the curve is tracked using a simple Eulerian description, i.e. the curve's height is tracked at a fixed set of z -values.

5.3.2 Mass Transfer Boundary Conditions

The inlet concentration boundary condition in the core region ($0 \leq r \leq R_1$) is:

$$\phi(r, 0) = \phi_0 = 1.0 \quad (5.26)$$

and $\phi = 0.0$ for $r > R_1$. The value of ϕ_0 is chosen so that the baseline molar concentration of Zn vapor appropriately lower than the chosen molar concentration of the solid phase. The Dirichlet boundary condition for concentration is implemented using the "scheme D" presented in [105]. At the outlet, a zero-gradient condition is assumed for the concentration:

$$\frac{\partial \phi}{\partial z}(r, L) = 0 \quad (5.27)$$

which is implemented using the method presented in [105] for Neumann boundary conditions. Similar to the flow model, a symmetry boundary condition is implemented on $r = 0$ by setting $g_2 = g_4$. The collision terms involving $\frac{1}{r}$ are likewise ignored on these nodes.

The reaction rate is assumed to follow a first-order kinetic model in terms of ϕ_w , the concentration on the wall:

$$r'' = k\phi_w \quad (5.28)$$

We also assume that the mole balance in the normal direction on $r = \mathcal{W}(z)$ includes the mass flux induced by the growth of the solid layer, as in [125]:

$$D \frac{\partial \phi}{\partial n} - u_n \phi = k\phi \quad (5.29)$$

where n is the normal direction pointing into the fluid domain, and k is the kinetic constant. In order to implement this boundary condition on a curved boundary, we used the method in [104], in which both the tangential and normal mass fluxes are calculated at the intersection of the outgoing population e_a and the boundary, and are then projected onto the incoming population with velocity $e_{\bar{a}}$. The presence of a tangential mass flux on a curved boundary is an important consideration for accurate implementation of this boundary condition.

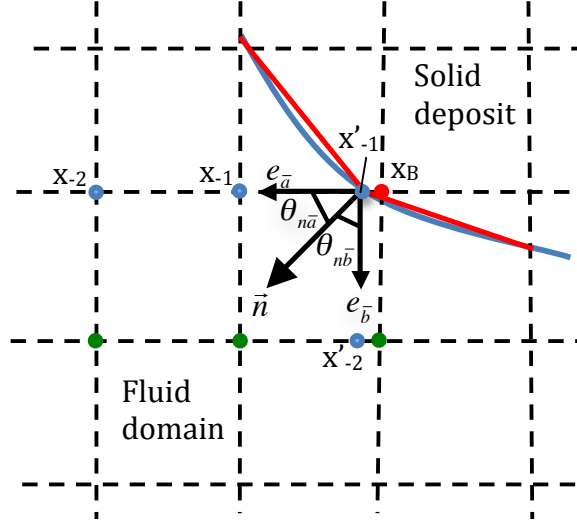


Figure 5.2: Schematic of boundary treatment at solid-fluid interface.

Figure 5.2 illustrates how the boundary condition in Eq. 5.29 is implemented. The values of \hat{g}_a and $\hat{g}_{\bar{a}}$ at points x_{-1} and x_{-2} are used in the calculation as well as $\hat{g}_{\bar{b}}$ and \hat{g}_b at x'_{-1} and x'_{-2} . The vectors e_a and e_b are perpendicular, and constitute basis vectors for calculation of the tangential and normal mass fluxes. The green points are used to interpolate the value of $\hat{g}_b(x'_{-2})$, which generally does not reside on a regular node point. Values at x'_{-1} are determined from non-equilibrium extrapolation from x_{-1} and x_{-2} , as described in [127]. The curved boundary, shown in blue, is approximated as piecewise linear, as shown by the red lines. The normal and tangential mass fluxes are projected onto the \bar{a} -direction using the known relationships between θ_w , $\theta_{n\bar{a}}$, and $\theta_{n\bar{b}}$.

Finally, the projected mass flux is implemented as a Neumann boundary condition, as described in [104].

Once all incoming populations have been determined, the wall concentration profile $\phi_w(z)$ is then calculated from g_2 on the boundary nodes using Eq. (41b) in [104]. A profile of the reaction rate can then be determined from the definition $r''(z) = k\phi_w(z)$.

5.3.3 Non-Dimensional Parameters

The relevant non-dimensional numbers in this system are the Reynolds number, given by:

$$Re = \frac{u_{av}N_r}{\nu} = \frac{u_{av}N_r}{(\tau_F - \frac{1}{2})\frac{c^2}{3}\delta t} \quad (5.30)$$

with

$$u_{av} = \frac{Q_C + Q_A}{\pi N_r^2} \quad (5.31)$$

where Q_A and Q_C are the volumetric flow rates through the annular and core regions of the inlet, respectively, determined analytically from Eqs. 5.20 and 5.21. N_r is the number of lattice units in the radial direction.

The Mach number is defined as:

$$Ma = \frac{u_{av}}{c} \quad (5.32)$$

The Schmidt number is defined as:

$$Sc = \frac{\nu}{D} = \frac{(\tau_F - \frac{1}{2})}{(\tau_M - \frac{1}{2})} \quad (5.33)$$

The Peclet number is defined as:

$$Pe = \frac{u_{av}N_r}{D} = \frac{u_{av}N_r}{(\tau_M - \frac{1}{2})\frac{c^2}{3}\delta t} \quad (5.34)$$

The Damköhler number is defined as:

$$Da = \frac{kN_r}{D} = \frac{kN_r}{(\tau_M - \frac{1}{2})\frac{c^2}{3}\delta t} \quad (5.35)$$

We also define a second Damköhler number as the ratio of the reaction rate to the advective mass transfer rate:

$$Da_2 = \frac{k_1}{u_{av}} \quad (5.36)$$

In the current work, this parameter is only of interest for cases with axially-varying kinetics, and k_1 is defined as the initial value of the kinetics constant at the inlet.

The non-dimensional time is defined using diffusive scaling:

$$t^* = \frac{N_t D}{N_r^2} \quad (5.37)$$

where N_t is the number of time steps.

5.4 Model Validations

Several validation problems were selected to verify the accuracy of both the flow and mass transfer models. In particular, it was important to verify the accuracy of the chosen boundary condition implementations, as well as the formulation of the governing equations in axisymmetric coordinates. For all cases, the parameters $\tau_{F0} \dots \tau_{F6}$ are taken as those used in [102] and the parameters $\tau_{M0}, \tau_{M1}, \tau_{M3}$ are all taken to be 1.0, as in [109]. The assigned values for these parameters were not found to significantly affect the accuracy of the model.

Four validation problems were selected as shown in Fig. 5.3. The first two problems are only to verify the flow model, and no mass transfer is present. Problem I is unsteady axisymmetric flow in a semi-infinite contracting circular tube, in which the tube is initially filled with fluid at rest, which is then squeezed out by a steadily contracting wall, i.e. the tube wall radius decreases at a constant rate. Problem II is starting transient Poiseuille flow, in which the fluid is initially at rest and is then subjected to a constant body force or pressure gradient in the axial direction. Problem III is steady convective-diffusion in an annular region ($R_i < r < R_o$) with wall injection, in which fluid is injected radially at a constant rate at $r = R_i$, and two different Dirichlet boundary conditions are applied for concentration at R_i and R_o . Problem IV is temporally and spatially periodic convective diffusion in slug flow,

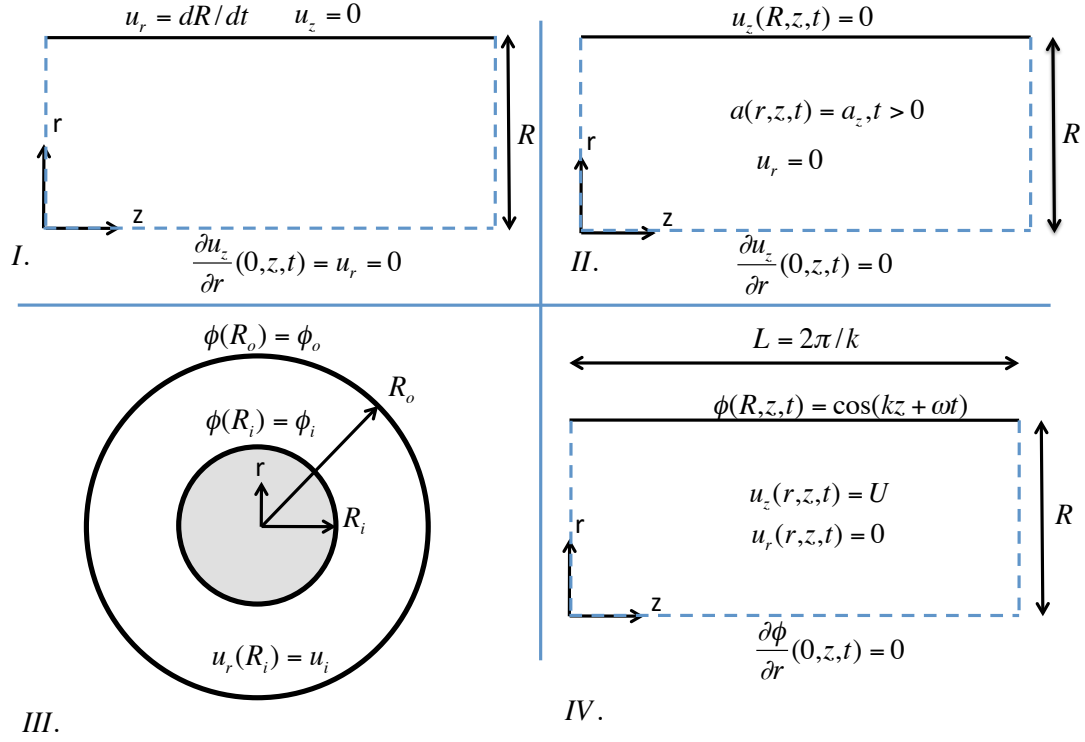


Figure 5.3: Schematics of validation problems I-IV.

in which the flow velocity profile is assumed to be uniform, and a sinusoid Dirichlet boundary condition is applied at the tube wall. The analytical solutions for problems I and II are presented in [128] and [129], respectively, and the solutions for problems III and IV are both presented in [109].

The absolute value of relative error $|(u_{LBM} - u_{exact})/u_{exact}|$ for the velocities was examined for problems I and II, and similarly for the concentration ϕ in problems III and IV. The relative errors were found to be $<1\%$ for all locations and time steps examined, and thus we conclude that the models are sufficiently accurate. It was also found that when examining the time-normalized globally-averaged error for problem IV, that the CDE model is second-order accurate in space and first-order accurate in time, as was found in [109].

5.5 Results and Discussion

Following the validation studies presented in the previous section, the model is now applied to investigate the heterogeneous hydrolysis of steam with Zn vapor in a tubular reactor under a negative axial temperature gradient. For all cases, the simulation is initialized with the fluid at rest and the Zn vapor concentration set to zero everywhere. Thus, initially, only the background flow of steam is present. The flow boundary conditions are then applied and the flow is allowed to develop until it reaches a steady-state, and then the mass transfer boundary conditions are applied. This sequence is followed in order to decouple the development of the initial flow field from the results for different cases. The simulations use $N_r = 40$ for all cases.

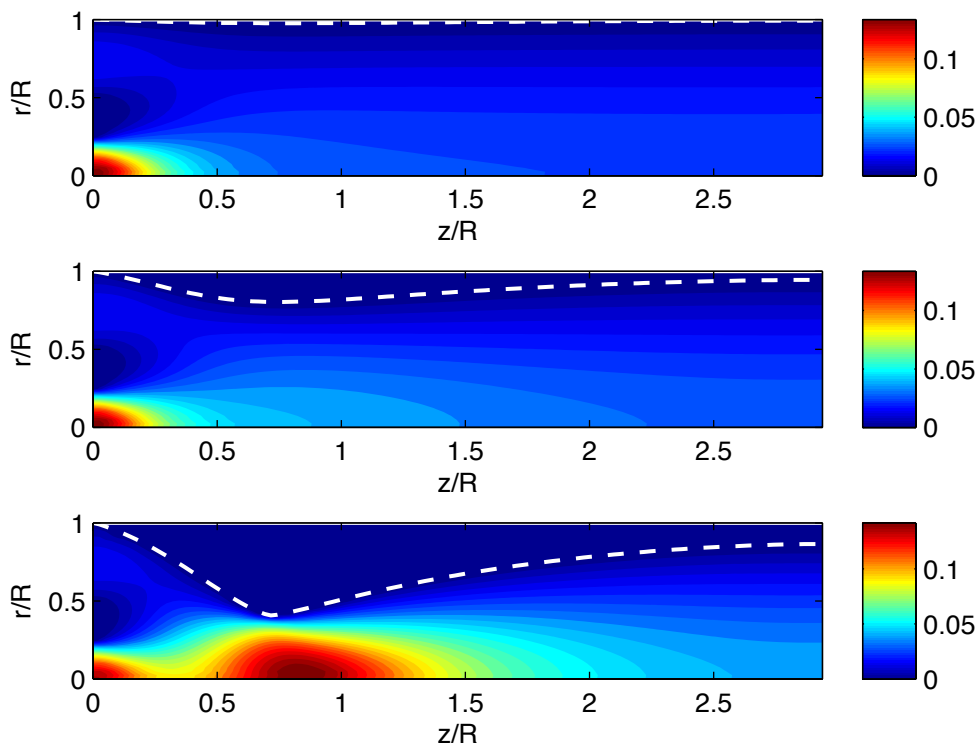


Figure 5.4: Contours of u_z (lattice units) for $Sc = 0.7$, $Da = 1.0$, and $Re = 1.0$, at $t^* = 612.5, 6862.5, 9362.5$. The dashed white line indicates the deposition profile at each time step.

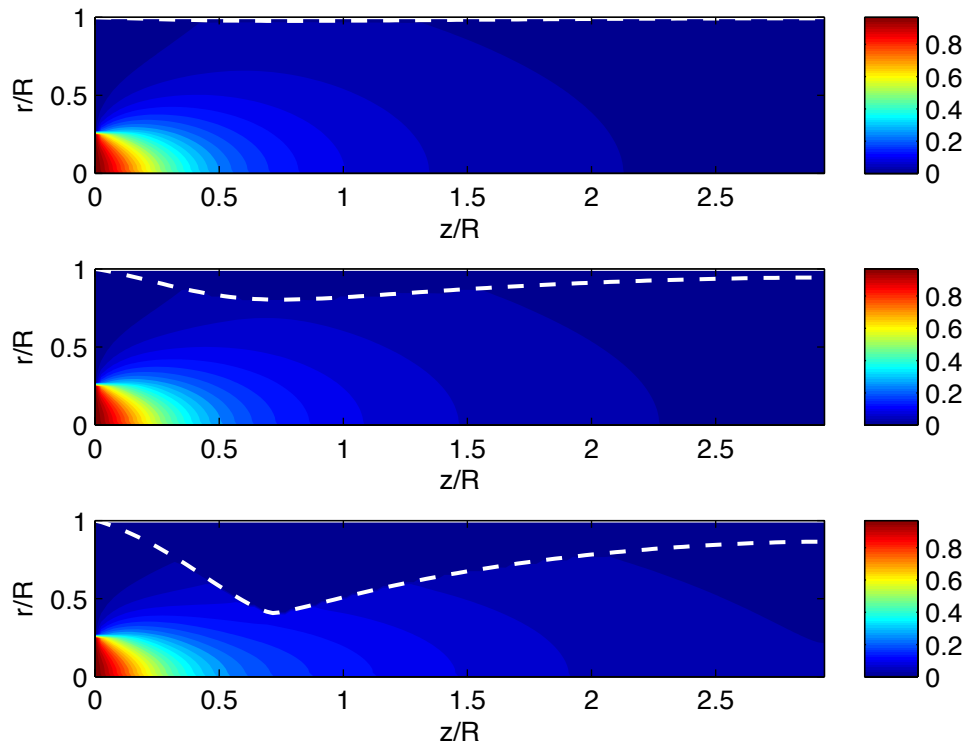


Figure 5.5: Contours of ϕ for $Sc = 0.7$, $Da = 1.0$, and $Re = 1.0$, at $t^* = 612.5, 6862.5, 9362.5$. The dashed white line indicates the deposition profile at each time step.

The evolution of the axial velocity u_z and Zn-vapor concentration ϕ for a typical case with $Sc = 0.7$, $Da = 1.0$, and $Re = 1.0$ is shown in Figs. 5.4 and 5.5, respectively for three instants in time. As the solid ZnO layer (shown by the dashed white line) grows inward, the axial velocity in the throat region increases since the inlet mass flux is fixed. The velocity boundary layer is also seen to be thinnest at the point of fastest deposition since the reduction in cross-sectional area causes the flow to accelerate. Due to the relatively low value of Da in this case, the concentration contours in Fig. 5.5 do not show the presence of a boundary layer adjacent to the solid ZnO boundary. It is also apparent that the contours of constant concentration are stretched axially at later time steps owing to the stronger effect of advection due to increasing velocities. For increasing values of Da , the results are qualitatively similar to Fig. 5.5, except with a more pronounced concentration boundary layer, as the case of $Da \rightarrow \infty$ represents a zero concentration boundary condition.

5.5.1 Effect of Re

Figure 5.6 shows the effect of increasing Re for $Re \leq 1.0$ for $Da = 20.0$, $Sc = 0.7$, and $Q_r = 1.0$ for different time steps. The plots for $Re = 0.01$ and $Re = 0.1$ are virtually identical since for very low flow velocities the problem is essentially diffusion-dominated with advection playing a minimal role in mass transport. For $Re = 1.0$, the deposit exhibits a similar profile to the lower Re cases, however the growth is faster over each time interval. This is because the ϕu term in the total inlet mass flux is larger at higher flow velocities, and hence the total mass flux into the system is significantly larger for $Re = 1.0$ compared to the lower Re cases.

Figure 5.7 shows the effect of Re on the evolution of the deposition profile for $Re > 1$, with all other non-dimensional quantities the same as those in Fig. 5.6. Increasing Re primarily has the effect of changing the shape of the deposition profile such that the axial location of fastest deposition is shifted downstream, as well as increasing the total amount of deposition over any time interval. The shifting of the deposition profile downstream with increasing Re is due to the advection of mass increasing downstream with Re , and the increased rate of overall deposition is again

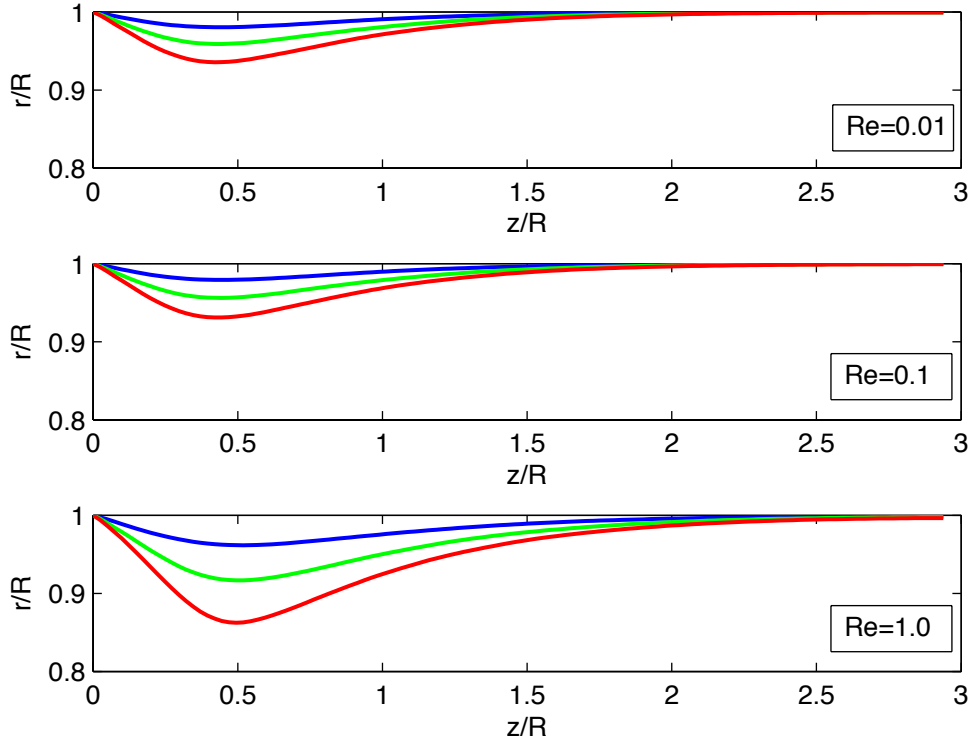


Figure 5.6: Deposition profiles for different values of Re , with $Da = 20.0$, $Sc = 0.7$, $Q_A/Q_C = 1.0$. Results for $t^* = 456.2$ are shown in blue, $t^* = 925.0$ in green, and $t^* = 1393.8$ in red.

due to higher advective mass flux into the system at higher Re . Hence, for constant Sc , the value of Re is a strong predictive factor in the problem, with $Re < 1$ representing one regime with minimal differences in the evolution of the ZnO deposition profile, and $Re > 1$ representing a regime with significant sensitivity to Re .

5.5.2 Effect of Da

Figure 5.8 shows the effect of Da for moderate-to-high values of Da with $Re = 10.0$, $Sc = 0.7$, and $Q_r = 5.0$. At low t^* , the deposition profiles for $Da = 5.0, 10.0$, and 20.0 are nearly identical. This is because for this range of Da , the kinetics are very fast relative to the rate of diffusion, and hence the reaction is mass transport-limited. At higher values of t^* , the radial diffusion length decreases due to the growth of the solid deposit, and thus the mass transfer resistance due to diffusion also decreases. In

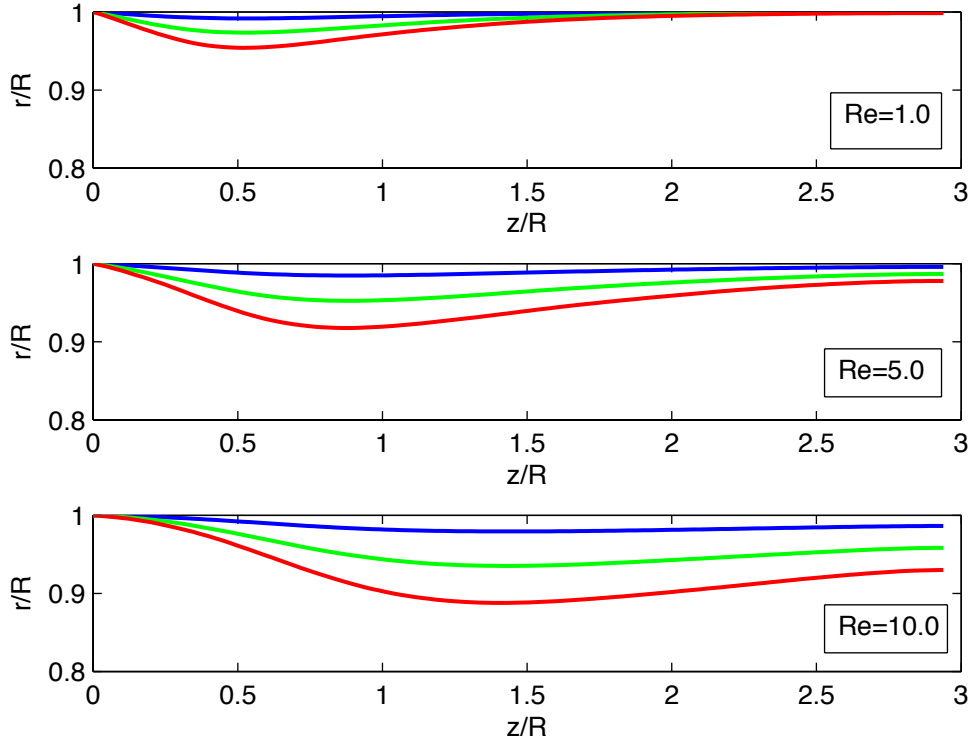


Figure 5.7: Deposition profiles for different values of Re , with $Da = 20.0$, $Sc = 0.7$, $Q_A/Q_C = 1.0$. Results for $t^* = 167.0$ are shown in blue, $t^* = 508.0$ in green, and $t^* = 848.9$ in red.

this regime, the kinetics begin to play a stronger role in the rate of reaction, and the deposition profiles become more sensitive to Da , with higher Da resulting in faster deposition. Faster deposition results in a faster decrease in diffusion length, and thus the differences in the deposition profiles for different Da become more pronounced over time. At high Da the axial location of fastest deposition is rather insensitive to Da , because the initial location is strongly mass transfer-controlled.

Figure 5.9 shows the effect of Da for $Da \leq 1.0$, with all other conditions the same as those in Fig. 5.8. In this range, the reaction is kinetics-limited, and hence the deposition profiles immediately show sensitivity to Da at low t^* . For higher Da , the deposition is faster and occurs further upstream, as a higher amount of reactive species that contacts the wall will react rather than be transported downstream. The

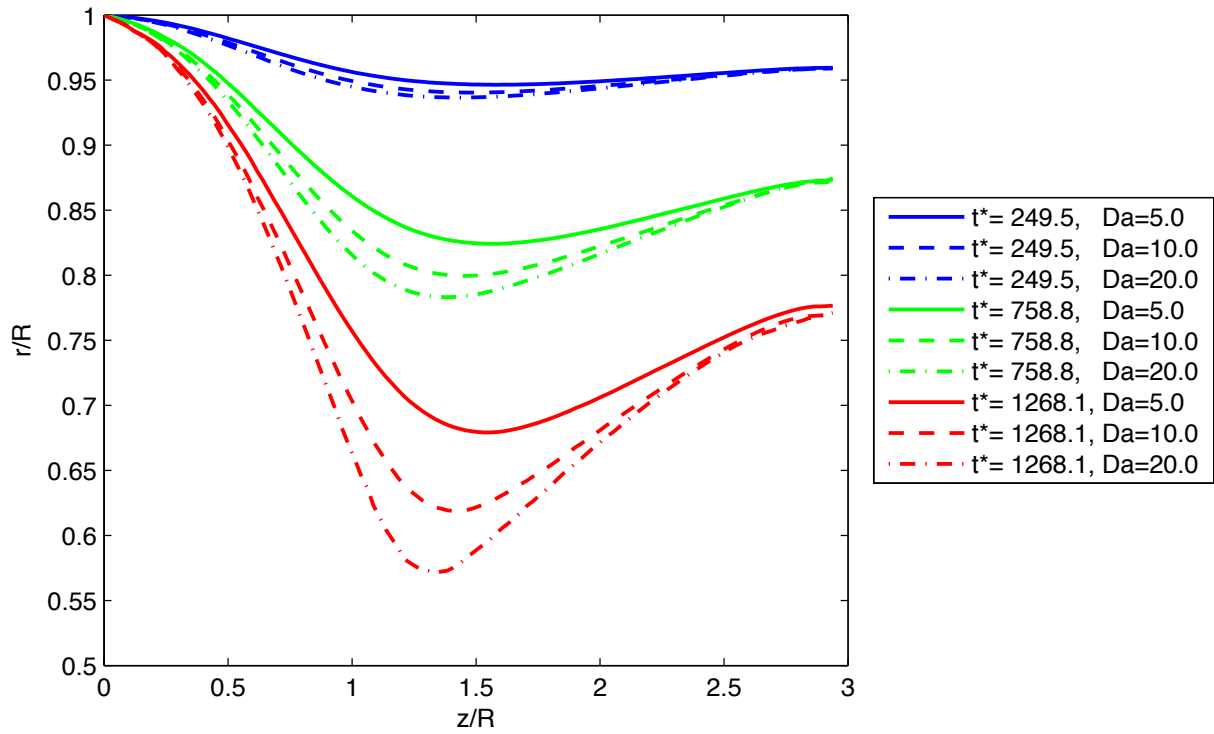


Figure 5.8: Deposition profiles for different values of Da , $Re = 10.0$, $Sc = 0.7$, $Q_A/Q_C = 5.0$.

long vertical tick marks in Fig. 5.9 indicate the axial position of fastest deposition for each case. Thus, while increasing Re has the effect of pushing the location of fastest deposition downstream for constant Da , increasing Da has the opposite effect for constant Re .

5.5.3 Effect of Sc

In section 5.5.1, the effect of changing Re for constant Sc was examined, which is equivalent to changing Pe . Figure 5.10 shows the effect of changing Sc and Re simultaneously for $Pe = 10.0$ and $Da = 20.0$. In Fig. 5.10, it is apparent that when Pe is held constant, the results are virtually identical for any value of Sc . Any differences in the deposition profiles can be attributed to differences in numerical error, as the value of Ma is different for each case. This insensitivity to Sc for constant Pe indicates that in the moderate Re regime, the actual predictor of the deposition profile is Pe . However, it is possible that under turbulent flow conditions, Re would play a role independent

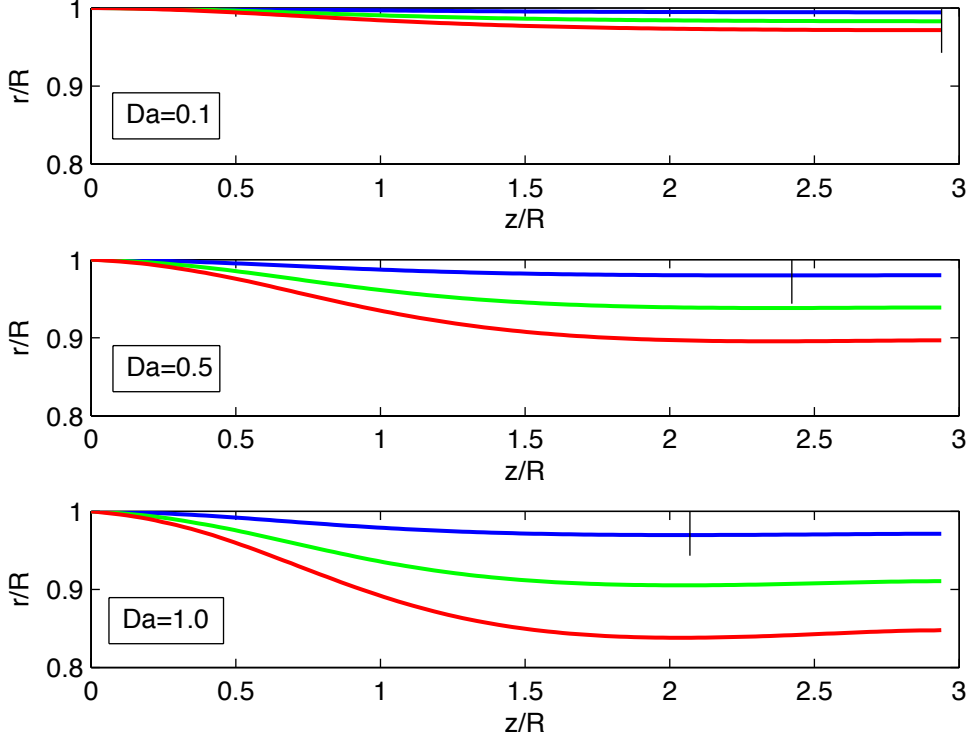


Figure 5.9: Deposition profiles for different values of Da , $Re = 10.0$, $Sc = 0.7$, $Q_A/Q_C = 5.0$. Results for $t^* = 249.5$ are shown in blue, $t^* = 758.8$ in green, and $t^* = 1268.1$ in red.

of the value of Pe as discussed in [121], but an investigation into this effect is beyond the scope of the current work.

5.5.4 Effect of Q_A/Q_C

The effect of changing the annular-to-core flow rate ratio Q_A/Q_C is shown in Fig. 5.11 for $Re = 1.0$, $Sc = 0.7$ and $Da = 10.0$. Despite the non-uniform velocity profiles at the inlet, for a constant value of Re , the hydrodynamic entry length is roughly the same for each case, and hence the axial location of fastest deposition is nearly identical for the three cases shown. This is likewise found to hold for lower values of Da . Although the inlet velocity profiles are very different for these cases, the flow develops to nearly the same velocity profile at a relatively low value of z/R for all cases. As the ratio Q_A/Q_C is increased for constant Re , Q_C is decreased, which

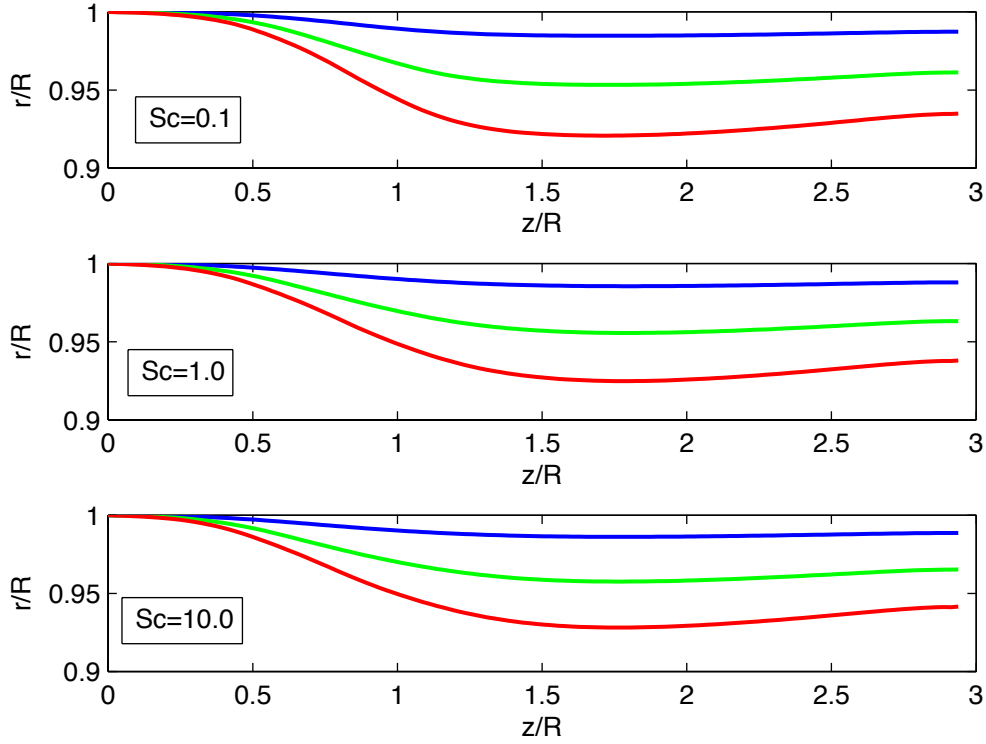


Figure 5.10: Deposition profiles for different values of Sc , $Pe = 10.0$, $Da = 20.0$, $Q_A/Q_C = 5.0$ at $t^* = 102.1$ (blue) $t^* = 311.1$ (green) and $t^* = 519.4$ (red).

decreases the total flux of reactive species into the system. Hence, for higher Q_A/Q_C , the total amount of deposition is decreased for any value of t^* . Thus, the value of Q_C is important in determining the total mass flux of reactant into the system, and thus the overall rate of deposition, but the results are relatively insensitive to Q_A/Q_C for any given Q_C .

5.5.5 Effect of $\phi_{(s)}$

Here, we examine the effect of the product molar density $\phi_{(s)}$ on the deposition profile. As discussed in [125], the interface velocity u_w is typically very small for gas/solid precipitation, and in fact can be safely ignored for large values of $\phi_{(s)}$ with minimal impact on the results. Thus, for high values of $\phi_{(s)}$, the problem is quasi-steady in time. Deposition profiles are shown for different values of $\phi_{(s)}$ in Fig. 5.12. Physically,

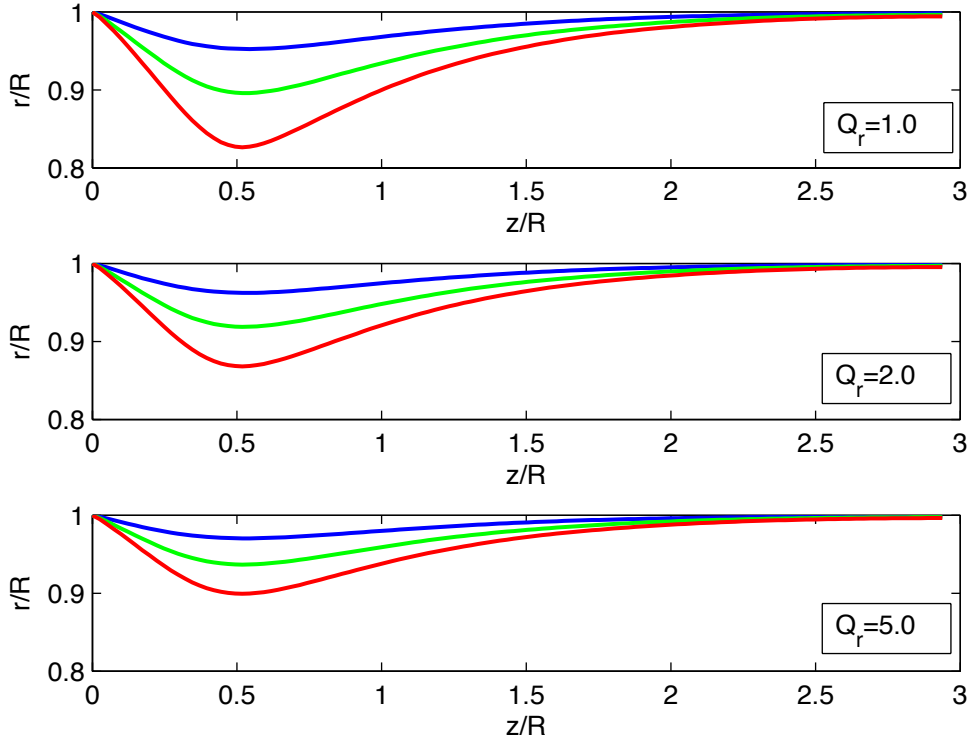


Figure 5.11: Deposition profiles for different values of Q_A/Q_C , $Re = 1.0$, $Sc = 0.7$, $Da = 10.0$. Results for $t^* = 1237.5$ are shown in blue, $t^* = 1862.5$ in green, and $t^* = 2487.5$ in red.

different values of $\phi_{(s)}$ represent different solid products, or different morphologies of the same material. Hence, a product with a higher porosity would correspond to a solid with a lower molar density. The deposition profile for $\phi_{(s)} = 500.0$ at the earliest time overlaps with the profile for $\phi_{(s)} = 1000.0$ at the second time instant, and with the profile for $\phi_{(s)} = 2000.0$ at the fourth time instant. This is to be expected, as the growth of the deposit should be twice as slow when the density of the solid is doubled, and so on. This illustrates that the shape of deposition profile for a material with a given $\phi_{(s)}$ can be easily inferred from results for other values of $\phi_{(s)}$, as the results scale predictably for slow growth conditions. As $\phi_{(s)}$ is decreased significantly for a given k and ϕ_0 , the wall velocities will become comparable to the axial velocity of the flow, and the growth may not be quasi-steady; however investigation of this regime this is

beyond the scope of the current work.

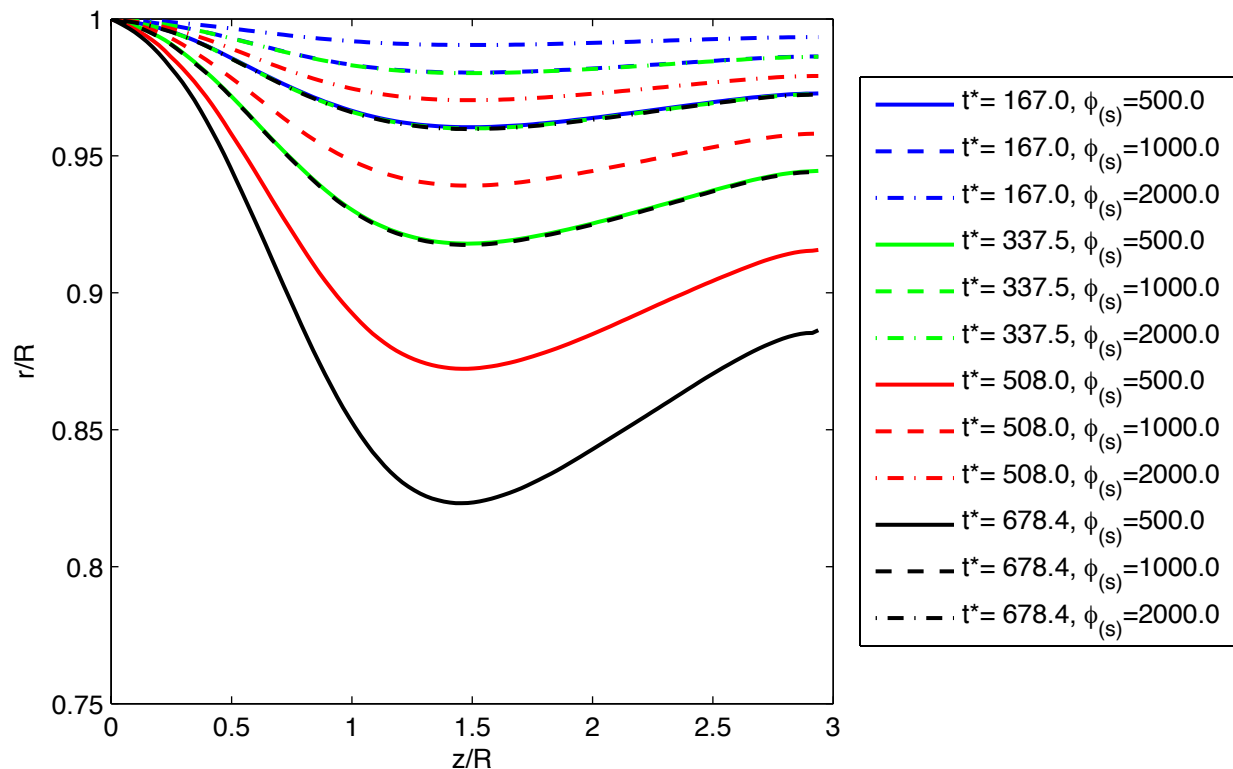


Figure 5.12: Deposition profiles for different values of $\phi_{(s)}$, $Re = 10.0$, $Sc = 0.7$, $Da = 10.0$, and $Q_A/Q_C = 5.0$.

5.5.6 Effect of Da_2 with Variable Kinetics

The heterogeneous hydrolysis of steam by Zn vapor is optimally performed non-isothermally under a negative axial temperature gradient, as discussed in [58] and experimentally verified in [130]. The reaction should ideally begin at a high temperature to minimize the use of carrier gas, and the reactor temperature should then decline downstream in order to take advantage of faster kinetics and obtain higher equilibrium yields. Thus, it is of particular interest to examine cases where the kinetic constant varies due to a negative temperature gradient in the axial direction.

Accordingly, we now examine the effect of $Da_2 = k_1/u_{av}$ for cases with axially-varying kinetics. The kinetic constant is assumed to be constant at $k = k_1$ for $z < z_0$ and then increases as $k = k_1 + k_2 \left(\frac{z-z_0}{N_z/2} \right)^2$ for $z \geq z_0$. For the following cases, we also

define $Da = k_1 R/D$ in order to characterize the initial reaction rate separately from the axial variation in kinetics. The kinetic constant is used as a proxy for the tube wall temperature, and we assume that the temperature gradient does not affect the flow or mass transfer. The increase in k is used to simulate both the increase in kinetics and the shifting of equilibrium conditions toward ZnO production at lower temperatures [58], although the current rate law does not explicitly account for reaction equilibrium.

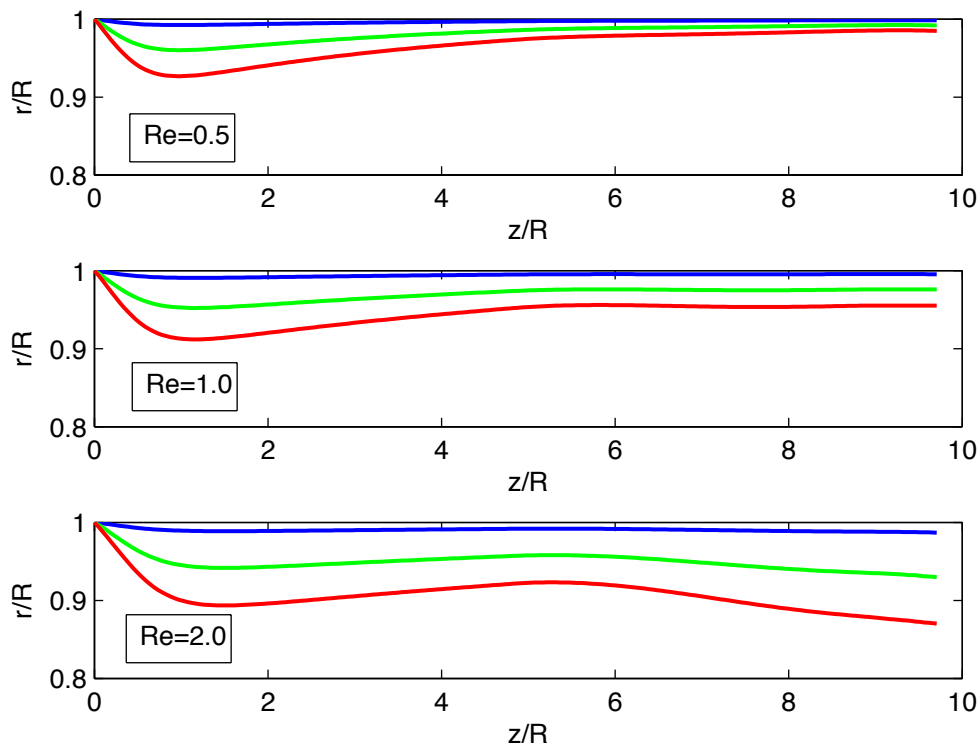


Figure 5.13: Deposition profiles for the varying kinetics case with $Sc = 1.0$, $Da = 0.1$, $Q_A/Q_C = 5.0$, and various values of Re . Results for $t^* = 1516.6$ are shown in blue, $t^* = 7707.1$ in green, and $t^* = 13897.6$ in red

Results are shown in Fig. 5.13 for $Da = 0.1$, $k_2/k_1 = 50.0$, $Sc = 1.0$, $z_0 = 5N_r$, and various values of Re . Since Da_2 can be written as $Da_2 = Da/ReSc$, we vary Re in order to change Da_2 while holding the kinetics profile, Sc and Da constant. As Re is increases, the deposition profile transitions from exhibiting a single maximum to exhibiting two local maxima. This phenomenon was also consistently observed in

experimental results that were obtained using a non-isothermal laboratory-scale tube reactor for the heterogeneous hydrolysis of steam with Zn vapor [130]. Moreover, as Re increases, the relative size of the second maximum increases and the location of the maximum occurs further downstream.

For a given kinetics profile, the appearance of this two-peak deposition profile is found to depend on Da_2 , which is the ratio of the reaction rate to the advective transport rate in the constant kinetics (entrance) region. As Re is increased with constant Da and Sc , Da_2 is decreased by definition, and the relative size of the second deposition peak is found to increase, as shown in Fig. 5.13. This is because as the flow rate increases, the kinetics at the inlet become slower compared to advection and thus more species is advected downstream rather than deposited. The concentrations are thus higher in the downstream section with faster kinetics, resulting in a rapid increase in reaction rates. For high enough values of Da_2 , the second peak in the deposition profile does not occur, as very little reactant remains to be transported to the downstream region with faster kinetics. It is also found that for a constant value of Da_2 , varying the value of Sc does not significantly change the shape of the deposition profile, and therefore has no effect independent of Da_2 , similar to what was found for the constant kinetics case in Section 5.5.3.

For a constant value of Da_2 , the shape of the kinetics profile also influences the shape of the deposition profile. Figures 5.14 and 5.15 show the effect of varying the values of z_0 and k_2/k_1 , respectively for $Da_2 = 0.1$. As shown in Fig. 5.14, as z_0 is increased, the second increase in the deposition is pushed correspondingly further downstream, shortly downstream from z_0 . Increasing the value of k_2/k_1 increases the relative size of the second maximum, as shown in Fig. 5.15. At a given Da_2 and z_0 , for low enough values of k_2/k_1 , the second maximum will not occur, as the slow increase in kinetics does not make the case significantly different from a constant kinetics case, as shown in Fig. 5.15 for $k_2 = 20k_1$. As $z_0 \rightarrow 0$, only a single deposition maximum is observed, because most of the limiting reactant is depleted very close to the entrance due to the sharply increasing kinetics. Likewise, if z_0 is too large, only one maximum is observed, because most of the limiting reactant is depleted before z_0 is reached. As

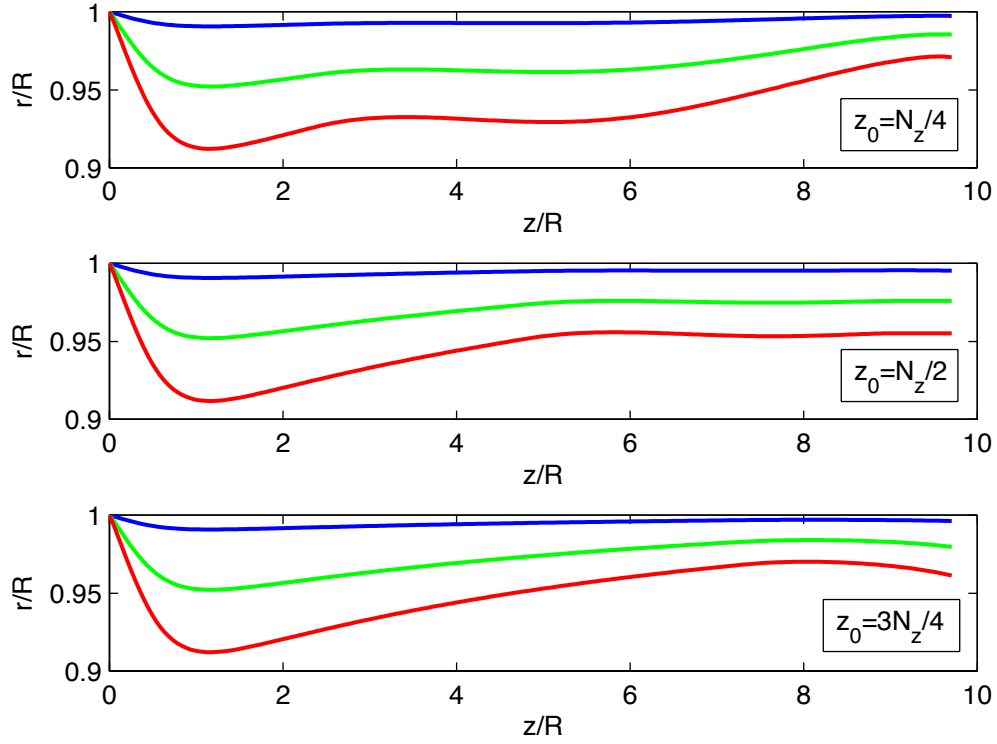


Figure 5.14: Deposition profiles for the varying kinetics case with $Re = 1.0$, $Sc = 1.0$, $Da = 0.1$, $Q_A/Q_C = 5.0$, and various values of z_0 . Results for $t^* = 1516.6$ are shown in blue, $t^* = 7707.1$ in green, and $t^* = 13897.6$ in red

Da_2 is increased, it is found that a larger value of k_2/k_1 is required for the same value of z_0 , in order for the two-maxima deposition profile to occur. This is because the effect of advection is weaker in the constant kinetics section, resulting in lower concentrations in the high kinetics region, which must then be overcome with a sharper increase in kinetics. Similarly as Da_2 is increased, a lower value of z_0 is required to produce a two-maxima deposition profile for the same value of k_2/k_1 , as the kinetics must rise sharply before a significant amount of the limiting reactant has been depleted.

5.5.7 Comparison to Experiments

Figure 5.16 shows experimental data for the entrance section of the reaction tube from Experiment 4, where the temperature profile was measured to be approximately

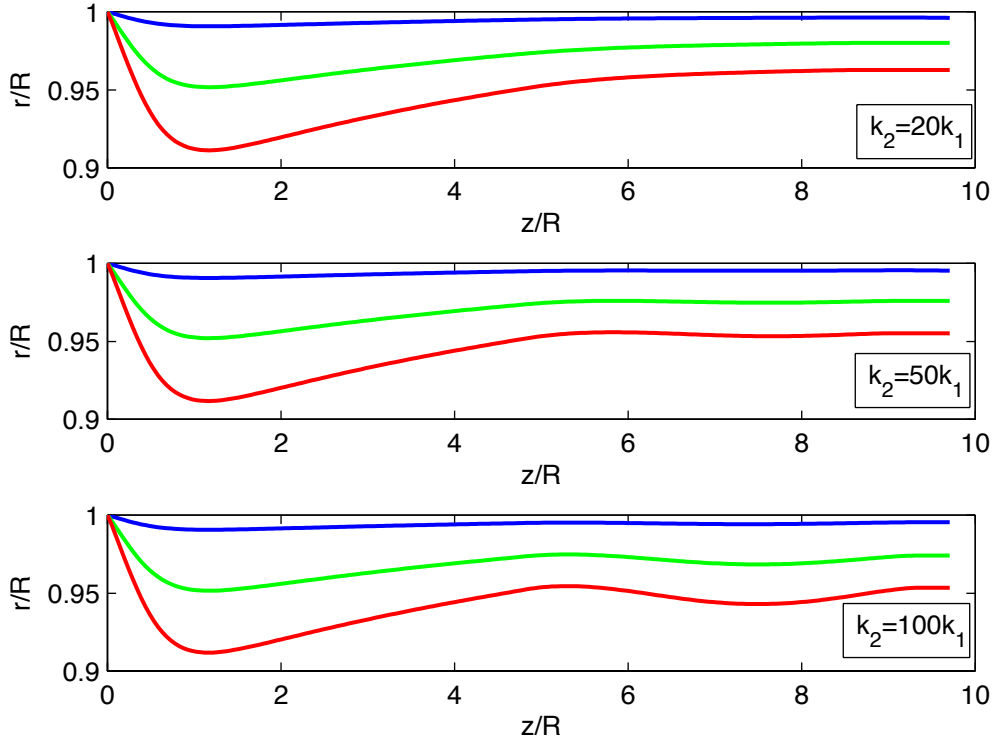


Figure 5.15: Deposition profiles for the varying kinetics case with $Re = 1.0$, $Sc = 1.0$, $Da = 0.1$, $Q_A/Q_C = 5.0$, and various values of k_2/k_1 . Results for $t^* = 1516.6$ are shown in blue, $t^* = 7707.1$ in green, and $t^* = 13897.6$ in red

constant in the first 5cm of the tube, along with model data for similar conditions ($Re \approx 20$, $Da \approx 10$). There is qualitative agreement between the measured ZnO mass distribution from the experiment and the simulation, where the deposited ZnO mass in the latter case can be interpreted as proportional to the area under the deposition curve. In both cases, there is a very large deposit centered near $z/R = 5$ followed by a gradual tapering off of the mass deposition due to Zn being depleted from the gas mixture, and a constant value of k . This general trend was observed for all of the previously discussed cases with constant kinetics. Overall, the results for constant temperature conditions agree reasonably well in a qualitative sense.

Figure 5.17 shows the simulation results for $Da_2 = 0.05$, $k_2/k_1 = 1000$ compared to the full ZnO deposition profile for Experiment 4 ($Da_2 \approx 0.5$). Although the

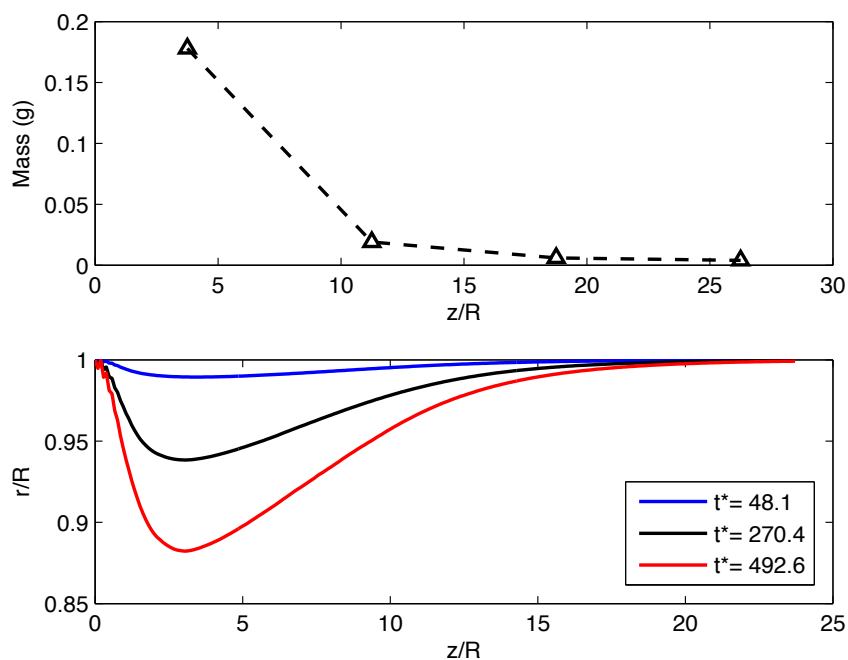


Figure 5.16: Comparison of constant temperature experimental data from Experiment 4 (top) with simulation for similar values of non-dimensional parameters (bottom).

comparison is somewhat tenuous because condensation of Zn also occurred in this experiment, it is apparent that the model can also capture the relatively large increases in ZnO deposition that were observed in several experiments.

It was found that by matching the non-dimensional parameters, the simulation could not match the trend in the ZnO deposition for experiments. For similar reactor lengths, the model requires lower values Da_2 , and higher values of k_2/k_1 for the second deposition peak to appear. For the model, it is found that $Da_2 < 1$ is required for the second peak in deposition to occur with an increasing kinetics profile, which was also the range of conditions for the experiments. Therefore, a qualitative validation can still be made from this observation.

The differences in the simulation and experimental results are likely due to several simplifying assumptions that were made in the model (first-order kinetic rate law, constant fluid density, binary diffusion, and no condensation of Zn occurs). In particular, because the first-order rate law in the model accounts for changes in kinetics but

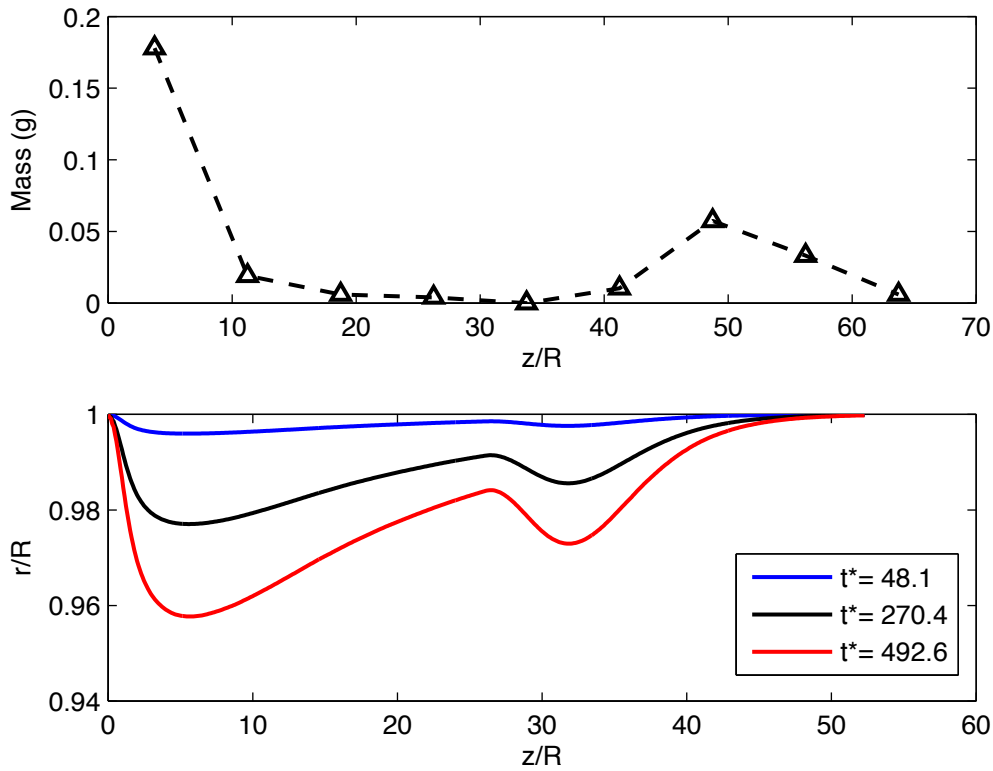


Figure 5.17: Comparison of non-isothermal experimental data from Experiment 4 (top) with simulation for similar values of non-dimensional parameters (bottom).

not equilibrium, it may be difficult to draw a completely fair comparison between the two in non-isothermal conditions. The change in temperature in the experiment would also decrease the mass diffusivities of the different species, which may also explain the discrepancy between the values of Da_2 required to match the trend in ZnO deposition.

Thus, there are numerous points of difference in the dynamics of the model and the real reactor, so care should be taken in drawing strong conclusions about the predictive power of the current LB model. The parametric analysis of the model, however, reveals many of the important dynamics that would still be important in a real reactor utilizing heterogeneous hydrolysis with Zn vapor.

5.6 Conclusions

The reactive gas/solid precipitation of ZnO in a circular tube has been simulated using multiple-relaxation-time lattice Boltzmann schemes in axisymmetric cylindrical coordinates for both flow and mass transfer. A D2Q9 scheme is used for the incompressible fluid flow, and a D2Q5 scheme is used for the mass transfer. The model assumes first-order kinetics at the solid boundary and a third-kind boundary condition for curved surfaces. The flow and mass transfer models are both validated using several problems in axisymmetric cylindrical coordinates with analytical solutions.

The deposition of solid products is found to depend strongly on whether the mass transfer is diffusion or advection-limited, with the results being nearly identical for diffusion-limited conditions due to the assumption of constant concentration at the inlet. In the advection-limited regime, the axial location of fastest mass deposition is found to scale with Pe , or equivalently with Re for constant Sc . The results are insensitive to Sc for a given value of Pe .

It is also found that the results depend strongly on whether the reaction is kinetics- or diffusion-limited, with the axial location of fastest deposition scaling inversely with Da under diffusion-limited conditions. Under diffusion-limited conditions, the reaction transitions from being diffusion-limited to kinetics-limited as the solid deposit grows and diffusion lengths are decreased. Thus, over short time scales, the results are nearly independent of Da for $Da > 5$.

Finally, the effect non-isothermal conditions are simulated by axially varying the kinetic constant. The results show that the value of $Da_2 = Da/ReSc$ determines whether the deposition profile has one or two peaks for a given kinetics profile, with the two-peak pattern occurring at lower values of Da_2 . Likewise, the shape kinetics profile has an effect on the deposition profile, with sharp increases in kinetics at moderate distances from the tube entrance tending to produce the second maximum in the deposition profile.

The model and results help to gain insight into the reactive deposition of ZnO in heterogeneous water-splitting using Zn vapor. More generally, this approach may be applicable to similar heterogeneous reactive/precipitation processes in axisymmetric

cylindrical coordinates in other engineering situations.

Chapter 6

CONCLUSIONS AND FUTURE WORK

6.1 Conclusions

As shown in Chapter 2, the heterogeneous hydrolysis with Zn vapor under a temperature gradient offers a 38% increase in cycle efficiency, assuming complete conversion in the dissociation and quench steps of the process, when compared to the best constant temperature case with a 1:1 steam to Zn stoichiometry. The results for cycle efficiency and heat recovery are found to be insensitive to the shape of the temperature profile for any initial and final temperatures, assuming that Zn condensation does not occur. The largest benefits to efficiency are that this method ensures complete conversion if the outlet temperature in the reactor is 800K or less, where the reaction equilibrium favors formation of H₂ and ZnO, and that near complete elimination of inert carrier gas is possible if the initial temperature approaches the normal boiling point of Zn (1180K). It is also found that the potential autothermicity of the reactor is maximized under these conditions, and the heat of the reaction is around 96% of the heat required to vaporize the reactants and bring them to the inlet temperature. Model results indicate that the condensation of Zn can be avoided if the temperature gradient and reactant flow rate are matched properly for a given reactor geometry, as the reaction can lower the partial pressure of Zn faster than the decrease in saturation pressure due to the falling temperature.

In Chapter 3, experimental investigations with a laboratory-scale tube reactor demonstrated nearly complete Zn conversions with a steam to Zn stoichiometry of 5:1 or greater, and conversions of around 45% with a nearly 1:1 stoichiometry. Significant condensation of Zn was observed in many cases, however the reactor has demonstrated notable improvements in the amounts of steam and inert gas used per unit of hydrogen produced, which would translate into significant gains in cycle efficiency for a real

process. Possible evidence of the intended equilibrium shift toward ZnO formation is observed in the cooler section of the reactor, as sharp increases in ZnO deposits were observed despite lower Zn partial pressures.

In Chapters 4 and 5, a lattice Boltzmann model of a reactive precipitation process in a circular tube was developed, which features a third-kind boundary condition compatible with curved boundaries in order to model the first-order kinetics of the reaction under the dilute approximation. The model simulates the transient accumulation of solid deposits on the walls of a circular tube. A parametric study of the relevant non-dimensional numbers in the system reveals the underlying dynamics of the deposition process, and helps to predict the shape of the deposit profile over time. The axial location of the peak in the deposition profile is found to increase with the value of Pe for a given value of Da for $Pe > 1$. It is also found that the axial location decreases with increasing Da for a given value of Pe , for $Da < 1$. The deposition profile is also found to be insensitive to Da for $Da > 5$ over short time scales, with differences only becoming pronounced when the diffusion lengths decrease due to significant deposition. The deposition is also relatively insensitive to Pe for $Pe < 1$, where the mass transport is diffusion-dominated.

The model results for the case with axially-increasing kinetics, which simulate both faster kinetics and shifting of equilibrium at lower temperatures, are found to be qualitatively similar to results that were consistently observed in the experimental investigation in Chapter 3, with a second maximum in the deposition profile occurring shortly downstream from the increase in kinetics. Both these simulations and experiments have $Da_2 \ll 1$. The appearance of this second maximum is found to depend on the advective Damköhler number in the entrance region, $Da_2 = \frac{k_1}{u_{av}}$, for a given kinetics profile, with the relative size of the second deposit increasing as Da_2 is decreased.

Regarding reactor operation, the LBM results indicate that the solid deposits are more evenly distributed at lower values of Da_2 , as shown in Fig. 5.9 and Fig. 5.13. For higher values of Da_2 , the deposits are more concentrated at a single axial location near the tube entrance. Operating at low Da_2 would allow more solid mass to be deposited before obstruction of the flow occurs, but would require a longer reactor

channel for complete conversion to occur. There is thus likely a trade-off between the amount of Zn that can be reacted before removing the deposits becomes necessary, and the required volume of the reactor.

6.1.1 Original Contributions

- The benefits of heterogeneous hydrolysis with Zn vapor under a temperature gradient have been quantified in terms of predicted cycle efficiency, heat recovery, and hydrolysis conversion, accounting for reaction equilibrium and Zn vapor saturation.
- A proof-of-concept reactor has been developed which successfully demonstrates the reaction under temperature swings from 1170K to 800K. Possible evidence for the equilibrium shift is observed experimentally at lower temperatures, and the reactor demonstrates hydrogen generation with significantly reduced steam and inert gas usage compared to previous approaches.
- A lattice Boltzmann model for a reactive heterogeneous precipitation process in axisymmetric cylindrical coordinates was developed and validated. A parametric study was conducted to explain the development of the solid deposition profile under different kinetics, mass transfer, and flow conditions. This modeling approach can be extended to study other reactor configurations, and may also be useful in other contexts such as geological and biological flows.

6.2 Recommendations for Future Work

6.2.1 Improvement of Current Reactor Design

The reactor design presented in Chapter 3 could be improved in terms of Zn conversion at low steam and inert gas flow rates. As discussed in Chapter 3, the current reactor design was unable to achieve complete conversion in most experiments due to a disadvantageous match between the temperature profile, reaction rates, and reactant flow rates. The reactor would be able to achieve complete conversion with low steam and inert gas usage by either making the reactor longer and using the current available range of reactant flow rates, developing a way of delivering lower flow rates of reactants to the reactor, or providing additional surface area for the reaction in the entrances region of the reaction tube without disrupting the flow of reactants.

If any of these changes are made to the current experimental setup, the theoretically predicted possibility of complete Zn conversion with minimal steam and inert gas usage could be achieved.

6.2.2 Further Confirmation of Equilibrium Shift

In Chapter 3, the observation of increased ZnO deposits was attributed mostly to the heterogeneous reaction being favored lower temperatures. It seems likely that this is the case, as the heterogeneous reaction is observed along with Zn condensation, and is expected to dominate than the oxidation of solid or liquid Zn. This conclusion could be strengthened by repeating experiments where Zn condensation occurred with varying time spans. If the oxidation of deposited Zn is occurring, the measured proportions of ZnO should increase over time. The degree to which the ZnO content increases would indicate which reaction is favored at lower temperatures, with high changes in ZnO proportions over time indicating significant oxidation of deposited Zn.

6.2.3 Removal of ZnO Deposits

One issue that was not addressed in this work was the design of a practical, continuously operating reactor utilizing the heterogeneous hydrolysis of Zn vapor. The need to remove the deposited ZnO presents a challenge for a continuous or semi-continuous process. While this was beyond the scope of the current work, there are numerous possibilities that could be pursued.

One possibility is to initially coat the inside of the reaction channel with a slurry of ZnO and water, and then to evaporate the water as the reactor is brought to the operating temperature, forming a sintered layer of ZnO as the substrate for the reaction. Sintering of ZnO powder has been observed to occur in this temperature range [131]. The layer would then adhere only weakly to the reaction channel and could possibly be removed by mechanical means after significant deposition has occurred on the sintered substrate.

It may also be possible to create the reactor channel out of pre-molded ZnO, and then simply pulverized the entire reactor channel after the reaction has proceeded. It was also suggested to use a fluidized bed of ZnO particles as the substrate for the reaction [86].

A similar concept has been explored recently [74, 75], in which the oxidation of Zn/ZnO powder mixtures with steam and CO₂ was investigated at temperatures just

under the melting point of Zn (670K). This reaction is of interest because the solid product of the quench step usually contains Zn with significant amounts of ZnO, and the two are not easily separable before hydrolysis. This Zn/ZnO mixture is referred to as solar Zn. It was found that the presence of ZnO actually aids in the oxidation of Zn at temperatures below the melting point of Zn (693K). In these studies, inert gas/oxidant mixtures were used, as well as varying proportions of Zn/ZnO. It may be possible to combine the current approach with this recently proposed approach to develop an optimal reactor design.

6.2.4 Two-Step Heterogeneous Hydrolysis of Solar Zn

To explain the mechanism of Zn evaporation and oxidation when solar Zn is used, one can examine two cases. In the first case, only inert gas is injected to the Zn/ZnO powder mixture at nearly the melting point of Zn, and the solid Zn is allowed to sublime until the gas mixture becomes saturated with Zn vapor. No reaction occurs as there is no oxidant present. In the second case, only steam is injected, and while some of the Zn sublimates, the high partial pressure of steam causes a fast reaction with the solid Zn surface, as well as the heterogeneous reaction with any evaporated Zn on the surfaces of the Zn and ZnO particles. This surface reaction acts as a sink for Zn vapor from the atmosphere, which allows the sublimation from Zn particles to continue until the Zn surfaces have been completely passivated by the growing layer of ZnO.

By injecting a mixture of steam and inert gas, these two effects are essentially allowed to compete with one another. When more inert gas is added, the rate of Zn sublimation and subsequent heterogeneous hydrolysis dominates the oxidation of the solid Zn surface, and a larger amount of Zn can evaporate before being passivating by steam. As the proportion of ZnO particles in the solid mixture increases, any evaporated Zn is more likely to react on a ZnO particle rather than a Zn particle, and thus its heterogeneous reaction will not contribute to the passivation Zn particles. As the inert gas usage and the ZnO particle usage increase, the conversion of Zn to ZnO also increases, however there are thermal losses due to heating of inert gas and ZnO. Due to the Zn particles being directly exposed to steam, it seems that some degree of

Zn passivation, and incomplete conversion, is inevitable in this approach.

The study in Ref. [75] reported limited Zn conversions of $< 70\%$ at 700K in 8% H₂O in Ar atmospheres, and could only achieve complete conversion by operating at nearly 1000K. However, complete conversion proved to be possible with CO₂ under similar conditions. The authors attributed the limited conversion to sintering of the ZnO particles and hollow ZnO shells around areas of Zn particles. However, after breaking up the sintered areas and reacting the mixture again, only minimal gains in conversion were achieved, so it is questionable whether sintering was the only effect preventing reaction, and whether significant passivation had occurred on the Zn particle surface as well.

The kinetics of the heterogeneous reaction of steam with Zn were found to be significantly higher than those with CO₂ and Zn [86], which may explain the discrepancy, rather than sintering. This difference in reaction kinetics is further supported by the fact that, in cases where passivation occurred, the reaction with CO₂ took several times longer to level off compared to steam, despite higher partial pressures of CO₂ [75]. In a similar study that tested the reaction of solar Zn with steam, nearly complete conversion was demonstrated in minutes under similar temperatures and steam partial pressures [73]. However, the average Zn particle size in Ref. [73] was orders of magnitude lower than in Ref. [75], which may account for the higher conversions, rather than sintering. Thus, if the Zn particles after quenching are larger than 100 nm, directly exposing solar Zn to steam may not yield high conversions. If the Zn particles after quench are consistently on the scale of 10 nm or less, complete conversion via the low temperature hydrolysis of solar Zn would likely be feasible.

However, if the required steam/inert gas flow rates are very high compared to the amount of Zn present, this approach may not be feasible from an efficiency standpoint. Although a mechanically-stirred batch reactor has demonstrated conversions near 80% using very little inert gas for the oxidation of solar Zn by CO₂, this level of performance has yet to be demonstrated with steam as the oxidant [132].

The solar Zn particle mixture after the quench step can be divided into “passivated Zn” and “exposed” Zn as shown in Fig. 6.1. While the passivated Zn can

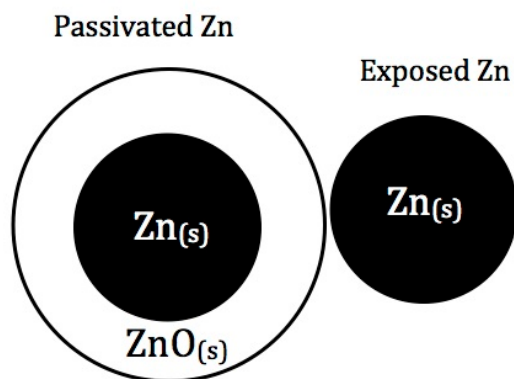


Figure 6.1: Passivated and exposed Zn after the quench step

evaporate in principle, the rate of evaporation is around ten times slower than a minimally oxidized Zn particle [133]. This implies that in the approach described in [75], exposed Zn will evaporate much more quickly and tend to oxidize the surface of passivated Zn particles even further, limiting overall conversion, or requiring very long residence times to convert the passivated Zn. The exposed Zn can also undergo direct oxidation and become passivated itself in this approach.

One advantage of the reactor design presented in the current work is that the evaporation of Zn and oxidation of Zn are done in separate areas of the reactor. Thus, the Zn that is put into the reactor is not available to be oxidized by steam until after it has evaporated. This advantage can be applied to the general gas/solid reaction of steam with solar Zn, as shown in Fig. 6.2, and a two-step gas/solid hydrolysis approach can be developed.

The approach would be to heat the solar Zn along with a flow of inert gas, allowing any exposed or passivated Zn in the particles to evaporate. The powder continues to flow toward the oxidation zone such that by the time the powder reaches the end of the evaporation zone, only Zn vapor and solid ZnO particles remain. The Zn vapor/inert gas mixture is then mixed with steam, and the ZnO particles serve as a substrate for the heterogeneous reaction with Zn vapor. Thus, ideally, all the Zn could be evaporated without encouraging passivation, and the final product would be pure ZnO particles

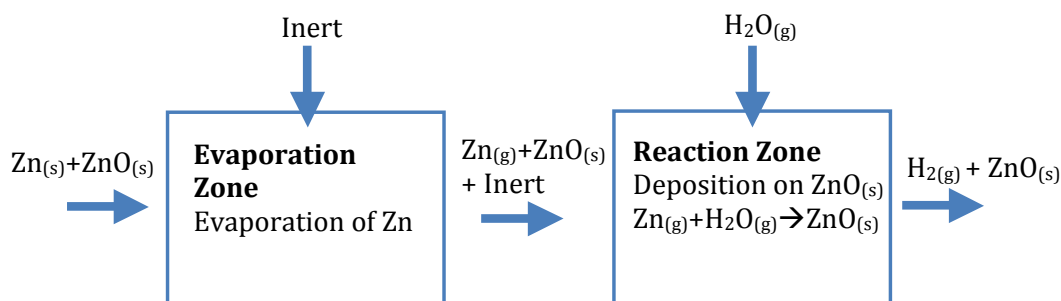


Figure 6.2: Schematic of two-step hydrolysis of solar Zn. Evaporation and oxidation are conducted in separate steps, preventing passivation of Zn particles

which could be recycled back to the reduction step.

One topic that should be investigated to assess this two-step hydrolysis with solar Zn is what range of temperature and inert sweep gas rates need to be applied to solar Zn in order to quickly evaporate all of the Zn. It should be determined whether the required residence times would be significantly longer than those required for directly oxidizing solar Zn, and whether the required temperatures and inert gas flow rates would be feasible from an efficiency standpoint. These questions could be investigated using thermogravimetric analysis (TGA) of solar Zn in inert gas atmospheres.

If the evaporation is reasonably fast, the two-step hydrolysis approach would likely offer an improvement over the approach presented by [75], as complete conversion could be guaranteed at low temperatures by eliminating the passivating oxidation of Zn particles altogether. The additional surface area per unit volume and enhanced mass transfer provided by aerosolized ZnO particles could also help to prevent condensation of Zn.

Although a perfect quench step has not yet been achieved, a hydrolysis method that utilizes pure Zn as a reactant, such as the one in this work, may also be worth pursuing, as ideally the quench step will eventually give a high Zn yield with future design iterations. It may also be the case that using ZnO particles as a reaction substrate so significantly benefits the hydrolysis conversion by adding reaction sites that ZnO particles should be added in the hydrolysis step even when the the quench

product does not contain a significant amount of ZnO.

In the case where a two-step gas/solid hydrolysis reactor is pursued, it seems likely that some amount of heterogeneous hydrolysis and deposition of ZnO on the walls of the reactor will be unavoidable. Thus, even though the reactor would ideally be a continuous design with ZnO particles being recovered at the outlet, some amount of ZnO would build up inside of the reactor over time due to uncontrolled reaction with steam on reactor walls. The issue of removing the deposits is thus partially mitigated by using ZnO particles as a substrate, but the previously mentioned solutions of molding the reactor from ZnO, or removing the deposits by mechanical means should still be considered in any case. The methods used in this work for predicting the transient accumulation of ZnO deposits are thus still of value in alternate reactor designs for hydrolysis with Zn vapor.

6.2.5 Improvements to LB Model

The LB model presented in this work is a good first approximation to the actual system in question, and can make useful predictions regarding the underlying dynamics of ZnO deposition process. However, there are many additions and refinements that can be made to incorporate additional detail and physics into the model.

Since the convective-diffusion equation (CDE) describes both heat and mass transport phenomena, the same D2Q5 scheme for the CDE that was used for mass transport could be used to describe the heat transport in the gas mixture. The layer of ZnO growth that is predicted by the model can also be coupled to a thermal model by including the effect of conduction through the ZnO layer. This is possible with a new method of applying the thermal boundary condition at the interface of the two phases [134], although this method would require modification for axisymmetric coordinates. The heat transfer model can be coupled to the mass transfer model by adding the heat of the reaction as a thermal source term on the solid/gas boundary where the reaction occurs.

The treatment of the reaction boundary condition for mass transfer can also be

improved. The rate law that was derived in [86] is:

$$r'' = k(T) \left(P_{Zn} P_{H_2O} - \frac{P_{H_2}}{K_{eq}(T)} \right) \quad (6.1)$$

whereas in the current work, the “dilute” approximation has been used, thus the P_{H_2} term is small, and $P_{H_2O} \approx const$, thus the approximate rate can be written as:

$$r'' = k_2 P_{Zn} \quad (6.2)$$

where P_{H_2O} has been “lumped” into k_2 . This formulation is used as a first approximation where only one mass transfer model is needed, and also because of its compatibility with the curved boundary condition implementation presented in [104]. If the H_2 concentration field was of interest, the model could be refined by adding a second mass transfer population for H_2 , which could also be accurately modeled under the “dilute” approximation, as there would be minimal interaction between Zn and H_2 in this limit. An additional population could also be added for the temperature, which also is governed by a CDE. Finally, the equilibrium constant and kinetics can be defined in terms of temperature, so that the surface temperature is also coupled to the reaction rate.

Thus, by adding two additional D2Q5 passive scalar models, a much more refined model can be constructed while still retaining accuracy under the dilute approximation. The additional computational cost of these models would be significant, approximately halving the speed of simulations, however they would offer a much more accurate picture of the effect of non-isothermal conditions than the assumptions that were used to model this effect in Chapter 5.

Another minor shortcoming of the current LB model is that it is not accurate under the assumption of a stoichiometric mixture of steam and Zn, rather it is only accurate when the proportion of Zn is small. These conditions are sufficient to study the underlying dynamics of the system, however they are not of the highest interest, as they represent conditions where cycle efficiency is not optimal.

For the case where the initial gas mixture is roughly half steam and half Zn, there is a significant decrease in the density of the gas mixture from the beginning of

the reactor channel to the end due to the deposition of mass from the gas phase. It may be possible to simulate the effect of the loss of fluid density by using a multicomponent LB model, for example similar the one presented in [135]. The relevant sources and sinks of each species could conceivably be incorporated into the boundary condition to be consistent with the reaction rate, however there is currently no third-kind boundary condition for curved boundaries that is readily compatible with a multi-component model, to our knowledge. However, this approach would allow for the potentially significant variation in fluid density to be incorporated into the model.

The most accurate model that could be developed for the diffusion and flow of the gas mixture would be the Stefan-Maxwell diffusion model coupled with the Navier-Stokes equations. Such a model is possible with the lattice Boltzmann method [136], however the boundary conditions for these models have not been developed to the same extent as simpler models, i.e., in [104].

Finally, any of these methods of modeling the deposition of solid ZnO that have been presented can be adapted to model different systems. The method of tracking the solid/gas interface could easily be extended to model the surface ZnO growth of a population of aerosolized ZnO particles undergoing hydrolysis on their surface, and the fluid flow model could likewise track the motion of the growing particles using methods for particle suspensions, which are now well-developed in the context of the LBM [137]. The computational cost of resolving individual particles in the simulation may be great, however, so it may instead be desirable to alter the current model of a single reactor channel to account for the loss of Zn vapor due to reaction on aerosolized particles. Then, the effect of ZnO accumulation on the channel walls could be investigated for different particle loading conditions, and hopefully minimized to allow for more continuous operation.

6.2.6 Investigation of Heat Recovery

Another topic that is not discussed in the current work is the heat transfer required to generate the desired temperature gradient. For any initial reaction temperature, outlet temperature, and reactant flow rate, a certain amount of cooling must be

provided from another working fluid, or possibly from pre-heating a solid such as ZnO powder. The required flow rate of a given working fluid, the required initial temperature, etc. can be studied using a relatively simple 1D shell-and-tube heat exchanger model, in which the heat of the reaction is lumped into a temperature-dependent effective specific heat of the reactive gas mixture. This assumption is accurate in the limit where the mixture composition follows equilibrium for any temperature. Then, for any initial reactant gas mixture composition, the equilibrium mole fraction of each species becomes a unique function of temperature $x_i(T)$ that can be determined from the equilibrium constant.

The effective specific heat can be defined in terms of the standard molar enthalpies of each species in the system by considering the definition of constant pressure specific heat for a mixture:

$$c_{P,eff}(T) = \sum_i \frac{d}{dT}(x_i \Delta H_i) = \sum_i \left(\frac{dx_i}{dT}(T) \Delta H_i(T) + x_i(T) \frac{d\Delta H_i}{dT}(T) \right) \quad (6.3)$$

where ΔH_i is the molar enthalpy of species i . The term $\frac{dx_i}{dT}$ is related to the reaction rate induced by a small change in temperature and thus equilibrium composition, and the second term in Eq. 6.3 is simply the molar-averaged specific heat of the mixture. Hence, the local reaction rate is incorporated into the effective specific heat as an additional function of temperature. The functions $x_i(T)$, $\frac{d\Delta H_i}{dT}(T)$ can be determined numerically in an initial computation using the chosen initial gas mixture composition, and then polynomial functions can be fit to them for ease of implementation.

The energy balance for the inside of the heat exchanger/reactor can be written as:

$$\dot{n}_{mix}(T_{mix})c_{P,eff}(T_{mix})\frac{dT_{mix}}{dz} = 2\pi R_i h_i(z)(T_{mix} - T_w) \quad (6.4)$$

where $\dot{n}_{mix}(T_{mix})$ is the local molar flow of the reactive mixture, R_i is the inner radius of the tube where the reaction is occurring, and h_i is the convective heat transfer coefficient.

On the outside of the tube, the heat balance is given similarly in terms of the flow rate of the working fluid (wf) being used for heat recovery.

$$\dot{n}_{wf}(T_{wf})c_{P,wf}(T_{wf})\frac{dT_{wf}}{dz} = 2\pi R_o h_o(z)(T_w - T_{wf}) \quad (6.5)$$

and finally the heat balance through the tube wall is given by:

$$R_o h_o(z)(T_w - T_{wf}) = R_i h_i(z)(T_{mix} - T_w) \quad (6.6)$$

These three equations can be solved numerically for the temperature profiles $T_w(z)$, $T_{mix}(z)$, and $T_{wf}(z)$. The two differential equations for the working fluid and the reactive mixture should be integrable using the Runge-Kutta method, and the wall temperature can be determined at each value of z by iterating T_w to satisfy Eq. 6.6.

This model is valuable because of its simplicity, and also because of the strong coupling with the thermodynamics of the reaction, and can be a useful tool in determining the proper length scale of reactor that is required to achieve a certain temperature difference for given initial flow rates and temperatures of working fluid and reactive mixture, or alternatively what flow rate of working fluid is required for a given reactor length and temperature range, etc. The effect of aerosolized ZnO particles can also be included in the effective specific heat, if such a reactor is to be pursued. By examining the path of P_{Zn} with temperature and comparing it to the saturation curve for Zn, as was done in Chapter 2, the model can also be used to identify heat transfer conditions that are favorable for avoiding condensation of Zn.

6.3 Future of Solar Thermochemical Cycles

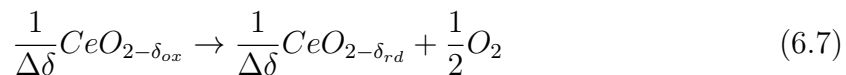
6.3.1 Materials

As discussed in Chapter 1, zinc oxide was initially considered an attractive metal oxide for use in solar thermochemical cycles due to its favorability in terms of reaction temperature, high oxygen looping, etc.. However, because of the noted inefficiency and low yield of the recombination reaction, as well as low yield from the hydrolysis step, it was decided by the US Department of Energy to terminate research on the process in the near future [42]. Indeed, interest in the Zn/ZnO cycle seems to be waning with

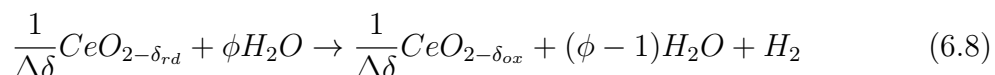
research groups worldwide, and non-volatile metal oxides such as CeO_2 are growing in popularity.

The partial reduction of CeO_2 occurs without any significant volatility of the metal, in other words, the metal oxide stays in the solid phase and only oxygen gas is evolved, and thus no quench step is necessary to prevent recombination after reduction.

The partial reduction of non-stoichiometric ceria is shown below:



and the oxidation of partially-reduced non-stoichiometric ceria by steam is given by:



where $\Delta\delta = \delta_{ox} - \delta_{rd}$ is the change in oxygen non-stoichiometry. The nonstoichiometry swing $\Delta\delta$ can be increased by operating at higher temperatures, but eventually this causes volatility, which is sought to be avoided in this approach [138].

The degree of partial reduction and oxidation are sensitive to the temperatures of reduction of oxidation, as well as the partial pressures of oxygen and oxidant in reduction and oxidation steps, respectively. There have been several analyses on the efficiency of this thermochemical cycle, each with varying assumptions about reduction and oxidation operating conditions, as well as the amount of work required for inert gas separation. Due to the very low partial pressures of oxygen required for reduction, high amounts of inert gas or vacuum are required for the reduction step. Due to the high stoichiometries of oxidant (i.e., steam or CO_2) required for oxidation, there is significant additional heating of reactants that is required per unit of fuel produced. Owing to both of these effects, as well as the low oxygen stoichiometry change of the metal oxide in the process, most estimates of the ideal efficiency of this process are considerably lower than those for the Zn/ZnO cycle [139]. However, due to the non-volatile nature of the metal oxide, it may be substantially more feasible than the Zn/ZnO cycle in the short-term.

Other non-volatile materials have also been investigated for use in solar thermochemical cycles, including perovskites [140] and hercynite materials [141]. Perovskite

materials are also being designed from scratch to have optimal thermodynamic characteristics for both CO₂ and water-splitting cycles [142], ammonia synthesis from water and N₂ [143], and oxygen separation [144]. Thus in the future, redox materials may be synthesized artificially with their physical and thermodynamic properties specially tailored to the intended process.

Hercynite cycles were considered particularly attractive because it was found that they could be cycled between oxidation and reduction at nearly constant temperature [145], giving the prospect of a cycle that needed no temperature swing or heat recovery. However, Ermanowski et. al have suggested that isothermal water-splitting may be less efficient in practice, because a large portion of the reduced oxide's heat can not be utilized for pre-heating of steam or CO₂. With an optimal temperature swing, more heat can be recycled between reduction and oxidation, however if the temperature swing is too high (i.e., the reduction temperature is too high), the required solar input begins to lower efficiency, or there is solar heat being absorbed that is unnecessary for heating steam and other purposes [146].

Although non-volatile metal oxides such as ceria have their benefits, notably in eliminating the need for a quench step, there are still issues to resolve. An important consideration is the small amount of oxygen that can be looped per unit mass of the metal oxides. Identifying materials with increased values of $\Delta\delta$ without significantly decreasing the necessary oxygen partial pressure for reduction, and without increasing the oxidant partial pressure required for oxidation significantly should be pursued [146].

6.3.2 Reactor Design

There have been many advancements in reactor designs that take advantage of the non-volatile nature of metal oxides such as ceria. With no quench step necessary in these cases, the designs become much more simple and elegant. In order to facilitate heat recovery, as well as to demonstrate an entire solar thermochemical cycle in a single closed-system, there have been several designs for reactors that combine oxidation and reduction into a single reactor. One design uses a series of packed-beds of metal-oxide to create separate reduction chambers and oxidation chambers with different pressures

[147]. The particles are recycled to the initial reduction chamber from the oxidation chamber using a screw-feeder with built-in heat recovery. The pressure separations allow for off-gassing of the majority of oxygen and hydrogen (in the case of water-splitting) in separate stages so that the partial pressure of oxygen in the final hydrogen product gas is negligible.

Another recent design which combines the oxidation and reduction steps into a single reactor was designed at the University of Minnesota for use with ceria [148]. In this design, the gas flows can be switched between inert gas and oxidant, with both occurring in the same packed beds of ceria, and utilizes heat exchangers to recover heat from exiting gases in order to pre-heat entering gases (either inert gas or oxidant, depending on mode of operation). A number of designs also allow for reduction and oxidation of ceria in the same chamber by using counter-rotating ceria discs for solid-solid heat recovery. This design sends newly-reduced ceria to the oxidation zone by means of the rotation of the disc, and the counter-rotation of different discs allows for pre-heating before reduction, and cooling before oxidation [138].

6.3.3 Future of the Zn/ZnO Cycle

In principle, the utilization of concentrated solar energy for large scale high throughput processes for syngas/hydrogen production still looks promising. Developments in thermochemical cycles are likely to be made for non-volatile metal oxides in coming years. The solar reduction of ZnO has been demonstrated on a pilot-plant scale, and it appears that an optimal reactor design for the hydrolysis step utilizing the heterogeneous reaction of Zn vapor with steam is well within reach of being demonstrated. The Zn/ZnO cycle still offers very high theoretical efficiency compared to other methods of solar hydrogen production, and interest could return to this particular process when a breakthrough has been made in producing high Zn yields in reduction using lower amounts of inert gas. As discussed in Chapter 2, any potential benefits of optimizing the hydrolysis step become less significant as the quench efficiency is decreased, thus further development in this area is critical for an efficient thermochemical cycle.

BIBLIOGRAPHY

- [1] IPCC, 2014, "Climate Change 2014: Synthesis Report. Contribution of Working Groups I, II and III to the Fifth Assessment Report of the Intergovernmental Panel on Climate Change," Core Writing Team, R.K. Pachauri and L.A. Meyer (eds.). IPCC, Geneva, Switzerland.
- [2] Hubbert, M.K., 1956, "Nuclear Energy and the Fossil Fuels," *Presented before the Spring Meeting of the Southern District, American Petroleum Institute, San Antonio Texas*. March 7-9, 1956.
- [3] US Energy Information Agency. "International Energy Outlook 2016," [www.eia.gov/outlooks/ieo/pdf/0484\(2016\).pdf](http://www.eia.gov/outlooks/ieo/pdf/0484(2016).pdf).
- [4] Olayele, F.B., 2015, "The Geopolitics of Oil and Gas," International Association for Energy Economics. www.iaee.org.
- [5] Jackson, J.K., 2016, "U.S. Trade Deficit and the Impact of Changing Oil Prices," Congressional Research Service, <https://www.fas.org/sgp/crs/misc/RS22204.pdf>.
- [6] US Department of Energy, "History of Hydropower," <http://energy.gov/eere/water/history-hydropower>.
- [7] Wind Energy Foundation, "History of Wind Energy," <http://windenergyfoundation.org/about-wind-energy/history/>.
- [8] US Department of Energy Office of Energy Efficiency and Renewable Energy, "Hydropower Technology Development," <http://energy.gov/eere/water/hydropower-technology-development>.
- [9] Pryor, S.C. and Barthelmie, R.J., 2010, "Climate Change Impacts on Wind Energy: A Review," *Renewable and Sustainable Energy*, **14**-1, pp. 430-437.
- [10] Boehlert, B., Strzepek, K.M. Gebretsadik, Y., Swanson, R., McCluskey, A., Nuemann, J.E., McFarland, J., and Martinich, J., 2016, "Climate Change Impact and Greenhouse Gas Mitigation Effects on U.S. hydropower generation," *Applied Energy*, **183**, pp. 1511-1519.
- [11] Kreith, F., and Goswami, D.Y (eds.), 2007, "Handbook of Energy Efficiency and Renewable Energy," Boca Raton, FL., Taylor and Francis Group.
- [12] Markvart, T., 1994, "Solar Electricity, 2nd edition," West Sussex, England, John Wiley and Sons.

- [13] Herrando, M., Markides, C.N., and Helgart, K., 2014, "A UK-based assessment of hybrid PV and solar-thermal systems for domestic heating and power: System performance," *Applied Energy*, **122**, pp. 288-309.
- [14] Nules, V.M.B., Queiros, C.S., Lourenco, M.J.V. Santos, F.J.V., and Nieto de Castro C.A., 2016, "Molten Salts as Engineering Fluids-A Review: Part I. Molten Alkali Nitrates," *Applied Energy*, **183**, pp. 603-611.
- [15] U.S. Environmental Protection Agency, 2016, "Inventory of US Greenhouse Gas Emissions and Sinks: 1990-2016," <https://www3.epa.gov/climatechange/Downloads/ghgemissions/US-GHG-Inventory-2016-Main-Text.pdf>.
- [16] Wind, J., 2016, "Hydrogen-fueled automobiles-Passenger cars and buses," *Compendium of Hydrogen Energy* pp. 3-21.
- [17] U.S. Energy Information Administration, 2016, "Annual Energy Outlook 2016- With Projections to 2040," www.eia.gov/forecasts/aeo.
- [18] Marxer, D., Furler, P., Scheffe, J., Geerlings, H., Falter, C., Batteiger, V., Sizmann, A., and Steinfeld, A., 2015, "Demonstration of the Entire Production Chain to Renewable Kerosene via Solar Thermochemical Splitting of H₂O and CO₂," *Energy & Fuels*, **29**, pp. 3241 -3250.
- [19] Loutzenhiser, P.G., Stamatiou, A., Villasamil, W., Meier, A., and Steinfeld, A., 2011, "Concentrated Solar Energy for Thermochemically Producing Liquid Fuels from CO₂ and H₂O," *The Member Journal of the Minerals Metals & Materials Society*, **63**-1, pp. 32-34.
- [20] Rifkin, J., 2002, "The Hydrogen Economy," Penguin Putnam Inc.
- [21] Yilmza, F., Tolga Balta, M., and Selbas, R., 2016, "A Review of Solar Based Hydrogen Production Methods," *Renewable and Sustainable Energy Reviews*, **56**, pp. 171-178.
- [22] Fletcher, E.A., and Moen, R.L., 1977, "Hydrogen and Oxygen from Water: The Use of Solar Energy in a One-Step Effusional Process is Considered," *Science*, **9**(197), pp. 1050-1056.
- [23] Patrice, C, Abanades, S., Florent, L., and Flamant, G., 2008, "Analysis of Solar Chemical Processes for Hydrogen Production from Water Splitting Thermochemical Cycles," *Energy Conversion and Management*, **49**, pp. 1547-1556.
- [24] Besenbruch, G., 1982, "General Atomic sulfur iodine thermochemical water-splitting process," *Proceedings of the American Chemical Society*, **27**(1), pp. 48-53.
- [25] Steinfeld, A., Palumbo, R., 2001, "Solar Thermochemical Process Technology," *Encyclopedia of Physical Science and Technology*, R. A. Meyers Ed., Academic Press, Vol. 15, pp. 237-256.

- [26] Abanades, S., Charvin, P., Flamant, G., Neveu, P., 2006, "Screening of Water-splitting Thermochemical Cycles Potentially Attractive for Hydrogen Production by Concentrated Solar Energy," *Energy*, **31**, pp. 2805-2822.
- [27] Palumbo R., Ledé, J., Boutin, O., 1998, "The Production of Zn from ZnO in a High-Temperature Solar Decomposition Quench Process - I. The Scientific Framework for the Process," *Chemical Eng. Science*, **53**, pp. 2503 - 2517.
- [28] Felder, R. and Meier, A., 2008, "Well-to-Wheel Analysis of Solar Hydrogen Production and Utilization for Passenger Car Transportation," *Solar Energy Engineering*, **130** (1), 011017 (10 pages).
- [29] Steinfeld, A., 2004, "Solar Thermochemical Production of Hydrogen: a Review," *Solar Energy*, **78**, pp. 603-615.
- [30] Perkins C., and Weimer A. W., 2009, "Solar-thermal production of renewable hydrogen," *AIChE Journal*, **55**(2), pp. 286-293.
- [31] Steinfeld, A., 2002, "Hydrogen via a Two-Step Water-Splitting Thermochemical Cycle based on Zn/ZnO Redox Reactions," *Int. J. Hydrogen Energy*, **27**, pp. 611-619.
- [32] Muller, R., Haeberling, P., Palumbo, R.D., 2006, "Further Advances Toward the Development of a Direct Heating Solar Thermal Chemical Reactor for the Thermal Dissociation of ZnO_(s)," *Solar Energy*, **80** (5), pp. 500-511.
- [33] Koepf, E., Advani, S.G., Steinfeld, A., and Prasad, A.K., 2012, "A Novel Beam-Down, Gravity-fed, Solar Thermochemical Receiver/Reactor for Direct Solid Particle Decomposition: Design, Modeling, and Experimentation," *Int. J. of Hydrogen Energy*, **37** pp. 16871-16887.
- [34] Koepf, E., 2014, "Solar Hydrogen by Thermochemical Water Splitting Cycles: Design, Modeling and Demonstration of a Novel Receiver/Reactor for the High Temperature Decomposition of ZnO using Concentrated Sunlight," Doctoral thesis, University of Delaware.
- [35] Koepf, E. E., Lindemer, M.D., Advani, S. G., and Prasad, A. K., 2013, "Experimental Investigation of Vortex Flow in a Two-Chamber Solar Thermochemical Reactor," *ASME Journal of Fluids Engineering*, **135**, 111103 (12 pages).
- [36] Koepf, E. E., Advani, S. G., Prasad, A. K., and Steinfeld, A., 2015, "Experimental Investigation of the Carbothermal Reduction of ZnO Using a Beam-Down, Gravity-Fed Solar Reactor," *Industrial and Engineering Chemistry Research*, **54**, pp. 8319-8332.
- [37] Villasmil, W., Brkic, M., Wuillemain, D., Meier, A., and Steinfeld, A., 2014, "Pilot Scale Demonstration of a 100-kWth solar thermochemical plant for the Thermal Dissociation of ZnO," *Journal of Solar Energy Engineering*, **1**, 011016 (11 pages).

- [38] Koepf, E., Villasmil, W., and Meier, A., 2016, "Demonstration of a 100-kWth High-Temperature Solar Thermochemical Reactor Pilot Plant for ZnO Dissociation," *AIP Conference Proceedings*, **1734**, 120005 (8 pages).
- [39] Schunk, L., Haerberling, P., Wepf, S., Wuillemin, D., Meier, A., and Steinfeld, A., 2008, "A Receiver-Reactor for the Solar Thermal Dissociation of Zinc Oxide," *ASME J. Sol. Energy Eng.*, **130** (2), 021009.
- [40] Schunk, L. O., Lipinski, W., and Steinfeld, A., 2009, "Heat Transfer Model of a Solar Receiver-Reactor for the Thermal Dissociation of ZnO-Experimental Validation at 10 kW and Scale-Up to 1 MW," *Chem. Eng. J.*, **150** (2-3), pp. 502-508.
- [41] Koepf, E., Villasmil, W. and Meier, A., 2015, "High Temperature Flow Visualization and Aerodynamic Window Protection of a 100-kWth Solar Thermochemical Receiver-Reactor for ZnO Dissociation," *Energy Procedia*, **69**, pp. 1780-1789.
- [42] Perret, R., 2011, "Solar Thermochemical Hydrogen Production Research (STCH): Thermochemical Cycle Selection and Investment Priority," *Sandia National Laboratories*, Sandia Report SAND 2011-3622.
- [43] Watson, L.R., Theim, T.L., Dressler, R.A., Salter, R.H., Murad, E., 1993, "High Temperature Mass Spectrometric Studies of the Bond Energies of Gas Phase ZnO, NiO, and CuO," *Journal of Physical Chemistry*, **97**, pp. 5577-5580.
- [44] Weidenkaff, A., Steinfeld, A., Wokaun, A., Auer, P.O., Eichler, B., and Reller, A., 1999, "Direct Solar Thermal Dissociation of Zinc Oxide: Condensation and Crystalization of Zinc in the Presence of Oxygen," *Solar Energy*, **65**(1) ,pp. 59-69.
- [45] Keunecke, M., Meier, A., and Palumbo, R., 2004, "Solar Thermal Decomposition of Zinc Oxide: An Initial Investigation of the Recombination Reaction in the Temperature Range 1100-1250K," *Chemical Eng. Science*, **59**, pp. 727-744.
- [46] Alxneit, I., 2008, "Assessing the Feasibility of Separating a Stoichiometric Mixture of Zinc Vapor and Oxygen by a Fast Quench - Model Calculations," *Journal of Solar Energy*, **82**, pp. 959-964.
- [47] Gstoehl, D., Brambilla, A., Schunk, L.O., and Steinfeld, A., 2008, "A Quenching Apparatus for the Gaseous Products of the Solar Thermal Decomposition of ZnO," *J. Mater. Science*, **43**, pp. 4729-4736.
- [48] Chueh, W. C., Falter, C., Abbott, M., Scipio, D., Furler, P., Haile, S. M., and Steinfeld, A., 2010, "High-Flux Solar-Driven Thermochemical Dissociation of CO₂ and H₂O Using Nonstoichiometric Ceria," *Science*, **330**, pp. 1797-1801.
- [49] Haring, H. W., 2008, "Industrial Gases Processing," Wiley.
- [50] EPA Clean Air Technology Center, 1999, "Nitrogen Oxides (NO_x), Why and How They are Controlled," EPA-456/F-99-006R, <https://www3.epa.gov/ttnecat1/dir1/fnoxdoc.pdf>.

- [51] Hänchen, M. Stiel, A., Jovanovic, Z.R., and Steinfeld, A., 2012, “Thermally Driven Copper Oxide Redox Cycle for the Separation of Oxygen from Gases,” *Industrial Chemistry Research*, **51** pp. 7013-7021.
- [52] Alonso, E., Gallo, A., Perez-Rabago, C., Fuentealba, E., 2016, “Thermodynamic Study of CuO/Cu₂O and Co₃O₄/CoO Redox Pairs for Solar Energy Thermochemical Storage,” *AIP Conference Proceedings*, **1734**, 050004 (8 pages).
- [53] Bazan, J.C., Gshaidler, M.E., and Alimenti, G.A., 1999, “Gravimetric Study of the Interaction of Water Vapour with Metallic Zinc,” *J. Thermal Analysis and Calorimetry*, **55**, pp. 569-579.
- [54] Berman, A., and Epstein, M., 2000, “The Kinetics of Hydrogen Production in the Oxidation of Liquid Zinc with Water Vapor,” *Int. J. Hydrogen Energy*, **25**, pp. 957-967.
- [55] Wegner, K., Ly, H. C., Weiss, R.J., Sotiris, P.E., and Steinfeld, A., 2005, “In-situ Formation and Hydrolysis of Zn Nanoparticles for H₂ Production by the 2-step ZnO/Zn Water-Splitting Thermochemical Cycle,” *Int. J. Hydrogen Energy*, **31**, pp. 55-61.
- [56] Delalu, H., Vignalou, J.R., Elkhatib, M., and Metz, R., 2000, “Kinetics and Modeling of Diffusion Phenomena Occurring During the Complete Oxidation of Zinc Powder: Influence of Granulometry, Temperature and Relative Humidity of the Oxidizing Fluid,” *Solid State Sciences*, **2**, pp. 229-235.
- [57] Alimenti, G., Gschaidler, M., Bazan, J., and Ferreira, M., 2004, “Theoretical and Experimental Study of the Interaction of O₂ and H₂O With Metallic Zinc-Discussion of the Initial Step of Oxide Formation,” *J. Colloid Interface Sci.*, **276**, pp. 24-38.
- [58] Lindemer, M.D., Advani, S.G., and Prasad, A.K., 2016. “Hydrogen Production via the Heterogeneous Hydrolysis of Zn Vapor Under a Temperature Gradient: Modeling and Efficiency Analysis,” *Int. J. of Hydrogen Energy*, **41**, pp. 10556-10567.
- [59] Ernst, F.O., Steinfeld, A., and Pratsinis, S.E., 2009, “Hydrolysis Rate of Sub-micron Zn Particles for Solar H₂ Synthesis,” *Int. J. Hydrogen Energy*, **34**, pp. 1166-1175.
- [60] Vishnevetsky, I., and Epstein, M., 2007, “Production of Hydrogen from Solar Zinc in Steam Atmosphere,” *Int. J. Hydrogen Energy*, **32**, pp. 2791-2802.
- [61] Weidenkaff, A., Reller, A.W., Wokaun, A., and Steinfeld, A., 2000, “Thermogravimetric Analysis of the ZnO/Zn Water Splitting Cycle,” *Thermochimica Acta*, **359**, pp. 69-75.
- [62] Lv, M., Zhou, J., Yang, W., and Cen, K., 2010, “Thermogravimetric Analysis of the Hydrolysis of Zinc Particles,” *Int. J. Hydrogen Energy*, **35**, pp. 2617-2621.

- [63] Weiss, R.J., Ly, H.C., and Wegner, K., 2005, “ H_2 Production by Zn Hydrolysis in a Hot-Wall Aerosol Reactor,” *AIChE Particle Technology and Fluidization*, **51**(7), pp. 1966-1970.
- [64] Ernst, F. O., Tricoli, A., and Pratsninis, and Sotiris, E., 2006, “Co-synthesis of H_2 and ZnO by In-Situ Zn Aerosol Formation and Hydrolysis,” *AIChE Environmental and Energy Eng.*, **52**(9), pp. 3297-3303
- [65] Funke, H.H., Diaz, H., Liang, X., Carney, C.S., Weimer, A.W., and Li, P., 2008, “Hydrogen Generation by Hydrolysis of Zinc Powder Aerosol,” *Int. J. Hydrogen Energy*, **33**, pp. 1127-1134.
- [66] Hamed, A. T., Venstrom, L., and Alshare, A., 2009, “Study of a Quench Device for the Synthesis and Hydrolysis of Zn Nanoparticles: Modeling and Experiments,” *J. Solar Energy Eng.*, **131**(3), 031018 (9 pages).
- [67] Melchior , T., Piatkowski, N., and Steinfeld, A., 2009, “ H_2 Production by Steam-quenching of Zn Vapor in a Hot-Wall Aerosol Flow Reactor,” *Chem. Eng. Science*, **64**, pp. 1095-1101.
- [68] Chambon, M., Abanades, S., and Flamant, G., 2009, “Kinetic Investigation of Hydrogen Generation from Hydrolysis of SnO and Zn Solar Nanopowders,” *Int. J. of Hydrogen Energy*, **34**, pp. 5326 - 5336.
- [69] Ma, X., Zacariah, M.R., 2010, “Size-resolved Kinetics of Zn Nanocrystal Hydrolysis for Hydrogen Generation,” *Int. J. of Hydrogen Energy*, **35**, pp. 2268-2277.
- [70] Hamed, T.A., Davidson, J.H., and Stolzenburg, M., 2008, “Hydrolysis of Evaporated Zn in a Hot Wall Flow Reactor,” *J. Solar Energy Eng.*, **130**, 041010 (7 pages).
- [71] Nicodemus, J., and Davidson, J.H., 2015, “Mechanisms of Hydrolysis in a Transverse Jet Zinc Aerosol Reactor,” *Chemical Eng. Science*, **122**, pp. 514-522.
- [72] Nicodemus, J. H., Davidson, J. H., 2012, “Fluid Dynamics of a Traverse Jet Reactor for Zinc Aerosol Hydrolysis,” *Journal of Solar Energy Engineering*, **134**, 041018 (9 pages).
- [73] Abanades, S., 2012, “Thermogravimetry of CO_2 and H_2O Reduction form Solar Nanosized Zn Powder for Thermochemical Fuel Production,” *Industrial & Engineering Chemistry Research*, **51**, pp. 741-750.
- [74] Stamatiou, A., Steinfeld, A., and Jovanovic, Z.R., 2013, “On the Effect of the Presence of Solid Diluents during Zn Oxidation by CO_2 ,” *Industrial and Engineering Chemistry Research*, **52**, pp. 1859-1869.
- [75] Weibel, D., Jovanovic, Z.R., Galvez, E., Steinfeld, A., 2014, “On the Mechanism of Zn Particle Oxidation by H_2O and CO_2 in the Presence of ZnO,” *Chemistry of Materials*, **26**, pp. 6486-6495.

- [76] Rager, T., 2012, "Re-evaluation of the Efficiency of a Ceria-based Thermochemical Cycle for Solar Fuel Generation," *Chem. Commun.*, **48**, pp. 10520-10522.
- [77] Reisman, A., Berkenblit, M., Ghez, R., and Chan, S.A., 1972, "The Equilibrium Constant for the Reaction of $\text{ZnO} + \text{H}_2$ and the Chemical Vapor Transport of ZnO via the $\text{Zn} + \text{H}_2\text{O}$ reaction," *J. Electronic Mat.*, **1**(3), pp. 395 - 419.
- [78] Yaws, C.L., Narasimham, P.K., and Gabbula, C., 2005, "Yaws Handbook of Antoine Coefficients for Vapor Pressure," Norwich, New York, Knovel.
- [79] Clarke, J. A., and Fray, D.J., 1979, "Oxidation of Zinc Vapour Hydrogen-Water Vapour Mixtures," *Trans. Inst. Min Metall. C*, **88**, pp. C161-C166.
- [80] Lewis, L.A., and Cameron, A.M., 1995, "Oxidation Kinetics of Zinc Vapor in $\text{CO}:\text{CO}_2$ Mixtures: Part I. Comparison with Past Literature," *Metall. Mater. Trans. B.*, **26B**, pp. 911-918.
- [81] Lewis, L.A., and Cameron, A.M., 1995, "Oxidation Kinetics of Zinc Vapor in $\text{CO}:\text{CO}_2$ Mixtures: Part II. Application of Plug Flow Concepts," *Metall. Mater. Trans. B.*, **26B**, pp. 919-924.
- [82] Osborne, J.M., Rankin, W.J., and McCarthy, D.J., 2001, "The Oxidation of Zinc Vapor in $\text{CO}-\text{CO}_2-\text{N}_2$ Gas Mixtures," *Metall. Mater. Trans. B*, **32B**, pp. 37-45.
- [83] Cox, A., and Fray, D.J., 2000, "Zinc Reoxidation in the Shaft of a Zinc-Lead Imperial Smelting Furnace-2: Zinc-Carbon-Oxygen System in Combination with Sinter and Coke Substrates," *Trans. Inst. Min. Metall. C*, **109**, pp. C105-C111.
- [84] Cox, A., and Fray, D.J., 2000, "Zinc Reoxidation in the Shaft of a Zinc-Lead Imperial Smelting Furnace-2: Zinc-Carbon-Oxygen System with Deposition Initiated on a Quartz Substrate and Subsequent Propagation on Zinc Oxide," *Trans. Inst. Min. Metall. C*, **109**, pp. C97-C104.
- [85] Cox, A., and Fray, D.J., 2003, "The Kinetics of the Oxidation of Zinc Vapour Carbon Dioxide and Water Vapour on Quartz, Zinc Oxide, Sinter and Coke Substrates," *Metall. Mater. Proc.: Principles and Technologies*, **1**, pp. 95-105.
- [86] Venstrom, L., 2012, "The Oxidation of Zinc Vapor and Non-stoichiometric Ceria by Water and Carbon Dioxide to Produce Hydrogen and Carbon Monoxide," Doctoral thesis, University of Minnesota.
- [87] Silberberg, M.S., 2003, "Chemistry: The Molecular Nature of Matter and Change," 3rd edition, New York, McGraw-Hill.
- [88] Venstrom, L., and Davidson, J.H., 2011, "Splitting Water and Carbon Dioxide via the Heterogeneous Oxidation of Zinc Vapor: Thermodynamic Considerations," *J. of Solar Energy Eng.*, **133**, 011017 (8 pages).

- [89] Nauman, E.B., 2008, "Chemical Reactor Design, Optimization, and Scaleup," Hoboken, N.J., Wiley.
- [90] Kaliakin, V.N., 2002, "Introduction to Approximate Solution Techniques, Numerical Modeling, and Finite Element Methods," New York, Marcel Dekker.
- [91] Barin, I., Knacke, O., 1973, "Thermochemical Properties of Inorganic Substances," Berlin, Springer-Verlag.
- [92] National Institute of Standards and Technology, "NIST Chemistry Webbook," <http://webbook.nist.gov/chemistry>.
- [93] Bird, R.B., Stewart, W.E., and Lighfoot, E. N., 2002, "Transport Phenomena, 2nd Edition," New York, John Wiley and Sons, Inc.
- [94] Muller, R., and Steinfeld, A., 2008, "H₂O-Splitting Thermochemical Cycle Based on ZnO/Zn-Redox: Quenching the Effluents from the ZnO Dissociation," *Chem. Eng. Sci.*, **63**, pp. 217 - 227.
- [95] Schwabl, F., 2006, "Statistical Mechanics, 2nd Ed.," Springer, Berlin, Heidelberg, New York.
- [96] Harris, S., 1999, "An Introduction to the Theory of the Boltzmann Equation," Dover Publications, Inc. Mineola, New York.
- [97] Succi, S., 2009, "The lattice Boltzmann equation for fluid dynamics and beyond," *Oxford Science Publications*, New York.
- [98] Dickerson, Richard E. and Gray, Harry B. and Haight, Gilbert P. 1979. "Chemical principles, Third edition" The Benjamin/Cummings Publishing Company, Inc. , Menlo Park, CA.
- [99] He, X., and Luo, L.-S., 1997, "A Priori Derivation of the Lattice Boltzmann Equation," *Physical Review E*, **55-6**, R6333 (4 pages).
- [100] He, X., Luo, L.-S., 1997, "Lattice Boltzmann model for the incompressible Navier-Stokes equation," *Journal of Statistical Physics*, **88**, pp. 927-944.
- [101] Lallemand, P., and Luo, L.-S., 2000, "Theory of the lattice Boltzmann Method: Dispersion, Dissipation, Isotropy, Galilean Invariance, and Stability," NASA/CR-2000-210103, ICASE Report No. 2000-17.
- [102] Lallemand, P., Luo, L., 2002, "Lattice Boltzmann method for moving boundaries," *Journal of Computational Physics*, **184**, pp. 406-421.
- [103] Yoshida, H. and Nagaoka, M., 2010, "Multiple-relaxation-time lattice Boltzmann model for the convective anisotropic diffusion equation," *Journal of Computational Physics*, **229**, pp. 7774-7795.

- [104] Li, L., Mei, R., and Klausner, J. F., 2013, “Boundary conditions for thermal lattice Boltzmann equation method,” *Journal of Computational Physics*, **237**, pp. 366-395.
- [105] Liu, C.-H., Lin, K.-H., Mai, H.-C., Lin, C.-A., 2010, “Thermal boundary conditions for thermal lattice Boltzmann simulations,” *Computers and Mathematics with Applications*, **59**, pp. 2178-2193.
- [106] Cui, S., Hong, N., Shi, B., and Chai, Z., 2016, “Discrete Effect on the Halfway Bounce-back Boundary Condition of Multiple-relaxation-time Lattice Boltzmann Model for Convective-diffusion Equations,” *Physical Review E*, **93**, 043311 (13 pages).
- [107] Chai, Z., and Zhao, T.S., 2014. “Nonequilibrium Scheme for Computing the Flux of the Convective-diffusion Equation in the Framework of the Lattice Boltzmann Method,” *Physical Review E*, **90**, 013305 (15 pages).
- [108] Zhou, J. G., 2011, “Axisymmetric lattice Boltzmann method revised,” *Physical Review E*, **84**, 036704 (10 pages).
- [109] Li, L., Mei, R., and Klausner, J. F., 2013, “Multiple-relaxation time lattice Boltzmann model for axisymmetric convection diffusion equation,” *International Journal of Heat and Mass Transfer*, **67**, pp. 338-351.
- [110] He, X., Chen, S. and Doolen, G.D., 1998, “A Novel Thermal Model for the Lattice Boltzmann Method in Incompressible Limit,” *Journal of Computational Physics*, **146**, pp. 282-300.
- [111] Li, Y., and Shan, X., 2011, “Lattice Boltzmann method for adiabatic acoustics,” *Philosophical Transactions of the Royal Society-A*, **369**, pp. 2371-2380.
- [112] He, X., and Li, N., 2000, “Lattice Boltzmann simulation of electrochemical systems,” *Computer Physics Communications*, **129**, pp. 158-166.
- [113] Parmigiani, A, Huber, C., Chopard, B., Latt, J., and Bachmann, O., 2009, “Application of the multi distribution function lattice Boltzmann approach to thermal flows,” *The European Physical Journal-Special Topics*, **171**, pp. 37-43.
- [114] Chai, Z., Zhao T.S. 2013, “Lattice Boltzmann model for the convective-diffusion equation,” *Physical Review E*, **83**, 063309 (15 pages).
- [115] Kang, Q., Zhang, D., Lichtner, P.C., Tsimpanogiannis, I.N., 2004, “Lattice Boltzmann model for crystal growth from supersaturated solution,” *Geophysical Research Letters*, **31**, pp. L21604.
- [116] Lu, G., Depaolo, D.J., Kang, Q., Dong, Z., 2009, “Lattice Boltzmann simulation of snow crystal growth in clouds,” *Journal of Geophysical Research*, **114**, pp. D07305.

- [117] Kang, Q., Lichtner, P.C., Viswanathan, H.S., Abdel-Fattah, A.I., 2010, "Pore scale modeling of reactive transport involved in geologic CO₂ sequestration," *Transport in Porous Media*, **82**, pp. 197-213.
- [118] Sergi, D., Grossi, L., Leidi, T., and Ortona, A., 2014, "Surface growth effects on reactive capillary-driven flow: Lattice Boltzmann investigation," *Engineering Applications of Computational Fluid Mechanics*, **8-4**, pp. 549-561.
- [119] Harrison, S.E., Smith, S.M., Bernsdorf, J., Hose, D.R., Lawford, P.V., 2007, "Application and validation of the lattice Boltzmann method for modeling flow-related clotting," *Journal of Biomechanics*, **40**, pp. 3023-3028.
- [120] Huang, R., Wu, H., 2014, "An immersed boundary lattice-Boltzmann method for solid-liquid phase change," *Journal of Computation Physics*, **277**, pp. 305-319.
- [121] Hawkins, C., Angeluta, L., Hammer, O., and Jamtveit, B., 2013, "Precipitation dendrites in channel flow," *Euro. Phys. Letters*, **102**, 54001 (6 pages).
- [122] Zou, Q., He, X., 1997, "On pressure and velocity boundary conditions for the lattice Boltzmann BGK model," *Physics of Fluids*, **9**, pp. 1591- 1598.
- [123] Premnath, K. N. and Abraham, J., 2005, " Lattice Boltzmann Model for Axisymmetric Multiphase Flows," *Phys. Rev. E*, **71**, 056706 (14 pages).
- [124] Reis, T. and Phillips, T.N., 2008, "Numerical Validation of a Consistent Axisymmetric Lattice Boltzmann Model," *Physical Review E*, **77**, 026703 (6 pages).
- [125] Li., X., Huang, H. and Meakin, P., 2010, "A three-dimensional level set simulation of coupled reactive transport and precipitation/dissolution," *International Journal of Heat and Mass Transfer*, **53**, pp. 2908-2923.
- [126] Huang, R. and Wu, H., 2014, "An immersed boundary-thermal lattice Boltzmann method for solid-liquid phase change," *Journal of Computational Physics*, **277**, pp. 305-319.
- [127] Guo, Z., Zheng, C., Shi, B., 2002, "An extrapolation method for boundary conditions in lattice Boltzmann method," *Physics of Fluids*, **14-6**, pp. 2007-2010.
- [128] Uchida, S., and Aoko, H., 1977, "Unsteady flows in a semi-infinite contracting or expanding pipe," *Journal of Fluid Mechanics*, **32**, pp. 371-387.
- [129] Langlois, W.E., Deville, M.O., 1964., "Slow Viscous Flow," Macmillian.
- [130] Lindemer, M.D., Advani, S.G., and Prasad, A.K., 2016, "Experimental Investigation of Heterogeneous Hydrolysis of Zn Vapor Under a Temperature Gradient," *Int. J. of Hydrogen Energy*, accepted
- [131] Whittemore, O.J., and Varela, J.A., 1981, "Initial Sintering of ZnO," *J. Amer. Ceram. Soc.*, **64**(11), pp. C154-C155.

- [132] Weibel, D., 2016, “The Reaction of Particulate Zn-ZnO Mixtures with CO₂ and H₂O for the Production of CO and H₂,” Doctoral thesis, ETH Zurich.
- [133] Tringe, J.W., Levie, H.W., El-Dasher, B.S., Swift, R., and Wall, M.A., 2011, “In situ Observation of the Formation of Hollow ZnO Shells,” *Applied Physics Letters*, **98**, 241907 (3 pages).
- [134] Yoshida, H. Kobayashi, T., Hayahsi, H. Kinjo, T., Washizu, H. and Fukuzawa, K., 2014, “Boundary Condition at a Two-phase Interface in the Lattice Boltzmann Method for the Convection-diffusion Equation,” *Physical Review E*, **90**, 013303 (10 pages).
- [135] Bao, J. and Schaefer, L., 2013, “Lattice Boltzmann Equation Model for Multi-component Multi-phase Flow with High Density Ratios,” *Applied Mathematical Modeling*, **37**, pp. 1860-1871.
- [136] Asinari, P., 2009, “Lattice Boltzmann Scheme for Mixture Modeling: Analysis of the Continuum Diffusion Regimes Recovering Maxwell-Stefan Model and Incompressible Navier-Stokes Equations,” *Physical Review E*, **80**, 056701 (15 pages).
- [137] Ladd, A.J.C., 2015, “Lattice-Boltzmann Method for Suspensions of Solid Particles,” *Molecular Physics*, **113**, pp. 2531-2537.
- [138] Agrafiotis, C., Roeb, M., and Sattler, C., 2016, “A Review on Solar Thermal Syngas Production via Redox-pair-based Water/Carbon Dioxide Splitting Thermochemical Cycles,” *Renewable and Sustainable Energy Reviews*, **42**, pp. 254-285.
- [139] Krenzke, P.T. and Davidson, J.H., 2015, “On the Efficiency of Solar H₂ and CO Production via the Thermochemical Cerium Oxide Redox Cycle: The Option of Inert- Swept Reduction” *Energy and Fuels*, **29**, pp. 1045-1054.
- [140] McDaniel, A.H., Amborisni, A., Coker, E.N., Miller, J.E., Cheuh, W.C., O’Hayre, R. and Tong, J., 2014, “Nonstoichiometric Perovskite Oxides for Solar Thermochemical H₂ and CO Production,” *Energy Procedia*, **49**, pp. 2009 - 2018.
- [141] Scheffe, J.R., Li, J., and Weimer, A.W., 2010, “A Spinel Ferrite/Hercynite Water-splitting Redox Cycle,” *International Journal of Hydrogen Energy*, **35**, pp. 3333-3340.
- [142] Michalsky, R., Botu, V., Hargus, C.M., Peterson, A.A., and Steinfeld, A., 2015, “Design Principles for Metal Oxide Redox Materials for Solar-Driven Isothermal Fuel Production,” *Advanced Energy Materials*, **5**, 1401082 (10 pages).
- [143] Michalsky, R., Pfromm, P.H., and Steinfeld, A., 2015, “Rational Design of Metal Nitride Redox Materials for Ammonia Synthesis,” *Royal Society Interface Focus*, **5**, 20140084 (10 pages).

- [144] Ezbiri, M., Allen, K.M., Galvez, M.E., Michalsky, R. and Steinfeld, A., 2015, "Design Principles of Perovskites for Thermochemical Oxygen Separation," *ChemSusChem*, **8**, pp. 1966-1971.
- [145] Muhich, C.L., Evanko, B.W., Weston, Kayla C., Lichty, P. Liang, X., Martinek, J., Musgrave, C.B., and Weimer, A.W., 2013, "Efficient Generation of H₂ by Splitting Water with an Isothermal Redox Cycle," *Science*, **341**-6145, pp. 540-542.
- [146] Ermanoski, I., Miller, J.E., and Allendorf, M.D., 2014, "Efficiency Maximization in Solar Thermochemical Fuel Production: Challenging the Concept of Isothermal Water-splitting," *Physical Chemistry Chemical Physics*, **16**, 8418 (10 pages).
- [147] Ermanoski, I., Grobbel, J., Singh, A., Lapp, J. Brendelberger, S., Roeb, M., Sattler, C., Whaley, J., McDaniel, A., and Siegel, N. P., 2016, "Design and Construction of a Cascading Pressure Reactor Prototype for Solar- Thermochemical Hydrogen Production," *AIP Conference Proceedings*, **1734**, 120001 (8 pages).
- [148] Hathaway, B.J., Bala Chandran, R., Sedler, S. Thomas, D., Gladen, A., Chase, T., and Davidson J.H., 2016, "Effect of Flow Rates on Operation of a Solar Thermochemical Reactor for Splitting CO₂ Via the Isothermal Ceria Redox Cycle," *Journal of Solar Energy Engineering*, **138**, 011007 (12 pages).
- [149] Acheson, D.J., 2010, "Elementary Fluid Dynamics," Oxford University Press, Milton Keynes, UK.
- [150] He, X., Zou Q., Luo, L.-S., and Dembo, M., 1997, "Analytic solutions of simple flows and analysis of nonslip boundary conditions for the lattice Boltzmann BGK model," *J. Stat. Phys.*, **87**, pp. 115-136.
- [151] Elsevier Author and User Rights. https://www.elsevier.com/__data/assets/pdf_file/0007/55654/AuthorUserRights.pdf.

Appendix A

**ADDITIONAL DESIGN DETAILS FOR LABORATORY-SCALE
HYDROLYSIS REACTOR**

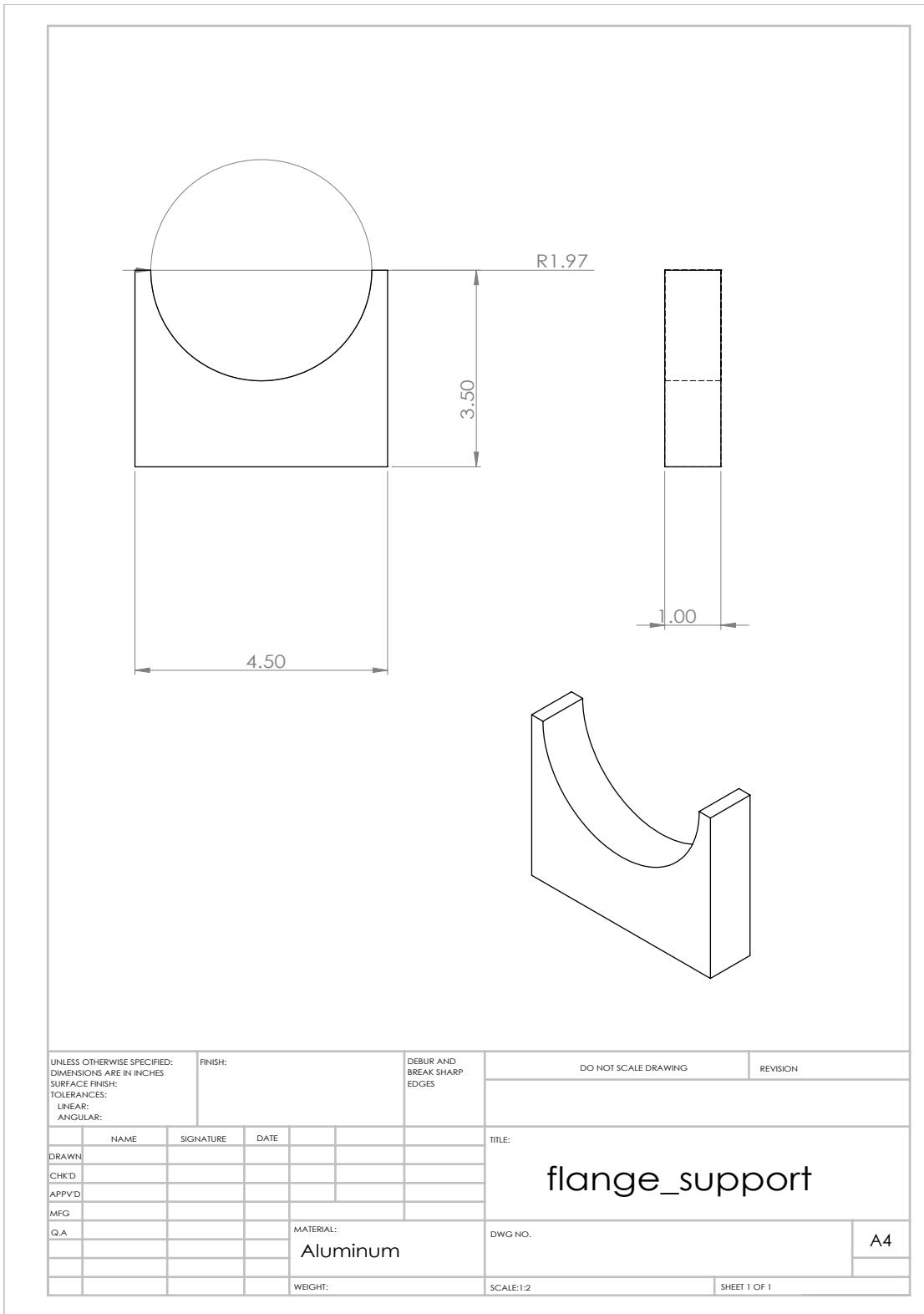


Figure A.1: Technical drawing of flange support.

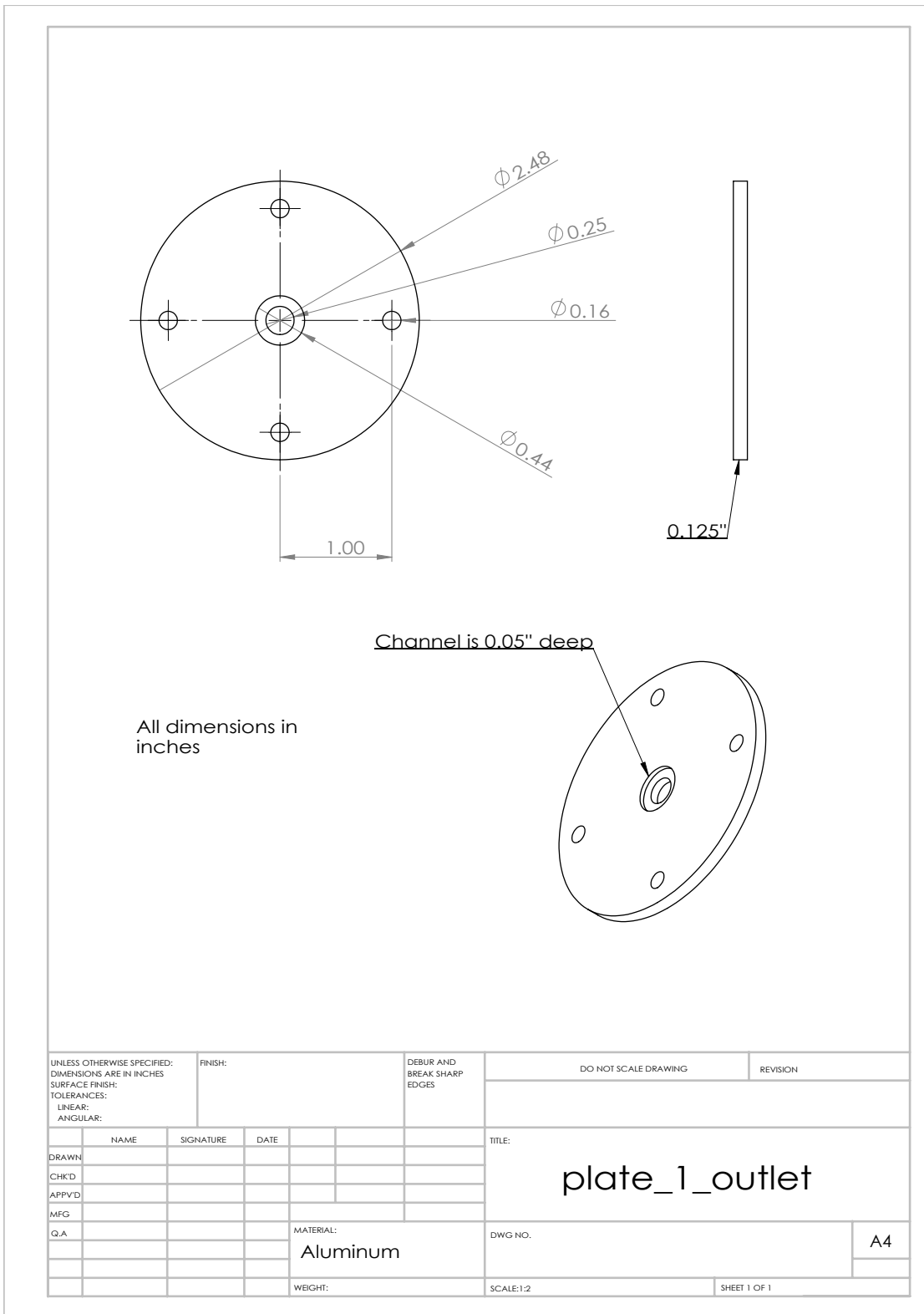


Figure A.2: Technical drawing of plate 1 (outlet).

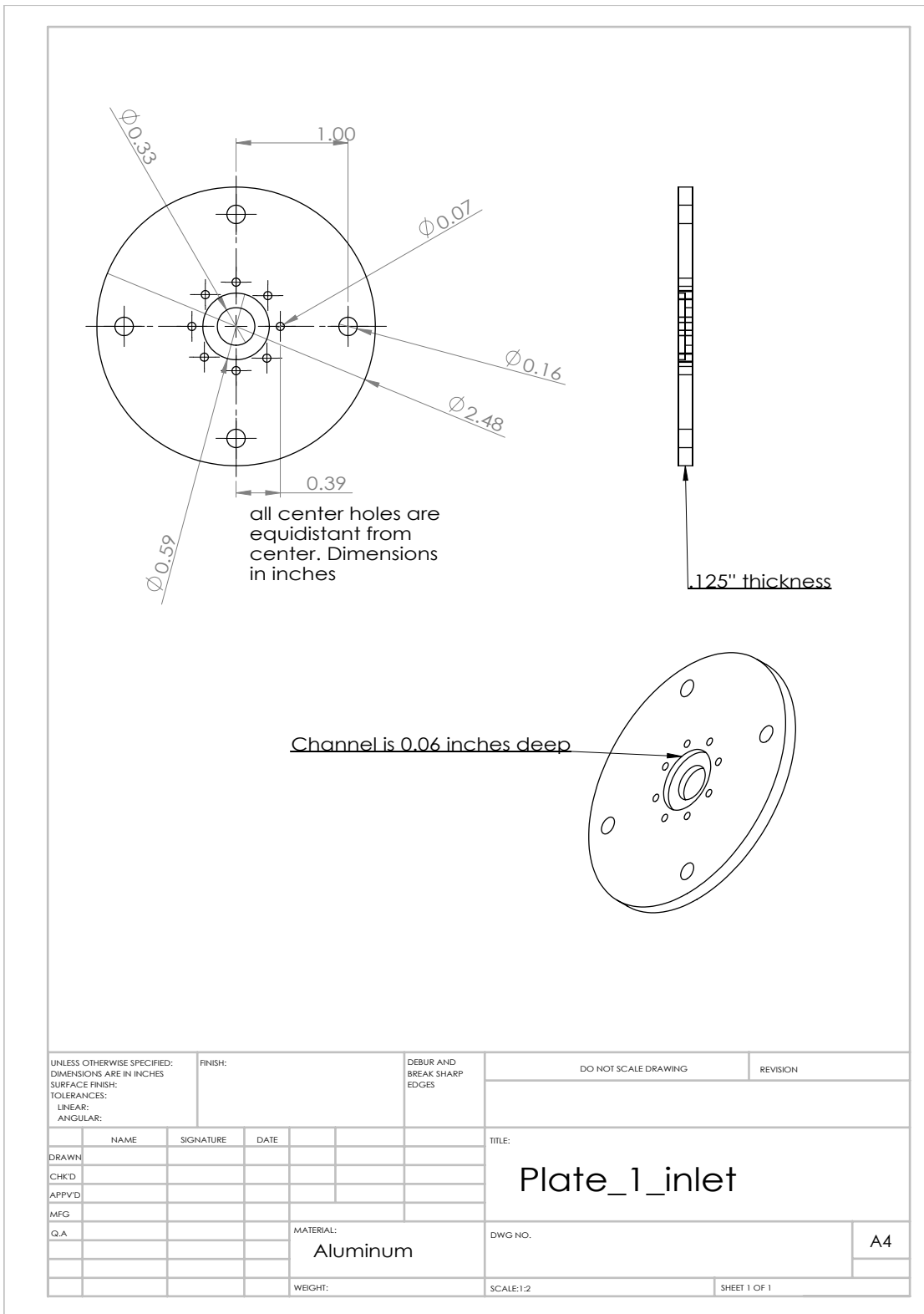


Figure A.3: Technical drawing of plate 1 (inlet).

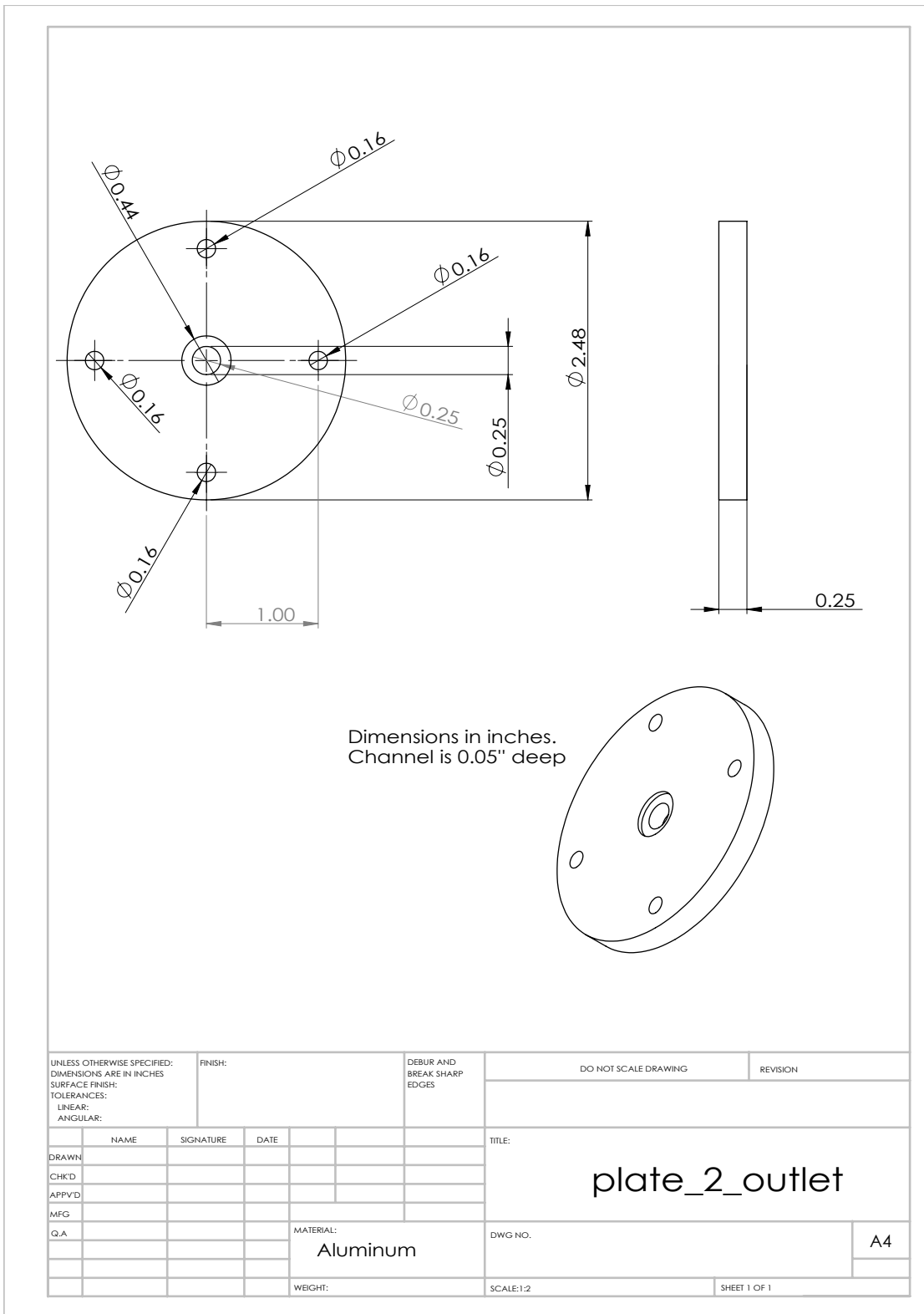


Figure A.4: Technical drawing of plate 2 (outlet).

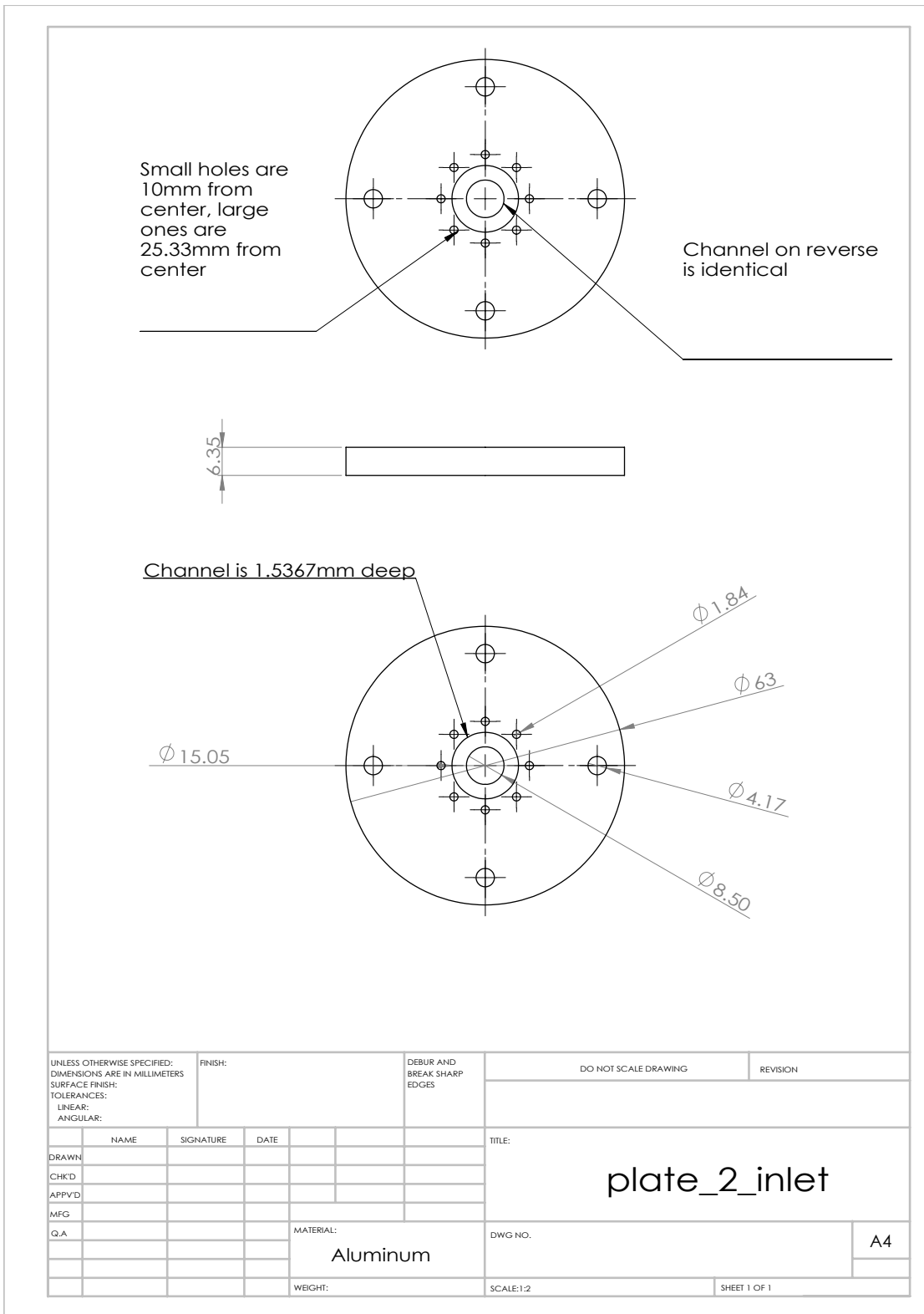


Figure A.5: Technical drawing of plate 2 (inlet).

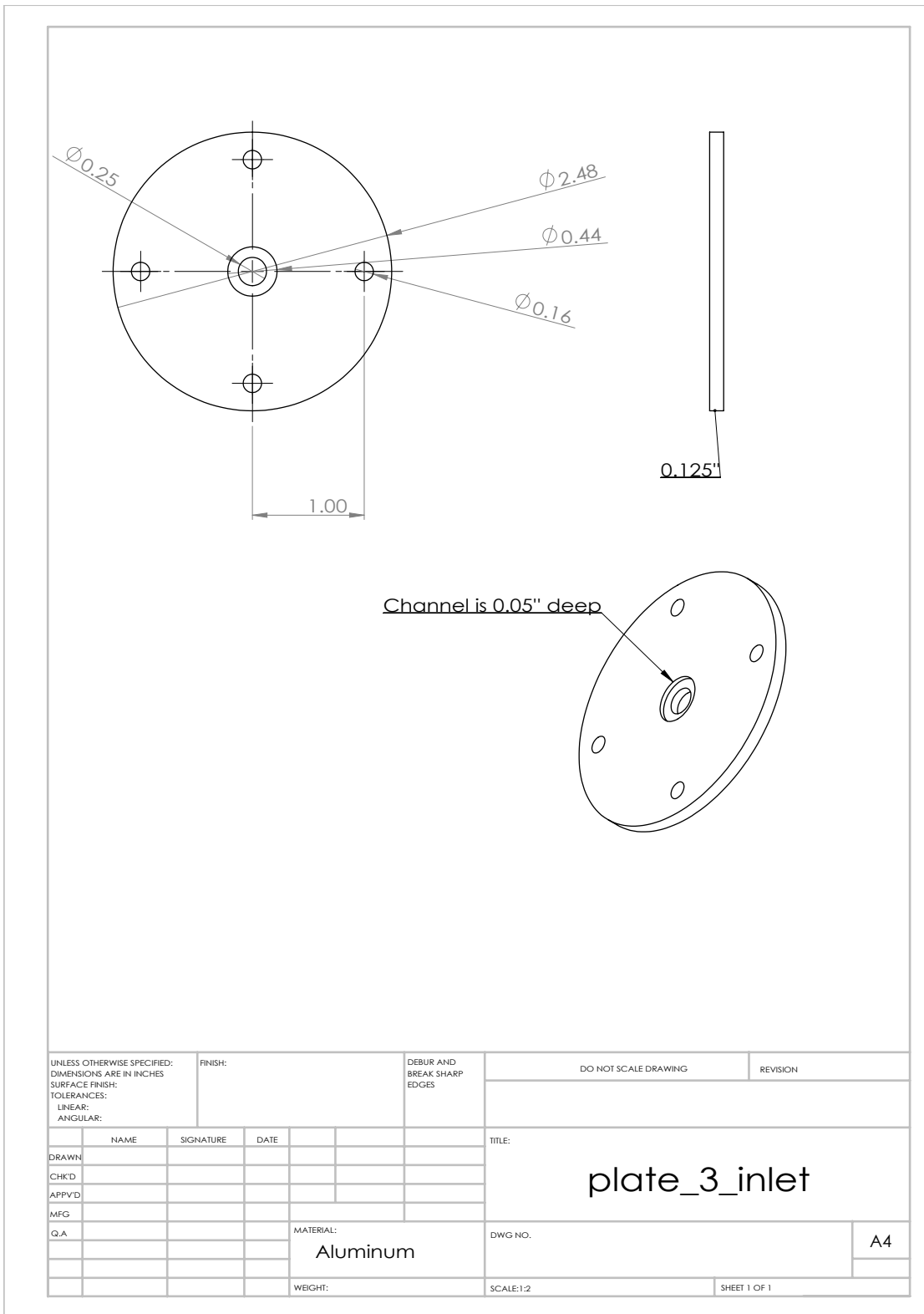


Figure A.6: Technical drawing of plate 3 (outlet).

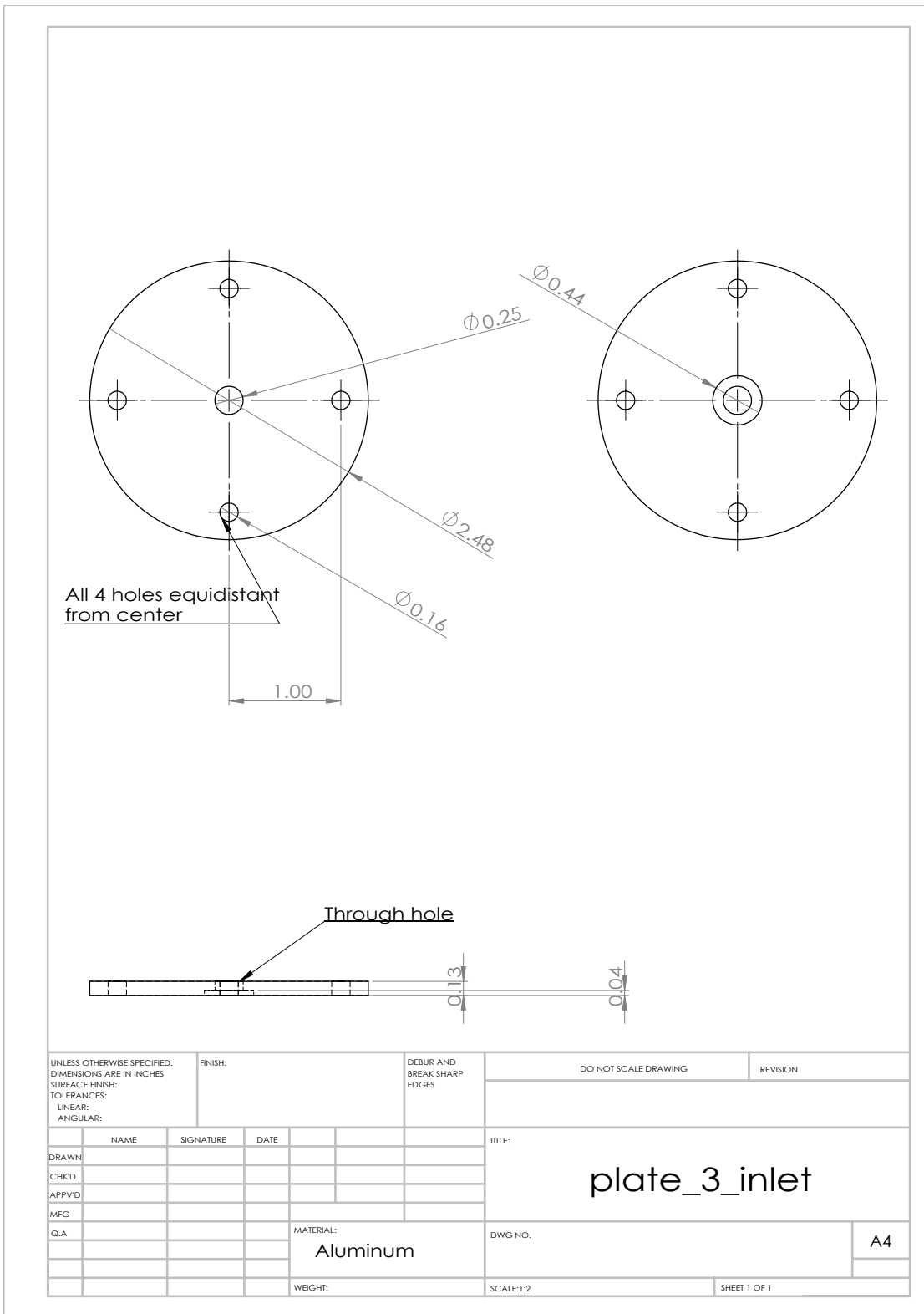


Figure A.7: Technical drawing of plate 3 (inlet).

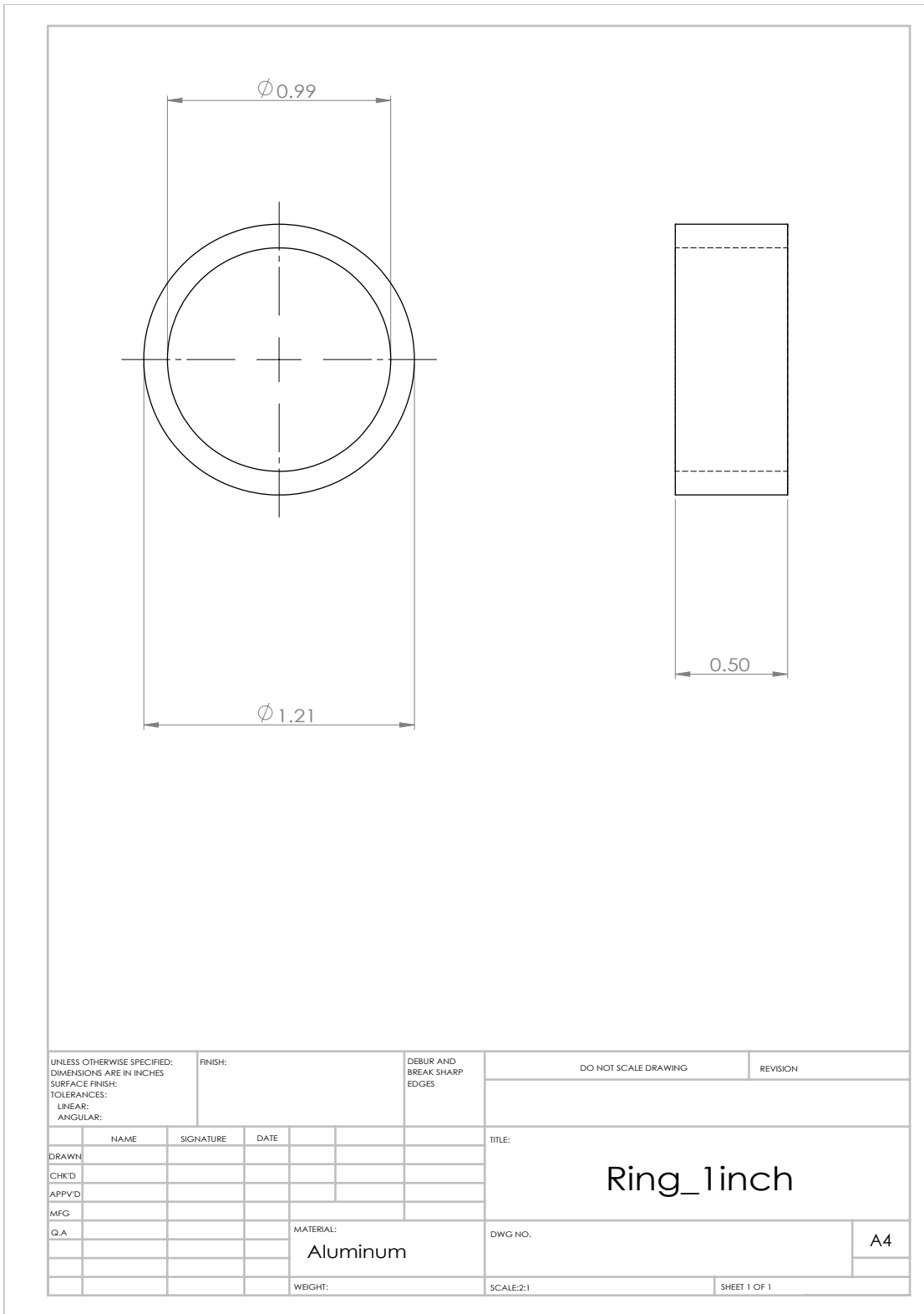


Figure A.8: Technical drawing of pressing ring.

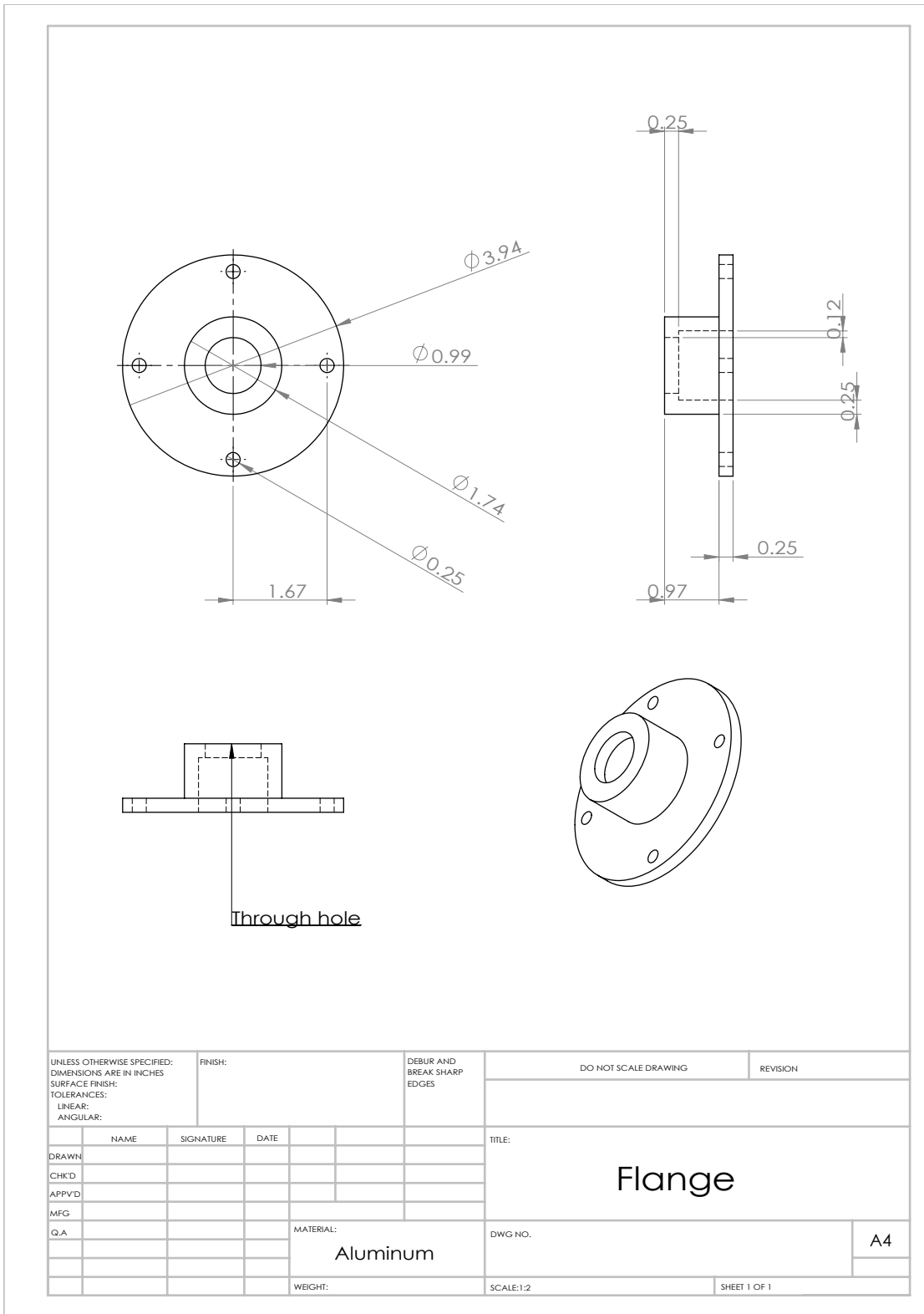


Figure A.9: Technical drawing of flange.

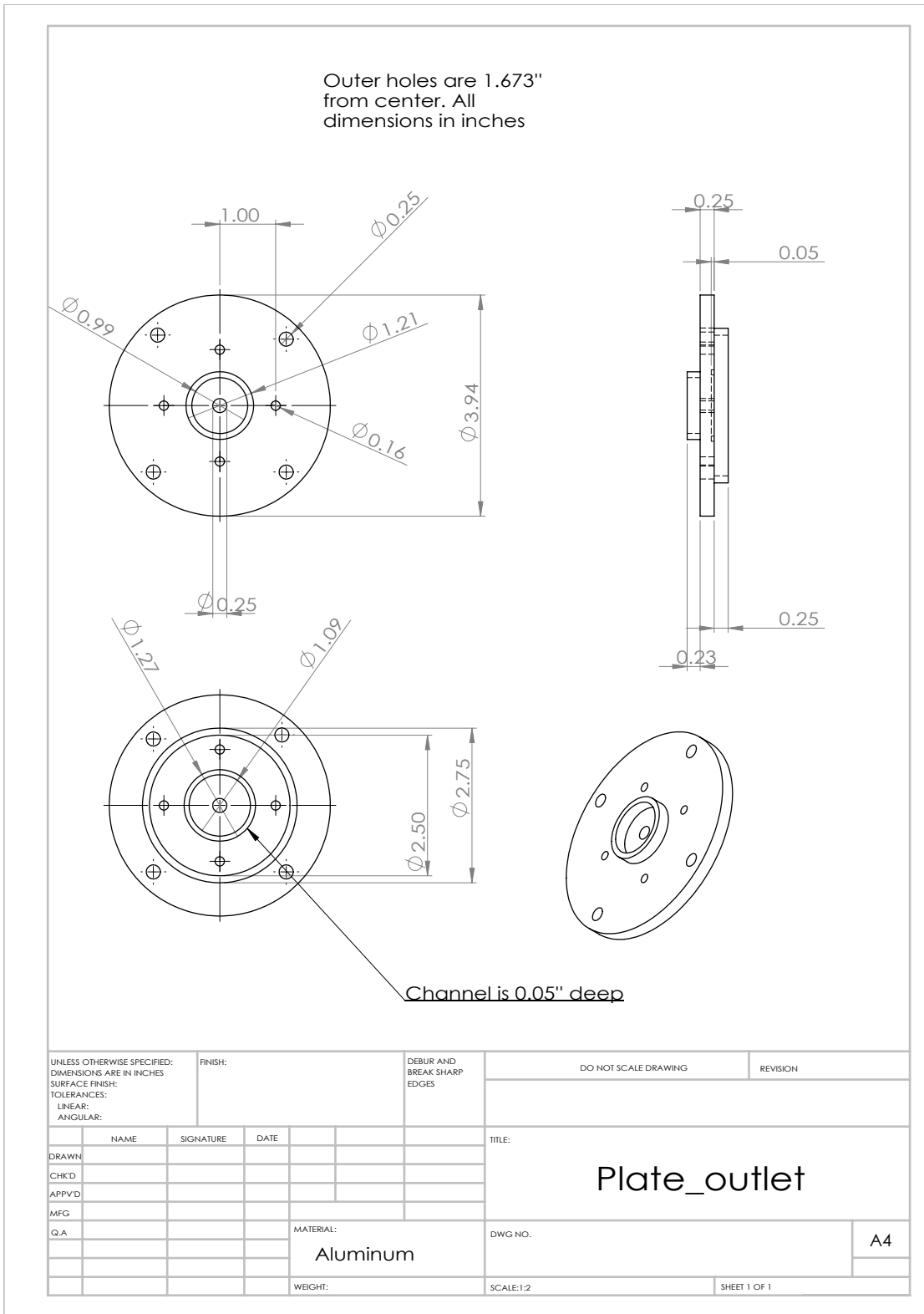


Figure A.10: Technical drawing of outlet plate.

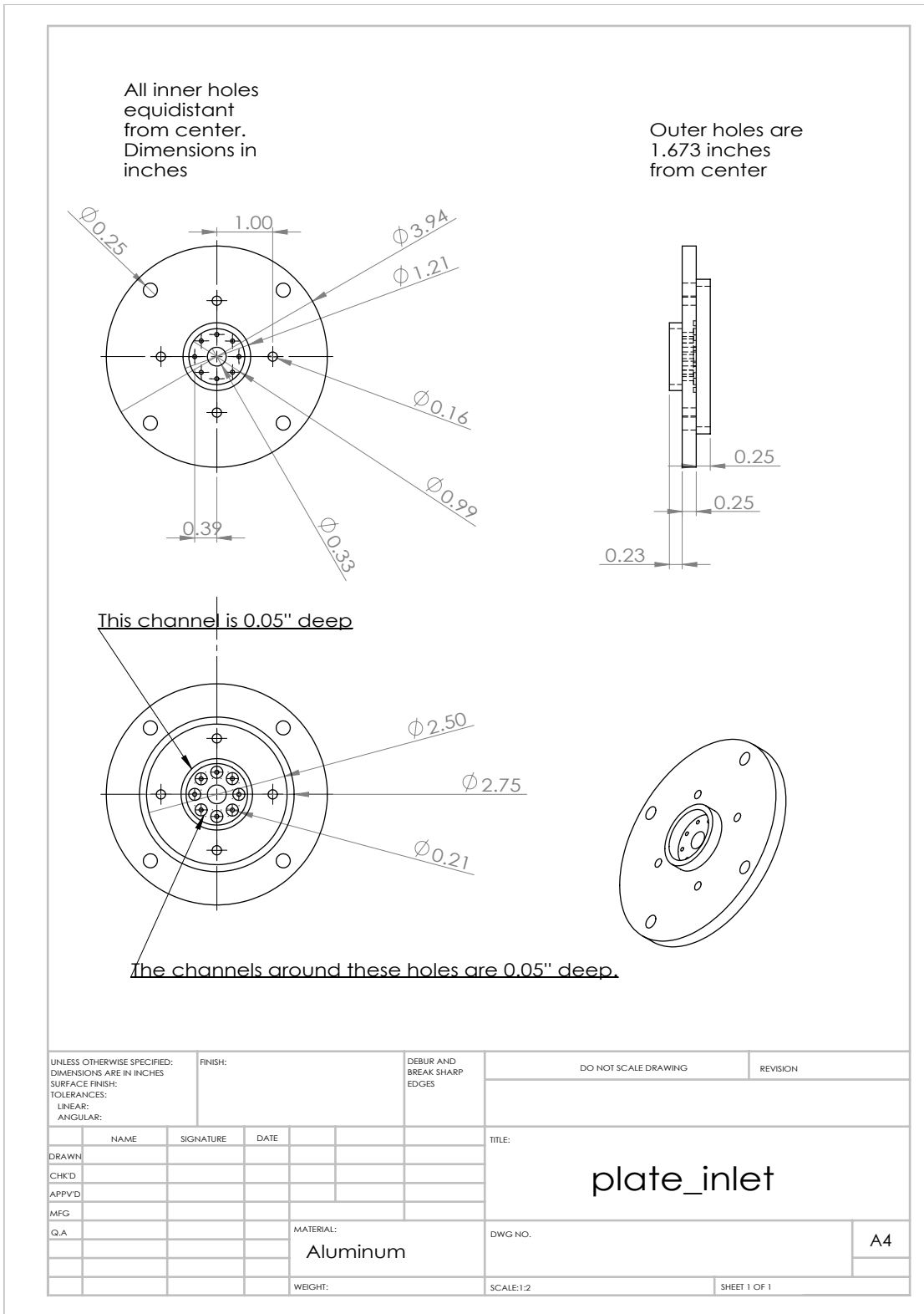


Figure A.11: Technical drawing of inlet plate.

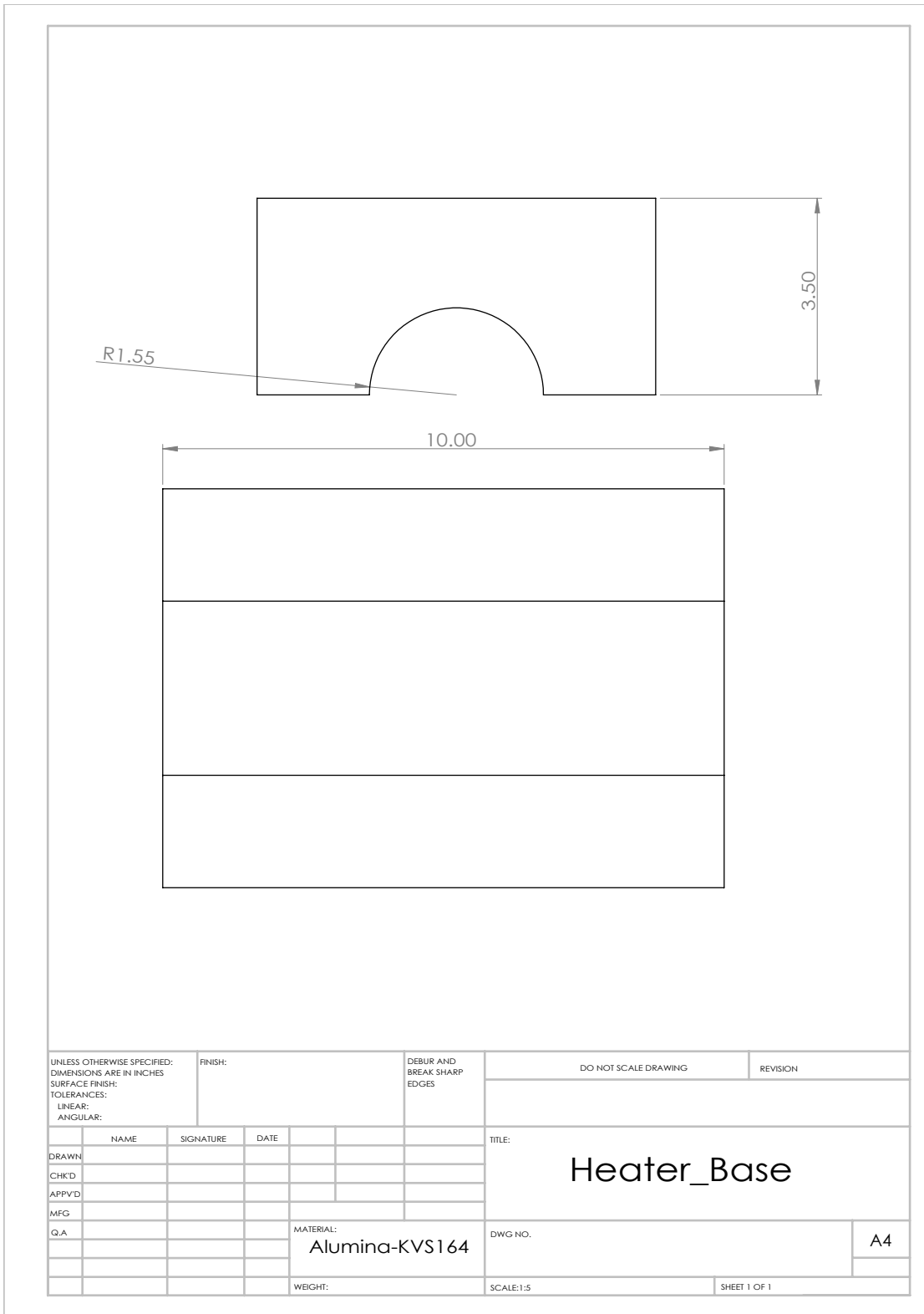


Figure A.12: Technical drawing of heater base.

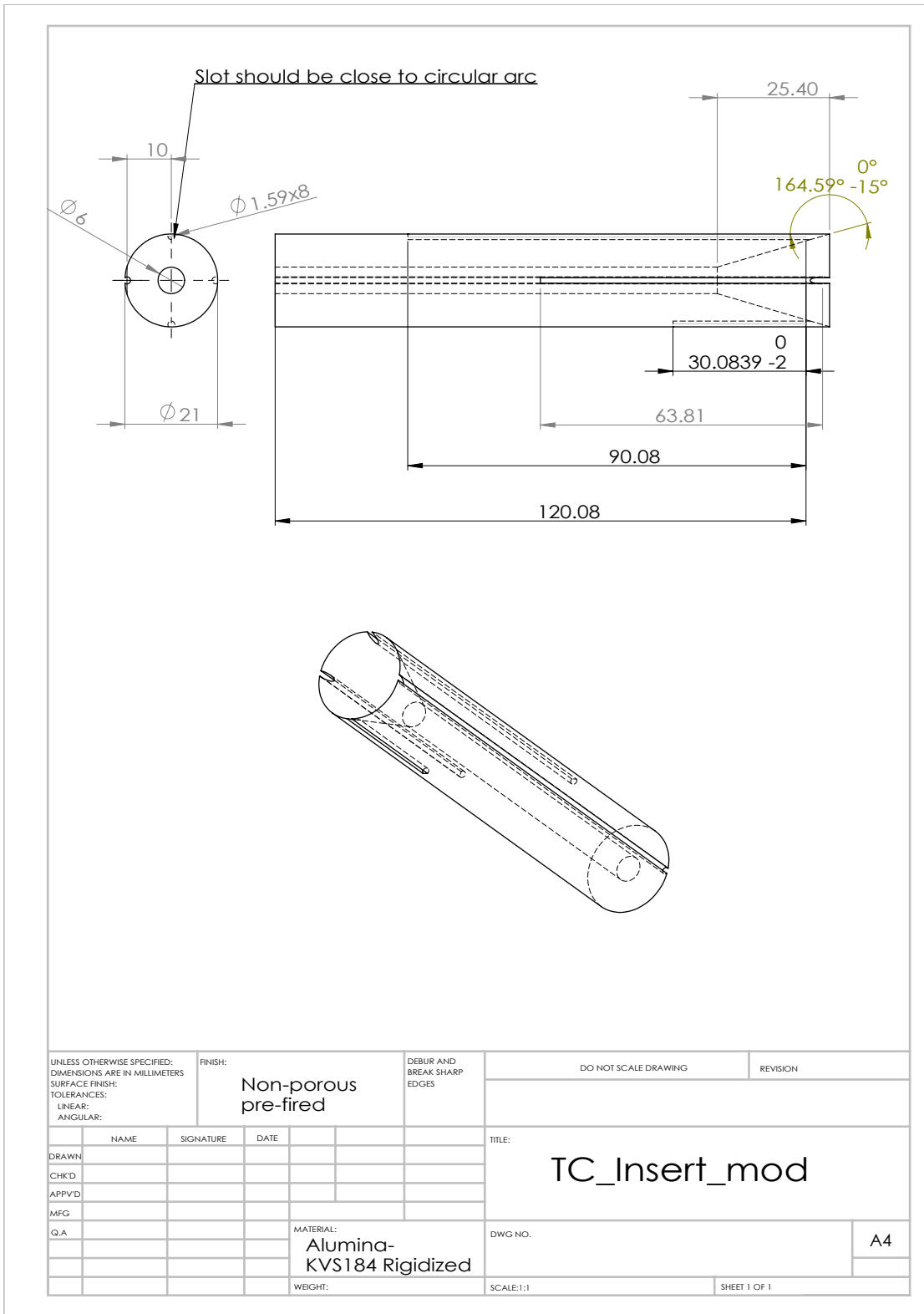


Figure A.13: Technical drawing of thermocouple insert.

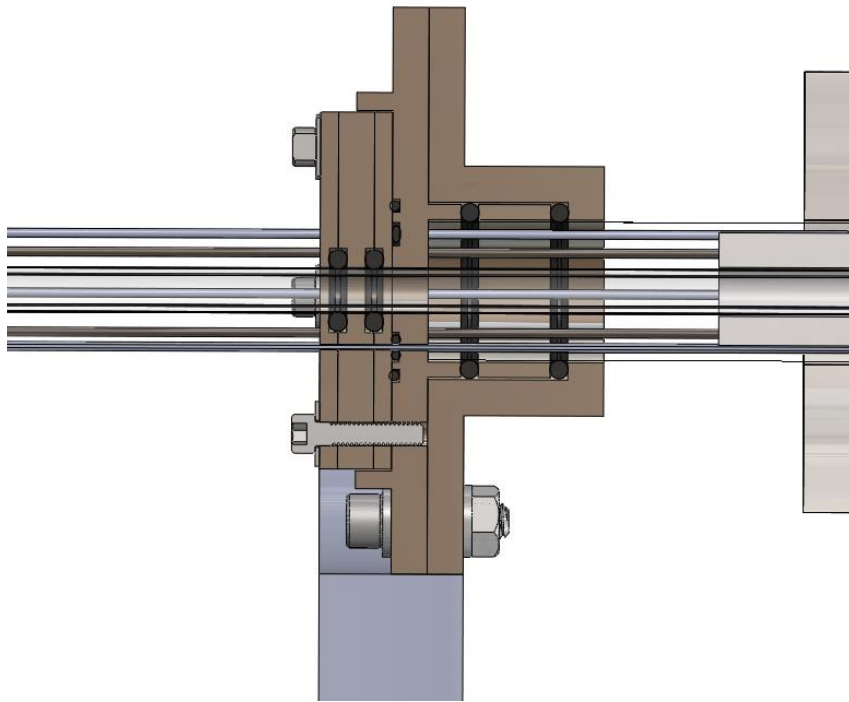


Figure A.14: Cross-section of entrance sealing assembly.

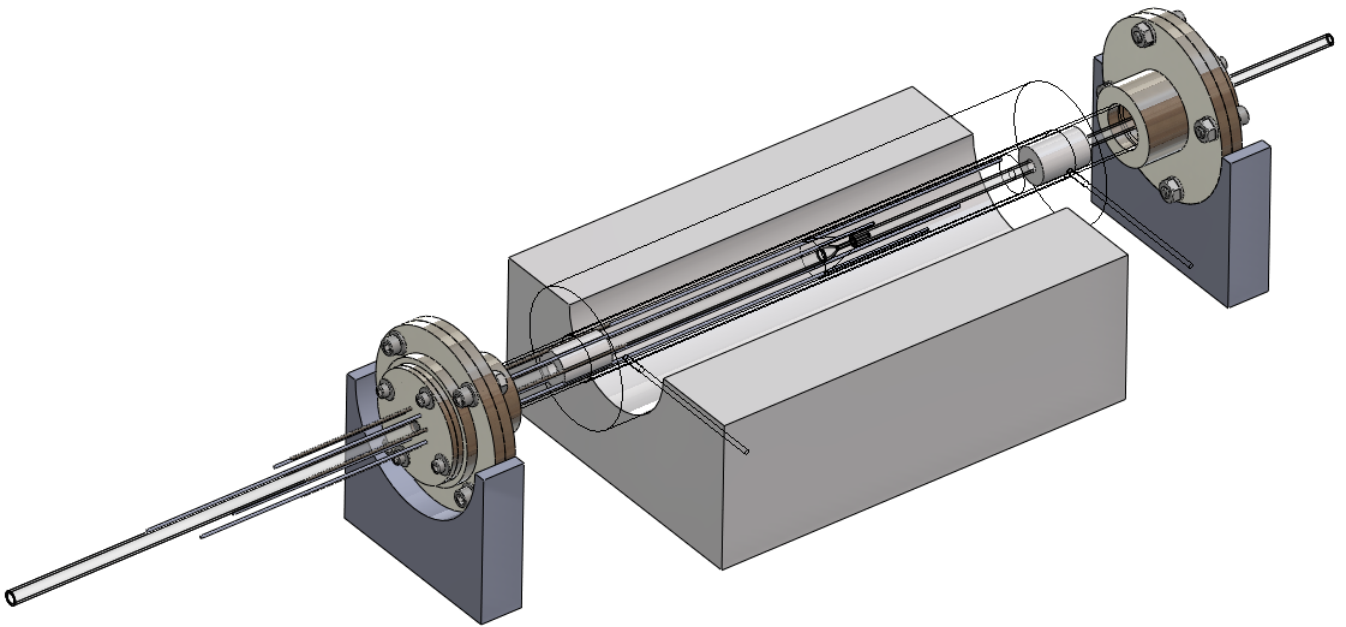


Figure A.15: Assembled reactor with heater made transparent.

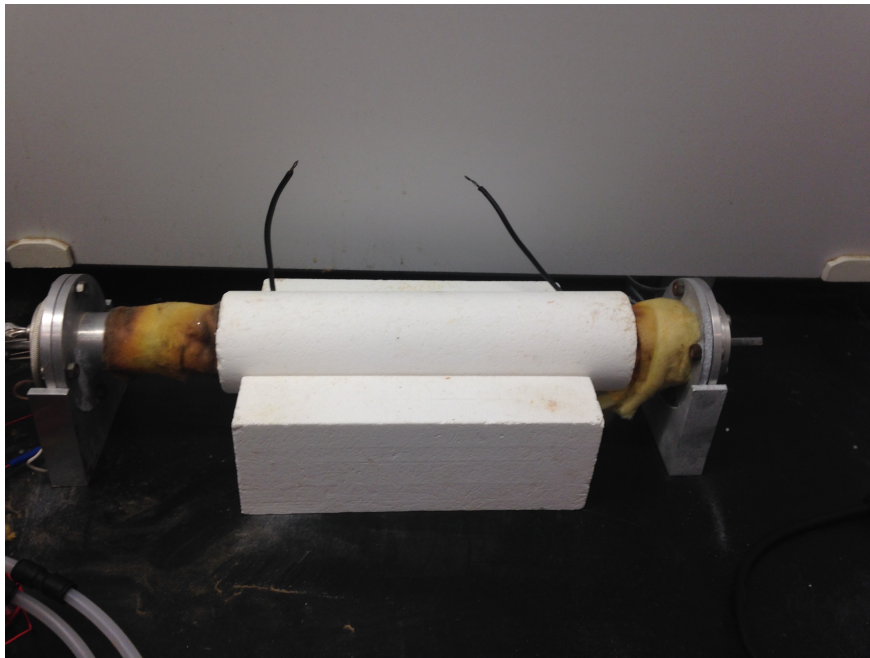


Figure A.16: View of assembled laboratory-scale hydrolysis reactor. Insulation has been removed from sealing assemblies at inlet and outlet.

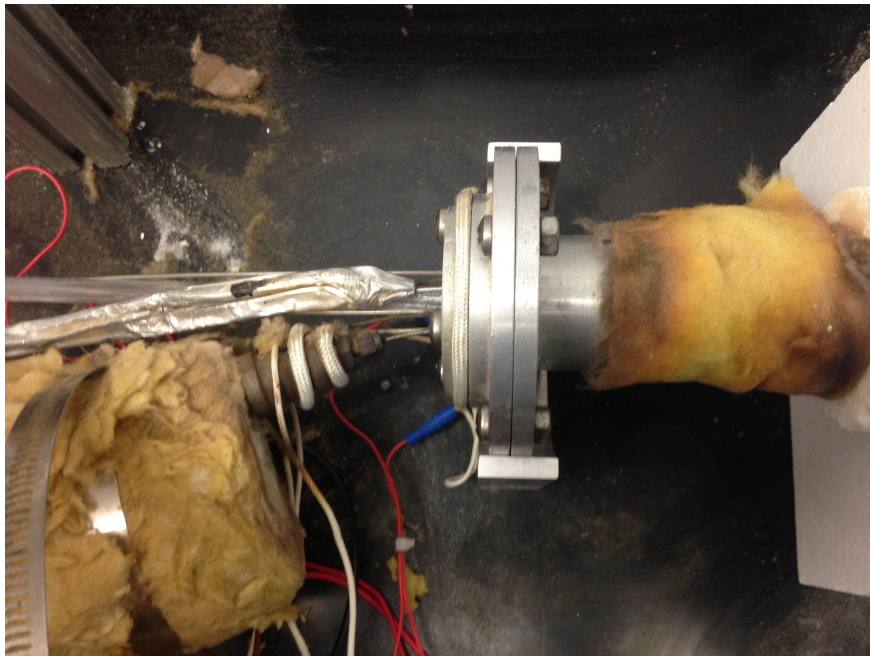


Figure A.17: Inlet sealing assembly. Steam enters from boiler, on bottom left, with inert gas flows enter just above. Heating tape has been wrapped around these components, as well as the entrance sealing assembly.

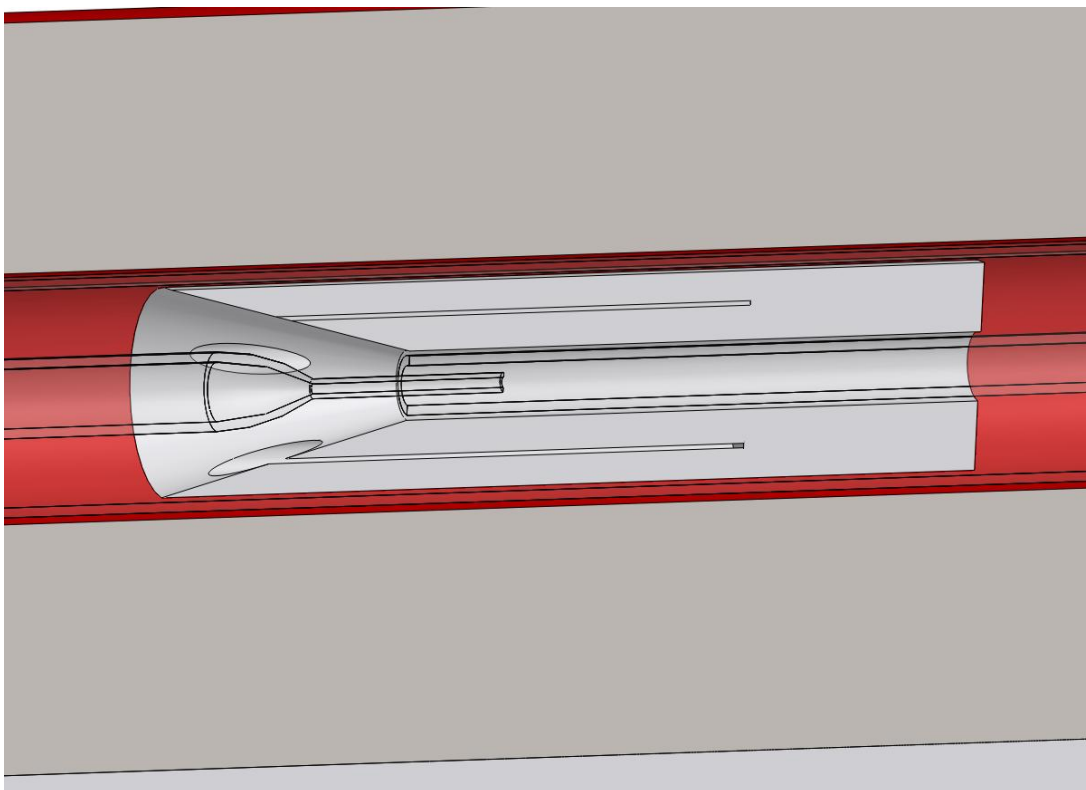


Figure A.18: Rendering of mating of Zn tube (left) and reaction tube (right), with TC insert surrounding both. Steam flows in the narrow annular region between the tapered end of the Zn tube and the reaction tube.

Appendix B

LATTICE BOLTZMANN PROGRAMMING GUIDE

This section will briefly explain a general programming strategy for the LBM, as well as explain the method used for the simulations in this work.

B.1 General Programming Approach

The first consideration is defining the objects in memory that are necessary for the simulation. The required matrices for a D2Q9 model of size $N_x \times N_y$ are:

- The distribution function f , a $9 \times N_x \times N_y$ matrix
- The equilibrium distribution function f^{eq} , a $9 \times N_x \times N_y$ matrix
- Fluid density ρ , a $N_x \times N_y$ matrix
- Hydrodynamic velocities u, v both $N_x \times N_y$ matrices

Other parameters such as the sound speed, average density, and relaxation time must also be defined as scalars.

The general algorithm for the LBM can be divided into a few main subroutines. For a single timestep, the algorithm for a simple flow, i.e., flow in channel, can be written as:

1. Collision

- At each node, and for each population a , change the value of f_a according to the BGK (or MRT) collision step

$$\hat{f}_a(\vec{x}, t) = f_a(\vec{x}, t) - \frac{1}{\tau}(f_a(\vec{x}, t) - f_a^{eq}(t)) \quad (\text{B.1})$$

2. Streaming

- At each node, and for each population a , stream the value of f_a to the nearest-neighbor point according to the velocity \vec{e}_a .

$$f_a(\vec{x} + \vec{e}_a \delta t, t + \delta t) = \hat{f}_a(\vec{x}, t) \quad (\text{B.2})$$

3. Boundary Conditions

- Along nodes adjacent to the solid boundaries, i.e., at $j = 1, j = N_y$, perform the bounce-back on the outgoing populations f_a to determine the values of the unknown populations $f_{\bar{a}}$ from outside of the fluid domain.

$$\hat{f}_{\bar{a}}(\vec{x}_f, t) = \hat{f}_a(\vec{x}_f, t) \quad (\text{B.3})$$

- At the horizontal boundaries i.e., $i = 1, i = N_x$, apply either periodic boundary conditions or pressure/velocity inlet/outlet conditions, depending on the problem.

4. Equilibrium

- At each node, calculate the fluid density ρ and hydrodynamic velocities u, v .

$$\rho = \sum_a f_a \quad (\text{B.4})$$

$$\rho \vec{u} = \sum_a \vec{e}_a f_a \quad (\text{B.5})$$

- Using these values, calculate the equilibrium distributions for each population f_a^{eq} .

$$f_a^{eq} = w_i \rho \left(1 + \frac{3\vec{e}_a \cdot \vec{u}}{c^2} + \frac{9(\vec{e}_a \cdot \vec{u})^2}{2c^4} - \frac{3\vec{u} \cdot \vec{u}}{2c^2} \right) \quad (\text{B.6})$$

For problems with more complicated geometries, or with particles suspended in the flow, it may also be useful to include a “phase field” array, i.e., an array which is 0 for fluid nodes and 1 for solid nodes. Then an additional subroutine can be added to update this value as the boundaries or particles move. It is then only necessary to complete the above subroutines on nodes which are defined as fluid, and can be skipped for solid nodes.

B.2 Programming for Gas/solid Reactive Precipitation Model

The code used in this work is based on the general algorithm presented above, however with additional modifications. The algorithm for the mass transfer is the same as that for the flow, hence each of the steps in the algorithm are simply repeated for the mass transfer model. There are also additional subroutines which move the the location of the solid boundary, then detect the new boundaries and calculate the distances from each boundary node, and other functions which are necessary for this particular problem.

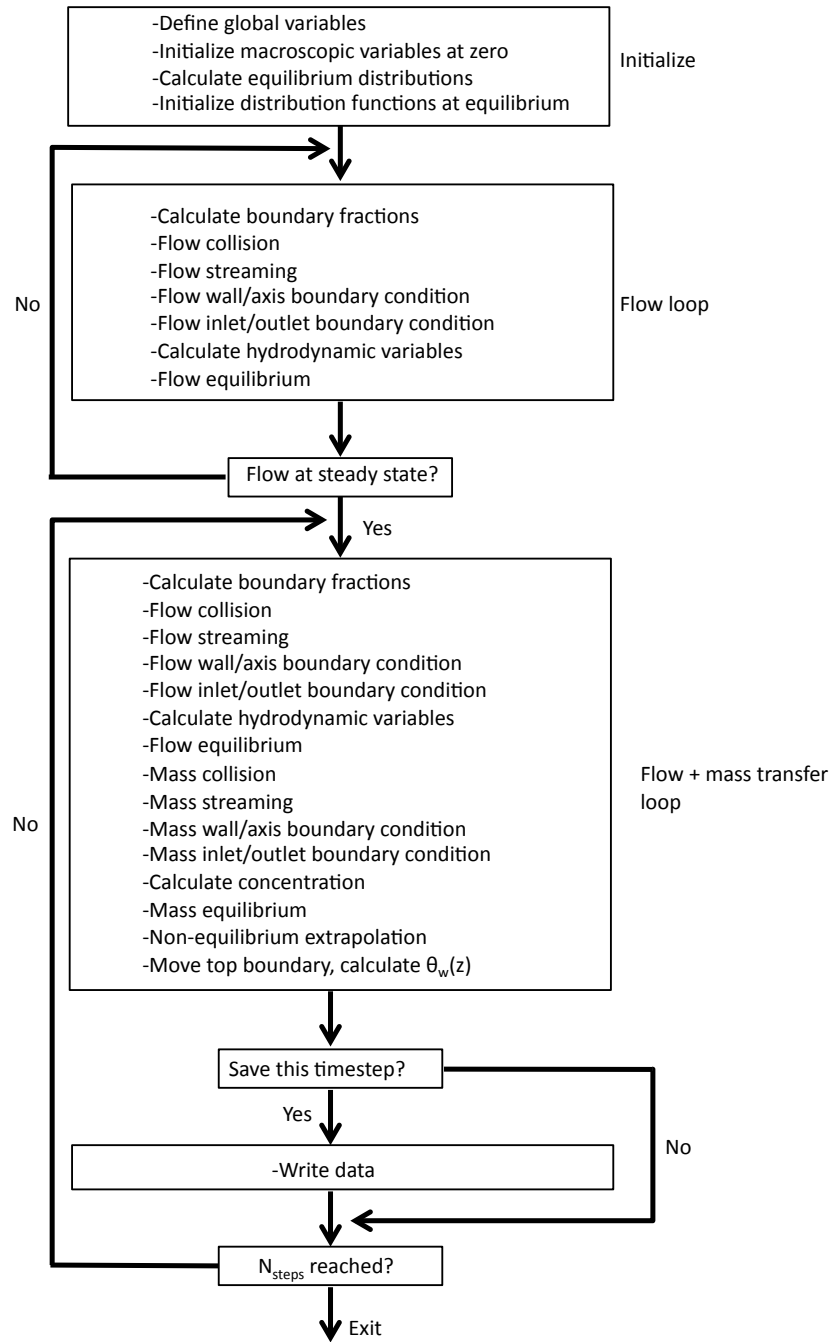


Figure B.1: Flowchart of lattice Boltzmann simulation subroutines.

Appendix C

VALIDATION OF LATTICE BOLTZMANN CODES

Several validation problems were selected to verify the accuracy of both the flow and mass transfer models. In particular, it was important to verify the accuracy of the chosen boundary condition implementations, as well as the formulation of the governing equations in axisymmetric coordinates. For all cases where multiple relaxation times were used, the parameters $\tau_{F0} \dots \tau_{F7}$ are taken to be those that were used in [102] and the parameters $\tau_{M0}, \tau_{M1}, \tau_{M3}$ are all taken to be 1.0, as in [109]. The assigned values for these parameters were not found to significantly affect the accuracy of the model.

C.1 Cartesian D2Q9 Flow and Mass Transfer Model

The D2Q5 code that was used for mass transfer in axisymmetric cylindrical coordinates in this work was originally implemented as a D2Q9 BGK model that used cartesian coordinates, the formulation and derivation of which is found in [114]. This model is implemented with the typical D2Q9 BGK model for flow that is presented in [100], and described in Chapter 4. The collision step is given by:

$$\hat{g}_a(\vec{x}, t + \delta t) = g_a(\vec{x}, t) + \omega(g_a(\vec{x}, t)) + S_a(\vec{x}, t) \quad (\text{C.1})$$

where ω is a general collision operator, and S_i is a source term. For the BGK case, ω is defined by:

$$\omega = -\frac{1}{\tau}(f(\vec{v}, \vec{x}, t) - f^{eq}(\vec{v}, t)) \quad (\text{C.2})$$

with the source term given by:

$$S_a(\vec{x}, t) = w_a \left(1 - \frac{1}{2\tau_s}\right) \delta t \frac{\mathbf{c}_a \cdot (P\nabla\phi/\rho_0 + \phi\mathbf{a})}{c_s^2} \quad (\text{C.3})$$

and the equilibrium distributions given by:

$$g_a^{eq} = w_a \phi \left(\left[1 + \frac{\mathbf{e}_a \cdot \mathbf{u}}{c_s^2} + \frac{(\mathbf{e}_a \cdot \mathbf{u})^2}{2c_s^4} - \frac{\mathbf{u} \cdot \mathbf{u}}{2c^2} \right] \right) + \Lambda_a \frac{\phi P}{\rho_0 c_s^2} \quad (\text{C.4})$$

where the constants Λ_a are given in [114]. The post-collision distributions then stream to neighboring nodes at the next time step, as in the flow model.

$$g_a(\vec{x} + \vec{e}_a \delta t, t + \delta t) = \hat{g}_a(\vec{x}, t) \quad (\text{C.5})$$

The local concentration is then given by:

$$\phi = \sum_a g_a \quad (\text{C.6})$$

The diffusivity is related to the solute relaxation time, time step, and sound speed by:

$$D = \left(\tau_s - \frac{1}{2}\right) \frac{c^2}{3} \delta t \quad (\text{C.7})$$

The forcing term due to acceleration \mathbf{a} is given by:

$$F_a(\vec{x}, t) = w_a \left(1 - \frac{1}{2\tau_f}\right) \delta t \left[\frac{\mathbf{e}_a - \mathbf{u}}{c_s^2} + \frac{(\mathbf{e}_a \cdot \mathbf{u})}{c_s^2} \mathbf{e}_a \right] \cdot (\rho_0 \mathbf{a}) \quad (\text{C.8})$$

where the weight functions w_a are given by $w_0 = 1/4$, $w_a = 1/9$ for $a = 1, \dots, 4$ and $w_a = 1/36$ for $a = 5, \dots, 8$. Additional details, including the weight functions and derivation of the scheme, can be found in [100].

C.1.1 Couette Flow with Wall Injection and Asymmetric Wall Concentrations

The first problem considered was Couette flow in an infinite channel with mass transfer and vertical flow injection from the walls. A y-velocity v_0 is injected at the bottom wall ($y = 0$), and removed at the top wall ($y = H$), so that both boundaries have a vertical velocity of v_0 . As in the typical Couette flow, the top wall also moves in the x-direction at u_0 , and the bottom wall is fixed, with a no slip boundary condition on both walls. The boundary conditions are implemented using the method for moving boundaries in [102]. The concentration is assumed to be constant at $\phi_0 = 0.0$ at the bottom wall and $\phi_1 = 1.0$ at the top wall. Periodic boundary conditions are enforced in the x-direction to simulate an infinite channel, and thus the problem has no x-dependence. The LBM solution is given in [114]. The LBM results as well as the analytical solutions for $u_0 = 0.001$ and $v_0 = 0.001$ (lattice units), with $\tau_F = 0.714$,

$\tau_M = 1.66$, and $N_y = 60$ are shown in Fig. C.1 for the velocity, Figs. C.2 and C.3 for the mass fluxes, and Fig. C.4 for the concentration profile.

$$u_x = u_0 \left(\frac{\exp(Re \frac{y}{H}) - 1}{\exp(Re) - 1} \right) \quad (\text{C.9})$$

$$u_y = v_0 \quad (\text{C.10})$$

$$\phi(y) = \phi_0 + (\phi_1 - \phi_0) \left(\frac{\exp(Pe \frac{y}{H}) - 1}{\exp(Pe) - 1} \right) \quad (\text{C.11})$$

where

$$Re = \frac{Hv_0}{\nu} \quad (\text{C.12})$$

and

$$Pe = \frac{Hv_0}{D} \quad (\text{C.13})$$

The mass fluxes can be calculated as:

$$J_x = -D \frac{\partial \phi}{\partial x} + \phi u_x = u_0 \left(\frac{\exp(Re \frac{y}{H}) - 1}{\exp(Re) - 1} \right) \left[\phi_0 + (\phi_1 - \phi_0) \left(\frac{\exp(Pe \frac{y}{H}) - 1}{\exp(Pe) - 1} \right) \right] \quad (\text{C.14})$$

and

$$J_y = -D \frac{\partial \phi}{\partial y} + \phi u_y = v_0 \left(\phi_0 - \frac{\phi_1 - \phi_0}{\exp(Pe) - 1} \right) \quad (\text{C.15})$$

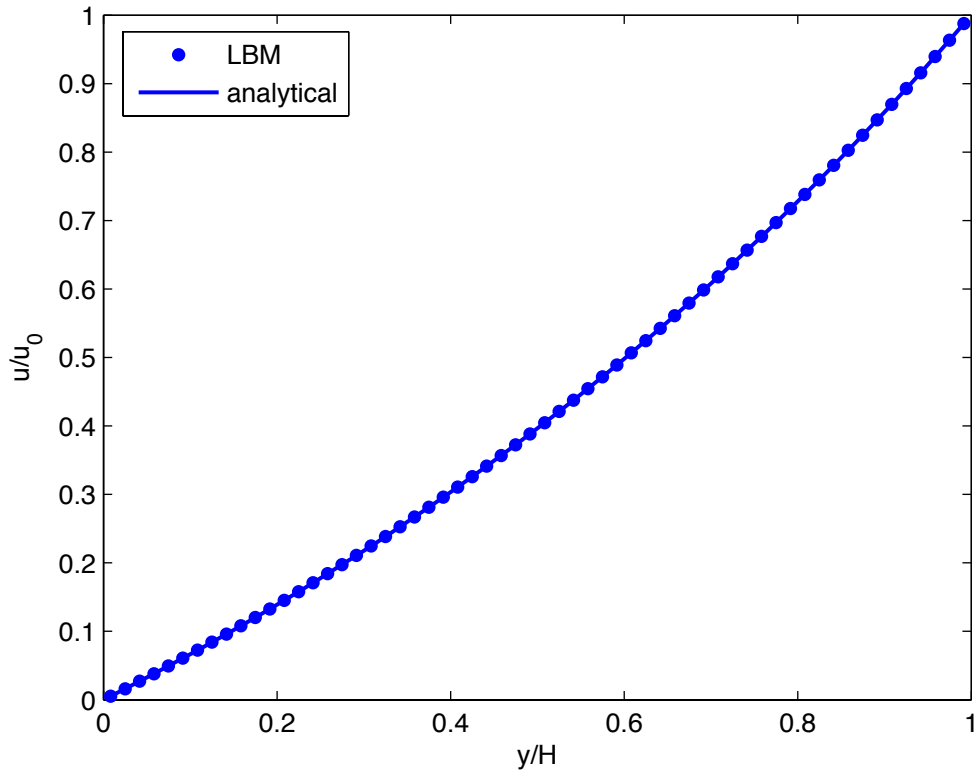


Figure C.1: Solution for horizontal velocity in Couette flow with wall injection.

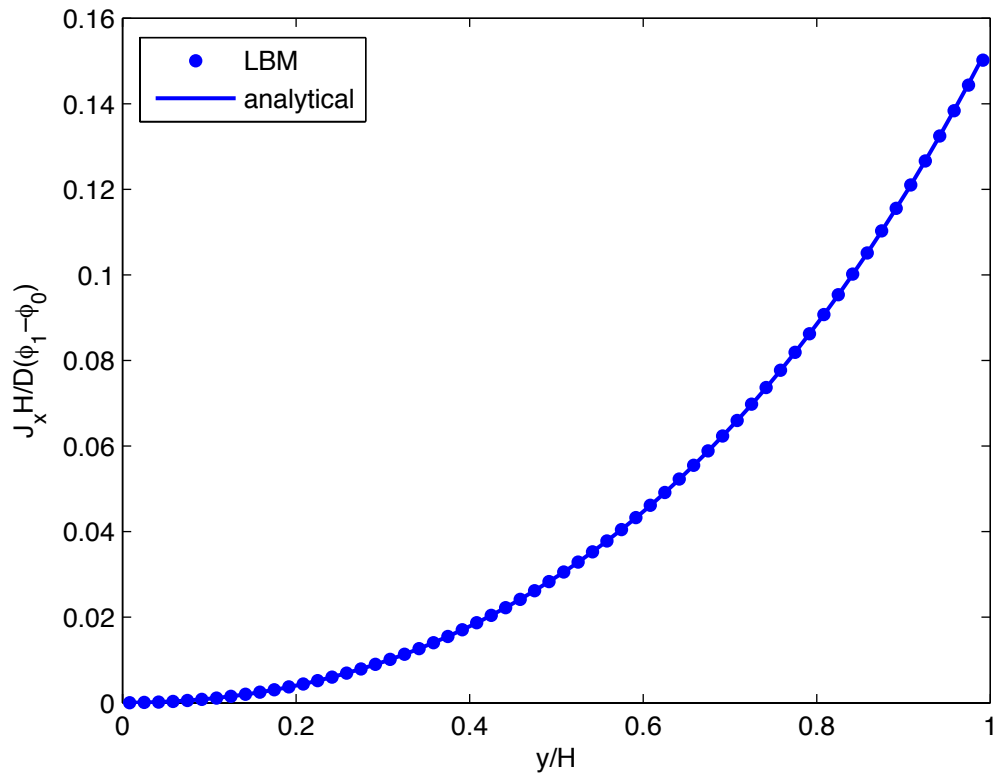


Figure C.2: Solution for horizontal mass flux in Couette flow with wall injection.

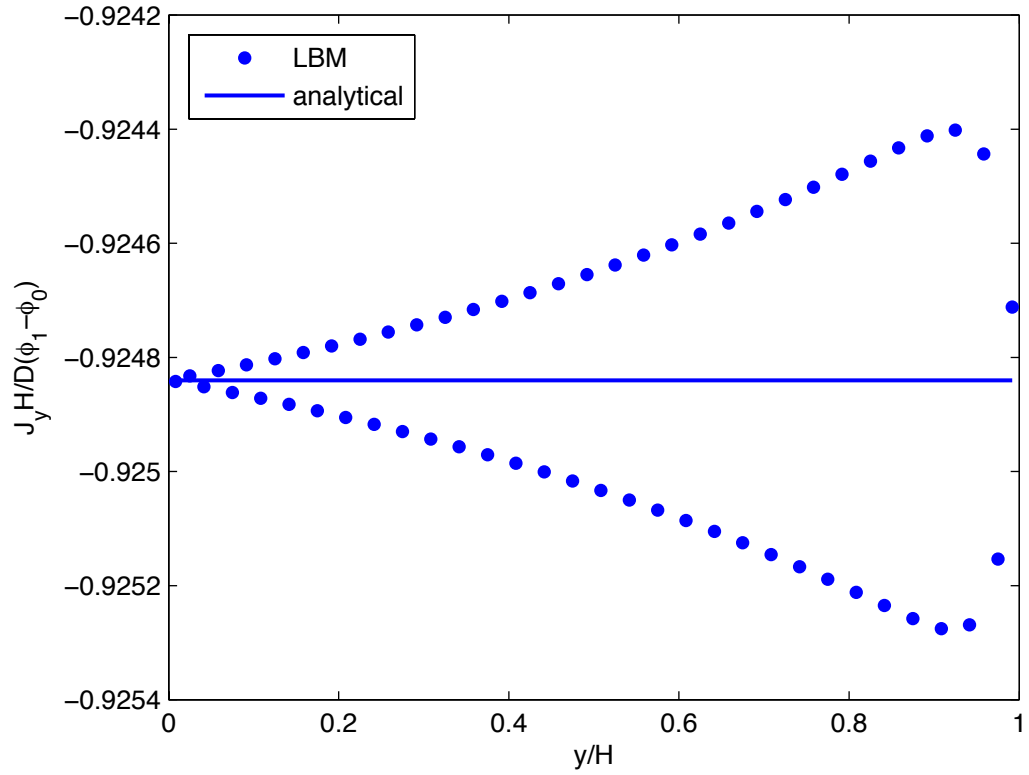


Figure C.3: Solution for vertical mass flux in Couette flow with wall injection.

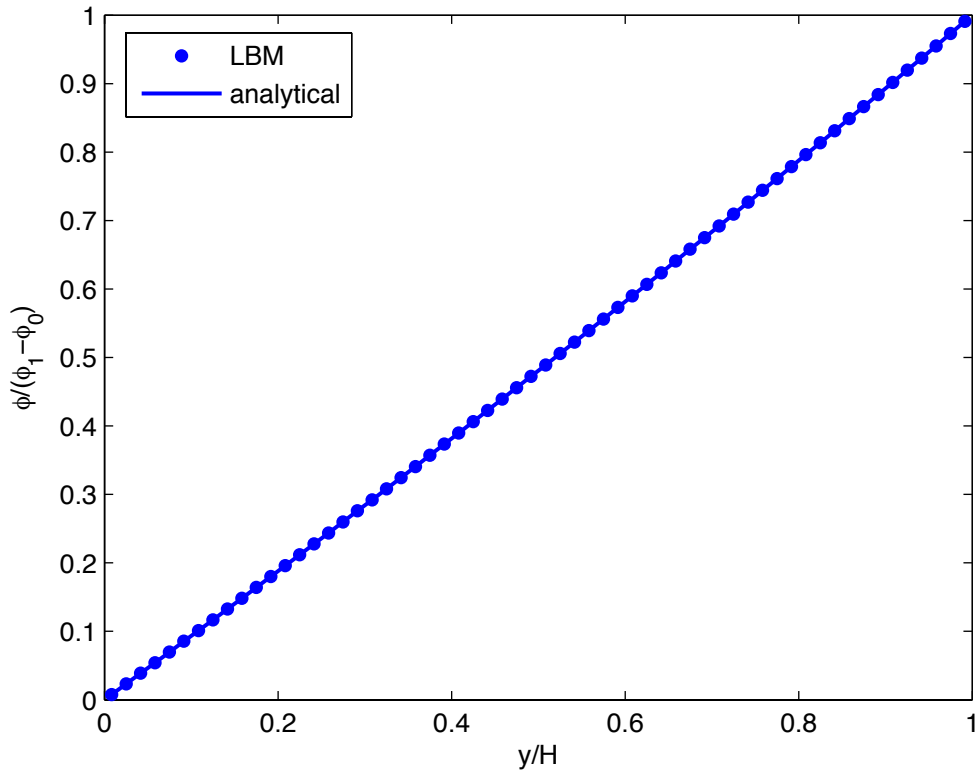


Figure C.4: Solution for concentration in Couette flow with wall injection

C.1.2 Plane Poiseuille Flow with Asymmetric Wall Concentrations

The cartesian D2Q9 BGK model was also validated for Plane Poiseuille flow in an infinite channel with asymmetric wall concentrations. The concentrations at the bottom and top walls ($y = 0$ and $y = H$, respectively) are held constant at $\phi_0 = 0.0$ and $\phi_1 = 1.0$ respectively. The walls are stationary, and the flow is driven by a constant body force a_x in the x-direction, and no-slip is assumed to hold at both the top and bottom walls. Periodic boundary conditions are enforced in the x-direction. The analytical solution, given in [114], is:

$$u_x = \frac{a_x H^2}{2\nu} \frac{y}{H} \left(1 - \frac{y}{H}\right) \quad (\text{C.16})$$

$$u_y = 0 \quad (\text{C.17})$$

$$\phi = \phi_0 + (\phi_1 - \phi_0) \frac{y}{H} \quad (\text{C.18})$$

$$J_x = \phi u_x = \frac{a_x H^2}{2\nu} \frac{y}{H} \left(1 - \frac{y}{H}\right) \left[\phi_0 + (\phi_1 - \phi_0) \frac{y}{H}\right] \quad (\text{C.19})$$

$$J_y = -D \frac{\partial \phi}{\partial y} = -(\phi_1 - \phi_0) \frac{D}{H} \quad (\text{C.20})$$

where

$$Re = \frac{H u_0}{\nu} \quad (\text{C.21})$$

and

$$Pe = \frac{H u_0}{D} \quad (\text{C.22})$$

Comparisons between the LBM solution and the analytical solution are given for the x-velocity, mass fluxes, and concentration in Figs. C.5, C.6, C.7, and C.8 respectively for $\frac{a_x H^2}{8\nu} = 0.001$ (lattice units), with $\tau_F = 0.714$, $\tau_M = 1.66$, and $N_y = 60$.

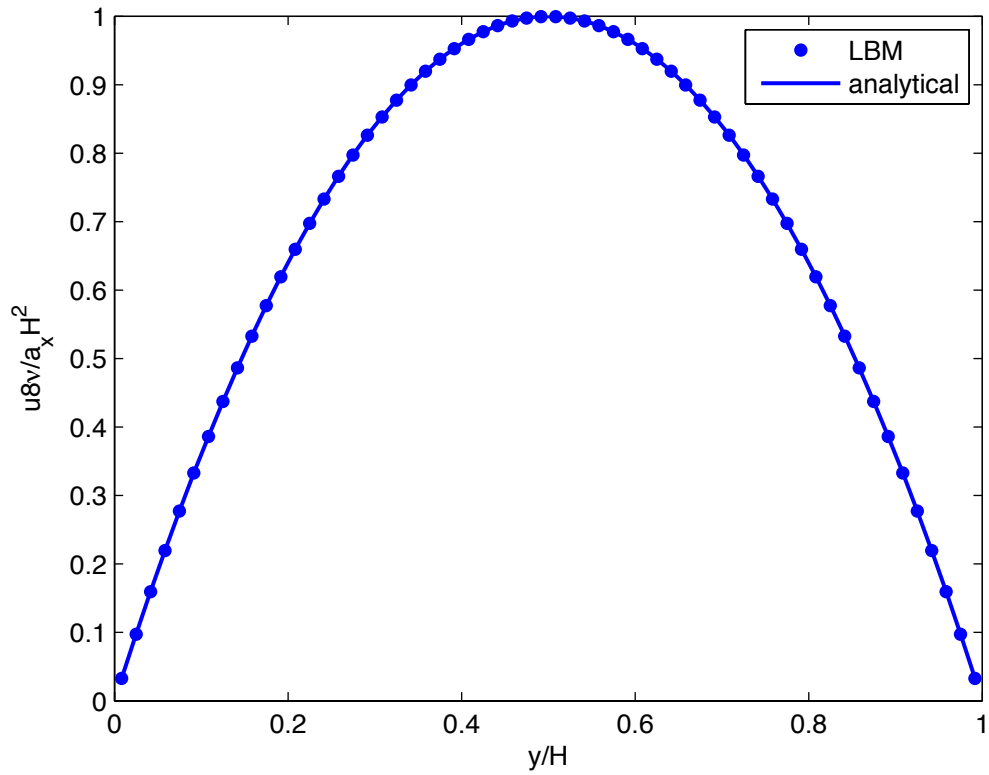


Figure C.5: Velocity solution for plane Poiseuille flow with asymmetric wall concentrations

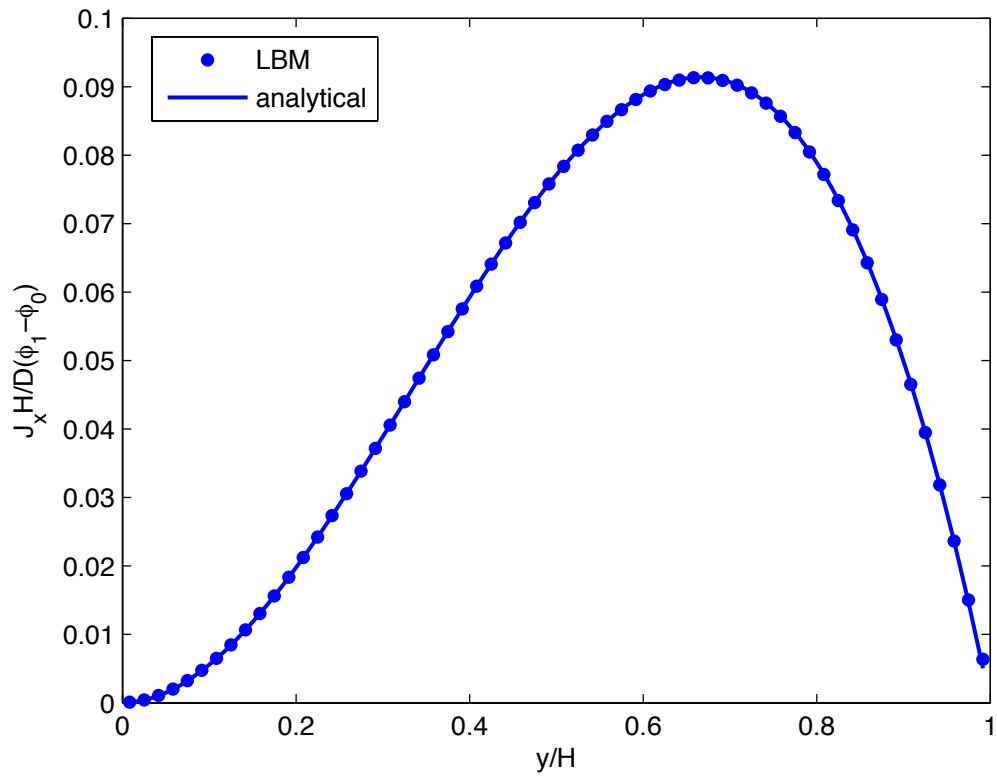


Figure C.6: Solution for horizontal mass flux in plane Poiseuille flow with asymmetric wall concentrations.

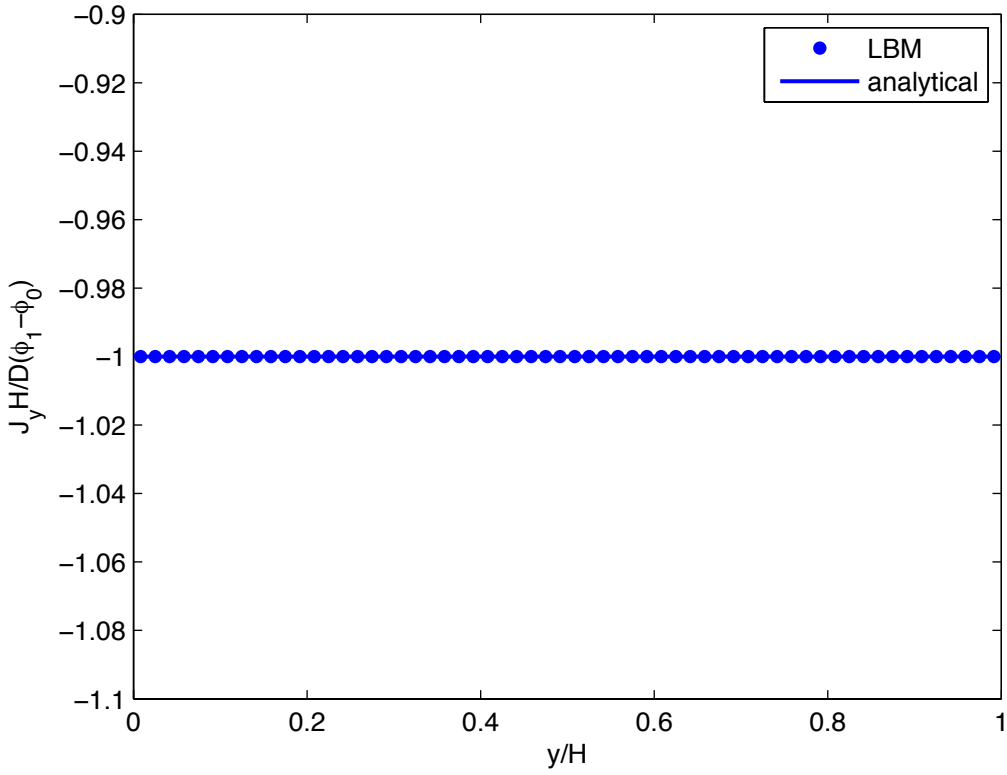


Figure C.7: Solution for vertical mass flux in plane Poiseuille flow with asymmetric wall concentrations.

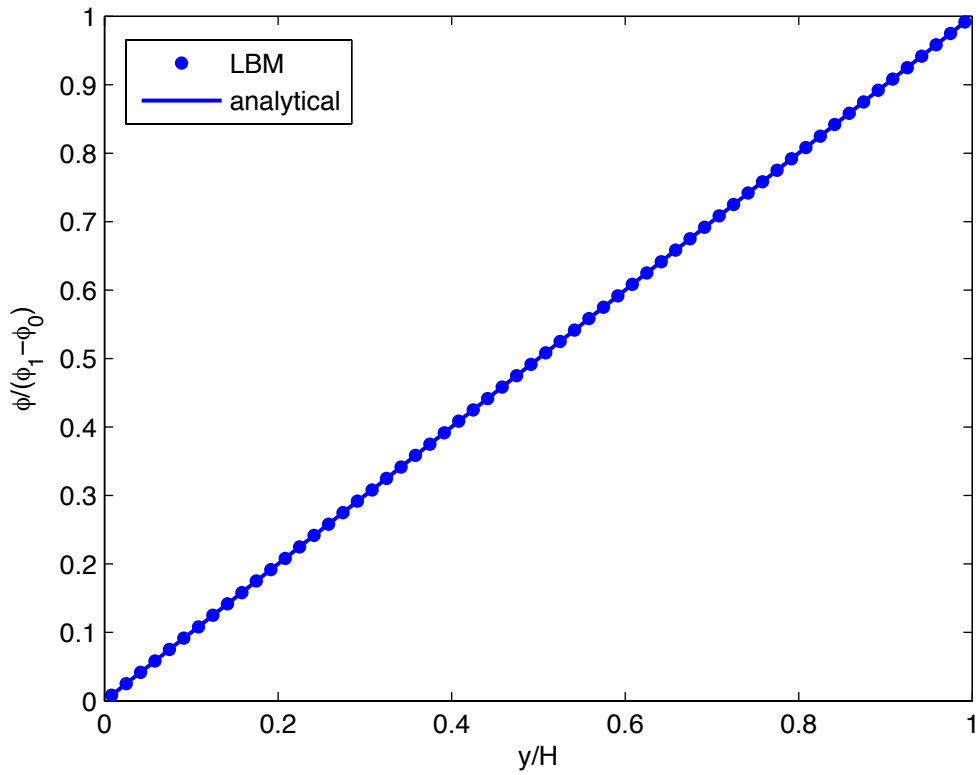


Figure C.8: Solution for concentration in plane Poiseuille flow with asymmetric wall concentrations.

C.1.3 Squeezing Flow between Parallel Plates

An additional validation problem to test the implementation of a vertically moving boundary condition for the flow model was the slow squeezing flow between infinitely wide parallel plates with length L . An analysis of a similar problem, squeezing flow between parallel discs, is presented in [149]. In this problem, a fluid is initially at rest between two plates, and for $t > 0$ the top wall begins to move slowly at constant rate \dot{H} in the vertical direction. The problem has analytical solution for the Stokes flow case, where the Reynolds number defined as:

$$Re = \frac{\dot{H}H}{\nu} \quad (\text{C.23})$$

is $\ll 1$. The analytical solution is given by:

$$u_x = \frac{6x\dot{H}}{H^3} \left(\frac{y^3}{3} - \frac{Hy^2}{2} \right) \quad (\text{C.24})$$

$$u_y = \frac{6x\dot{H}}{H^3} y(y - H) \quad (\text{C.25})$$

$$P - P_0 = \frac{3\rho\nu\dot{H}}{H^3} (x^2 - L^2) \quad (\text{C.26})$$

for any value of H . The solution for the horizontal velocity distribution is shown in Fig. C.9 for $Re = 0.001$.

For this problem, the relative error defined as $\mathbf{E} = |(u_{LBM} - u_{analytical})/u_{analytical}|$ was examined for both horizontal and vertical velocity distributions, and are shown in Figs. C.10 and C.11, respectively.

The x-velocity errors are very low for all time steps examined. The error increases over time because of accumulation of error, as well as the fact that fewer grid points are used in the computation as the wall squeezes down. It is also apparent that the errors tend to increase near the solid boundaries for both velocities. This is simply an artifact of the “finite-slip” issue with the LBM [150]. Near solid boundaries, the LBM will usually give velocities that several orders of magnitude lower than the characteristic velocity of the problem, but not exactly zero. Thus, when calculating

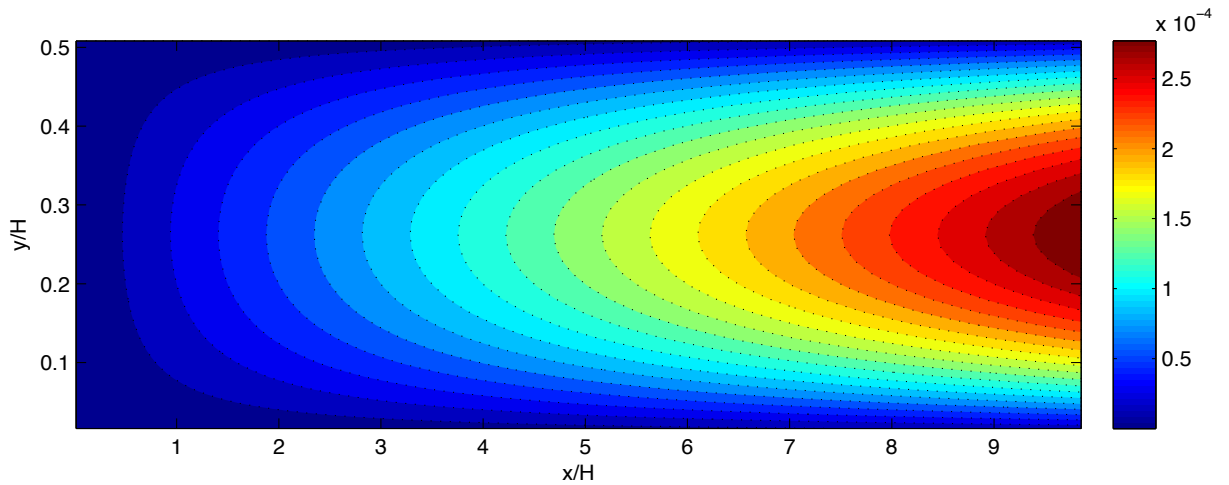


Figure C.9: Contours of axial velocity for squeezing flow between parallel plates at $h = 0.5H$ (lattice units).

the error for a problem where the analytical solution goes to zero near a boundary, the analytical solution may approach zero faster than the LBM solution, resulting in an increase in error. For the horizontal velocity, the velocity \dot{H} is seen to be implemented with a high degree of accuracy at the top boundary, shown in Fig. C.10. The effect of the velocity slip is seen to be worse for the vertical velocity near the bottom plate, as shown in Fig. C.11.

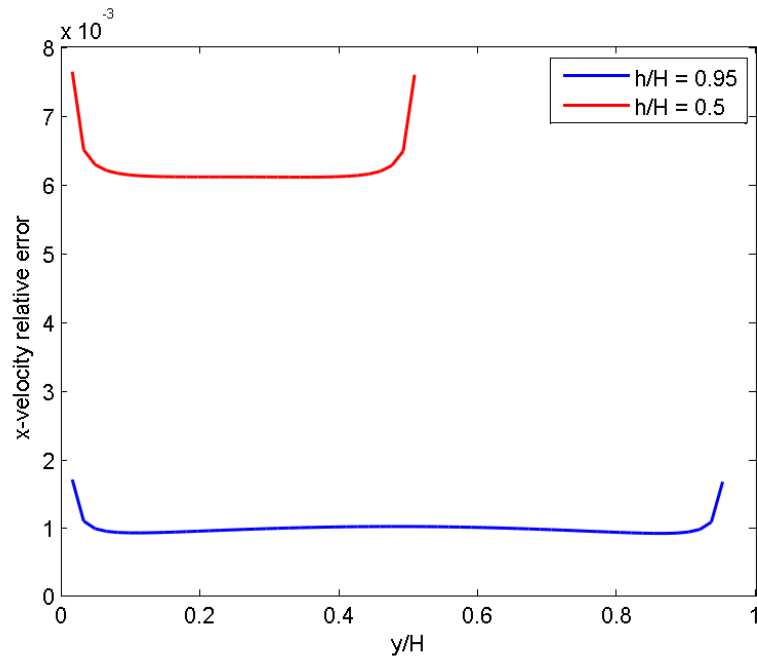


Figure C.10: Profiles of x-velocity relative error at $x = 0$ for squeezing flow between parallel plates.

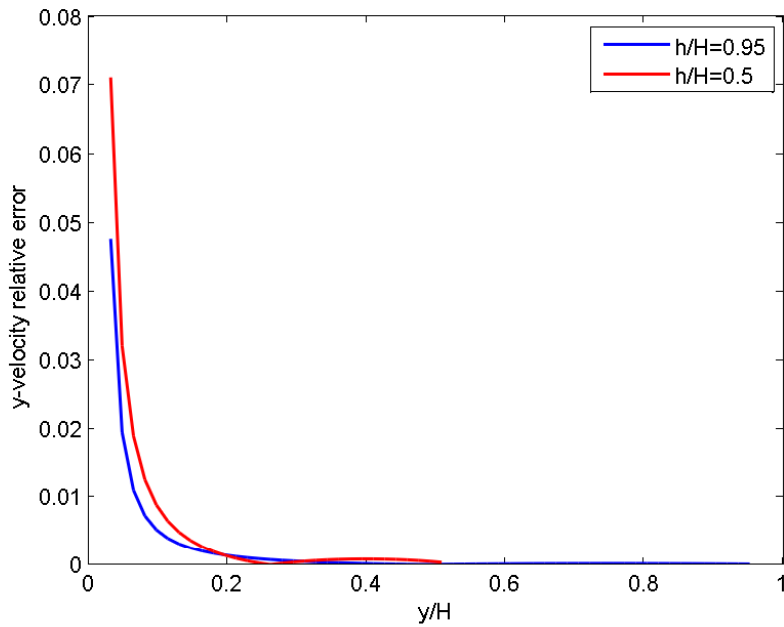


Figure C.11: Profiles of y-velocity relative error at $x = 0$ for squeezing flow between parallel plates.

C.2 Axisymmetric D2Q9 MRT Flow Model

The code for the Cartesian D2Q9 BGK flow model was later extended to the axisymmetric D2Q9 MRT flow model presented in [104] in order to investigate flows in tubes. Several other problems with moving boundaries were tested.

C.2.1 Squeezing Flow in an Annular Region

In this validation problem, the fluid is initially at rest in an annular region, i.e., between a solid cylinder of radius R_i and a larger hollow cylinder of inner radius R_o . The inner cylinder is allowed to expand or contract in the radial direction at constant rate $\frac{dR_i}{dt}$ and the outer cylinder is allowed to expand or contract in the radial direction at rate $\frac{dR_o}{dt}$. The analytical solution under Stokes flow conditions is:

$$P(z) = P_0 + \frac{\left(\frac{dR_o}{dt} - \frac{R_i}{R_o} \frac{dR_i}{dt}\right) 4\mu (z^2 - L^2)}{\frac{R_o^3}{4} - \frac{R_i^2 R_o}{2} + \frac{R_i^4}{4R_o} - (R_o^2 - R_i^2) \left(\frac{R_o}{4} (2 \ln\left(\frac{R_o}{R_i}\right) - 1) + \frac{R_i^2}{4R_o}\right) / \ln\left(\frac{R_o}{R_i}\right)} \quad (\text{C.27})$$

$$u_z(r, z) = -\left(\frac{dR_o}{dt} - \frac{R_i}{R_o} \frac{dR_i}{dt}\right) z \left[r^2 - R_i^2 - (R_o^2 - R_i^2) \ln\left(\frac{r}{R_i}\right) / \ln\left(\frac{R_o}{R_i}\right) \right] / \left[\frac{R_o^3}{4} - \frac{R_i^2 R_o}{2} + \frac{R_i^4}{4R_o} - (R_o^2 - R_i^2) \left(\frac{R_o}{4} (2 \ln\left(\frac{R_o}{R_i}\right) - 1) + \frac{R_i^2}{4R_o}\right) / \ln\left(\frac{R_o}{R_i}\right) \right] \quad (\text{C.28})$$

and the r -velocity by:

$$u_r(r, z) = \left(\frac{dR_o}{dt} - \frac{R_i}{R_o} \frac{dR_i}{dt}\right) \left[\frac{r^3}{4} - \frac{R_i^2 r}{2} + \frac{R_i^4}{4r} - (R_o^2 - R_i^2) \left(\frac{r}{4} (2 \ln\left(\frac{r}{R_i}\right) - 1) + \frac{R_i^2}{4r}\right) / \ln\left(\frac{R_o}{R_i}\right) \right] / \left[\frac{R_o^3}{4} - \frac{R_i^2 R_o}{2} + \frac{R_i^4}{4R_o} - (R_o^2 - R_i^2) \left(\frac{R_o}{4} (2 \ln\left(\frac{R_o}{R_i}\right) - 1) + \frac{R_i^2}{4R_o}\right) / \ln\left(\frac{R_o}{R_i}\right) \right] + \frac{R_i}{r} \frac{dR_i}{dt} \quad (\text{C.29})$$

The velocity distributions for a typical case with $\frac{dR_o}{dt} = -0.0001$ and $\frac{dR_i}{dt} = 0$ are shown in Figs. C.12 and C.13.

The relative error $\mathbf{E} = |(u_{LBM} - u_{analytical}) / u_{analytical}|$ was examined for both axial and radial velocity distributions using both a BGK collision and an MRT collision.

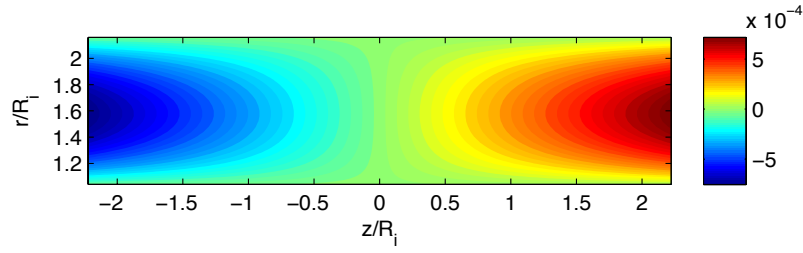


Figure C.12: Contours of z -velocity for squeezing flow in an annular region (lattice units).

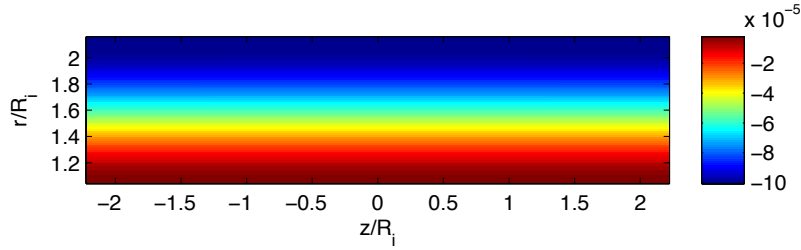


Figure C.13: Contours of r -velocity for squeezing flow in an annular region (lattice units).

Figures C.14 and C.15 show the r -velocity errors for a BGK model and an MRT model respectively. It is apparent that the MRT model significantly reduces the error in all cases examined. Similar to the results in Section C.1.3, the errors increase near the inner wall due to the finite velocity slip and the definition of the relative error.

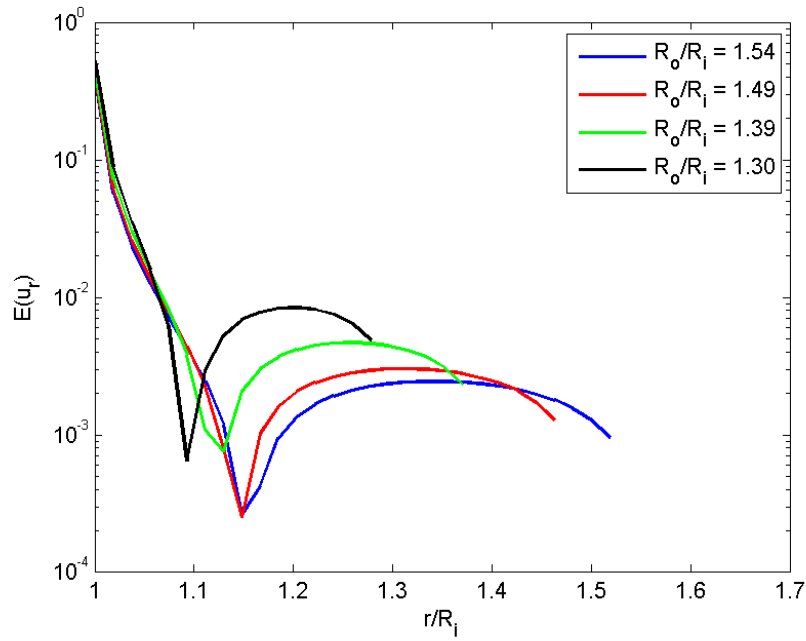


Figure C.14: Profiles of r-velocity relative error for BGK case, squeezing flow in an annular region.

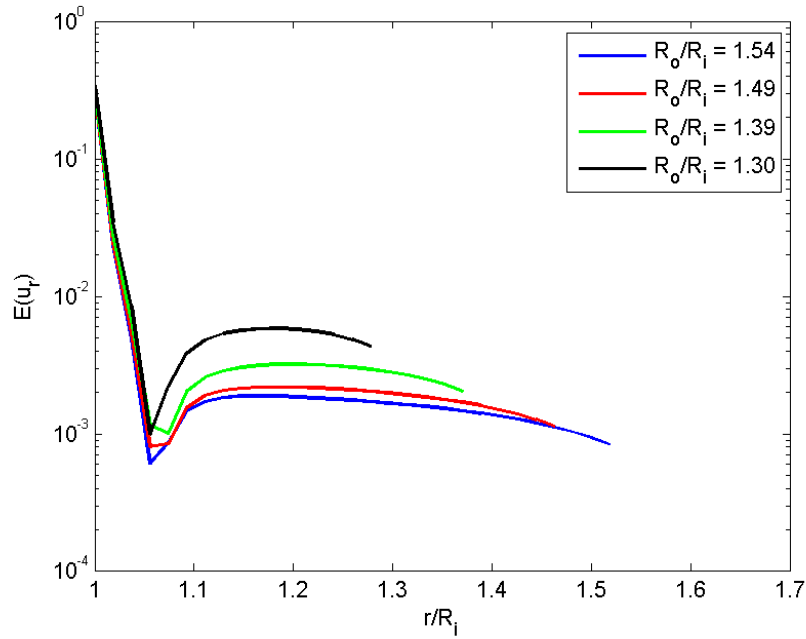


Figure C.15: Profiles of r-velocity relative error for MRT case, squeezing flow in an annular region.

C.2.2 Squeezing Flow in a Contracting Tube

In order to validate the implementation of the no-slip boundary condition in axisymmetric coordinates, we consider a tube of initial radius R_0 and half-length L immersed in a viscous fluid. The tube radius is then prescribed to decrease at a fixed rate dR/dt . For low, finite Re , where $Re = \frac{RdR/dt}{\nu}$, the approximate analytical solution is given by [128]:

$$u_r(r) = 2\frac{dR}{dt}\left(\frac{r}{R} - \left(\frac{r}{R}\right)^3\right) + \frac{dR}{dt}Re\left(\frac{5}{18}\frac{r}{R} - \frac{7}{12}\left(\frac{r}{R}\right)^3 + \frac{1}{3}\left(\frac{r}{R}\right)^5 - \frac{1}{36}\left(\frac{r}{R}\right)^7\right) + O(Re^2) \quad (\text{C.30})$$

$$u_z(r, z) = -\frac{4z}{R^3}\frac{dR}{dt}(R^2 - r^2) + \frac{z}{2R}\frac{dR}{dt}Re\left(\frac{5}{18} - \frac{7}{6}\left(\frac{r}{R}\right)^2 + \left(\frac{r}{R}\right)^4 - \frac{1}{9}\left(\frac{r}{R}\right)^6\right) + O(Re^2) \quad (\text{C.31})$$

The problem is simulated in LBM with $N_r = 40$ and $N_z = 300$. Profiles of the relative error $\mathbf{E} = |(u_{LBM} - u_{analytical})/u_{analytical}|$ at $z = 3L/4$ are shown for the radial and axial velocities in Figs. C.16 and C.17, respectively, for different values of R/R_0 .

The error in Fig. C.16 increases suddenly towards the centerline $r = 0$ due to the finite slip velocity of the LBM, and because the analytical solution for $u_r \rightarrow 0$. The horizontal axis is terminated near $r/R_0 = 0.1$ in order to highlight the low range of the error at higher values of r/R_0 . Similarly, the error in Fig. C.17 increases towards the tube wall at $r = R$, where the no-slip condition holds. Hence, the local increases in errors are an artifact of the well-known velocity slip issue in LBM [150], and the errors for the rest of the domain remain acceptably low.

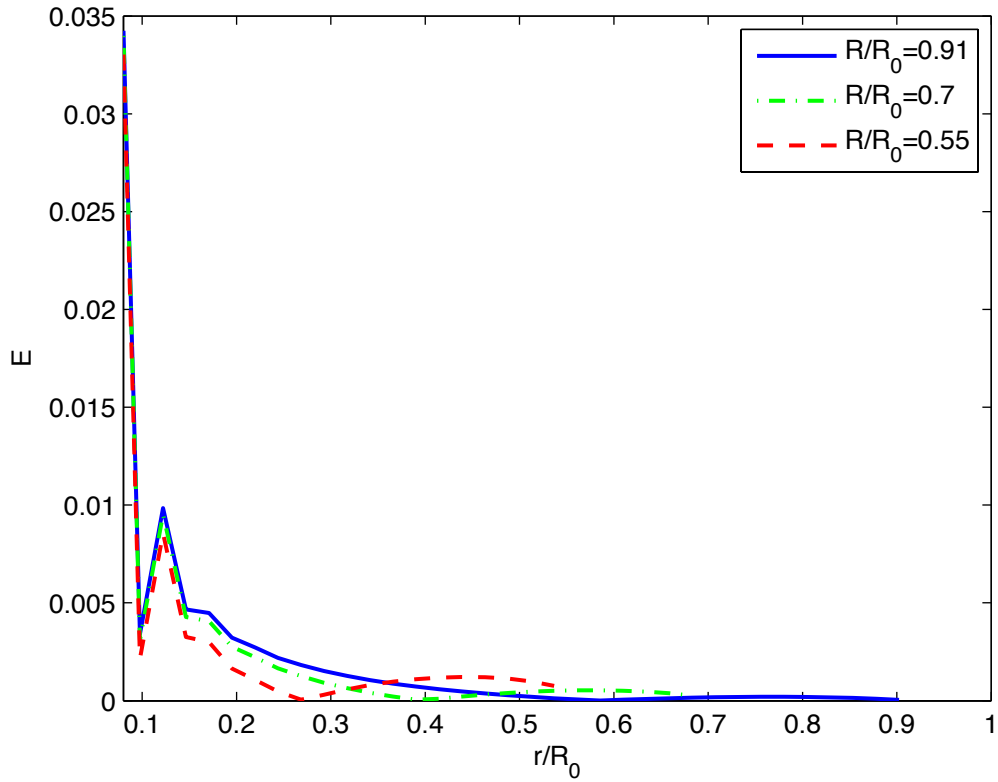


Figure C.16: Relative error profiles for u_r at $z = L/2$ and $Re = 0.001$ for flow in a contracting tube of initial radius R_0 and half-length L at different values of R/R_0 .

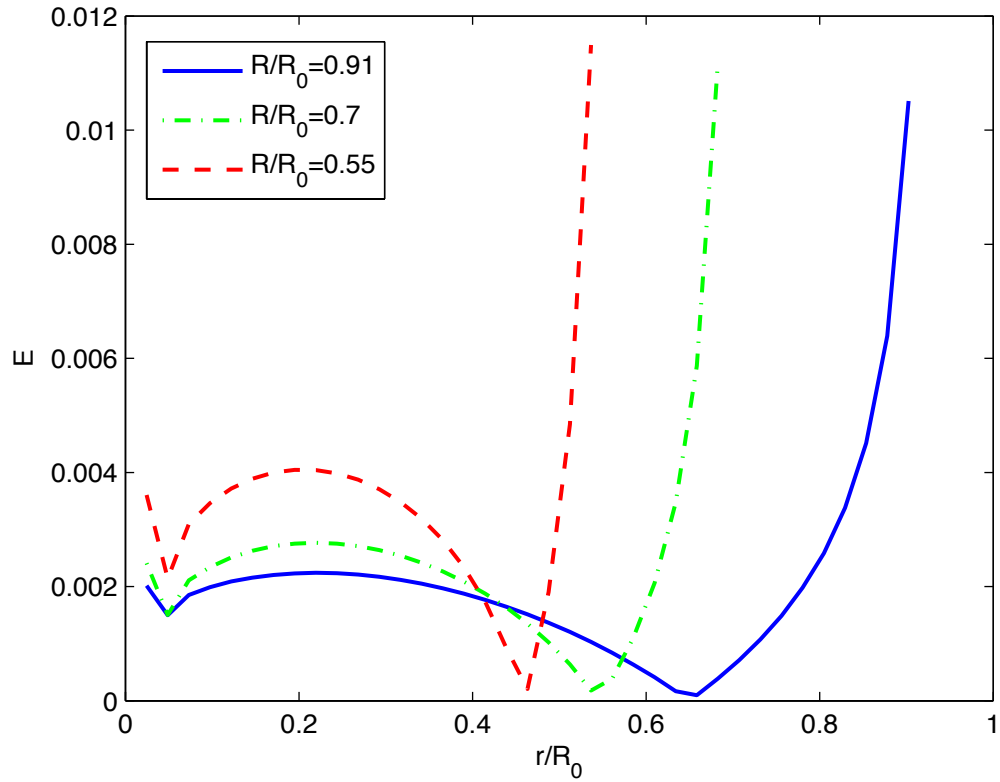


Figure C.17: Relative error profiles for u_z at $z = L/2$ and $Re = 0.001$ for flow in a contracting tube of initial radius R_0 and half-length L at different values of R/R_0 .

C.2.3 Starting Transient Poiseuille Flow

In order to validate the transient performance of the axisymmetric LB model for flow, we examine the case of an infinitely long pipe of radius R , which has zero velocity everywhere for $t = 0$, and is then subject to a constant axial acceleration a_z for $t > 0$. As described in [129], the analytical solution is given by:

$$u_z(r, t) = \frac{a_z}{4\nu}(R^2 - r^2) - \frac{2a_z R^2}{\nu} \sum_{n=0}^{\infty} \frac{J_0(\lambda_n \frac{r}{R})}{\lambda_n^3 J_1(\lambda_n)} \exp\left(-\frac{\lambda_n^2 \nu t}{R^2}\right) \quad (\text{C.32})$$

where J_0 and J_1 are the first-kind Bessel functions of orders 0 and 1, respectively, and the λ_n are the roots of J_0 .

The problem is implemented using LBM with $N_r = 40$ and $N_z = 5$ with periodic boundary conditions in z for the flow variables. Profiles of the relative error \mathbf{E} for the axial velocity are shown in Fig. C.18 for different values of non-dimensional time. The analytical solution is computed using the first 10 terms of the infinite series. The error is $< 1\%$ for all times shown. As in the contracting tube problem, the error increases near the tube wall due to the finite slip velocity and the definition of E . The errors increase over time because additional terms in the infinite series are needed for accuracy at low t , so the calculated error is likely to be lower than the true error for these cases.

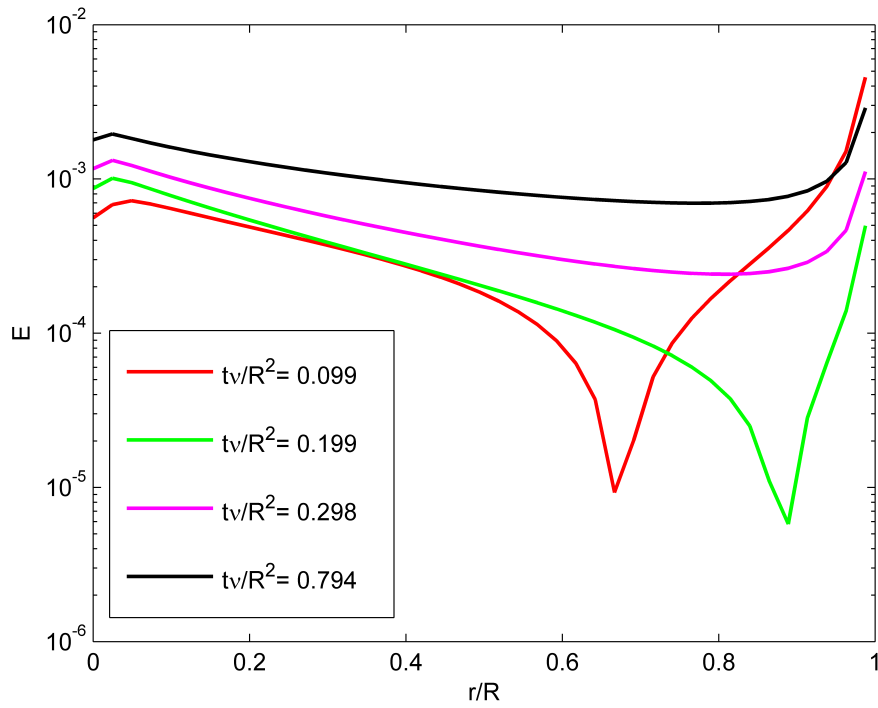


Figure C.18: Relative error profiles for u_z for $Re = 10$ for starting Poiseuille flow at different values of non-dimensional time $t\nu/R^2$.

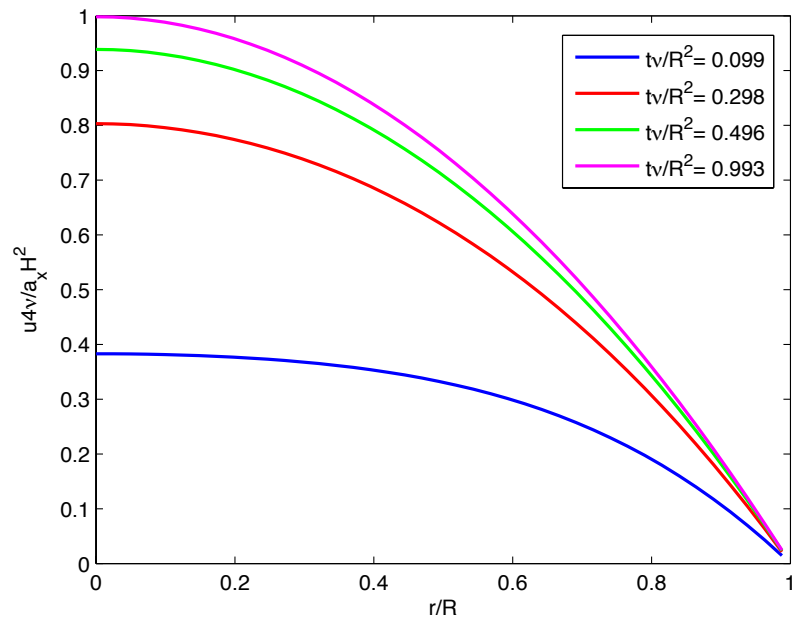


Figure C.19: Evolution of velocity profile for starting transient Poiseuille flow

C.3 Axisymmetric D2Q5 MRT Model for Mass Transfer

C.3.1 Steady Convective-Diffusion in an Annular Region with Wall Injection

As a check on the accuracy of the mass transfer model, we use a validation problem presented in [109]. We consider a cylinder of radius R_i with a radial flow of velocity $u_{r,i}$ injected through the outer cylinder wall. The fluid then exits radially through the inner wall at $r = R_o$. The concentration at $r = R_i$ is set to $\phi_i = 0.5$ and the concentration at another radial location $r = R_o$ is set to $\phi_o = 1.0$. The axial velocity u_z is assumed to be zero everywhere and the problem is thus independent of z . The analytical solution for the radial velocity is given by:

$$u_r(r) = \frac{u_{r,i}R_i}{r} \quad (\text{C.33})$$

which is prescribed directly in order to decouple the flow model from the mass transfer model, i.e., the flow is not solved using LBM. The analytical solution for the concentration is given by:

$$\phi(r) = \frac{\phi_o(R_o^{Pe} - r^{Pe}) + \phi_i(r^{Pe} - R_i^{Pe})}{R_o^{Pe} - R_i^{Pe}} \quad (\text{C.34})$$

where

$$Pe = \frac{u_{r,i}R_i}{D} \quad (\text{C.35})$$

The problem is implemented using LBM with $N_r = 40$ and $N_z = 5$ with periodic boundary conditions in z for all variables. Profiles of the relative error \mathbf{E} for concentration are shown in Fig. C.20 for different values of Pe and $R_o/R_i = 10.0$. The errors are $< 1\%$ except for at high values of Pe , due to the assumption of low Ma being violated for increasing flow velocity [103].

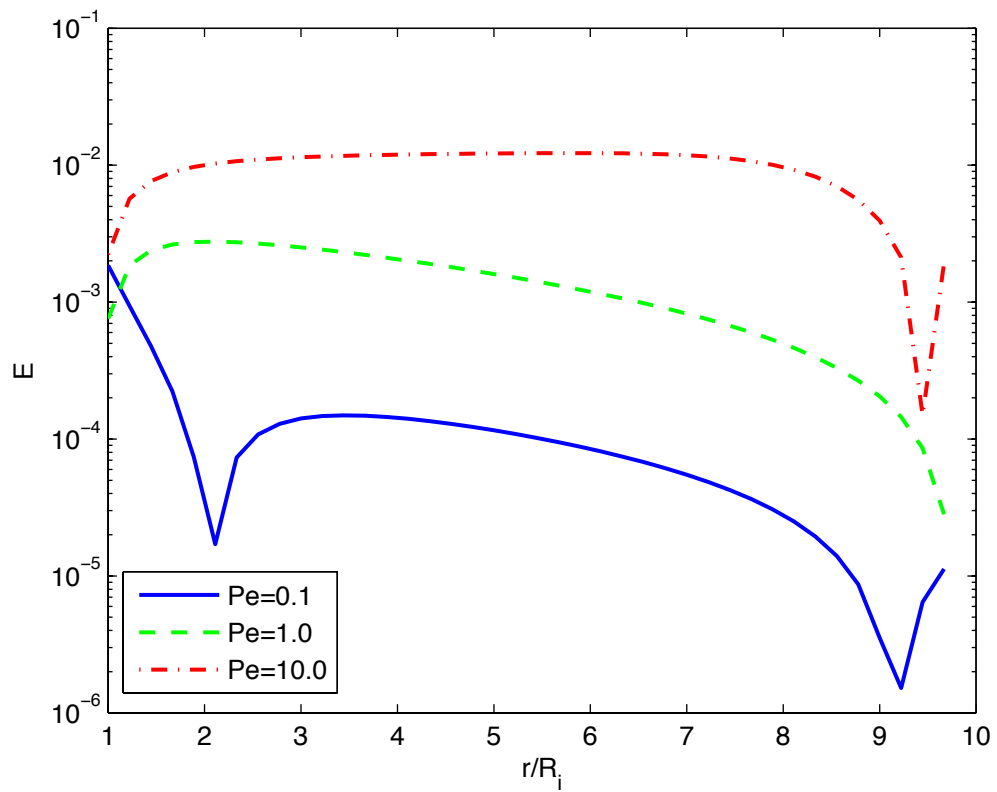


Figure C.20: Profile of relative error for species concentration ϕ for convective-diffusion in an annular region with wall injection for various values of Pe .

C.3.2 Periodic Convective-Diffusion in Slug Flow

Finally, in order to validate the transient performance of the mass transfer model, we examine another validation problem presented in [109], namely, periodic convective diffusion in slug flow. We consider a section of a pipe of length L and radius R with a uniform axial velocity U . The concentration boundary condition is prescribed as $\phi(R, z, t) = \cos(\mathbf{k}z + \omega t)$ with $\mathbf{k} = 2\pi/L$ and $\omega = 2\pi/\Gamma$, where Γ is the time period of oscillation. The Strouhal and Peclet numbers are defined as $St = \sqrt{\frac{R^2}{\Gamma D}}$ and $Pe = \frac{RU}{D}$, respectively.

The analytical solution for the concentration in the pipe is given by:

$$\phi(r, z, t) = \text{Real} \left[e^{i(\mathbf{k}z + \omega t)} \frac{\mathbf{I}_0(\sigma r)}{\mathbf{I}_0(\sigma R)} \right] \quad (\text{C.36})$$

where $\sigma = \mathbf{k} \sqrt{1 + \frac{\omega + iU}{D\mathbf{k}^2}}$, and \mathbf{I}_0 is the modified first-kind Bessel function of order 0. The normalized accumulated global error \mathbf{E}_2 is given by:

$$\mathbf{E}_2 = \left[\frac{1}{\Gamma} \int_0^\Gamma \frac{1}{N_r N_z} \sum_{r,z} (\phi_{LBM} - \phi_{ex})^2 \delta t \right]^{1/2} \quad (\text{C.37})$$

The length $L = 2N_r$ for all cases. A logarithmic plot of \mathbf{E}_2 at different values of $1/N_r$ and τ_M is shown in Fig. C.22 for $Pe = St = 20.0$. The plot verifies that the model exhibits second-order accuracy in space, and because the number of time steps is quadrupled when N_r is doubled, the temporal accuracy of the mass transfer model is first-order, as was found in [109].

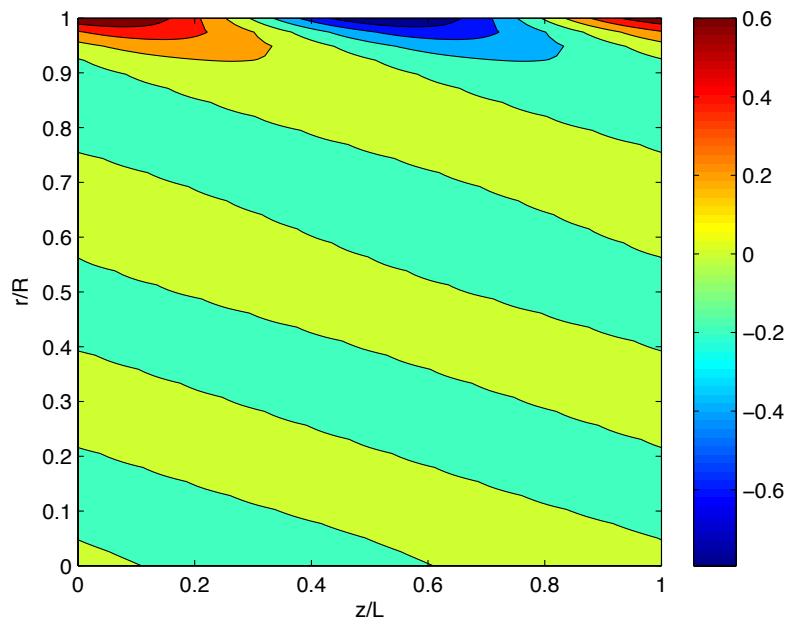


Figure C.21: Contours of concentration for periodic convective-diffusion in slug flow

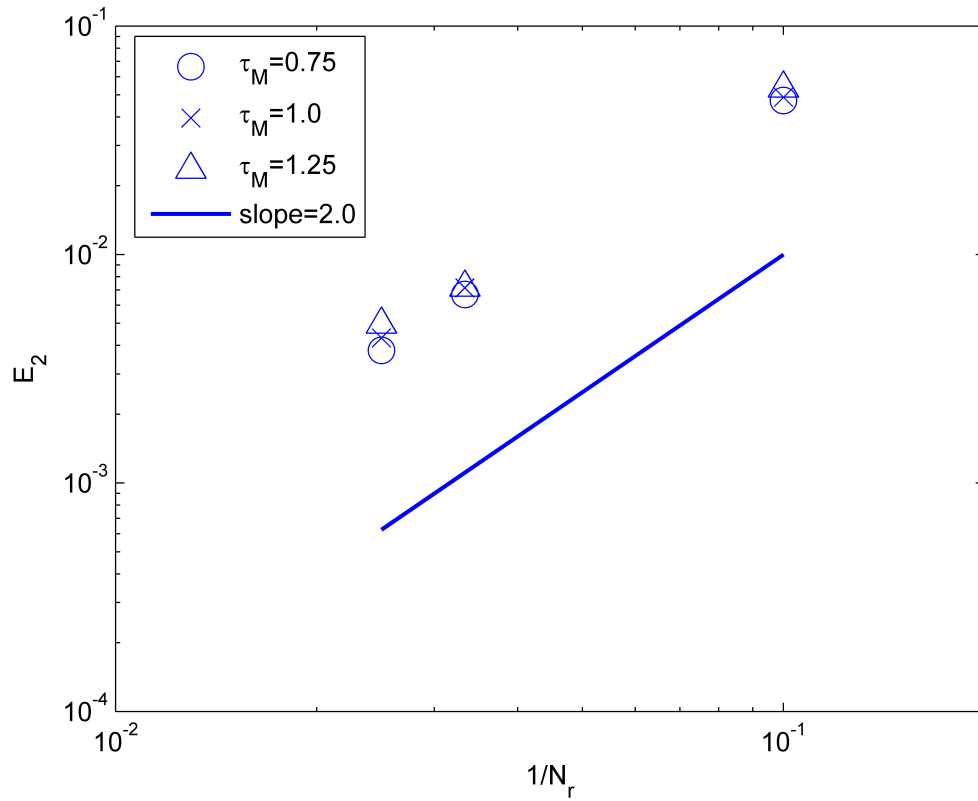


Figure C.22: Normalized cumulative global error E_2 after one period Γ for $St = 20$, $Pe = 20$ for periodic diffusion in slug flow.

C.4 Third-Kind Mass Transfer Boundary Condition and Interface Tracking

In order to validate the third-kind boundary condition for mass transfer, including kinetics and diffusion at the solid boundary, as well as the motion of the solid boundary as solid mass is deposited, one can consider a problem similar to the validation problem presented in [125].

For a pure diffusion problem, i.e., with no bulk fluid flow, the 1-D convective-diffusion equation, when non-dimensionalized by $\phi^* = \phi/\phi_0$, $x^* = x/L$, $t^* = tu_w/L$, reduces to:

$$\frac{d\phi^*}{dt^*} = \frac{1}{Pe} \frac{d^2\phi^*}{dx^{*2}} \quad (\text{C.38})$$

where $Pe = u_w L/D$, and u_w is the velocity of moving solid boundary. For slow growth, i.e., $Pe \ll 1$, a quasi-steady approximation can be applied, and the time derivative can be neglected.

At the solid boundary $x = S$, the reaction-diffusion boundary condition is given by:

$$D \frac{d\phi}{dx}(S) = -k\phi(S) \quad (\text{C.39})$$

which and considering the material derivative $\frac{D}{Dt} = \frac{d}{dt} + u_w \frac{d}{dx}$, the boundary condition can be written in non-dimensional form as:

$$\frac{D\phi^*}{Dt^*}(S) = -Da\phi^*(S) \quad (\text{C.40})$$

where $Da = kL/D$. Thus, for $Da \ll 1$, the quasi-steady approximation can likewise be applied.

If the velocity of the solid boundary is determined by a mass balance of the reaction rate with the deposited mass, the velocity is given as:

$$\frac{d\mathcal{W}}{dt} = -\frac{k\phi(S)}{\phi_{(s)}} \quad (\text{C.41})$$

where $\phi_{(s)}$ is the molar density of the solid phase. Then, for $\phi(0, t) = \phi(x, 0) = \phi_0$ and $\mathcal{W}(t = 0) = W_0$, the analytical solution for $\mathcal{W}(t)$ is given by:

$$\mathcal{W}(t) = W_0 - \frac{D}{k} + \sqrt{\frac{D^2}{k^2} - 2Dt \frac{\phi_0}{\phi_{(s)}}} \quad (\text{C.42})$$

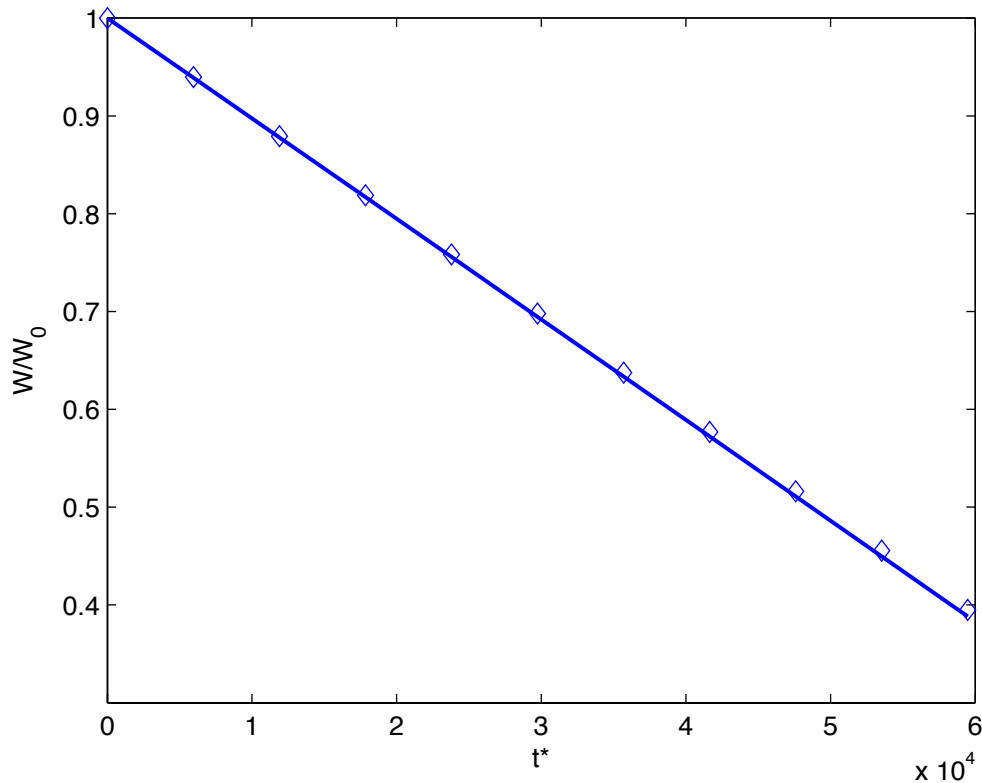


Figure C.23: Validation of third-kind boundary mass transfer boundary treatment and interface tracking scheme for slow growth with kinetics-limited reaction. Here, the time is scaled as $t^* = tD/L^2$.

The analytical solution, along with the LBM results are shown in Fig. C.23. The problem is implemented in LBM with periodic boundary conditions in the direction perpendicular to the wall. The solid boundary remains a flat plane, consistent with the assumption of 1D diffusion. The error is seen to increase as time goes on, due to fewer lattice points being used in the computation, as well as accumulation of error. Over short time spans, the agreement between the analytical solution and the LBM solution is very good.

Appendix D

PERMISSION FROM ELSEVIER

Table of Author's Rights			
	Preprint version (with a few exceptions- see below *)	Accepted Author Manuscript	Published Journal Articles
Use for classroom teaching by author or author's institution and presentation at a meeting or conference and distributing copies to attendees	Yes	Yes	Yes
Use for internal training by author's company	Yes	Yes	Yes
Distribution to colleagues for their research use	Yes	Yes	Yes
Use in a subsequent compilation of the author's works	Yes	Yes	Yes
Inclusion in a thesis or dissertation	Yes	Yes	Yes
Reuse of portions or extracts from the article in other works	Yes	Yes with full acknowledgement of final article	Yes with full acknowledgement of final article
Preparation of derivative works (other than for commercial purposes)	Yes	Yes with full acknowledgement of final article	Yes with full acknowledgement of final article
Preprint servers	Yes	Yes with the specific written permission of Elsevier	No
Voluntary posting on open web sites operated by author or author's institution for scholarly purposes	Yes (author may later add an appropriate bibliographic citation, indicating subsequent publication by Elsevier and journal title)	Yes, with appropriate bibliographic citation and a link to the article once published	Only with the specific written permission of Elsevier
Mandated deposit or deposit in or posting to subject-oriented or centralized repositories	Yes under specific agreement between Elsevier and the repository	Yes under specific agreement between Elsevier and the repository**	Yes under specific agreement between Elsevier and the repository
Use or posting for commercial gain or to substitute for services provided directly by journal	Only with the specific written permission of Elsevier	Only with the specific written permission of Elsevier	Only with the specific written permission of Elsevier

** Voluntary posting of Accepted Author Manuscripts in the arXiv subject repository is permitted.

Figure D.1: Elsevier Table of Author Rights [151]

Appendix E

PUBLICATIONS

1. Lindemer, M.D., Advani, S.G., and Prasad, A.K. 2016. “Hydrogen Production via the Heterogeneous Hydrolysis of Zn Vapor Under a Temperature Gradient: Modeling and Efficiency Analysis”. *Int. J. of Hydrogen Energy* **41** pp. 10556-10567.
2. Lindemer, M.D., Advani, S.G., and Prasad, A.K. 2017. “Experimental Investigation of Heterogeneous Hydrolysis of Zn Vapor Under a Temperature Gradient” *Int. J. of Hydrogen Energy*, in press
3. Lindemer, M.D., Advani, S.G., and Prasad, A.K. 2017. “Lattice Boltzmann Simulation of Reactive Gas/solid Precipitation Process in a Circular Tube” in preparation